

Spin-Orbit Enhanced Superconductivity in Graphene Heterostructures

Thesis by
Yiran Zhang

In Partial Fulfillment of the Requirements for the
Degree of
Doctor of Philosophy

The logo for the California Institute of Technology (Caltech), featuring the word "Caltech" in a bold, orange, sans-serif font.

CALIFORNIA INSTITUTE OF TECHNOLOGY
Pasadena, California

2025
Defended August 13, 2024

© 2025

Yiran Zhang

ORCID: 0000-0002-8477-0074

All rights reserved

ACKNOWLEDGEMENTS

Six years is a long time. A mixed feeling of anticipation and nostalgia surges toward the end of my PhD journey. The period is undoubtedly a transformative one, surrounded by tremendous support and help from amazing people. I can not imagine a better PhD without everyone around and shall take the chance to express my most sincere gratitude.

First and foremost, I would like to thank my advisor Stevan Nadj-Perge for his unconditional support and exceptional mentorship. I still recall the excitement of joining the group when I started at Caltech; thank you for taking me in. I appreciate his delicate balance between allowing freedom for pursuing my own passion yet providing critical insights when I am at unexplored territories. His enthusiasm regarding physics always motivates me to question every aspect of the puzzles and to realize my full potential during the explorations. From him, I learned how to choose and approach problems gracefully, when to persist and to pause, and even about scientific writing. Most importantly, his solid research style deeply shaped my research taste and vision. These are lifetime lessons and I feel immensely grateful.

I have the privilege to share the thrill of discoveries and spend a majority of my time working with two most capable colleagues, Harpreet Arora and Robert Polski. This thesis would not have been possible without you. Fabrication and cleanroom business are sometimes dark magic, so thank you for guiding me through the door. Harpreet, I always admire your courage to try insane ideas and as the first member of the group, you paved a long way for us to thrive. Your persistence and faith in new discoveries are inspiring and I will never forget the astonishing moments together witnessing the magic of tungsten diselenide. It is satisfying to see how the SOC dream pans out over the five years adventures. I adopted the fearlessness from you. Robbie, you are unarguably the kindest person I have worked with. There were countless times I knocked on your office bothering you with measurements and data analysis, or dragged you to cleanroom fighting for machine time at late nights. You are also a master of instrumentation: our dilution fridge is one of the coldest in the field, thanks to you. It is your efforts that enable the transport team to see the finest beauty of quantum materials.

The other group members from Nadj-Perge lab also greatly enlighten me from various perspectives. I appreciate the numerous discussions with Hyunjin Kim and

Youngjoon Choi; they provide a microscopic view of graphene systems and the occasional chats about philosophy of physics research are refreshing. I would like to thank several experienced postdocs for their expertise. Thank you Haoxin Zhou for advanced 2D materials fabrication and characterization techniques, Lingyuan Kong for educating me on unconventional superconductivity in the same office; Ding Zhong was the one who taught me the game-changing WSe_2 exfoliation during the early years. Soudabeh Mashhadi, Hechen Ren, and Jeannette Kemmer provided innovative help and created a productive atmosphere. To the newest generation in the lab, Eli Baum, Justin Siu Chi Wang, and Ankan Mukherjee, you bring in different points of view that challenge me and promote my critical thinking. I wish you all good luck in your future PhD endeavors; it certainly will be rewarding. I was also lucky to spend summers with undergraduate students Ryan de Silva, Addison Davis Olmsted, Pranav Parakh, for exfoliation, electronic schemes, and laughter.

Over the course of many research projects, I have benefited greatly from working with many other collaborators at Caltech and worldwide. I would like to shout out to our theory gang: Jason Alicea, Felix von Oppen, Yuval Oreg, Gil Refael, Alex Thomson, Cyprian Lewandowski, Étienne Lantagne-Hurtubise, Gal Shavit, Zhiyu Dong, Yang Peng. You are the group of people who can quickly shed light on the physics and clear the fog. You always remind me of Occam's razor and to look at experimental data without prejudices. Thank you for the intense weekly meetings over the past five years. Some of the experimental progress was made in collaboration with Andrea Young, Ludwig Holleis, Caitlin Patterson at UCSB; thank you for showing me around and sharing your detailed understanding. Thank you David Hsieh and Youngjoon Han for showing me the optical setup and SHG characterization. Our amazing transport devices would not have been made without the delicate setup in KNI; thanks Guy Derose, Alex Wertheim, Matthew Hunt, Nathan Lee, and Kelly McKenzie for the hard work and maintenance. Nai-Chang Yeh, I appreciate you taking me as a summer undergraduate researcher in your group at Caltech, and it was invaluable experience entering the field of two-dimensional materials. I am fortunate to have Jason Alicea, David Hsieh, and Joseph Falson for being my defense committee as well as my candidacy committee. Thank you all for critical feedback during annual TAC meetings, and Jason, I still recall your comment at my candidacy exam: "Phenomenal job! Keep up the great work." I am glad I did so.

I also deeply appreciate the friendships and companies which enrich my life outside

the lab. To Sijia Wang, Duxing Hao, Xuejian Shen, Christina Wang, Jieyu Zheng, Ke Sun, Qiyuan Zhao, Xiaozhou Feng, Yangrui Chen, everyone from NP lab, and lots of people I didn't mention, thank you for staying around regardless my up and downs. I have known some of you for ten years, and thank you for meeting up, and reminding me where I came from. I am fortunate to chat at Friday dinners, enjoy mountains, beaches, snows around California together, explore the wilderness over the Greater LA area, and pick up new hobbies like bouldering and skiing. Thank you for being by my side.

Lastly, I would also like to mention important people in Shanghai without whom I would probably never have been here in the first place. I would like to thank my high school physics teacher Qian Wan. You are the first magician I met and I was inspired by the elegance of physics you derived from scratches. I still remember your saying: physics is simple yet elegant. Toward the end of my PhD journey, I couldn't agree more. To my parents, being away from home is never easy, and you are the teachers of my lifetime. You taught me to work hard, be humble and responsible, and chase excellence; the spirits are imprinted in me profoundly. Over the past years phone calls, I was not good at explaining the immediate use of my quantum-material research, but I guess it is all about appreciating the beauty and elegance along the journey. Fear less, keep going, and never stop.

Yiran Zhang
Pasadena, CA
August 2024

ABSTRACT

Flat electronic bands in moiré and crystalline graphene multilayers showcase emergent correlated phenomena including correlated insulators, superconductivity, topological orders, etc. This thesis focuses on the electrical transport characterization of superconductivity in moiré and crystalline graphene, with the proximity of a layer of tungsten diselenide (WSe_2) that induces spin-orbit coupling (SOC). The interplay between spontaneous symmetry-breaking and explicit spin-orbit interactions emerges various unconventional superconducting pairing.

In the case of moiré graphene multilayers, superconductivity in twisted bilayer graphene persists much far away from the magic angle at which electronic correlations dominate. At the lowest twist angle 0.79° , superconductivity appears despite the absence of any insulating states. By changing the moiré twist angle, the ratio between Coulomb interactions and kinetic energy is reduced, and we thus established a hierarchy of various symmetry-breaking orders. Importantly, superconductivity is tightly related to the half-filling symmetry-breaking reconstructions. We further generalize the twisted moiré graphene to trilayer, quadrilayer and pentalayer cases. Characterizations around their respective magic angle show that superconductivity is more prominent in filling phase space when the number of layers is increased.

We then investigated the effect of SOC on correlated phases in crystalline Bernal-stacked bilayer graphene. Surprisingly, placing monolayer WSe_2 on bilayer graphene promotes Cooper pairing to an extraordinary degree: field-induced superconductivity is stabilized at zero magnetic field, exhibits an order of magnitude enhancement in critical temperature and occurs over a density range that is wider by a factor of eight. The superconductivity descends from a broken-symmetry parent state with two out of the four spin-valley flavors being predominantly populated. Moreover, the superconductivity arises only for perpendicular electric fields that push hole wavefunctions toward WSe_2 , indicating that proximity-induced Ising spin-orbit coupling plays a key role in stabilizing the pairing.

The last part of the thesis focuses on a new degree of freedom: interfacial twisting between graphene and WSe_2 . We experimentally demonstrate the “moiréless” tuning of superconductivity in Bernal bilayer graphene proximitized by WSe_2 . The precise alignment between the two materials systematically controls the strength of the induced Ising SOC, profoundly altering the phase diagram. As Ising SOC

is increased, superconductivity onsets at a higher displacement field and features a higher critical temperature, reaching up to 0.5K. Within the main superconducting dome and in the strong Ising SOC limit, we find an unusual phase transition characterized by a nematic redistribution of holes among trigonally warped Fermi pockets and enhanced resilience to in-plane magnetic fields. Moreover, we identify two additional superconducting regions, one of which descends from an inter-valley coherent normal state and exhibits a Pauli-limit violation ratio exceeding 40, among the highest for all known superconductors.

PUBLISHED CONTENT AND CONTRIBUTIONS

Manuscripts covered in this thesis:

Arora, H. S.* , Polski, R.* , Zhang, Y.* , Thomson, A., Choi, Y., Kim, H., Lin, Z., Wilson, I. Z., Xu, X., Chu, J.-H., Watanabe, K., Taniguchi, T., Alicea, J., Nadj-Perge, S. Superconductivity in metallic twisted bilayer graphene stabilized by WSe₂. *Nature* **583**, 379-384. ISSN: 0028-0836. arXiv: [2002.03003](https://arxiv.org/abs/2002.03003). <https://www.nature.com/articles/s41586-020-2473-8> (2020). H.S.A., R.P., Y.Z., and S.N.-P. designed the experiment. Y.Z. made and measured some of the devices. H.S.A., R.P., Y.Z., and S.N.-P. analyzed the data. Y.Z. co-wrote the manuscript with input from other authors.

Zhang, Y.* , Polski, R.* , Lewandowski, C., Thomson, A., Peng, Y., Choi, Y., Kim, H., Watanabe, K., Taniguchi, T., Alicea, J., von Oppen, F., Refael, G., Nadj-Perge, S. Promotion of superconductivity in magic-angle graphene multilayers. *Science* **377**, 1538-1543. ISSN: 2375-2548. arXiv: [2112.09270](https://arxiv.org/abs/2112.09270). <https://www.science.org/doi/10.1126/science.abn8585> (2022). Y.Z. and R.P. performed the measurements, fabricated the devices, and analyzed the data, with input and materials provided by others. Y.Z. co-wrote the manuscript with input from other authors.

Polski, R.* , Zhang, Y.* , Peng, Y., Arora, H. S., Choi, Y., Kim, H., Watanabe, K., Taniguchi, T., Refael, G., von Oppen, F., Nadj-Perge, S. Hierarchy of symmetry breaking correlated phases in twisted bilayer graphene. arXiv: [2205.05225](https://arxiv.org/abs/2205.05225) (2022). Y.Z. and R.P. performed the measurements, fabricated devices, and analyzed the data, with input and materials provided by others. Y.Z. co-wrote the manuscript with input from other authors.

Zhang, Y., Polski, R., Thomson, A., Lantagne-Hurtubise, É., Lewandowski, C., Zhou, H., Watanabe, K., Taniguchi, T., Alicea, J., Nadj-Perge, S. Enhanced superconductivity in spin-orbit proximitized bilayer graphene. *Nature* **613**, 268-273. ISSN: 0028-0836. arXiv: [2205.05087](https://arxiv.org/abs/2205.05087). <https://www.nature.com/articles/s41586-022-05446-x> (2023). Y.Z. and S.N.-P. designed the experiment. Y.Z. performed the measurements, fabricated the devices, and analyzed the data, with input and materials provided by others. Y.Z. co-wrote the manuscript with input from other authors.

Holleis, L., Patterson, C. L., Zhang, Y., Vituri, Y., Yoo, H. M., Zhou, H., Watanabe, K., Taniguchi, T., Berg, E., Nadj-Perge, S., Young, A. F. Nematicity and orbital depairing in superconducting Bernal bilayer graphene with strong spin orbit coupling. to appear in *Nature Physics*. arXiv: [2303.00742](https://arxiv.org/abs/2303.00742) (2023). Y.Z. fabricated the device and performed the initial measurements.

* indicates co-first authorship

Zhang, Y., Shavit, G., Ma, H., Han, Y., Watanabe, K., Taniguchi, T., Hsieh, D., Lewandowski, C., von Oppen, F., Oreg, Y., Nadj-Perge, S. Twist-programmable superconductivity in spin-orbit coupled bilayer graphene. to appear on arXiv. Y.Z. and S.N.-P. designed the experiment. Y.Z. fabricated the devices, performed the measurements, and analyzed the data. Y.Z. co-wrote the manuscript with input from other authors.

Other contributed manuscripts

- Choi, Y., Kemmer, J., Peng, Y., Thomson, A., Arora, H. S., Polski, R., Ren, H., Alicea, J., Refael, G., Watanabe, K., Taniguchi, T., Nadj-Perge, S. Electronic correlations in twisted bilayer graphene near the magic angle. *Nature Physics* **15**, 1174-1180. ISSN: 1745-2473. arXiv: [1901.02997](https://arxiv.org/abs/1901.02997). <https://www.nature.com/articles/s41567-019-0606-5> (2019).
- Choi, Y., Kim, H., Peng, Y., Thomson, A., Lewandowski, C., Polski, R., Zhang, Y., Arora, H. S., Watanabe, K., Taniguchi, T., Alicea, J., Nadj-Perge, S. Correlation-driven topological phases in magic-angle twisted bilayer graphene. *Nature* **589**, 536-541. ISSN: 0028-0836. arXiv: [2008.11746](https://arxiv.org/abs/2008.11746). <https://www.nature.com/articles/s41586-020-03159-7> (2021).
- Choi, Y., Kim, H., Lewandowski, C., Peng, Y., Thomson, A., Polski, R., Zhang, Y., Watanabe, K., Taniguchi, T., Alicea, J., Nadj-Perge, S. Interaction-driven band flattening and correlated phases in twisted bilayer graphene. *Nature Physics* **17**, 1375-1381. ISSN: 1745-2473. arXiv: [2102.02209](https://arxiv.org/abs/2102.02209). <https://www.nature.com/articles/s41567-021-01359-0> (2021).
- Kim, H., Choi, Y., Lewandowski, C., Thomson, A., Zhang, Y., Polski, R., Watanabe, K., Taniguchi, T., Alicea, J., Nadj-Perge, S. Evidence for unconventional superconductivity in twisted trilayer graphene. *Nature* **606**, 494-500. ISSN: 0028-0836. arXiv: [2109.12127](https://arxiv.org/abs/2109.12127). <https://www.nature.com/articles/s41586-022-04715-z> (2022).
- Kolář, K., Zhang, Y., Nadj-Perge, S., von Oppen, F., Lewandowski, C. Electrostatic fate of N -layer moiré graphene. *Physical Review B* **108**, 195148. ISSN: 2469-9969. arXiv: [2307.07531](https://arxiv.org/abs/2307.07531). <https://journals.aps.org/prb/abstract/10.1103/PhysRevB.108.195148> (2023).
- Kim, H., Choi, Y., Lantagne-Hurtubise, É., Lewandowski, C., Thomson, A., Kong, L., Zhou, H., Baum, E., Zhang, Y., Holleis, L., Watanabe, K., Taniguchi, T., Young, A. F., Alicea, J., Nadj-Perge, S. Imaging inter-valley coherent order in magic-angle twisted trilayer graphene. *Nature* **623**, 942-948. ISSN: 0028-0836. arXiv: [2304.10586](https://arxiv.org/abs/2304.10586). <https://www.nature.com/articles/s41586-023-06663-8> (2023).
- Kong, L., Papaj, M., Kim, H., Zhang, Y., Baum, E., Li, H., Watanabe, K., Taniguchi, T., Gu, G., Lee, P. A., Nadj-Perge, S. Observation of Cooper-pair density modulation state. arXiv: [2404.10046](https://arxiv.org/abs/2404.10046). (2024).

TABLE OF CONTENTS

Acknowledgements	iii
Abstract	vi
Published Content and Contributions	viii
Table of Contents	x
List of Illustrations	xiii
List of Acronyms	xxxiii
Chapter I: Introduction	1
1.1 The beauty of many-body electrons	1
1.2 Highly tunable two-dimensional materials	2
1.3 The electronic properties of monolayer graphene	4
1.4 Flat electronic bands: Twisted bilayer graphene	7
1.5 Flat electronic bands: Bernal bilayer graphene	11
1.6 Consequences of flat electronic bands: Stoner ferromagnetism	13
1.7 Spin-orbit coupling	16
1.8 Unconventional superconductivity from reduced symmetries	20
Chapter II: Device design and characterization	33
2.1 2D materials exfoliation	33
2.2 Van der Waals heterostructure assembly	39
2.3 Cleanroom processes	45
2.4 Electrical transport measurement	47
2.5 Penetration field capacitance measurement	50
2.6 Dilution refrigerator setup	52
Chapter III: Superconductivity in metallic twisted bilayer graphene stabilized by WSe ₂	55
3.1 Adding WSe ₂	55
3.2 TBG-WSe ₂ devices under study	56
3.3 Twist-angle dependent phase diagram	56
3.4 Disappearing insulating gaps	59
3.5 Evidence for spin-orbit interactions	61
3.6 Theory of spin-orbit coupling in TBG	64
3.7 Connection between superconductivity and Fermi-surface recon- struction	67
Chapter IV: Promotion of superconductivity in magic-angle graphene multi- layers	71
4.1 Alternating twisted graphene multilayers	71
4.2 TTG, TQG, and TPG devices under study	74
4.3 Insulators in TTG and TQG	78
4.4 Electric-field tunable superconductivity	79

4.5 Interplay between superconductivity, flavor symmetry-breaking transitions, and van Hove singularities	81
4.6 Extended superconducting pockets to $\nu \approx +5$ in TPG	83
4.7 Conclusion	90
Chapter V: Enhanced superconductivity in spin-orbit proximitized bilayer graphene	91
5.1 The advantages of Bernal bilayer graphene coupled to WSe ₂	91
5.2 Asymmetry with electrical displacement field	96
5.3 Estimating SOC strength	97
5.4 Superconductivity at zero magnetic field	99
5.5 Fermi surfaces of the flavor-polarized states	102
5.6 Doping-dependent Pauli-limit violation	106
5.7 Discussion	109
Chapter VI: Twist-programmable superconductivity in spin-orbit coupled bilayer graphene	113
6.1 Programmable Ising SOC by interfacial twisting between BLG and WSe ₂	113
6.2 Twist-programmable superconducting phase diagram	120
6.3 Superconductivity across nematic redistribution and from inter-valley coherence	123
6.4 Ultra-strong Pauli-limit violation: SC ₁ and SC ₃	126
6.5 Nematicity-intertwined B_{\parallel} depairing: SC ₂	128
Chapter VII: Discussion and outlook	134
7.1 Twisted moiré graphene	134
7.2 Crystalline graphene multilayers	136
Appendix A: Supplementary materials for Chapter 3	161
Appendix B: Supplementary materials for Chapter 4	162
Appendix C: Supplementary materials for Chapter 6	164

LIST OF ILLUSTRATIONS

<i>Number</i>	<i>Page</i>
1.1 Different 2D van der Waals materials. The crystal lattice of graphene (a), hexagonal boron nitride (b), and tungsten diselenide (c).	2
1.2 Ultra tunability of 2D van der Waals materials. Electrostatic gating controls the doping level, and multiple gates control the electrical displacement field. Moiré periodic potential is created by twisting two layers of lattice-matched materials or simply by putting together two materials with slight lattice mismatch. Additionally, stacking different materials on top of each other introduces ultra-clean interfaces for electrical transport measurements or induces proximity effect on demand.	3
1.3 Crystal structure of monolayer graphene. Carbon atoms form honeycomb lattice. Red and Blue circles mark the <i>A</i> and <i>B</i> sublattices.	4
1.4 Band structure of monolayer graphene. (a) Energy band dispersion of the monolayer graphene calculated from the tight-binding model. (b) First Brillouin zone of monolayer graphene.	6
1.5 Twisted bilayer graphene. (a) Two layers of graphene are twisted relative to each other with an angle θ forming moiré superlattice; moiré wavelength scales as $a_M \sim a/\theta$. (b) The valleys from two layers of graphene strongly hybridize forming moiré Brillouin zone. (c) Schematic shows band hybridization forming moiré flat bands.	8
1.6 Continuum model of TBG band structure for twist angles above, around, and below the magic angle, showing the flattest near the magic angle.	11
1.7 Electronic band structure of Bernal bilayer graphene. (a) Crystal structure of Bernal bilayer graphene. The sublattices on different layers are marked out. (b),(c) Band structure of BLG at zero displacement field for large (b) and small (c) energy ranges. (d) Band structure of BLG at a large finite <i>D</i> field.	12

1.8	Flavor symmetry breaking in moiré graphene flat bands. (a)-(d) Configuration for flavor polarization at different filling factors; here twist bilayer graphene as an example.	15
1.9	Band structure with Rashba and Ising SOC. (a),(b) Energy and momentum relation for Rashba- (a) and Ising- (b) type spin-orbit interactions. (c),(d) Constant energy contour showing the spin winding for the two cases.	19
1.10	A depiction showing two time-reversal paths of electrons. Weak localization and weak anti-localization interference constructively and destructively. Conductance forms dip and peak at zero magnetic field.	20
1.11	A depiction showing spin-valley energy levels moving with magnetic field. Microwave photon probes the transitions that can back track the SOC at zero magnetic field.	21
1.12	Uemura plot showing T_c compared to T_F across various superconductors. Reprinted from [16], with permission from the copyright holder, Springer Nature.	23
1.13	Superconducting pairing wavefunctions showing s -wave (a), p -wave (b), and d -wave (c).	24
1.14	Unconventional pairing in high-temperature superconductor. (a) Temperature versus hole doping level for the copper oxides, indicating where various phases occur. (b) Superconducting gap and pseudogap amplitude in momentum space. Reprinted from Ref. [77], with permission from the copyright holder, Springer Nature.	24
1.15	Spinless p -wave pairing. (a) Sketch of Kitaev's 1D p -wave superconducting tight binding chain [93]. (b) Braiding two pairs of Majorana quasiparticles.	27
1.16	Rashba SOC + B_{\parallel} + superconductivity. (a) 1D parabolic bands with Rashba SOC. (b) With Rashba SOC and in-plane magnetic field. (c) Further increasing in-plane magnetic field. (d) Inducing superconductivity.	29

1.17	Ising superconductivity. (a) Ising SOC band splitting. (b) Ising pairing across K and K' valley. (c) Side view and top view of monolayer transition metal dichalcogenides. (d) In-plane field dependence of Ising superconductivity showing Pauli-limited violation. Reprinted from Ref. [100], with permission from The American Association for the Advancement of Science.	31
2.1	Exfoliation tapes. Different tapes with bulk crystals of graphite (a), hBN (b), and WSe ₂ (c).	34
2.2	Different 2D materials flakes. Optical images of graphene multilayers (a), thick (top) and thin (bottom) hBN (b), and WSe ₂ layers (c).	38
2.3	Raman spectroscopy mapping of trilayer graphene. (a) An optical image of trilayer graphene multilayers. (b) Raman spectroscopy 2D peak width mapping of the trilayer graphene area. The rhombohedral (ABC-) trilayer area has a wider 2D Raman peak in comparison to the Bernal (ABA-) stacked area.	38
2.4	PC/PDMS stamps. Optical images of PC/PDMS stamps. From left to right are PC on flat PDMS stamp, PC on domed PDMS stamp, and also polypropylene carbonate (PPC) on domed PDMS stamp.	39
2.5	A transfer setup used to make van der Waals heterostructure stacks.	40
2.6	Dry flake transfer process with PC/PDMS stamp. (a)–(e), Critical steps in the stacking process. (f) Optical images of a typical flake and stacks at different stages of the fabrication.	42
2.7	AFM cutting. (a) Schematic showing d.c. AFM cutting. (b) Optical image of graphene multilayers by AFM cutting.	45
2.8	Optical images of different devices. (a) An optical image showing twisted bilayer graphene with WSe ₂ Hall bar geometry. (b) An optical image showing Bernal bilayer graphene with WSe ₂ dual-gated device in R_{xx} geometry.	47
2.9	Transport measurement geometry. (a) A Hall bar geometry. (b)–(e) The combination of the four configurations can give V_{xx} and V_{xy} components.	48
2.10	Penetration field capacitance measurement. (a) Electrical circuit of penetration field capacitance measurement. (b) an optical image of vertical HEMT mount.	51

2.11	Dilution refrigerator setup. (a) Oxford Triton dilution refrigerator setup; here showing the fridge, measurement rack, gas handling rack, and magnet power supply. (b) Inside dilution fridge; from top to bottom are PT1 plate, PT2 plate, still plate, cold plate, and mixing chamber plate with sample loading at the bottom.	52
2.12	Sample puck. (a),(b) Configuration for out-of-plane magnetic field measurements. (c) Configuration for large in-plane magnetic field measurements.	54
3.1	The lattice constant of graphene (a) and WSe ₂ (b). Stacking them together introduces proximitized SOC to graphene (c).	55
3.2	Bottom-gated WSe ₂ -TBG devices. (a) the typical geometry for TBG-WSe ₂ devices, including WSe ₂ and TBG in between two hBN and a globe gold gate. (b) R_{xx} versus filling factor ν measured from different contacts with uniform twist angle $\theta = 0.88^\circ$. right inset shows the optical image of the device and left inset shows the gate curve as a function of displacement field.	57
3.3	R_{xx} versus temperature and filling factor ν for TBG-WSe ₂ devices with twist angle $\theta = 1.10^\circ$ (a), 0.97° (b), 0.87° (c), and 0.79° (d), respectively.	58
3.4	Superconducting Fraunhofer pattern measured from devices with twist angle $\theta = 0.97^\circ$ (a), 0.87° (b), and 0.79° (c), respectively.	58
3.5	Correlated insulating states for TBG-WSe ₂ device at $\theta = 0.97^\circ$. $\nu = +2$ and $\nu = +3$ show activating behavior.	60
3.6	Large temperature range R_{xx} for $\theta = 0.87^\circ$ (a) and $\theta = 0.79^\circ$ (c) devices. Selective gate curves at different temperatures are shown in (b) and (d). (e) shows temperature dependence of conductance measured at the filling factors marked by the corresponding colored arrows in (a) and (c). The green lines correspond to activation fit. (f) shows metallic behavior around $\nu = +1$ and $\nu = +2$ for the $\theta = 0.87^\circ$ devices.	61

- 3.7 Characterizations for a second TBG-WSe₂ device at $\theta = 0.8^\circ$. (a) R_{xx} measured as a function of ν and temperature for a second TBG-WSe₂ device at $\theta = 0.8^\circ$. (b) Landau Fan diagram for the same device. (c) $I - V$ characteristic at different temperature showing a superconducting transition for Berezinskii–Kosterlitz–Thouless extraction. (d) Fraunhofer pattern measured from the device confirming the superconducting phase coherence. 62
- 3.8 Weak antilocalization signatures. (a) R_{xx} versus backgate voltage for the $\theta = 0.8^\circ$ device. (b),(e) Conductance change, relative to the 0 mT value, versus out-of-plane magnetic field and backgate voltages. (c),(d) Averaged data from (b) for different field ranges. The dashed lines are comparison to the weak antilocalization model used for monolayer graphene/TMD. 63
- 3.9 Landau fan diagrams for TBG-WSe₂. (a)-(c) Landau fan diagrams for three devices with $\theta = 0.97^\circ, 0.87^\circ$, and 0.79° , respectively. The main Landau level sequences are $\pm 2, \pm 4, \pm 6$, etc. that break four-fold degeneracy, consistent with the existence of SOC. (d),(e) quantum Hall conductance measured at different magnetic field showing quantized plateaus at $\pm 2, \pm 4, \pm 6e^2/h$, suggesting high quality of our devices. 65
- 3.10 Spin–orbit effect on TBG band structure. (a)–(f), Continuum-model results for valley K that include Ising and Rashba spin–orbit coupling at twist angles of 0.87° (a)–(c) and 0.79° (d)–(f). (a),(d) Band structure along the high-symmetry directions of the Brillouin zone. The color represents the out-of-plane spin projection, $\langle S_z \rangle$, and the dotted line denotes the chemical potential at $\nu = +2$. (b),(c),(e),(f) Energy of the conduction flat bands with spin–orbit coupling. Colored line indicates the in-plane spin projection. Black line corresponds to SOC-free case. 66

3.11	Phase diagram of various correlated phases focusing on superconductivity. The main panel plots critical temperature T_c as a function of twist angle; electron side (red dots) and hole side (blue dots). For hole side, T_c peaks around the magic angle, and for electron side T_c is somewhat suppressed at the magic angle due to the competition with correlated insulator at $\nu = +2$. When tuning away, electron-side T_c increases. On top, we show the rough ranges of various correlated phases, among which correlated insulator and ferromagnetism only appear around the magic angle. Ultimately, tuning away from the magic angle both electron and hole side superconductivity diminished together with the cascade of symmetry-broken transition around the half filling.	68
3.12	Hall density reset at different twist angles. Hall density (n_{Hall}) versus filling factor ν for TBG-WSe ₂ devices with angle $\theta = 0.79^\circ, 0.88^\circ, 0.97^\circ, 1.04^\circ, 1.1^\circ, 1.23^\circ$, respectively. The respect offset Hall density values are indicated by gray horizontal solid lines.	70
4.1	Schematics of the alternating twisted graphene multilayers. (a)-(c) schematics of alternating twisted trilayer (a), quadrilayer (b), and pentalayer (c) graphene, where each successive layer is twisted by an angle $\pm\theta$ relative to the previous one in an alternating sequence.	71
4.2	Band structure of twisted trilayer (a), quadrilayer (b), and pentalayer (c) graphene for angles close to the respective theoretical magic angle at zero D field (left) and $D/\epsilon_0 \approx 0.4 \text{ V nm}^{-1}$ (right) for valley K	74
4.3	Line cuts of R_{xx} versus filling factor ν for a range of temperatures (shown are traces taken first at 25 mK, then every 0.25 K from 0.25 K to 2 K, followed by every 1 K from 3 K to 7 K), from top to bottom measured at $D/\epsilon_0 = 0.22 \text{ V nm}^{-1}$ (a), -0.15 V nm^{-1} (b), and 0 V nm^{-1} (c), respectively.	75
4.4	R_{xx} versus temperature and ν around half filling, showing superconducting domes around $ \nu = 2$ in TTG, TQG, and TPG, respectively. Ginzburg–Landau coherence lengths ξ_{GL} versus ν for all three devices are superimposed on the R_{xx} versus T and ν plots.	76

- 4.5 Twisted graphene multilayers sample uniformity. (a)-(c) Leftmost optical images of the three twisted graphene multilayers. The scale bar in each panel corresponds to $5 \mu\text{m}$. R_{xx} versus density and displacement field (n - D) plots shown in the middle are obtained from electrodes marked with the corresponding colored lines. Rightmost plots are R_{xx} versus carrier density with top-gate voltage fixed at $V_{\text{tg}} = 0 \text{ V}$ (gate sweeps are along the grey dashed lines in the n - D plots). All the three devices have a high degree of homogeneity in twist angle with the same superconducting filling range and $|\nu| = 4$ carrier density for multiple contacts. The behavior of superconductivity and other symmetry-breaking features is highly reproducible for different contacts. 77
- 4.6 Half-filling correlated insulating state in TTG. (a) R_{xx} versus temperature and ν for the trilayer focusing around $\nu = +2$ at $D/\epsilon_0 = 0.26 \text{ V nm}^{-1}$. (b) Line cuts of R_{xx} versus ν for a range of temperatures on the electron side for TTG. (c) Conductance versus T^{-1} for TTG showing thermal activation behavior. (d) R_{xx} versus D and temperature at $\nu = +1.96$ in TTG. Out-of-plane (e) and in-plane (f) magnetic field dependence of R_{xx} versus ν in TTG. 79
- 4.7 Charge-neutrality insulating state in TQG. (a) Line cuts of R_{xx} versus ν for a range of temperatures around charge-neutrality point. (b) R_{xx} versus D and temperature around CNP in TQG. (c) Experimental charge-neutrality gap of TQG as a function of D field. (d) The continuum-model gap as a function of potential difference U . Inset, single-particle band structure of TQG (slightly above the magic angle) at $U = 0 \text{ meV}$ and 150 meV , respectively. 80
- 4.8 TTG, TQG, and TPG n - D phase diagrams. (a)-(c) R_{xx} versus filling factor ν and displacement field D for twisted trilayer (a), quadrilayer (b), and pentalayer (c) graphene, respectively. All data are taken at 25 mK , and the dark blue regions signal superconductivity. For electron-doped TTG and TQG, superconducting regions extend toward $\nu = +1$ at intermediate D field. 80

- 4.9 *D*-tuned superconductivity in the three structures. (a)-(c) R_{xx} versus temperature and *D* (or equivalent potential difference *U* between layers) for the filling factors indicated by arrows in Fig. 4.8. Critical temperature T_c is indicated by a dashed line that delineates 10% of the normal state resistance. T_c is maximized at finite *D* fields. Overall, superconductivity is suppressed more easily with *D* as the layer number is increased. (e),(f) Theoretical calculations of the inverse of the flat-band bandwidth for twisted trilayer, quadrilayer, and pentalayer graphene as a function of D/ϵ_0 (e) and potential difference *U* (f). For a fixed *D*, the bandwidth of the flat bands is larger for systems with more layers, but when expressed as a function of *U*, the flat-band broadening follows a similar trend across the different structures. 81
- 4.10 Interplay between superconductivity, flavor symmetry-breaking transitions and van Hove singularities in TTG and TQG. (a),(b) *D* field and ν dependence of R_{xx} (top) and Hall density (bottom, measured at $B = 0.9$ T) for TTG. Purple and grey dashed lines mark the filling factors where flavor symmetry-breaking transitions associated with $|\nu| = 2$ and $|\nu| = 3$ happen, respectively. The yellow line in (a) delineates the evolution of the vHs. (c),(d) *D* field and ν dependence of R_{xx} (top) and Hall density (bottom, measured at $B = 1.5$ T) for TQG. Superconducting T_c reaches its maximum (orange dot in (d)) exactly at the position of the vHs. When present, flavor symmetry-breaking transitions around $|\nu| \approx 3$ coincide with the termination of superconductivity ((a), (b), (d)). By contrast, superconductivity extends much further in the absence of a $|\nu| \approx 3$ reset (c). 83

- 4.11 Interplay between superconductivity, flavor symmetry-breaking transitions and van Hove singularities in TPG. (a) D field and ν dependence of Hall density for TPG measured at $B = 1.5$ T. (b) Schematic of Hall density (a) and R_{xx} (Fig. 4.8c) features for the pentalayer, including the boundary of the superconducting region (red), vHs/“gap” (dark blue), cascade (light blue), and $|\nu_{\text{flat}}| = 4$ Hall density reset (light purple). Sketches of the DOS around $\nu = +2$ for different D fields are shown on the right. The middle panel illustrates the flavor symmetry polarization observed in regions that support superconductivity. Flavor symmetry is preserved at higher D fields, as shown in the top and bottom panels. 84
- 4.12 Temperature dependence of TPG measured at different D fields. (a)-(e) R_{xx} versus filling factor ν and temperature measured at $D/\epsilon_0 = 0$ (a), 0.115 (b), 0.24 (c), 0.32 (d) and 0.44 V nm⁻¹ (e), respectively. 85
- 4.13 Superconductivity at extended filling factors in TPG. (a),(b) D field and ν dependence of R_{xx} (a) and Hall density (b), showing the region around the electron-side superconducting pocket. The grey line in (a) marks the vHs originating from the dispersive TBG-like bands. (c) The evolution of dV/dI as a function of I and B_{\perp} measured at $\nu = +4.6$, $D/\epsilon_0 = 0.12$ V nm⁻¹ (marked by a yellow dot in (a)), confirming the robustness of superconductivity above $\nu = +4$ 86
- 4.14 Hartree corrections in TPG. (a)-(d) Depiction of different approximation schemes used to understand the role of interactions in TPG. The Hartree correction shifts the flat band (purple) up in energy. Cascaded bands in (c) and (d) are shown in green. (d) corresponds to a minimum model of Hartree and Fock effects characterized by a Hartree shift and a Fock gap. (e),(f) Partial filling of each subsystem versus dielectric constant ϵ for a fixed flat-band filling $\nu_{\text{flat}} = +2$ (e) and a fixed total filling $\nu = +5$ (f), respectively. (g) Partial filling of each subsystem versus total filling ν for a fixed dielectric constant $\epsilon = 11.15$. Here, solid (dashed) lines correspond to a cascaded (uncascaded) solution with the cascade solution enabling higher filling of the flat-band subsystem. (h) Similar to (g) but the solid (dashed) lines correspond to a solution at potential difference $U = 0$ meV ($U = 34$ meV). 87

- 4.15 Van Hove singularities around $\nu = +6$ in TPG. (a),(b) R_{xx} and R_{xy} as a function of ν and B field measured at zero D field for TPG. The sign change in R_{xy} around $\nu = +6$ (marked by arrows in (a) and (b)) indicates vHs. (c),(d) R_{xx} (c) and Hall density (d) as a function of D and ν with gray dashed lines indicating ν linecuts (at $D = 0$) where plots in (a) and (b) were taken. (e) Band structure of TPG calculated using non-interacting model. Arrow indicates the position where vHs from dispersive TBG-like bands is expected. 88
- 4.16 Reset at $\nu \approx +4$ in TPG. (a) Line cuts of R_{xx} (top) and Hall density (bottom, measured at $T = 1.5$ K, $B = 0.5$ T) versus ν for a range of D fields (traces are shown for every 0.05 V nm⁻¹ for both R_{xx} and Hall density). Both the presence of Hall density resets around $\nu = +4$ and the development of superconductivity extending from $\nu = +2$ to $+5$ are shown to persist for a wide range of D fields. (b) R_{xx} versus D and ν measured at $T = 1.5$ K, $B = 0.5$ T (line cuts are shown in (c)). From all the above line cuts, Hall density resets and R_{xx} resistive features consistently exist around $\nu = +4$ 89
- 5.1 Spin-polarized superconductivity in intrinsic Bernal bilayer graphene. (a) Lattice structure of Bernal bilayer graphene. (b) Band structure calculated within a tight-binding model near the Brillouin zone corner. (c),(d) R_{xx} measured at fixed $B_{\parallel} = 0$ (c) and 165 mT (d) at a nominal temperature of 10 mK. (e) B_{\parallel} dependence of linear response resistivity measured at $D/\epsilon_0 = 1.02$ V/nm. (f) Doping dependence of R_{xx} measured at fixed $D/\epsilon_0 = 1.02$ V/nm and $B_{\parallel} = 165$ mT and variable temperatures. Inset measured at doping $n = -0.57 \times 10^{12}$ cm⁻² and the same D field. Reprinted from Ref. [55]; permission from The American Association for the Advancement of Science. 92
- 5.2 BLG-WSe₂ device structure. (a) Schematic of a BLG-WSe₂ structure showing the crystal lattice of Bernal-stacked bilayer graphene (blue and red) and a WSe₂ monolayer (yellow and purple) on top. (b) Schematic of a dual-gated device. Doping density n and D field are controlled by tuning top and bottom gate voltage v_t and v_b . (c) Optical image of the investigated device. The scale bar in the panel corresponds to 10 μ m. 93

- 5.3 Non-interacting valence bands of BLG-WSe₂. Non-interacting valence bands near the K and K' points of the Brillouin zone for $D/\epsilon_0 = -1$ V/nm (a) and 1 V/nm (b), calculated by including an Ising SOC ($\lambda_I = 1$ meV) on the top layer. Schematics show that when BLG is hole-doped, electronic wavefunctions are polarized toward the top layer for $D > 0$, and toward the bottom layer for $D < 0$ 95
- 5.4 Asymmetric n - D phase diagram of BLG-WSe₂. (a) R_{xx} versus doping density n and displacement field D measured at zero magnetic field. Flavor-polarized states show strong asymmetry with respect to the sign of D field. Superconductivity (delineated by a dashed line) spans across wide doping and D ranges at positive D fields (wavefunctions are strongly polarized toward the WSe₂). A competing resistive phase appears in the middle of the superconducting region, as marked by the grey arrow. (b),(d) dV/dI versus n and bias current I measured at $D/\epsilon_0 = 0.9$ V/nm (b) and -1 V/nm (d), respectively. (c) Blue and orange curves are line cuts from (b) and (d), respectively, with the densities marked by the colored bars. 96
- 5.5 Estimating different SOC strengths through quantum Hall effect and quantum oscillations. (a)-(e) R_{xx} versus $\nu = 2\pi\ell_B^2 n$ (ℓ_B is the Landau magnetic length) and D field at $B_\perp = 1$ T, 2 T, 3 T, 5 T, and 7 T, respectively. Arrows mark the transition of $|\nu| = 3$ quantum Hall states with D field. (f),(g) ΔR_{xx} versus $1/B_\perp$ (measured up to $B_\perp = 5$ T) at $D/\epsilon_0 = 0.2$ V/nm, $n = -3.5 \times 10^{11}$ cm⁻² (f) and $D/\epsilon_0 = -0.1$ V/nm, $n = -20 \times 10^{11}$ cm⁻² (g), respectively. The corresponding FFT data are shown in (h) and (i). Inset of (h) shows the FFT splitting B_{split} (marked by black arrows in the main panel) versus doping density n measured at $D/\epsilon_0 = 0.2$ V/nm. Colored lines show the FFT splitting predicted from band structure calculations for the same D field, using Ising SOC $\lambda_I = 0.7$ meV with Rashba SOC $\lambda_R = 0$ meV (purple line) and $\lambda_R = 4$ meV (yellow line). 98

- 5.6 Temperature dependence of superconductivity. (a)-(c) R_{xx} versus density n and temperature for hole doping, showing superconducting domes in the FP(2,2)₊ phase for $D/\epsilon_0 = 1$ V/nm (a), 0.9 V/nm (b), and 0.8 V/nm (c), respectively. A competing resistive phase intersects the superconducting domes at these D fields. (d) Line cuts of R_{xx} versus n for a range of temperatures (from 28 mK to 1 K) measured at $D/\epsilon_0 = 1$ V/nm. The inset shows the V - I plot at $n = -5.75 \times 10^{11}$ cm⁻² and various temperatures. The green dashed line marks where $V \sim I^3$, from which we determine $T_{BKT} = 260$ mK. (e) R_{xx} versus temperature measured at $n = -5.75 \times 10^{11}$ cm⁻² showing a superconducting transition. 100
- 5.7 Out-of-plane magnetic field dependence of superconductivity. (a) Critical current disappearing with B_{\perp} field measured at $D/\epsilon_0 = 0.9$ V/nm, $n = -5.05 \times 10^{11}$ cm⁻². (b) R_{xx} versus n and B_{\perp} field around the superconducting region for $D/\epsilon_0 = 1$ V/nm. 101
- 5.8 Transverse magnetic focusing with an out-of-plane magnetic field. (a) Non-local resistance R_{nl} measured as a function of n and B_{\perp} at $D/\epsilon_0 = 0.6$ V/nm with the measurement configuration shown in (b). 102
- 5.9 Band structure and Fermi surfaces for single spin-valley flavor. (a) Non-interacting valence bands near the K/K' point for at large displacement field featuring trigonal warped pockets and a flat portion of the band. (b) The evolution of Fermi surfaces as a function of doping for single spin-valley flavor. 103
- 5.10 Fan diagram and Fermi surfaces at $D/\epsilon_0 = -1$ V/nm. (a) R_{xx} versus B_{\perp} and doping density n for $D/\epsilon_0 = -1$ V/nm. (b) Fourier transform of $R_{xx}(1/B_{\perp})$ versus n and f_v for $D/\epsilon_0 = -1$ V/nm. The schematics on top show the corresponding symmetry-breaking Fermi surfaces. (c) R_{xx} versus doping density n for the same density range. (d-f) The same data as the one in (a)-(c), but zoom in certain density ranges. 104
- 5.11 Fan diagram and Fermi surfaces at $D/\epsilon_0 = 1$ V/nm. (a) R_{xx} versus B_{\perp} and doping density n for $D/\epsilon_0 = 1$ V/nm. (b) Fourier transform of $R_{xx}(1/B_{\perp})$ versus n and f_v for $D/\epsilon_0 = 1$ V/nm. The schematics on top show the corresponding symmetry-breaking Fermi surfaces. (c) R_{xx} versus doping density n for the same density range. (d),(e) Fermi level and Fermi surfaces of the FP(6)₊ (d) and the FP(6,6)₊ (e) phase. 105

- 5.12 Zoomed-in Fan diagram and Fermi surfaces at $D/\epsilon_0 = 1$ V/nm. (a) R_{xx} versus B_{\perp} and doping density n for $D/\epsilon_0 = 1$ V/nm. (b) Fourier transform of $R_{xx}(1/B_{\perp})$ versus n and f_v for $D/\epsilon_0 = 1$ V/nm. (c) R_{xx} versus doping density n for the same density range. The schematics show the corresponding symmetry-breaking Fermi surfaces. 106
- 5.13 Doping-dependent Pauli-limit violation.(a) R_{xx} versus in-plane magnetic field B_{\parallel} and doping density n for $D/\epsilon_0 = 1.1$ V/nm. The red line delineates the T -dependent superconducting dome, and open circles indicate the zero-magnetic-field critical temperature T_c^0 that is defined by the temperature at which R_{xx} is 50% of the normal state resistance. (b) The ratio of in-plane critical magnetic field $B_{c\parallel}$ to the Pauli-limit field $B_p = 1.86 \text{ T/K} \times T_c^0$ is plotted as a function of normalized temperature T/T_c^0 at two doping densities $n = -6 \times 10^{11} \text{ cm}^{-2}$ and $-7 \times 10^{11} \text{ cm}^{-2}$. Inset: the same data as in the main panel but plotted in $B_{c\parallel}$ versus T . (c) Pauli violation ratio $B_{c\parallel}^0/B_p$ as a function of density n . The doping trend of the PVR is well captured by a model (blue line in the inset) taking into account fixed Ising SOC together with doping-dependent Rashba SOC and constant orbital depairing. . 107
- 5.14 Depairing model for doping-dependent Pauli violation ratio. (a),(b) Pauli violation ratio expected in a system with: Ising g_I and Rashba $g_R k_F$ coupling (a), Ising g_I and orbital \tilde{g}_{orb} coupling (b). Note that \tilde{g}_{orb} is a dimensionless quantity: the corresponding orbital energy scale is $\tilde{g}_{\text{orb}}\mu_B B$ 109
- 5.15 Ground state selection by Ising SOC. (a),(b) Fermi surfaces of the $\text{FP}(2, 2)_+$ phase with Ising SOC and nematic order (a), or allowing for inter-valley coherent order (b). Dashed Fermi pockets correspond to the condition that nematic order is absent. (c) Schematics of a proposed scenario where Ising SOC tilts the energy balance toward IVC order, within which the development of superconductivity is more favored, at the expense of a state which is not conducive to pairing, e.g., a valley polarized state. 110

- 5.16 Additional device with different Ising SOC. (a) R_{xx} versus doping density n and displacement field D measured at zero magnetic field for an additional device. (b) R_{xx} versus B_{\perp} and doping density n for $D/\epsilon_0 = 1.1$ V/nm. (c) Fourier transform of $R_{xx}(1/B_{\perp})$ versus n and f_v for $D/\epsilon_0 = 1.1$ V/nm. (d) R_{xx} versus n at zero magnetic field for the same D field. The superconducting phase possesses a flavor-polarized normal state with two majority and four minority Fermi pockets (denoted as FP(2,4)₊). Schematic depicts the possible Fermi surface structures. (e) Device optical image. (f) R_{xx} versus density n and temperature showing a superconducting dome at $D/\epsilon_0 = 1.15$ V/nm. (g) R_{xx} versus n and B_{\perp} around the superconducting region for $D/\epsilon_0 = 1.1$ V/nm. 112
- 6.1 Schematics for interfacial twisting between BLG and WSe₂. (a) Schematic showing the twisting of the BLG-WSe₂ interface; tuning the interfacial twist angle θ between the two largely lattice-mismatched materials modifies the Ising SOC strength $|\lambda_I|$ and the correlated phase diagram. (b),(c) The schematics show the relative rotation between the BLG and WSe₂ Brillouin zones. At $\theta \approx 0^\circ$ (b), K/K' valleys of BLG couple more effectively to one of the two WSe₂ valleys, resulting in large induced Ising SOC. In contrast, at $\theta \approx 30^\circ$ (c), inter-valley and intra-valley tunneling between WSe₂ and BLG have the same amplitude by reflection symmetry so that Ising couplings of opposite sign cancel each other and result in vanishing proximity coupling. 114
- 6.2 Identifying the crystal edges of graphene and WSe₂. (a) Optical image of a WSe₂ crystal. (b) Second harmonic generation for the WSe₂ flake shown in (a). (c) Optical image of a large BLG flake. Straight edges form angles 150° that are consistent with the three straight edges being along zigzag- or armchair-edge direction. (d) Zoom-in image of the BLG in (c), showing small BLG pieces that are separated by atomic-force-microscope-actuated cutting. All the scale bars correspond to $10\mu\text{m}$ 116

- 6.3 Fabricating twisting BLG-WSe₂ on the same chip. (a)-(c) Flake transferring processes for the continuous interfacial twisting. The BLG pieces are sequentially picked up with an angle relative to WSe₂ in increment of 6°, from ~ 0° to 30°. (d) Optical image of the twisting stack, clearly showing that the BLG pieces form different twist angles relative to the WSe₂ crystal. (e) Optical image of the finished device set D1. All the scale bars correspond to 10μm. 117
- 6.4 Tunable Ising SOC by twisting between BLG and WSe₂. (a),(b) Non-interacting valence bands of BLG near the *K* and *K'* points of the Brillouin zone at $D/\epsilon_0 = 0.2$ V/nm, with proximitized Ising SOC $|\lambda_I| \approx 1.6$ meV (a) and 0.4 meV (b), respectively. (c),(d) R_{xx} versus out-of-plane magnetic field B_{\perp} and doping n measured at $D/\epsilon_0 = 0.2$ V/nm for devices with $|\lambda_I| \approx 1.6$ meV (c) and 0.4 meV (d), respectively. (e),(f) Fast Fourier transform (FFT) of $R_{xx}(1/B_{\perp})$ versus n and f_v , where f_v denotes the quantum oscillation frequency normalized to the Luttinger volume. The arrow-marked FFT splittings reflect the Ising-induced Fermi-surface imbalance within each valley, where larger Ising SOC (e) features a larger splitting than small Ising SOC (f). 118
- 6.5 Quantifying Ising SOC by quantum oscillations. (a) The same data as the one in Fig. 6.4e, but without frequency normalization to show B_{split} . (b),(c) Experimental (dots) doping-dependent frequency splitting around $f_v = 1/4$ measured at different D fields for a large Ising device (b; $|\lambda_I| \approx 1.4$ meV) and a small Ising device (c; $|\lambda_I| \approx 0.4$ meV). The dashed lines are B_{split} calculated from single-particle band structure using the corresponding Ising SOC values. 119
- 6.6 Ising SOC strength $|\lambda_I|$ versus BLG-WSe₂ interfacial twist angle θ ; data were extracted from three sets of devices D1-D3. The schematics show the relative rotation between the BLG and WSe₂ Brillouin zones. At $\theta \approx 0^\circ$, *K/K'* valleys of BLG couple more effectively to one of the two WSe₂ valleys, resulting in large induced Ising SOC. In contrast, at $\theta \approx 30^\circ$, inter-valley and intra-valley tunneling between WSe₂ and BLG have the same amplitude by reflection symmetry so that Ising couplings of opposite sign cancel each other and result in vanishing proximity coupling. 120

6.7	n - D phase diagrams for devices with various Ising SOC strengths. (a)-(f) R_{xx} versus doping density n and displacement field D for devices with Ising SOC strength $ \lambda_I \approx 0.4$ meV (a), 0.7 meV (b), 0.9 meV (c), 1.4 meV (d), 1.5 meV (e), and 1.6 meV (f), respectively.	121
6.8	Superconducting T_c versus Ising SOC and D field. (a) Optimal superconducting critical temperature T_c^{optimal} versus $ \lambda_I $ and D . (b),(c) R_{xx} versus doping n and temperature for a device with $ \lambda_I \approx 0.4$ meV, showing superconducting domes at $D/\epsilon_0 = 0.4$ V/nm (b) and 1 V/nm (c), respectively. (d),(e) R_{xx} versus doping n and temperature for a device with $ \lambda_I \approx 1.5$ meV, showing superconducting domes at $D/\epsilon_0 = 1.1$ V/nm (d) and 1.285 V/nm (e), respectively. (f),(g) Displacement field D_{onset} at which superconductivity onsets (f) and optimal critical temperature T_c^{optimal} (g) versus Ising SOC strength $ \lambda_I $.	122
6.9	The residual Cooper channel repulsion v_{TAM}^* versus doping n and interlayer potential difference U for $ \lambda_I = 0.4$ meV (left) and 1.4 meV (right), respectively.	123
6.10	Three superconducting regions SC_1 , SC_2 , and SC_3 . (a) R_{xx} versus doping density n and displacement field D for a device with Ising SOC strength $ \lambda_I \approx 1.5$ meV, focusing around the phase space where the three superconducting regions coexist.	124
6.11	Characterization of the three superconducting regions SC_1 , SC_2 , and SC_3 . (a)-(c) Temperature dependence of the three superconducting domes SC_1 (a), SC_2 (b), and SC_3 (c), respectively. (d)-(f) Critical current versus temperature at the corresponding D and n . (g)-(i) Critical current disappearing with B_{\perp} at the same D and n as in (d)-(f).	125
6.12	Ising symmetry-breaking Fermi surfaces of SC_1 . (a) R_{xx} versus n measured at $D/\epsilon_0 = 0.92$ V/nm. The inset shows R_{xx} versus n and temperature for the superconducting dome SC_1 . (b) Frequency-normalized FFT of $R_{xx}(1/B_{\perp})$ over the same doping range as in (a); schematics show the corresponding flavor symmetry-breaking Fermi surfaces.	126

- 6.13 SC₂ across nematic redistribution and SC₃ from inter-valley coherence. (a) R_{xx} versus B_{\perp} and doping density n measured at $D/\epsilon_0 = 1.265$ V/nm for a device with $|\lambda_I| = 1.5$ meV. (b) Frequency-normalized Fourier transform of $R_{xx}(1/B_{\perp})$ over the same doping range as in (a). The arrows mark the primary FFT peaks, as shown in (e). (c) R_{xx} versus doping density n measured at $D/\epsilon_0 = 1.265$ V/nm. Insets show R_{xx} versus n and temperature for the superconducting domes SC₂ (left) and SC₃ (right), respectively. (d) the same data as in (b). The green dashed line marks the continuous transition from FP(2, 2, 2) to FP(2, 4); black dashed lines mark first-order flavor symmetry-breaking transitions. (e) Intensity peaks in f_v extracted from (b). The black solid lines around $f_v = 1$ indicate the results from the Luttinger sum rule. Schematics show the possible flavor-polarized phases, from left to right corresponding to spin-valley locked nematic FP(2, 4), nematic FP(2, 2, 2) with two sizes (green and orange) of trigonal-warping pockets, and inter-valley coherent FP(1, 3, 1). . . . 127
- 6.14 B_{\parallel} dependence of SC₁. (a) R_{xx} versus n measured at $D/\epsilon_0 = 0.92$ V/nm. Inset shows R_{xx} versus n and temperature for the superconducting dome SC₁. (b) Frequency-normalized FFT of $R_{xx}(1/B_{\perp})$ over the same doping range as in (a). (c),(d) n -dependent R_{xx} versus in-plane magnetic field (c) or versus temperature (d), showing the disappearance of SC₁. . . . 128
- 6.15 In-plane field dependence of SC₂ and SC₃. (a) R_{xx} versus doping density n and in-plane magnetic field B_{\parallel} at $D/\epsilon_0 = 1.265$ V/nm for a device with $|\lambda_I| = 1.5$ meV. (b) R_{xx} versus n and temperature at $D/\epsilon_0 = 1.265$ V/nm. . . . 129
- 6.16 Temperature dependence of SC₃ measured at different in-plane magnetic field. (a) R_{xx} versus doping density n and in-plane magnetic field B_{\parallel} showing SC₃ evolution. (b)-(h) R_{xx} versus doping density n and temperature measured from $B_{\parallel} = 0$ T (b) to 6 T (h), 1 T increment step. (i) Optimal critical temperature T_c^{optimal} of SC₃ versus B_{\parallel} . The grey bar marks the Pauli limit B_p 130
- 6.17 In-plane magnetic field dependence of SC₂. (a),(b) R_{xx} versus temperature and B_{\parallel} at $n = -8.5 \times 10^{11}$ cm⁻² (a) and -6.9×10^{11} cm⁻² (b), respectively for $D/\epsilon_0 = 1.2$ V/nm. The colored dashed lines are quadratic fitting by $T_c(B_{\parallel}) = T_c(0) - \alpha \times B_{\parallel}^2$ 131

- 6.18 Coefficient α versus doping for SC₂. (a) Coefficient α versus doping n within the SC₂ dome at $D/\epsilon_0 = 1.2$ V/nm. (b) Normalized FFT of $R_{xx}(1/B_{\perp})$ over the same n and D range as in (a), focusing at low frequencies. Green dashed line marks the nematic redistribution of holes from FP(2, 4) to FP(2, 2, 2). Schematics in (a) show the Fermi-surface evolution versus n , where the smallest trigonal-warping pockets (green) grow rapidly from low to high doping ($-7.3 \lesssim n \lesssim -6.6 \times 10^{11} \text{ cm}^{-2}$). 132
- 6.19 B_{\parallel} dependence of pairing by interband interactions. (a),(b) Theoretical B_{\parallel} depairing with the prominent interband pairing (a) and the suppressed case by valley polarization (b). (c),(d) Theoretical α versus n for FP(2, 4) (c) and versus minority imbalance $\delta n_{\text{minority}}/n_{\text{minority}}$ for FP(2, 2, 2) (d). 133
- A.1 R_{xx} versus temperature and filling factor ν for a range of TBG-WSe₂ devices at different twist angles. 161
- C.1 Quantum oscillations and FFT measured at $D/\epsilon_0 = 1.2$ V/nm. (a) R_{xx} versus out-of-plane magnetic field B_{\perp} and doping density n measured at $D/\epsilon_0 = 1.2$ V/nm for a device with $|\lambda_I| \approx 1.5$ meV. (b) Frequency-normalized Fourier transform of $R_{xx}(1/B_{\perp})$ over the same density range as in (a). (c) Intensity peaks in f_{ν} from (b). (d) zoom-in image at low frequencies from (b). 165
- C.2 Quantum oscillations and FFT measured at $D/\epsilon_0 = 1.265$ V/nm. (a) R_{xx} versus out-of-plane magnetic field B_{\perp} and doping density n measured at $D/\epsilon_0 = 1.265$ V/nm for a device with $|\lambda_I| \approx 1.5$ meV. (b) Frequency-normalized Fourier transform of $R_{xx}(1/B_{\perp})$ over the same doping density range as in (a). (c) Intensity peaks in f_{ν} from (b). 166
- C.3 Identifying FP(2, 2, 2) and FP(1, 3, 1) frequencies from the raw data. (a) R_{xx} versus out-of-plane magnetic field B_{\perp} and doping density n measured at $D/\epsilon_0 = 1.2$ V/nm for a device with $|\lambda_I| = 1.5$ meV. (b) The same data as in (a), but plotted as a function of $1/B_{\perp}$. The corresponding frequencies are marked by colored arrows/lines. (c) Intensity peaks in f_{ν} extracted from the FFT data. 168

- C.4 FP(1, 3) and FP(1, 3, 1) at $D/\epsilon_0 = 0.85$ V/nm and 1 V/nm, respectively. (a),(b) R_{xx} versus out-of-plane magnetic field B_{\perp} and doping density n measured at $D/\epsilon_0 = 0.85$ V/nm (a) and 1 V/nm (b), respectively. (c),(d) Frequency-normalized Fourier transform of $R_{xx}(1/B_{\perp})$ at $D/\epsilon_0 = 0.85$ V/nm (c) and 1 V/nm (d), respectively. (e),(f) Intensity peaks in f_v extracted from the FFT data in (c) and (d). 169
- C.5 FP(1, 3, 1) at $D/\epsilon_0 = 1.2$ V/nm and 1.265 V/nm. (a),(b) R_{xx} versus out-of-plane magnetic field B_{\perp} and doping density n measured at $D/\epsilon_0 = 1.2$ V/nm (a) and 1.265 V/nm (b), respectively. (c),(d) Frequency-normalized Fourier transform of $R_{xx}(1/B_{\perp})$ at $D/\epsilon_0 = 1.2$ V/nm (c) and 1.265 V/nm (d), respectively. (e),(f) Intensity peaks in f_v extracted from the FFT data in (c) and (d). 170
- C.6 FFT of FP(1, 3) and FP(1, 3, 1) with data at lower magnetic field. (a),(c) Frequency-normalized Fourier transform of $R_{xx}(1/B_{\perp})$ at $D/\epsilon_0 = 0.85$ V/nm (a) and 1.2 V/nm (c), respectively. The R_{xx} data are used up to 0.23 T and 0.26 T respectively. (b),(d) R_{xx} variation ΔR_{xx} as a function $1/B_{\perp}$ measured at $n = -3.3 \times 10^{11} \text{ cm}^{-2}$, $D/\epsilon_0 = 0.85$ V/nm (b) and $n = -6 \times 10^{11} \text{ cm}^{-2}$, $D/\epsilon_0 = 1.2$ V/nm (d), respectively. 171
- C.7 Evolution of phase boundaries as a function of B_{\perp} . (a) R_{xx} versus out-of-plane magnetic field B_{\perp} and doping density n measured at $D/\epsilon_0 = 1.2$ V/nm for a device with $|\lambda_I| \approx 1.5$ meV. Phase boundaries are marked out in (b). The black arrows and dashed lines mark the phase boundaries that are not sensitive to B_{\perp} , suggestive of intervalley coherence with little or no net orbital moments. The red line draws the phase boundary of the spin-valley polarized FP(1); the boundary grows (orange arrow) with B_{\perp} due to large orbital moments. 173
- C.8 B_{\parallel} dependence of SC₂ at $D/\epsilon_0 = 1.265$ V/nm. (a) R_{xx} versus doping and B_{\parallel} focusing around SC₂ at $D/\epsilon_0 = 1.265$ V/nm. (b) Fitting coefficient α versus doping density n for SC₂ at the same D . (c) Frequency-normalized Fourier transform of $R_{xx}(1/B_{\perp})$ over the same doping range as in (b), focusing around low frequencies representing the two types of trigonal-warping pockets. Bottom panels show R_{xx} versus temperature and B_{\parallel} at different doping for $D/\epsilon_0 = 1.265$ V/nm. 174

- C.9 B_{\parallel} dependence of SC_2 at $D/\epsilon_0 = 1.2$ V/nm. (a) R_{xx} versus doping and B_{\parallel} focusing around SC_2 at $D/\epsilon_0 = 1.2$ V/nm. (b) Fitting coefficient α versus doping density n for SC_2 at the same D . (c) Frequency-normalized Fourier transform of $R_{xx}(1/B_{\perp})$ over the same doping range as in (b), focusing around low frequencies representing the two types of trigonal-warping pockets. Bottom panels show R_{xx} versus temperature and B_{\parallel} at different doping for $D/\epsilon_0 = 1.2$ V/nm. 175
- C.10 B_{\parallel} dependence of SC_2 at $D/\epsilon_0 = 1.07$ V/nm. (a) R_{xx} versus doping and B_{\parallel} focusing around SC_2 at $D/\epsilon_0 = 1.07$ V/nm. (b) Fitting coefficient α versus doping density n for SC_2 at the same D . (c) Frequency-normalized Fourier transform of $R_{xx}(1/B_{\perp})$ over the same doping range as in (b), focusing around low frequencies representing the single type of trigonal-warping pockets without nematic redistribution of holes. Bottom panels show R_{xx} versus temperature and B_{\parallel} at different doping at $D/\epsilon_0 = 1.07$ V/nm. At this D field, SC_2 does not onset from FP(2, 2, 2). The rapidly changed α with diminished values are accordingly absent. 176

LIST OF ACRONYMS

- 2D** two-dimensional
- AFM** atomic force microscope
- ARPES** angle-resolved photoemission spectroscopy
- BCS** refers to the conventional theory of superconductivity and its discoverers, Bardeen, Cooper, and Schrieffer
- BEC** Bose-Einstein condensate
- BKT** refers to the pinning of Cooper pairs across superconducting transition, named for Berezinskii, Kosterlitz, and Thouless
- BLG** Bernal-stacked bilayer graphene
- CI** correlated insulator
- CNP** charge neutrality point
- DOS** density of states
- hBN** hexagonal boron nitride
- HEMT** high electron mobility transistor
- IPA** isopropyl alcohol
- IVC** inter-valley coherent
- LL** Landau level
- MIBK** methyl isobutyl ketone
- PC** poly(bisphenol A carbonate), a polymer used for flake transfer
- PDMS** polydimethylsiloxane, a polymer used for flake transfer
- PMMA** polymethyl methacrylate, electron-beam resist
- PPC** polypropylene carbonate, a polymer used for flake transfer
- PVR** Pauli violation ratio
- SdH** Shubnikov de Haas, referring to resistance quantum oscillations associated with Landau levels
- SHG** second harmonic generation

- SOC** spin-orbit coupling
- SOI** spin-orbit interactions
- SQUID** superconducting quantum interference device
- STM** scanning tunneling microscopy
- TBG** twisted bilayer graphene
- TMD** transition metal dichalcogenide
- TPG** twisted pentalayer graphene
- TQG** twisted quadrilayer graphene
- TTG** twisted trilayer graphene
- vdW** van der Waals
- vHs** van Hove singularity, diverging density of states resulting from a band edge or saddle point
- WAL** weak antilocalization

Chapter 1

INTRODUCTION

1.1 The beauty of many-body electrons

The central theme of modern condensed matter physics is largely defined by the word *emergence* [1]. Emergence describes the fact that the behavior of a many-body interacting system is dramatically different from the behavior and fundamental laws of each constituting part. Here, the behavior means new quantum phases of matter or collective modes that arise from the interactions among microscopic degrees of freedom. The host of these enigmatic phenomena are typically quantum materials with strong correlations, i.e., electrons in the materials are quantum mechanically strongly entangled: can be strongly coherent or simply repulse each other, etc. The interplay between various interactions is complicated and the outcomes can be significant: the resulting broken-symmetry ground states are likely unprecedented and nowhere close to the starting point! Understanding these phases becomes the driving force behind the development of new theoretical frameworks and experimental tools.

A significant portion of experimental efforts have been dedicated to the design of new quantum materials. An ultimate dream is to have “super” materials that are robust yet highly tunable. Meanwhile, on-demand control [2] of perturbations to Hamiltonian will examine the key ingredients for certain quantum phenomena. Yet, the desire is somewhat contradictory: extreme high-energy robustness means the lost of low-energy delicate tuning. One may want to find a material playground that lies between these two extremes, combining the advantages of both.

The focus of this dissertation is on superconductivity originated from the flat bands of two-dimensional (2D) materials, for both moiré and crystalline cases. By introducing a moiré pattern on twisted 2D materials, an emergent length scale is engineered, leading to significant renormalization of the original energy scales. These moiré systems can then be described by the new length and energy scales, well fit the sweet spot of robust tunability. Similarly, band dispersion is highly tunable with simple experimental knobs for crystalline 2D materials. The ultra-clean nature reduces disorders, thus revealing some brand new finest insights into the correlated phase diagram. The interplay between explicit spin-orbit coupling and

spontaneous symmetry-breaking gives surprises of enhanced superconductivity.

1.2 Highly tunable two-dimensional materials

The intrinsic tunability of 2D materials stems from their reduced dimensionality. The isolation of monolayer graphene [3–5] by mechanical exfoliation marks the beginning of 2D materials. Following the isolation of monolayer graphene, many van der Waals (vdW) 2D materials have been exfoliated into monolayer or thin layers.

Crucially, each of them has its own character. Graphene monolayer is characterized by massless Dirac fermions [6, 7] with ultra high mobility (Fig. 1.1a). Hexagonal boron nitride (hBN; Fig. 1.1b), the cousin of graphene whose sublattices are replaced by boron and nitrogen atoms, is a big band-gap insulator. Transition metal dichalcogenides (TMDs; Fig. 1.1c), such as tungsten diselenide (WSe_2), are direct band gap semiconductors when thinned down to monolayer [8], and they feature strong spin-orbit coupling (SOC) that is extremely important for the dissertation. The category is not limited to these materials but has been extended to superconductors [9], magnets [10], charge density wave materials [11], and even high-temperature superconductors [12]. The first prominent tunability is electrostatic gating. Monolayer or

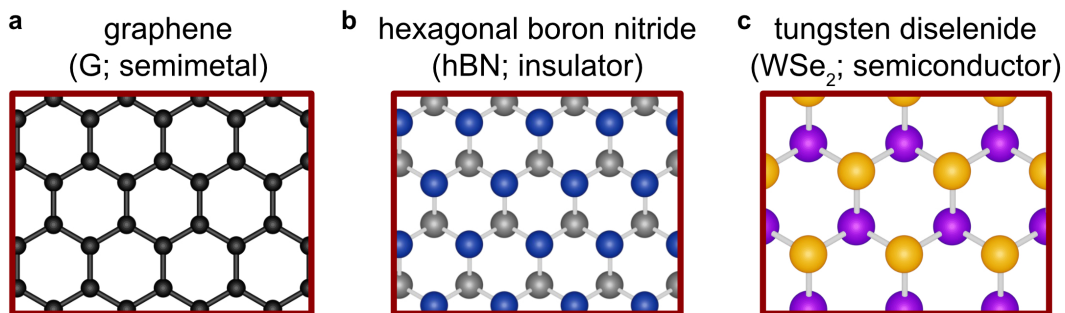


Figure 1.1: Different 2D van der Waals materials. The crystal lattice of graphene (a), hexagonal boron nitride (b), and tungsten diselenide (c).

several layers of 2D materials contain diluted amount of electrons. Additional carriers can be introduced or removed from the system by simple capacitance scheme. The Fermi level is highly tunable by reduced dimension without introducing additional scattering disorder brought by chemical doping. With two gate electrodes on top and bottom, the interlayer potential is independently modified. The band structures of certain systems, such as Bernal bilayer graphene, are highly sensitive to the electrical displacement field. The long-range Coulomb interactions are

weakly screened in a 2D system. By harnessing the low dimensionality, one can also change the screening layers to soften the Coulomb repulsion. Further advancement in the field of 2D materials is the introduction of hexagonal boron nitride (hBN) as dielectric for encapsulation [13, 14], along with stacking manipulation for complex vdW heterostructures. What makes these heterostructures unique, compared to syn-

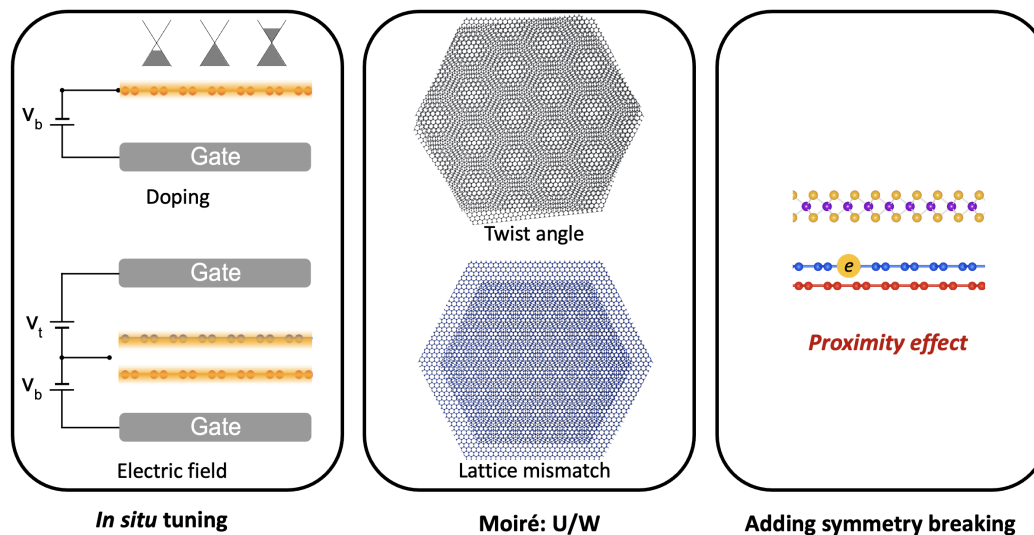


Figure 1.2: Ultra tunability of 2D van der Waals materials. Electrostatic gating controls the doping level, and multiple gates control the electrical displacement field. Moiré periodic potential is created by twisting two layers of lattice-matched materials or simply by putting together two materials with slight lattice mismatch. Additionally, stacking different materials on top of each other introduces ultra-clean interfaces for electrical transport measurements or induces proximity effect on demand.

thesized materials, is that the heterostructure stacking allows vastly different layers of materials to be on top of each other, forming a sandwich structure and coupled through vdW interactions. The relatively weak interlayer coupling turns out to be critical, since it allows arbitrary layer to rotate by an arbitrary angle with respect to another layer [15, 16], not necessarily the lowest energy structural order. It is this remarkable property of vdW materials that enables the field of “twistronics” to thrive.

Moiré structure by a twist is a model “super” material. The moiré pattern renormalizes band structure so that the relevant energy scale with strong correlations is accessible by simple electrostatic gating. For example, gate tuning in moiré systems is measured in the unit of number of electrons per moiré unit cell. The large *in situ* filling change is not easily accessible by chemically-doped bulk materials. As

a result, multiple energy bands can be completely populated or depleted simply by turning a simple gate voltage, a peculiar feature of interacting moiré systems. Second, the twist angle itself emerges as a new knob. At certain angle ranges, the Coulomb interactions win over kinetic energy; the angle tunes the relevance of repulsive Coulomb, thus helping to disentangle various quantum ground states.

Moiré is the case of relatively strong hybridization of the two layers. At the other end of the spectrum, the stacking of two largely lattice-mismatched materials significantly reduces the coupling. Yet, the strong perturbation from the start point of one material will be imprinted to the adjacent material with reduced energy scale, matching the correlations. This is the case for explicit spin-orbit interactions (SOI) to graphene proximitized by TMDs: the proximitized SOC does not dominate over spontaneously symmetry breaking in the graphene flat bands, delicately promoting proper parent states for superconductivity. The above unprecedented tunabilities are highlighted in Fig.1.2.

1.3 The electronic properties of monolayer graphene

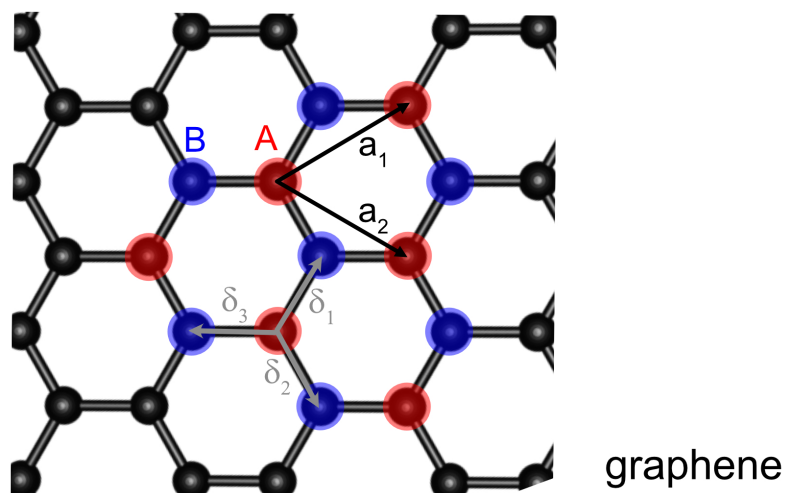


Figure 1.3: Crystal structure of monolayer graphene. Carbon atoms form honeycomb lattice. Red and Blue circles mark the A and B sublattices.

The dissertation focuses on graphene flat bands. Let us briefly review the electronic properties of monolayer graphene. Monolayer graphene is carbon atoms arranged into single-sheet honeycomb lattice. The honeycomb lattice contains two inequivalent sites; thus it can be treated as a triangular lattice with A and B sublattice sites (Fig. 1.3). The lattice constant is $a = 0.246$ nm [5]. The basis of Bravais lattice

vectors can be represented as

$$\mathbf{a}_1 = \frac{a}{2}(3, \sqrt{3}), \quad \mathbf{a}_2 = \frac{a}{2}(3, -\sqrt{3}), \quad (1.1)$$

and the vectors that connect sublattice A and its nearest neighbor are

$$\boldsymbol{\delta}_1 = \frac{a}{2}(1, \sqrt{3}), \quad \boldsymbol{\delta}_2 = \frac{a}{2}(1, -\sqrt{3}), \quad \boldsymbol{\delta}_3 = -a(1, 0). \quad (1.2)$$

Tight-binding Hamiltonian

Considering only nearest-neighbor hopping, the tight-binding Hamiltonian for graphene is

$$H_0 = -t \sum_{\langle ij \rangle} (\hat{a}_i^\dagger \hat{b}_j + \hat{b}_j^\dagger \hat{a}_i) \quad (1.3)$$

where i (j) labels sites in sublattice A (B), the fermionic operator \hat{a}_i^\dagger (\hat{a}_i) creates (annihilates) an electron at site A whose position is \mathbf{r}_i , and similarly for \hat{b}_i^\dagger (\hat{b}_i).

To calculate the dispersion relation, we transform from lattice space to the momentum space by using

$$\hat{a}_i^\dagger = \frac{1}{\sqrt{N}} e^{i\mathbf{k} \cdot \mathbf{r}_i} \hat{a}_\mathbf{k}^\dagger, \quad \hat{a}_i = \frac{1}{\sqrt{N}} e^{i\mathbf{k} \cdot \mathbf{r}_i} \hat{a}_\mathbf{k}, \quad (1.4)$$

where N is total number of unit cells. Substituting Eq. 1.3 to Eq. 1.2, we get:

$$\begin{aligned} H_0 &= \begin{pmatrix} \hat{a}_\mathbf{k}^\dagger & \hat{b}_\mathbf{k}^\dagger \end{pmatrix} \begin{pmatrix} 0 & -t\Delta_\mathbf{k} \\ -t\Delta_\mathbf{k}^* & 0 \end{pmatrix} \begin{pmatrix} \hat{a}_\mathbf{k} \\ \hat{b}_\mathbf{k} \end{pmatrix} \\ &= \begin{pmatrix} \hat{a}_\mathbf{k}^\dagger & \hat{b}_\mathbf{k}^\dagger \end{pmatrix} h(\mathbf{k}) \begin{pmatrix} \hat{a}_\mathbf{k} \\ \hat{b}_\mathbf{k} \end{pmatrix}, \end{aligned} \quad (1.5)$$

where

$$\Delta_\mathbf{k} = \sum_{\boldsymbol{\delta}} e^{i\mathbf{k} \cdot \boldsymbol{\delta}}. \quad (1.6)$$

The dispersion relation can be obtained by diagonalizing $h(\mathbf{k})$, we obtain:

$$E_{\pm}(\mathbf{k}) = \pm t \sqrt{1 + 4\cos\left(\frac{3}{2}k_x a\right)\cos\left(\frac{\sqrt{3}}{2}k_y a\right) + 4\cos^2\left(\frac{\sqrt{3}}{2}k_y a\right)} \quad (1.7)$$

or, it can be written as

$$E_{\pm}(\mathbf{k}) = \pm t\sqrt{3 + f(\mathbf{k})} \quad (1.8)$$

where

$$f(\mathbf{k}) = 2\cos(\sqrt{3}k_y a) + 4\cos\left(\frac{3}{2}k_x a\right)\cos\left(\frac{\sqrt{3}}{2}k_y a\right). \quad (1.9)$$

These are two gapless bands that touch at the Dirac points K and K' ; as shown in Fig.1.4. The Dirac points correspond to the points in \mathbf{k} space where $E(\mathbf{k}) = 0$.

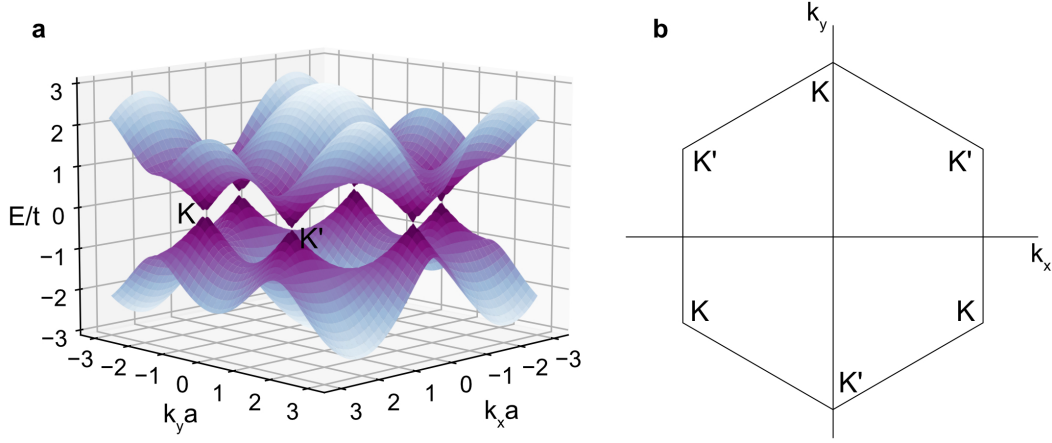


Figure 1.4: Band structure of monolayer graphene. (a) Energy band dispersion of the monolayer graphene calculated from the tight-binding model. (b) First Brillouin zone of monolayer graphene.

Low energy limit

We care about the behavior around the Dirac points since the Fermi level of intrinsic graphene lies around there. Let us look at the behavior of $\Delta_{\mathbf{k}}$ about the Dirac point K . Defining the relative momentum $\mathbf{q} = \mathbf{k} - \mathbf{K}$, we can write $\Delta_{\mathbf{k}}$ in terms of \mathbf{q} :

$$\begin{aligned} \Delta_{\mathbf{K}+\mathbf{q}} &= e^{-iK_x a} e^{-iq_x a} \left[1 + 2e^{i3(K_x+q_x)a/2} \cos\left(\frac{\sqrt{3}(K_y+q_y)a}{2}\right) \right] \\ &= e^{-iK_x a} e^{-iq_x a} \left[1 - 2e^{i3q_x a/2} \cos\left(\frac{\pi}{3} + \frac{\sqrt{3}a}{2}q_y\right) \right]. \end{aligned} \quad (1.10)$$

Now expanding around $\mathbf{q} = 0$ to first order, we have:

$$\Delta_{\mathbf{K}+\mathbf{q}} = -ie^{-iK_x a} \frac{3a}{2} (q_x + iq_y). \quad (1.11)$$

There is no physical significance for the phase, we thus have

$$\Delta_{\mathbf{K}+\mathbf{q}} = \frac{3a}{2}(q_x + iq_y). \quad (1.12)$$

About the Dirac point K , we thus have:

$$h(\mathbf{K} + \mathbf{q}) = v_F \begin{pmatrix} 0 & \pi^\dagger \\ \pi & 0 \end{pmatrix}, \quad (1.13)$$

where $v_F = \frac{3at}{2}$ is the Fermi velocity and $\pi = p_x - ip_y$, $\pi^\dagger = p_x + ip_y$. From the above equations, we see that the energy-momentum dispersion is linear, and is given by:

$$E_\pm(\mathbf{q}) = v_F |\mathbf{q}|. \quad (1.14)$$

1.4 Flat electronic bands: Twisted bilayer graphene

In this section, we briefly review how highly tunable flat electronic bands emerge from the twist of two layers of graphene. A moiré pattern is a long wavelength beating pattern from the combination of two periodic structures. One way to generate moiré pattern is by two periodic patterns of similar wavelength nearly aligned in angle. Two graphene sheets can form a moiré pattern when they are stacked on each other with a small rotational offset θ ; as shown in Fig. 1.5a. Twisted bilayer graphene (TBG) forms a periodic moiré wavelength L_M related to angle θ as

$$L_M = \frac{a}{2\sin(\theta/2)}, \quad (1.15)$$

which gives a unit cell area

$$A_M = \frac{\sqrt{3}a^2}{8\sin^2(\theta/2)}. \quad (1.16)$$

At the so-called magical angle $\theta_{\text{magic}} \approx 1.1^\circ$, the moiré periodicity is $L_M \approx 13$ nm. The periodicity determines both Coulomb interaction as well as moiré bandwidth. Coulomb interaction is straightforward— $e^2/(4\pi\epsilon L_M)$, on the order of 10 meV or so. The bandwidth is a bit tricky but an intuitive picture is shown in Fig. 1.5b and c. The Dirac cones of both layers at K and K' valleys are shifted by momentum wavevector reciprocal to moiré periodicity (Fig. 1.5b). Interlayer hybridization at the crossing point of the Dirac cones will open up superlattice gaps and isolate moiré bands (Fig. 1.5c). When the hybridization w and twist angle satisfies the condition $v_F |\mathbf{K}| \theta = w$, the bandwidth of isolated bands becomes suppressed because of this

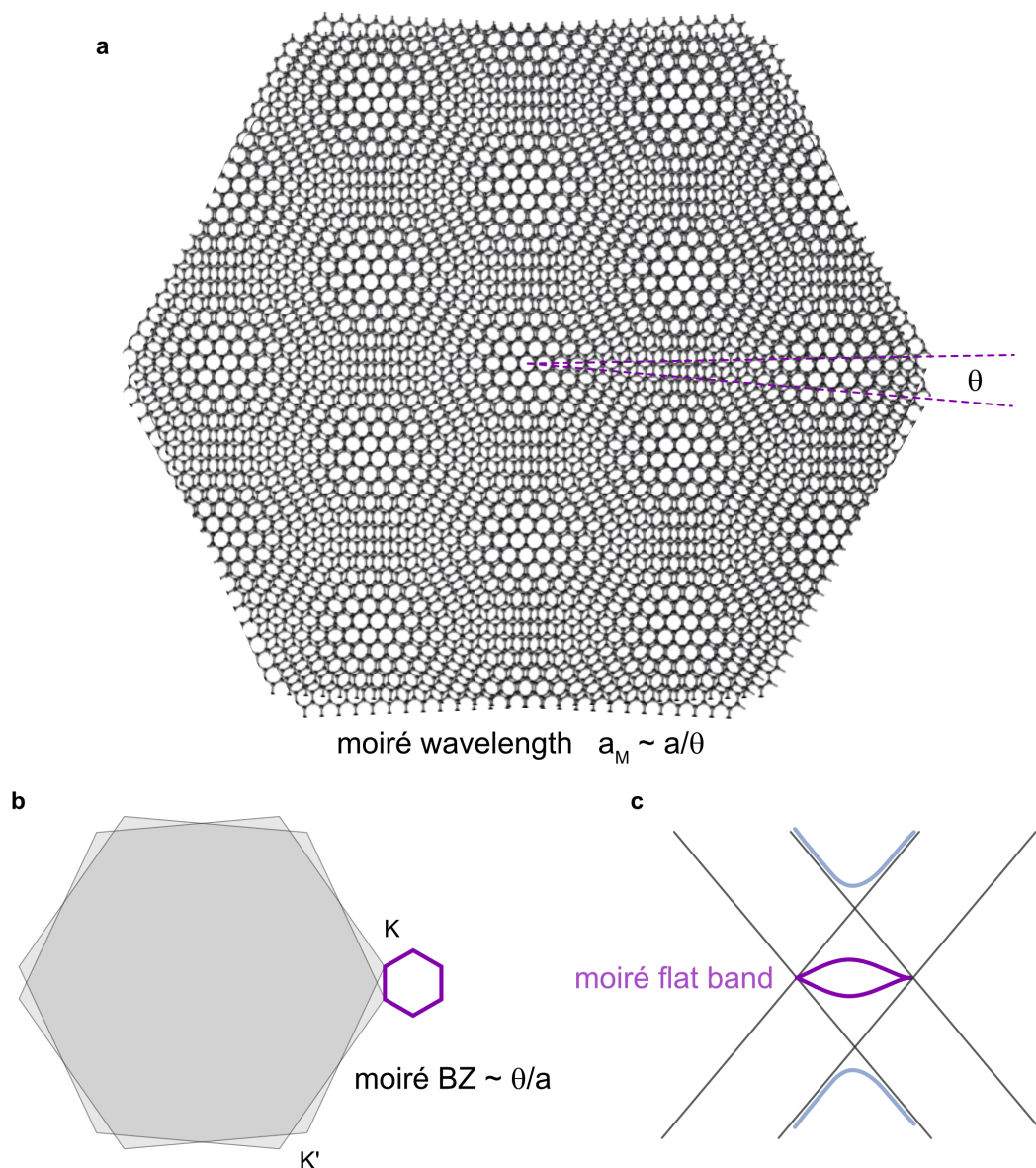


Figure 1.5: Twisted bilayer graphene. (a) Two layers of graphene are twisted relative to each other with an angle θ forming moiré superlattice; moiré wavelength scales as $a_M \sim a/\theta$. (b) The valleys from two layers of graphene strongly hybridize forming moiré Brillouin zone. (c) Schematic shows band hybridization forming moiré flat bands.

hybridization, which is known as the magic-angle condition ($\theta_{\text{magic}} \approx 1.1^\circ$ for twisted bilayer graphene). Around the magic angle, Coulomb interaction dominates over or is comparable with kinetic energy, the moiré system prefers to spontaneously break spin-valley symmetry to lower the total energy (see Section 1.6).

The system has attracted tremendous interest since the first observation of correlated

insulators and superconductors [16–20], which established TBG and beyond moiré systems as a new paradigm for twist-engineering strongly correlated physics. Since then, a plethora of new correlated ground states were observed in the moiré systems that reflect the rich interplay between interaction, topology, and various symmetry breaking. These include emergent ferromagnetism and quantum anomalous Hall insulators in hBN-aligned devices [21, 22], cascade of electronic transitions [23, 24], Pomeranchuk effect [25, 26], flavor symmetry breaking Chern insulators [27–33], fractional Chern insulators [34–37], strange metal [38], evidence for unconventional superconductivity [39, 40], inter-valley coherence [41, 42], etc. Soon, moiré structure is expanded to closely related graphene multilayer systems [43–49]. The community also innovated methods and material systems for insights and understanding of unconventional superconductivity in 2D tunable flat bands [50–58].

Bistritzer and MacDonald [59, 60] were among the first to consider the problem of twisting two monolayer graphene. They developed the so-called continuum model [59, 60], one of the most efficient ways to describe the single particle band structure of twisted bilayer graphene. The model may be expressed with the Hamiltonian of the top and bottom graphene layers along with a tunneling term that couples the two layers

$$H_{\text{cont}} = H_t + H_b + H_{\text{tun}}. \quad (1.17)$$

It is convenient to express the Hamiltonian in terms of second quantization, where $\psi_{t/b}$ and $\psi_{t/b}^\dagger$ are the annihilation and creation operators for the top/bottom layers, respectively. The first two terms on the right-hand side of Eq. 1.17 respectively denote the intralayer Dirac Hamiltonian of the top and bottom layers in the absence of tunneling, rotated symmetrically in opposite directions by $\theta/2$:

$$H_{t/b} = \int_{\mathbf{k}} \psi_{t/b}^\dagger(\mathbf{k}) h_{t/b}(\mathbf{k}) \psi_{t/b}(\mathbf{k}), \quad (1.18)$$

where

$$h_t(\mathbf{k}) = -v_F e^{i\theta\sigma^z/4} \mathbf{k} \cdot \boldsymbol{\sigma} e^{-i\theta\sigma^z/4}, \quad h_b(\mathbf{k}) = -v_F e^{-i\theta\sigma^z/4} \mathbf{k} \cdot \boldsymbol{\sigma} e^{i\theta\sigma^z/4}. \quad (1.19)$$

Here $\boldsymbol{\sigma}$ corresponds to Pauli matrices acting on sublattice indices. v_F is the Fermi velocity of graphene.

Modeling the layers without interlayer tunneling essentially models two Dirac cones separated by a twist-angle dependent wavevector $K_\theta \sim \sin(\theta/2)$. When considering

the interlayer tunneling term H_{tun} , the band crossing points tend to open an energy gap due to level repulsion. This term effectively energetically separates moiré bands from the higher energy bands. This term couples operators from top and bottom layers with offset momenta \mathbf{q}_ℓ , corresponding to the reciprocal lattice vectors of the moiré lattice

$$H_{\text{tun}} = \sum_{\ell=1,2,3} \int_{\mathbf{k}} \psi_t^\dagger(\mathbf{k}) T_\ell \psi_b(\mathbf{k} + \mathbf{q}_\ell) + h.c., \quad (1.20)$$

where

$$\mathbf{q}_\ell = k_\theta \left(-\sin \left[\frac{2\pi}{3} (\ell - 1) \right] \hat{\mathbf{x}} + \cos \left[\frac{2\pi}{3} (\ell - 1) \right] \hat{\mathbf{y}} \right), \quad k_\theta = \frac{4\pi}{3a} 2 \sin(\theta/2), \quad (1.21)$$

and using $\sigma_\pm = (\sigma_x \pm i\sigma_y)/2$, we get

$$T_\ell = w_0 + w_1 \left(e^{-2\pi(\ell-1)i/3} \sigma^+ + e^{2\pi i(\ell-1)/3} \sigma^- \right). \quad (1.22)$$

There are two coupling parameters w_0 and w_1 , which correspond to interlayer tunneling at AA and AB sites, respectively. The lattice relaxation of TBG at low angles results in slightly larger AB-type regions and smaller AA-type regions [61], so we have generally used $w_0 = 55$ meV and $w_1 = 105$ meV. The choice of parameters results in a magic angle $\sim 1.1^\circ$ and experimentally matches the gaps between moiré bands and dispersive bands.

Eventually, we produce a large matrix

$$H = \sum_{\mathbf{k}} \Psi^\dagger(\mathbf{k}) H(\mathbf{k}) \Psi(\mathbf{k}) \quad (1.23)$$

where

$$H(\mathbf{k}) = \begin{pmatrix} H_t(\mathbf{k}) & H_{\text{tun}} \\ H_{\text{tun}}^\dagger & H_b(\mathbf{k}) \end{pmatrix}. \quad (1.24)$$

The diagonal portion of the theory for the top layer is

$$H_t(\mathbf{k}) = \text{diag} (h_t(\mathbf{k} + \mathbf{G}_1), h_t(\mathbf{k} + \mathbf{G}_2), h_t(\mathbf{k} + \mathbf{G}_3), \dots). \quad (1.25)$$

Here, $\{\mathbf{G}_n\}$ is a set of N_{grid} reciprocal lattice vectors chosen in a symmetric fashion.

We shall take a look at the resulting band structure of twist bilayer graphene as a function of twist angle (Fig. 1.6). At certain twist angles, the Fermi velocity becomes zero, and the low-energy bands flatten considerably. The Fermi velocity can be approximated based on the dimensionless ratios [59] $\eta = w_0/w_1$ and $\alpha = \frac{w_1}{v_F k_\theta}$, k_F is the original Fermi velocity of monolayer graphene $\sim 10^6$ m/s. The low-energy continuum model Fermi velocity is approximately

$$v_{\text{cont}} = \frac{1 - 3\alpha^2}{1 + 3\alpha^2(1 + \eta^2)} v_F. \quad (1.26)$$

We see that to reduced the value v_{cont} , α needs to be optimized. Essentially, the twist angle θ that reduces v_{cont} is controlled by w_1 .

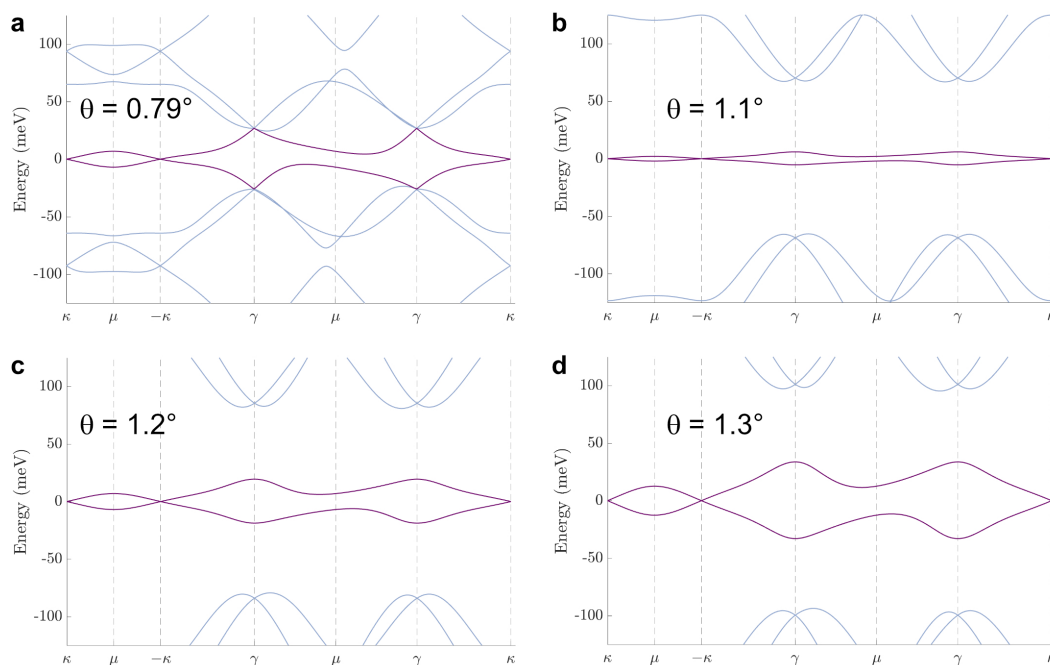


Figure 1.6: Continuum model of TBG band structure for twist angles above, around, and below the magic angle, showing the flattest near the magic angle.

1.5 Flat electronic bands: Bernal bilayer graphene

It turns out that flat electronic bands are not far away; they naturally emerge from crystalline graphene multilayers. We start with the simplest multilayer graphene, Bernal bilayer graphene (BLG; Fig. 1.7a); the results can be generalized to rhombohedral graphene multilayers.

Considering the low-energy continuum model commonly used to describe Bernal-stacked bilayer graphene [62], a perpendicular displacement field D from the top to

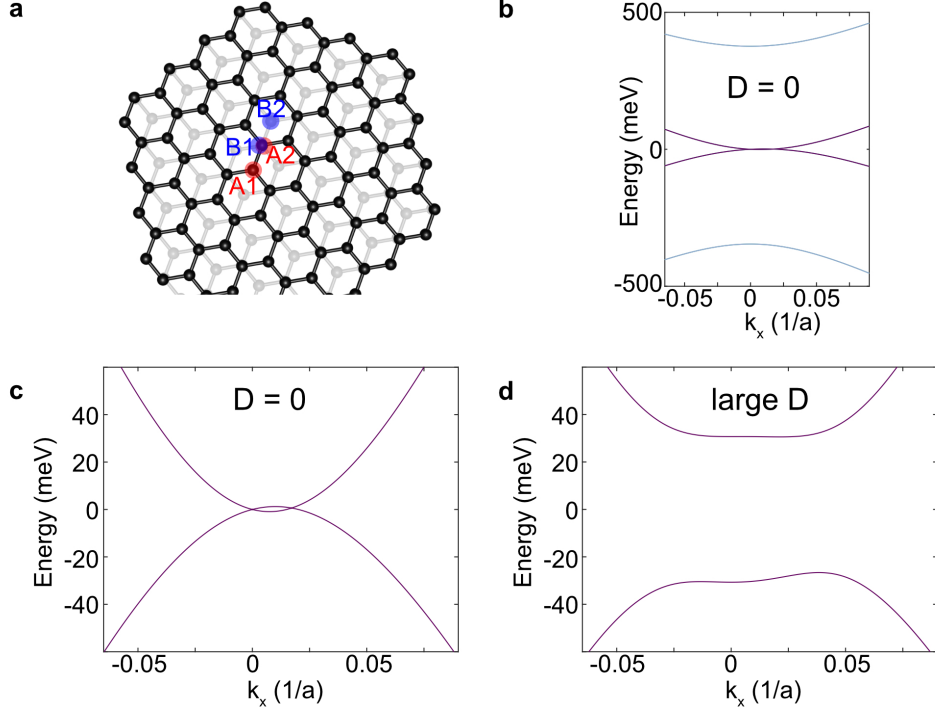


Figure 1.7: Electronic band structure of Bernal bilayer graphene. (a) Crystal structure of Bernal bilayer graphene. The sublattices on different layers are marked out. (b),(c) Band structure of BLG at zero displacement field for large (b) and small (c) energy ranges. (d) Band structure of BLG at a large finite D field.

the bottom layer generates a potential difference $u = -d_{\perp}D/\epsilon_{\text{BLG}}$ between the top and bottom layers. Here $d_{\perp} = 0.33$ nm is the interlayer distance and $\epsilon_{\text{BLG}} \sim 4.3$ is the relative permittivity of BLG. A continuum approximation of the band structure returns a Hamiltonian of the form

$$H_0 = \sum_{\xi=\pm} \sum_{\mathbf{k}} \psi_{\xi}^{\dagger}(\mathbf{k}) h_{0,\xi}(\mathbf{k}) \psi_{\xi}(\mathbf{k}),$$

$$h_{0,\xi}(\mathbf{k}) = \begin{pmatrix} u/2 & v_0\Pi^{\dagger} & -v_4\Pi^{\dagger} & -v_3\Pi \\ v_0\Pi & \Delta' + u/2 & \gamma_1 & -v_4\Pi^{\dagger} \\ -v_4\Pi & \gamma_1 & \Delta' - u/2 & v_0\Pi^{\dagger} \\ -v_3\Pi^{\dagger} & -v_4\Pi & v_0\Pi & -u/2 \end{pmatrix} \quad (1.27)$$

where $\Pi = (\xi k_x + i k_y)$ and $v_i \equiv \frac{\sqrt{3}a}{2} \gamma_i$. Here, $\xi = \pm 1$ indicates the valley that has been expanded about: $\mathbf{K}, \mathbf{K}' = (\xi 4\pi/3a, 0)$ with $a = 0.246$ nm the lattice constant of monolayer graphene. The 4×4 matrix $h_{\xi}(\mathbf{k})$ is expressed in the sublattice/layer basis corresponding to creation/annihilation operators of the form $\psi_{\xi}(\mathbf{k}) = (\psi_{\xi,A1}(\mathbf{k}), \psi_{\xi,B1}(\mathbf{k}), \psi_{\xi,A2}(\mathbf{k}), \psi_{\xi,B2}(\mathbf{k}))^T$, where A/B indicate the sublattices.

tice, 1, 2 indicate the layer, and the momentum k is measured relative to K_ξ (indices denoting the spin degrees of freedom have been suppressed). The values for the parameters entering into Eq. (1.27) are $\gamma_0 = 2.61$ eV (intralayer nearest-neighbor tunneling), $\gamma_1 = 361$ meV (leading interlayer tunneling), $\gamma_3 = 283$ meV (also known as trigonal warping term), $\gamma_4 = 138$ meV, and $\Delta' = 15$ meV (potential difference between dimer and non-dimer sites) [63].

In the absence of an applied displacement field and setting $v_3 = v_4 = 0$, the conduction and bands touch quadratically at charge neutrality. Two remaining bands are at significantly higher and lower energies (Fig. 1.7b); their wavefunctions are dominated by the “dimer sites,” i.e., the A2 and B1 which sit immediately on top of one another in the bilayer (Fig. 1.7a) and hybridize strongly through the onsite tunneling parameter γ_1 . Trigonal warping introduced by the v_3, v_4 associated hoppings in Eq. (1.27) splits the quadratic band touching (Fig. 1.7c) at charge neutrality into four distinct Dirac cones separated by van Hove singularities (vHs): one Dirac cone remains at $k = 0$, while the other three are located at C_3 -related momenta slightly away from the Dirac point. Turning on a displacement field D , a gap opens at charge neutrality and the vHs move apart in energy (Fig. 1.7d). Further, by flattening the band bottom, the applied D field also amplifies divergence of the density of states (DOS) close to the vHs. The low-energy states near K and K' become strongly layer- and sublattice-polarized; e.g., on A1 sites for the valence band and B2 sites for the conduction band, or vice versa for the other sign of D . That is, the low-energy wavefunctions near charge neutrality and under a large D field are strongly localized on the “non-dimer sites” of BLG.

1.6 Consequences of flat electronic bands: Stoner ferromagnetism

The above single-particle band structure calculations are great first glance of these systems. However, flat electronic bands quench the kinetic energy of electrons, making electron-electron interactions relevant. The interactions between electrons of different spins or flavors prefer to polarize electrons to specific flavors, whereas the polarization gains kinetic energy to the system. Eventually, when the band structure is flat enough, the gain in kinetic energy will be lower than the saving from the interactions. The system’s total potential is lowered; that is the key idea of Stoner ferromagnetism.

We start with a Stoner model in the context of graphene flat bands [24, 64]. We consider the grand potential per unit for graphene systems with four spin-valley

flavors

$$\frac{\Phi_{\text{MF}}(\{\mu_\alpha\})}{A} = \sum_\alpha E(\mu_\alpha) + V_{\text{int}} - \mu \sum_\alpha n(\mu_\alpha). \quad (1.28)$$

Here A is area of the system; or for moiré graphene is number of moié site. Additionally, $n(\mu_\alpha) = \int_0^\epsilon \rho(\epsilon) d\epsilon$ is the density for a given flavor, $E(\mu_\alpha) = \int_0^{\mu_\alpha} \epsilon \rho(\epsilon) d\epsilon$ is the total kinetic energy of a given flavor, and $\rho(\epsilon)$ is the density of states. The term V_{int} describes interaction between different flavors, which as a first approximation takes SU(4) symmetric:

$$V_{\text{int}} = \frac{U}{2} \sum_{\alpha \neq \beta} n(\mu_\alpha) n(\mu_\beta) \quad (1.29)$$

where U is the interaction strength. At fixed total chemical potential, the system would like to redistribution electrons to lower the total grand potential with respect to flavor densities. $n(\mu)$ is determined by graphene flat band structure. The minimization is in respective to individual flavor chemical potentials $\mu_\alpha = \mu(n_\alpha)$. The differential equation would reads:

$$\frac{\partial E}{\partial n_\alpha} + U \sum_{\alpha \neq \beta} n_\beta - \mu = 0. \quad (1.30)$$

Solving these four coupled equations gives $n_\alpha(\mu)$. We can then differentiate the equation with respect to μ and sum over all four flavors, we obtained density of states or compressibility:

$$\frac{dn}{d\mu} = \frac{\bar{\rho}}{1 + \bar{\rho}U} \frac{1}{a^2}. \quad (1.31)$$

Here $\bar{\rho} = \sum_\alpha \frac{\rho_\alpha}{1 - \rho_\alpha U}$ and $1/\rho_\alpha = d^2 E / dn_\alpha^2$ is the inverse single-particle density of states of flavor α . When $\rho_\alpha U = 1$, $\bar{\rho}$ diverges, corresponding to Stoner criterion.

We take twisted bilayer graphene as an example, shown in Fig. 1.8. Within the filling factors of the moiré flat bands, instead of filling all four spin-valley flavors equally, electrons in TBG prefer to filling certain flavors in comparison to other, simply to reduced the total energy as discussed. At $\nu \gtrsim +1$, flat band of one flavor is fully filled while the other three remain to be filled (Fig. 1.8a); similarly at $\nu \gtrsim +2$, flat bands of two flavors are fully filled while the other two remain to be filled (Fig. 1.8b); so on and so forth.

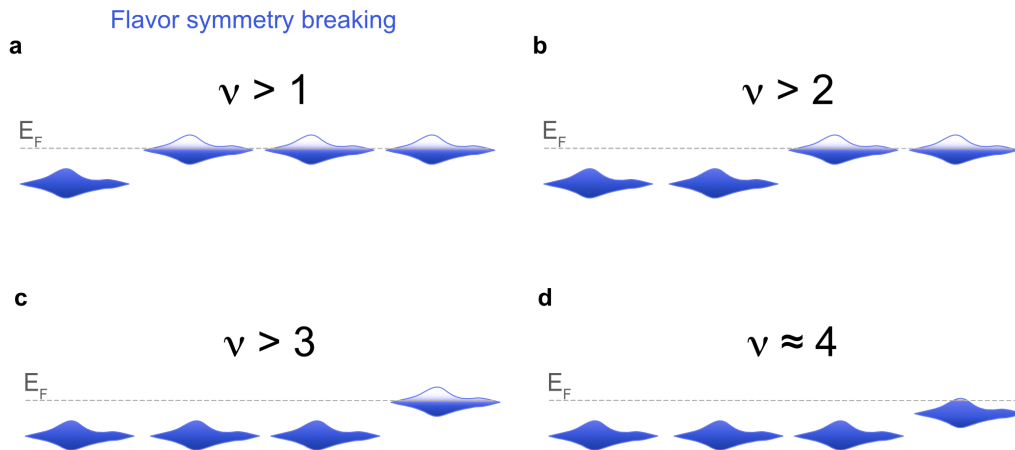


Figure 1.8: Flavor symmetry breaking in moiré graphene flat bands. (a)-(d) Configuration for flavor polarization at different filling factors; here twist bilayer graphene as an example.

The consequence of flavor polarization is significant: at different filling factors, the flavors form different spin-valley “magnets”, some of them break time-reversal symmetry, forming true orbital quantum anomalous Hall states. While the other preserve time-reversal, the delicate ground states dictate the occurrence of superconductivity.

Further lowering the spin-valley symmetry

In reality, interactions in graphene systems do not have perfect $SU(4)$ flavor symmetry; rather the symmetry are separate $SU(2)$ symmetry of electron spin and $U(1)$ symmetry of the two valleys. Interactions may thus exist which introduce additional scattering channels between the valleys, explicitly breaking the $SU(4)$ symmetry. One may modify the interaction potential to account for the symmetry breaking:

$$V_{\text{int}} = \frac{U}{2} \sum_{\alpha \neq \beta} n(\mu_\alpha) n(\mu_\beta) + J(n_1 - n_3)(n_2 - n_4). \quad (1.32)$$

Here, the number indices correspond to spin and valley configurations: $1 = \{K, \uparrow\}$, $2 = \{K', \uparrow\}$, $3 = \{K, \downarrow\}$, $4 = \{K', \downarrow\}$. The sign of J determines spin and valley polarizations; $J < 0$ so that the lowest energy two-fold states are spin polarized and valley unpolarized, or other combinations that favor alternative polarized order. The J term here physically corresponds to a Hund’s rule type anisotropy. Since the Stoner model calculation is performed on realistic band structure of graphene flat band, the realized phases are highly dependent on the band structure parameters.

The origin of above consideration regarding Stone physics and the detailed additional symmetry-breaking are consequences of long- and short-range Coulomb interactions. The screened Coulomb interaction is given by

$$H_c = \frac{1}{2} \sum_{\alpha, \beta, i, j} \int U(|\mathbf{r} - \mathbf{r}'|) \psi_{i\alpha}^\dagger(\mathbf{r}) \psi_{i\beta}^\dagger(\mathbf{r}') \psi_{j\beta}(\mathbf{r}') \psi_{i\alpha}(\mathbf{r}) d^2r d^2r' \quad (1.33)$$

where $\alpha, \beta = 1, \dots, 4$ runs over the spin and valley indices, and i, j are sublattices and layers. The interaction is taken to be $U(r) = \int \frac{d^2q}{(2\pi)^2} U(q) e^{i\mathbf{q}\cdot\mathbf{r}}$, where

$$U(q) = \frac{2\pi e^2 \tanh(qd)}{\epsilon q} \quad (1.34)$$

corresponding to screening by metallic gates at a distance d from the system. The screened Coulomb potential is assumed to depend only on the local density of electrons, and does not depend on any of the internal indices (such as spin and valley). This type of interaction is expected to dominate when the average distance between charge carriers is much larger than the inter-atomic spacing, and contributes to the onset of Stoner physics, which is SU(4) symmetric in spin and valley space.

We need to consider interaction terms beyond the long-range Coulomb interaction. Interactions at ranges of the order of a few lattice constants (either Coulombic or phonon-mediated) can depend on the spin and valley indices of the electrons, which give rise to specific types of flavor combinations. The short-range interactions here (J , etc.) are typically a fraction of the long-range U , but as illustrated being crucial.

Additional perturbation will also changes the ground state of the system. One famous example is twisted bilayer graphene aligned with hexagonal boron nitride. The broken C_2 symmetry changes the topological properties of the system and enables intrinsic integer quantum anomalous Hall state [21, 22]. New explicit symmetry breaking may have unprecedented effects on correlated phases. Our lab advances the proximity of WSe₂ to graphene flat bands and really alters the ground-state nature, promoting and enhancing unconventional superconductivity. Below is a brief introduction to spin-orbit coupling.

1.7 Spin-orbit coupling

Spin-orbit coupling (SOC) is a relativistic coupling interaction between electron spin and its motions. An example of this phenomenon is the spin-orbit interaction leading to shifts in an electron's atomic energy levels, due to electromagnetic

interaction between the electron's magnetic dipole, its orbital motion, and the electrostatic field of the charged nucleus. In solid states systems, spin-orbit interactions cause more pronounced effect to the electronic band structure around the Fermi level. One can think of SOC as a momentum-dependent effective magnetic field: the energy level of previously degenerate two spins are split in energy, depending on the specific momentum and the type of spin-orbit interactions. We briefly introduce some common types of SOC that maybe relevant for our graphene systems.

Rashba SOC

Rashba SOC is a momentum-dependent splitting of spin bands in bulk crystals and low-dimensional condensed matter systems, typically related to the inversion symmetry breaking at the interfaces. The splitting is a combined effect of spin-orbit interaction and asymmetry of the crystal potential, in particular in the direction perpendicular to the two-dimensional plane. The Rashba SOC Hamiltonian takes the form as following:

$$H_R = \alpha(\hat{z} \times \mathbf{p}) \cdot \sigma. \quad (1.35)$$

Here, α is the Rashba coupling strength, \mathbf{p} is the momentum and σ is the Pauli matrix; this is equivalent to two-dimensional version of Dirac Hamiltonian. In a two-dimensional system, the momentum is in plane, and there is spin winding (that is 90 degree rotation relative to the momentum direction) in the plane depending on the momentum. The Rashba term prefers to pin spins in-plane and encodes in-plane spin textures to the band structure (Fig. 1.9a,c).

In the case of graphene, due to the spin and valley degree of freedom, Rashba SOC can be represented as

$$H_R = \frac{\lambda_R}{2}(\tau_z \sigma_x s_y - \sigma_y s_x) \quad (1.36)$$

with τ_i and σ_i being the Pauli matrices acting on the valley and sublattice degree of freedom, and λ_R represents the characteristic energy splitting.

Kane-Mele SOC

Another type of SOC term called Kane-Mele SOC is intrinsic to graphene system [65]

$$H_{\text{Kane-Mele}} = \frac{\lambda_{KM}}{2} \tau_z \sigma_z s_z. \quad (1.37)$$

Kane-Mele SOC is proposed to realized quantum spin Hall insulator in graphene at an experimentally accessible low temperature [65]. However, the realization of quantum spin-Hall insulator is quite difficult since it strongly depends on the effects of temperature, chemical potential, Rashba SOC, disorder, and symmetry breaking fields. Recent experiments in mono- and bi-layer graphene suggest that Kane-Mele SOC falls somewhere in the range 40 to 80 μeV [66–68]. The Kane-Mele term is relatively small compared to other symmetry breaking fields, such as Rashba, making it inaccessible to quantum spin Hall state up to now.

Ising SOC

The third type of spin-orbit coupling is call Ising SOC; typically absent in intrinsic graphene. The term is important for TMDs. Considering monolayer TMD, the in-plane mirror symmetry is broken and electrons can experience in-plane electric fields. As a result, the SOC field has the form $S(k)\sigma_z$ and it pins electron spins to the out-of-plane directions, where $S(k)$ is a function that depends on the lattice structure. It couples out-of-plane spins to valley degree of freedom:

$$H_{\text{Ising}} = \frac{\lambda_I}{2}\tau_z s_z. \quad (1.38)$$

The Ising SOC is also called valley Zeeman SOC since the spins in two valleys are pinned out-of-plane directions and are splitted in a time-reversal fashion, i.e., as if the two valleys experience magnetic fields of opposite directions (Fig. 1.9b,d).

Probing spin-orbit coupling

One direct evidence of spin-orbit interaction is angle-resolved photoemission spectroscopy (ARPES), which maps out the energy and momentum relation and visualizes SOC energy splitting [69]. Famous examples include the discovery of topological insulator and the direct mapping of the spin textures coming from Rashba SOC in the system [70–73]. Direct momentum-resolved spectroscopy, however, requires large energy scale and a large enough sample for beam spots, both of which are absent in vdW heterostructures. Therefore, one may figure out other sensing methods for the small energy scale SOC in the system. Of course, even better to figure out which types.

We shall start with the most commonly used electrical transport technique to identify the existence of SOC. A well known transport signature that results from spin-orbit coupling is the weak antilocalization (WAL) effect, manifesting as a distinct conductance peak at low temperatures and around zero magnetic fields [74]. When

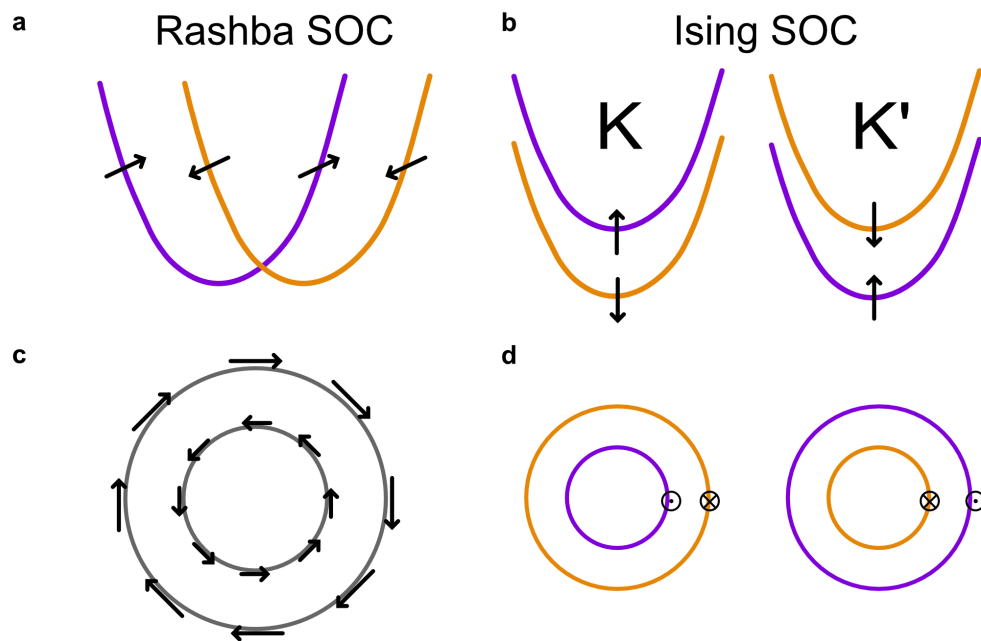


Figure 1.9: Band structure with Rashba and Ising SOC. (a),(b) Energy and momentum relation for Rashba- (a) and Ising- (b) type spin-orbit interactions. (c),(d) Constant energy contour showing the spin winding for the two cases.

electrical current flows in a material, electrons bounce randomly off defects in the material. In materials with some amounts of defects and at low enough temperatures, for the electrons to maintain phase coherence, an effect called weak localization occurs. Electrons that travel in opposite paths (clockwise and counterclockwise), returning to their origin, tend to constructively interfere (Fig. 1.10). Conductivity, as a result suffers since it is favorable for electrons to return rather than traveling through the material. The interference is jumbled, however, by a magnetic field, resulting in a distinct conductivity dip at zero magnetic field.

In a system with spin-orbit coupling, the spin of electron is coupled to its momentum. The spin of the carrier rotates as it goes around a self-intersecting path, and the direction of this rotation is opposite for the two directions about the loop. Because of this, the two paths along any loop interfere destructively which leads to a lower net resistivity. The peak is generally on the order of $\lesssim e^2/h$. However, the extraction of type and the strength of SOC in the system is convoluted, see discussion in Chapter 3.

Alternatively, the SOC-induced spin splitting can be extracted from resonant microwave measurements [66–68]. Due to the relative low energy scale, GHz range microwave photon is effective in triggering transitions (Fig. 1.11). The physics is

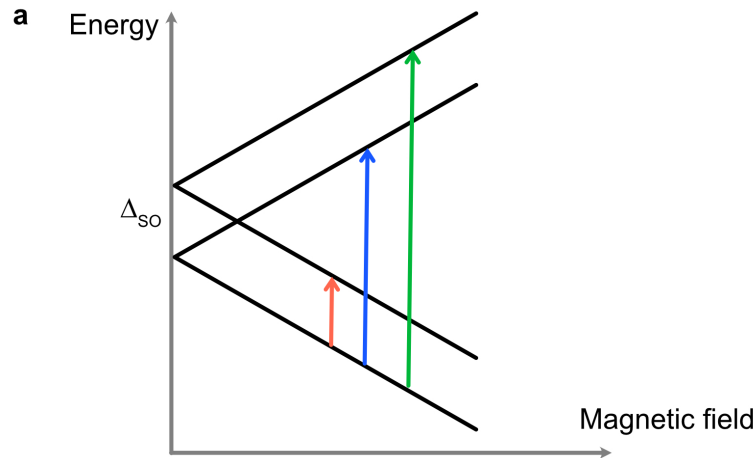


Figure 1.11: A depiction showing spin-valley energy levels moving with magnetic field. Microwave photon probes the transitions that can back track the SOC at zero magnetic field.

energy gap of the coherent quantum state (observed by various spectroscopic techniques), perfect diamagnetism (cancellation of magnetic fields in the superconductor by screening current), and the macroscopic phase coherence (electrons condense into one quantum state). Up to now, there are thousands of material discovered to exhibit superconductivity, a lot of them fall into the category of conventional superconductivity — a theory proposed by Bardeen, Cooper, and Schrieffer (BCS) in 1957 [76], providing a solid theoretical foundation for these fascinating experimental signatures. Many conventional metals, including aluminum, lead, niobium, exhibit superconductivity that is well described by BCS theory. However, the superconducting transition temperature is typically low, several Kelvin, well captured by the temperature limit predicted by the BCS theory ($\sim 30 - 40$ K). More recently, some unconventional superconductors such as high-temperature superconductors [77, 78] and exotic-pairing mechanism/symmetry superconductors [79–82] are not in line with the BCS phenomena. The understanding and discoveries of these unusual pairing are at the heart of current condensed matter research, potentially leading to practical applications.

Start with the BCS theory. At sufficiently low temperatures, electrons near the Fermi surface become unstable against the formation of pairs, called Cooper pairs. The binding will occur in the presence of an attractive potential, no matter how weak. In conventional superconductors, an attraction is generally attributed to an electron-lattice interaction, or electron-phonon coupling. An electron moving through a conductor will attract nearby positive charges in the lattice. This deformation of the

lattice causes another electron, with opposite spin, to move into the region of higher positive charge density. The two electrons then become correlated. The BCS theory requires only the potential being attractive, regardless of its origin. In the BCS framework, superconductivity is a macroscopic effect: there are a lot of electron pairs that overlap strongly and form a collective condensate. The breaking of one pair will change the energy of the entire condensate. Thus, the energy required to break any single pair is related to the energy required to break all.

The BCS theory generally considers pairing between spin-up and spin-down electrons and with an s -wave like isotropic pairing wavefunction. The superconducting transition temperature T_c is directly related to the density of states at the Fermi level $N(E_F)$, and also related to electron-phonon coupling in the system, taking the form:

$$k_B T_c = 1.134 \hbar \omega_c e^{-\frac{1}{N(E_F)V}}. \quad (1.40)$$

V is the electron-phonon coupling potential and $\hbar \omega_c$ is the Debye cutoff energy. From the formula, it is clear that the onset of superconductivity is related to the Debye cutoff frequency, determined by the material, and also by the density of states. Eventually, the theory predicted an upper bound for the transition temperature of conventional pairing, roughly 40 K. Additionally, for conventional pairing, the superconducting gap is directly proportional to the transition temperature as [83]

$$\Delta = 1.764 k_B T_c. \quad (1.41)$$

The formula is under the assumption that superconducting pairing is at the weak-coupling region, i.e., $N(E_F)V \ll 1$ and also spin singlet.

Strongly coupled superconductor

It turns out that twisted bilayer graphene is a superconductor that is at the strongly coupled regime. There are several quantities that are evidences of strong coupling. The pairing coherence length from BCS theory is given by $\xi = \frac{\hbar v_F}{\pi \Delta}$ (v_F is Fermi velocity). It can be experimentally determined by transport measurement, tracking the vortex depairing as a function of out-of-plane magnetic field, with an equation derived from Ginzburg-Landau theory $T_c/T_{c0} = 1 - (2\pi\xi^2/\Phi_0)B_\perp$, where $\Phi_0 = h/2e$. Normally, we measure superconducting transition temperature as a function of B_\perp . Empirically, higher the out-of-plane critical field is, smaller the coherence length is.

Small coherence length in comparison to average carrier distance is a strong indication of strong coupling. In BCS limit, the Cooper pairs are coherent over long

distances; the entire system forms a globe coherent order. When approaching the strongly coupled regime, the Cooper pairs are tightly bounded locally, more like molecules instead of long-range coherent waves. This limit is called Bose-Einstein condensate (BEC) regime with large phase space of tightly bounded pairs [84]. There are some other signatures, for example, pre-formed Cooper pairs above T_c without phase coherence, telling the BEC regime. The coupling strength can also be estimated from a dimensionless constant Δ/E_F , or comparing T_c to Fermi temperature T_F . The comparison plot is called Uemura plots [85], as shown in Fig. 1.12. At the right lower corner, we see some conventional BCS superconductors whose critical temperature is much smaller than Fermi temperature. While we approach the opposite diagonal corner, we see more and more unconventional superconductors including cuprates and graphene moiré superlattices. There is an upper bound for critical temperature at the BEC limit in the context of Fermi temperature, that is $T_c/T_F \sim 0.1 - 0.2$, as marked by the dashed line in Fig. 1.12.

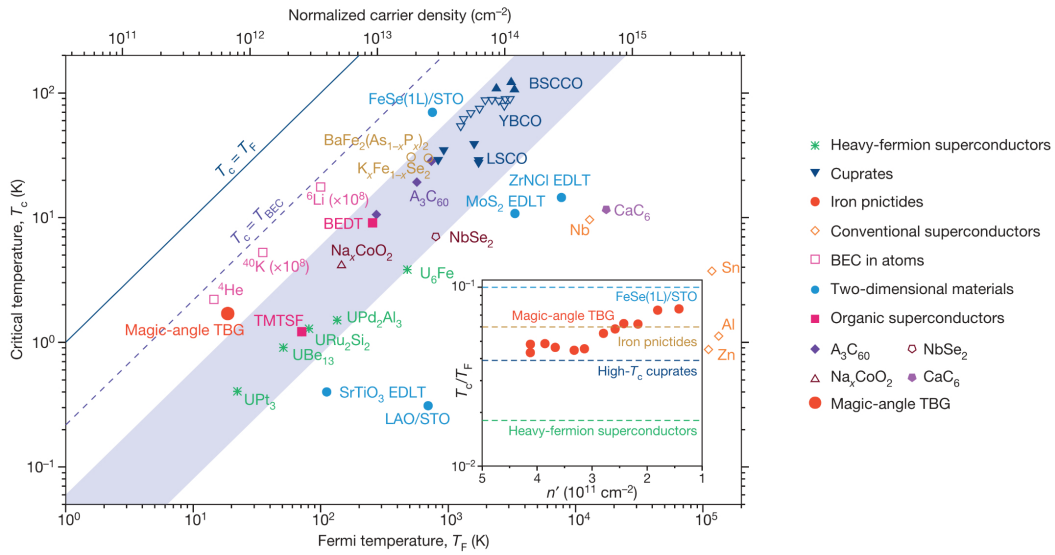


Figure 1.12: Uemura plot showing T_c compared to T_F across various superconductors. Reprinted from [16], with permission from the copyright holder, Springer Nature.

Other than the strongly coupled nature, pairing symmetry is another characteristic of unconventional pairing. We want to maintain the total Cooper pair wavefunctions being odd under two-electron exchange due to the fermionic nature. The total wavefunctions can be separated into spin and orbital configuration: spin singlet configuration $\frac{1}{\sqrt{2}}(|\uparrow\downarrow\rangle - |\downarrow\uparrow\rangle)$ combines with even parity wavefunctions (s - and d -wave; Fig. 1.13a and c) while spin triplet configuration ($|\uparrow\uparrow\rangle$, $|\downarrow\downarrow\rangle$, and

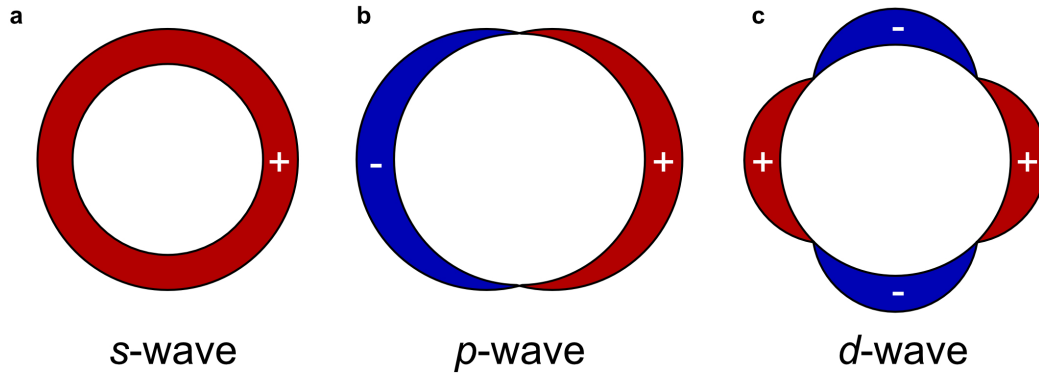


Figure 1.13: Superconducting pairing wavefunctions showing *s*-wave (a), *p*-wave (b), and *d*-wave (c).

$\frac{1}{\sqrt{2}}(|\uparrow\downarrow\rangle + |\downarrow\uparrow\rangle)$ combines with odd parity wavefunctions (*p*-wave; Fig. 1.13b). Most well-known superconductors are spin-singlet isotropic *s*-wave pairing, i.e., same sign and momentum-independent gap equation. The overall phenomena are well-understood. Unconventional pairing here has anisotropic momentum-dependent wavefunctions, accompanied by sign changes and gapless spectrum. Fully mapping out the momentum-dependent gap information is at the heart of understanding unconventional superconductors and has been quite challenging. Here are two important examples of unconventional pairing with anisotropic symmetry.

High-temperature superconductor: *d*-wave pairing

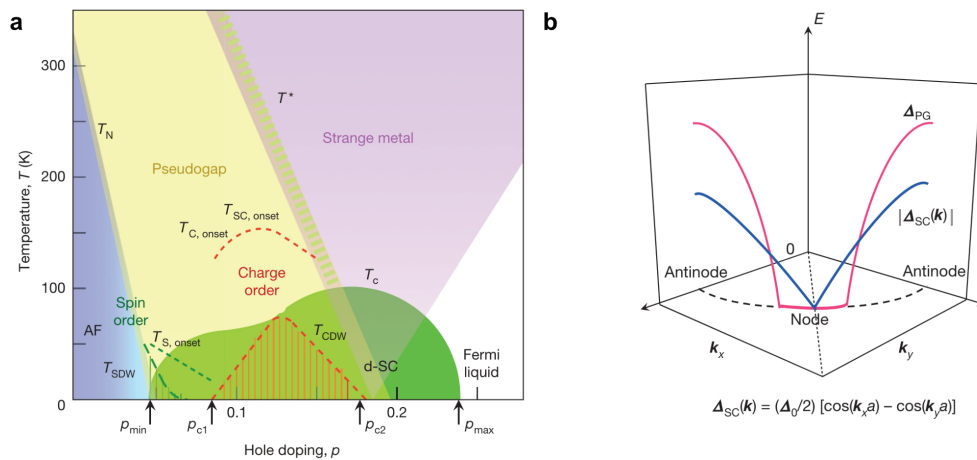


Figure 1.14: Unconventional pairing in high-temperature superconductor. (a) Temperature versus hole doping level for the copper oxides, indicating where various phases occur. (b) Superconducting gap and pseudogap amplitude in momentum space. Reprinted from Ref. [77], with permission from the copyright holder, Springer Nature.

The discovery of high-temperature superconductivity in the copper oxide perovskite $\text{La}_{2-x}\text{Ba}_x\text{CuO}_4$ [86] ranks among the major scientific events in modern condensed matter physics. The main reasoning is that the critical temperature of high- T_c far exceeds the BCS limit, reaching ~ 100 K for the famous YBaCuO. The physics of high- T_c is extremely rich; Fig. 1.14a shows a hole doping versus temperature phase diagram with a plethora of quantum phases. Zero-doping range is an antiferromagnetic Mott insulator coming from strong Coulomb repulsion. Slightly hole-doping onsets the high-temperature superconductivity. Within the superconducting phase, there is coexistence of spin orders, charge orders, etc., depending on the filling factors. Above the superconducting transition temperature, even more confusing pseudogap and strange metal behavior persist. The competition and incorporation between various orders make it extremely hard to conclude every details of the phase diagram.

Nevertheless, given the relatively high temperature scale, the d -wave pairing symmetry (Fig. 1.14b) in high T_c is the most successfully identified unconventional pairing. Phase-sensitive measurement [87] identified the sign change; ARPES [88] and scanning tunneling spectroscopy identify the rotational symmetry as well as the nodal and antinodal regions.

An intuitive understanding of the pairing mechanism is by approaching the problem from an unrealistic weak-coupling perspective [89]. For the case of repulsive interactions, if two-particle vertex function $\Gamma(\mathbf{k})$ is \mathbf{k} -dependent, a sign-changing superconducting order parameter (where $\Delta(\mathbf{k})$ and $\Delta(\mathbf{k} + \mathbf{q})$ have opposite sign) results for which interactions involving small momentum transfer are pair breaking, and those with large momentum transfer near \mathbf{q} promote pairing. In particular, if there are antiferromagnetic correlations, this typically implies a peak in Γ at the antiferromagnetic ordering vector, $\mathbf{q} = \mathbf{q}_{\text{AF}}$, which is also an ideal vector for scattering between ‘antinodal’ regions of the Fermi surface of the copper oxides shown in Fig. 1.14. The gap ‘nodes’ along the diagonals of the Brillouin zone are then, in turn, where the d -wave gap vanishes.

The above argument suggests that the antiferromagnetic correlation is directly related to the anisotropic d -wave like pairing symmetry. However, there remains puzzles that obscure the full understanding of the high temperature mechanism. Future efforts may help to fully uncover the mysteries and to push the limit for critical temperature.

Spinless p -wave pairing

Another kind of unconventional pairing is p -wave pairing, specifically 1D spinless p -wave superconductor or 2D $p_x \pm ip_y$ superconductor; or so called topological superconductivity. The occurrence of such kind of pairing requires the reduction of symmetry, where spin-orbit coupling can be quite useful. Let us see why such p -wave pairing is interesting.

Topological superconductivity is interesting because of its quasiparticles Majorana fermions. Majorana quasiparticles are their own anti-particles, featuring special exchange statistics. They are non-abelian anyons [90], meaning that particle exchanges are nontrivial operations which in general do not commute. Note that any fermions can be written as a combination of two Majorana quasiparticles and the exchange of two spatially separated Majoranas lead to the idea of decoherence invariant quantum computation [91]. Thinking of the particle being its own anti-particle means that the quasiparticle is an equal superposition of an electron and a hole. It naturally comes to the excitation in superconducting systems, Bogoliubov quasiparticles.

We start by introducing a simple Hamiltonian, describing a spinless p -wave superconductor. It is most intuitive to start from a 1D tight-binding chain (Fig. 1.15a) with p -wave superconducting pairing, as first introduced by Kitaev [92, 93]:

$$H_{\text{chain}} = -\mu \sum_{i=1}^N n_i - \sum_{i=1}^{N-1} \left(t c_i^\dagger c_{i+1} + \Delta c_i c_{i+1} + h.c. \right) \quad (1.42)$$

where $h.c.$ means hermitian conjugate, μ is the chemical potential, c_i is the electron annihilation operator for site i and $n_i = c_i^\dagger c_i$ is the number operator. The superconducting gap Δ and hopping t are assumed to be the same for all sites. Note that time-reversal symmetry is broken since we only consider one spin projection, i.e., effectively spinless. The spinless effectively guarantees that wavefunction being odd parity, p -wave naturally.

Each fermion operator can be written as the combination of two Majorana operators at real and imaginary part:

$$c_i = \frac{1}{2}(\gamma_{i,1} + i\gamma_{i,2}), \quad (1.43)$$

$$c_i^\dagger = \frac{1}{2}(\gamma_{i,1} - i\gamma_{i,2}). \quad (1.44)$$

We shall consider the simplest case $\mu = 0$ and $t = \Delta$, the Hamiltonian results in

$$H_{\text{chain}} = -it \sum_{i=1}^{N-1} \gamma_{i,2} \gamma_{i+1,1}. \quad (1.45)$$

However, the Majorana operators $\gamma_{N,2}$ and $\gamma_{1,1}$, which are localized at the two ends of the wire, are completely missing from Eq. 1.45. These two Majorana operators can equivalently be described by a single fermionic state with operator

$$\tilde{c}_M = (\gamma_{N,2} + i\gamma_{1,1})/2. \quad (1.46)$$

This is a highly non-local state since $\gamma_{N,2}$ and $\gamma_{1,1}$ are localized on opposite ends of the chain. Furthermore, since this fermion operator is absent from the Hamiltonian, occupying the corresponding state requires zero energy. Similarly, in a 2D $p_x \pm ip_y$ -wave superconductor, Majoranas appear in vortices in the superconducting pairing potential [94]. The magic of Majorana quasiparticle is the braiding statistics; as

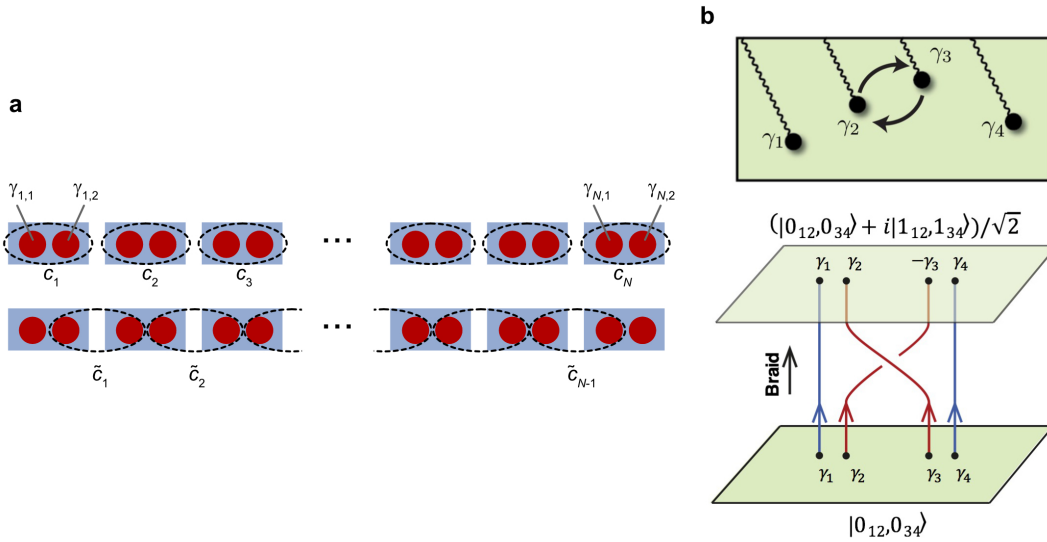


Figure 1.15: Spinless p -wave pairing. (a) Sketch of Kitaev's 1D p -wave superconducting tight binding chain [93]. (b) Braiding two pairs of Majorana quasiparticles.

illustrated in Fig. 1.15b. Note the braiding that involves Majoranas from different fermions, produces a superposition state of different number states. However, the total parity of each state in the superposition must be the same. Also whenever two exchanges involve some of the same Majoranas, the braid operators do not commute $[B_{i-1,i}, B_{i,i+1}] = \gamma_{i-1}\gamma_{i+1}$.

The advantage of Majorana-based qubits is encoding the quantum information in delocalized fermionic states. Therefore, they are expected to be robust against

most sources of decoherence which do not couple simultaneously to more than one Majorana mode, i.e., decoherence requires perturbations of the form $\gamma_i\gamma_j$, which are suppressed when Majorana i and j are spatially separated.

Intrinsic or natural spinless p -wave pairing/ $p_x \pm ip_y$ pairing is rare. In the context of superconductor, spin-triplet pairing is one of the promising routes. The spins pair along the same direction, therefore Zeeman field will not flip the spins to break superconductivity, unlike the spin-singlet case. Typically, large Pauli-limit violation is a strong indication of triplet pairing. However, to get the superconductivity that is truly topologically protected, additional constraints on pairing components are required. The definite evidence of intrinsic topological superconductivity is still an ongoing effort in condensed matter physics. Another important system is fractional quantum Hall states, where the even denominator fractional quantum Hall states are theoretical predicted to conducive to p -wave pairing hosting putative non-abelian anyons [94–96]. Further experimental efforts are needed for the demonstration of non-abelian statistics.

Can we realize Majorana quasiparticles, i.e., get spinless fermions, in an alternative more engineering approach? When spin degree of freedom is locked with momentum degree of freedom, it is spinless by definition since spin is not an independent quantum number. It naturally comes to the importance of spin-orbit coupling. To get a single band with lowest symmetries, we consider an 1D nanowire Hamiltonian with Rashba SOC and in-plane magnetic field [93]:

$$H_0(x) = \frac{k_x^2}{2m} - \mu + \tilde{\alpha}k_x\sigma_y + \frac{1}{2}\tilde{B}\sigma_z, \quad (1.47)$$

where we take $\hbar = 1$, $\tilde{\alpha} = \alpha E_\perp$, with E_\perp being the electric field perpendicular to the wire direction, is the strength of the Rashba spin-orbit field and $\tilde{B} = g\mu_B B$ is the Zeeman field. The schematics for eigenstates of Eq. 1.47 are shown in Fig. 1.16. Rashba SOC lifts the spin degeneracy, shifting the bands along k direction (Fig. 1.16a). However, at any given energy there is still spin degeneracy since time-reversal symmetry is not broken. Switching on a small in-plane magnetic field (Fig. 1.16b), the crossing at zero momentum turns into an anti-crossing. The Hamiltonian results in:

$$E_\pm(k_x) = \frac{k_x^2}{2m} - \mu \pm \sqrt{(\tilde{\alpha}k_x)^2 + \tilde{B}^2}. \quad (1.48)$$

Inside the gap, there is only one effective spin direction (dashed lines in Fig. 1.16). Therefore, if μ is placed inside the gap, spinless superconductivity can be induced

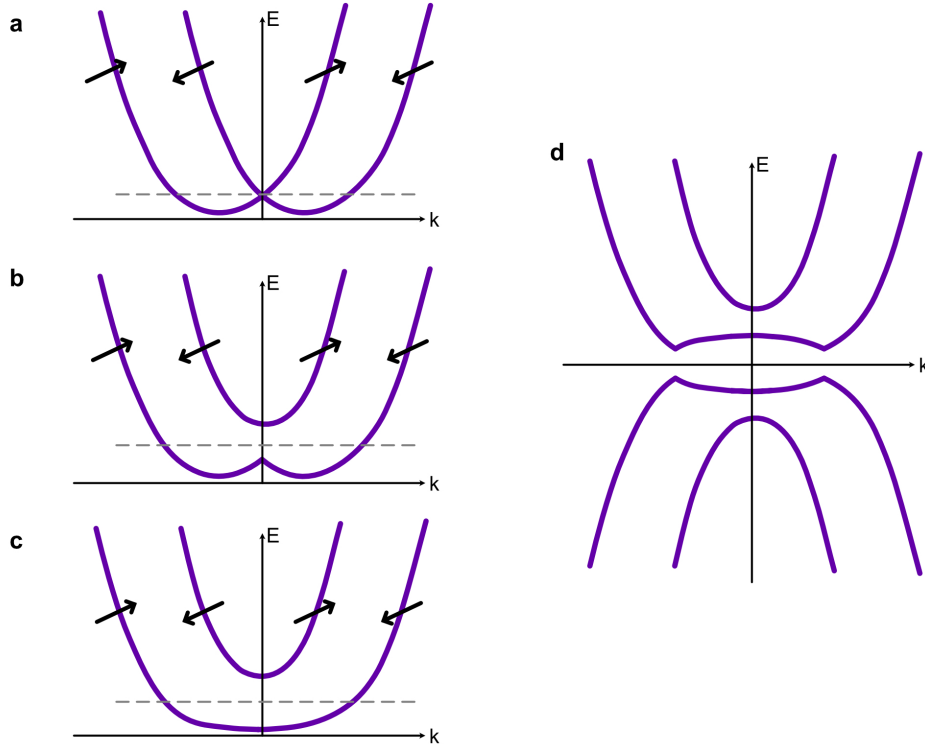


Figure 1.16: Rashba SOC + B_{\parallel} + superconductivity. (a) 1D parabolic bands with Rashba SOC. (b) With Rashba SOC and in-plane magnetic field. (c) Further increasing in-plane magnetic field. (d) Inducing superconductivity.

by the proximity effect. A larger magnetic field increases the gap size (Fig. 1.16c). Next we switch on also the proximity-induced superconducting pairing $\Delta > 0$ in Fig. 1.16d. The topological region is achieved by fine tuning the strength of all three quantities: the criteria for topological superconductivity is given by

$$|\tilde{B}| > \sqrt{\Delta^2 + \mu^2}. \quad (1.49)$$

Ising superconductivity

For conventional 2D superconductors, the orbital depairing is strongly suppressed, and the critical in-plane magnetic field is known as the Pauli limit. At the critical field, spin Zeeman energy is comparable to the superconductivity gap and therefore destroys superconductivity. For weak-coupling spin-singlet BCS superconductor, in-plane critical field is related to T_c as:

$$B_p = 1.86 \text{T K}^{-1} \times T_c^0. \quad (1.50)$$

One way to break the Pauli limit is spin-triplet pairing (pairing spins are aligned in the same direction); as discussed in the previous section. Here, we introduce the

Ising superconductivity, where superconductivity is strongly modified by the Ising SOC, also promotes strong violation of the Pauli limit.

Ising superconductivity stems from the fact that the bands in certain 2D materials are spin splitted and polarized in the out-of-plane z direction (Fig. 1.9b). This type of band structure comes from two symmetry requirements: (i) the material should be inversion asymmetric since inversion symmetry combined with time reversal symmetry ensures that every band is spin degenerate; (ii) the material respects the out-of-plane mirror symmetry M_z , which forbids the existence of in-plane spin polarization. Alternatively, such symmetry requirements can be understood from the SOC Hamiltonian $H_{\text{SOC}} \propto \mathbf{E} \times \mathbf{p} \cdot \mathbf{s}$, where \mathbf{E} is the internal electric field of the crystal, \mathbf{p} is the momentum of electron, and \mathbf{s} is the spin of electron. The M_z symmetry of the 2D material guarantees that the internal electric field \mathbf{E} lies in-plane. Since the electron momentum \mathbf{p} is also confined in the same plane, it is deduced that $H_{\text{SOC}} \propto s_z$, polarizing electron spins to the out-of-plane direction, or so called Ising SOC [97–99].

Ising SOC reduces the effects of in-plane Zeeman fields on the band structure. Since the in-plane s_x and s_y components are zero, the first-order energy shift by in-plane field vanishes, i.e., the band structure with Ising SOC is protected against in-plane Zeeman fields. Alternatively, the spin splittings due to Ising SOC can be viewed as built-in out-of-plane Zeeman fields which compete with external in-plane Zeeman fields. Since the first-order shift vanishes, the band energy shift $\delta E_{Z\parallel}$ due to the external in-plane Zeeman field comes from the second-order (and higher order) effects, which scales as $\delta E_{Z\parallel} \propto (g\mu_B B)^2 / \Delta_{\text{ising}}$, with Δ_{ising} being the band splitting induced by Ising SOC. The Zeeman energy for 10 T magnetic field is roughly 1 meV, dwarfed by the intrinsic Ising SOC in certain 2D materials. Such protection of superconductivity by Ising SOC against in-plane field is called Ising superconductivity.

The two symmetry requirements are satisfied by transition metal dichalcogenides (TMDs) monolayers, such as MoS₂ and NbSe₂ (Fig. 1.17c): monolayer is inversion asymmetric and has an out-of-plane mirror symmetry. The band edges of both valence bands and conduction bands are located at the corners of the Brillouin zone, K and K' valleys. Superconductivity exists in TMDs like intrinsic NbSe₂, TaS₂ and ionic gated MoS₂. When they are isolated to monolayer limit and at the layer decoupled limit, the superconductivity is consistent with Ising pairing [9, 100, 101]. Fig. 1.17b shows the experimental data of in-plane critical field $B_{c2\parallel}$ as a function

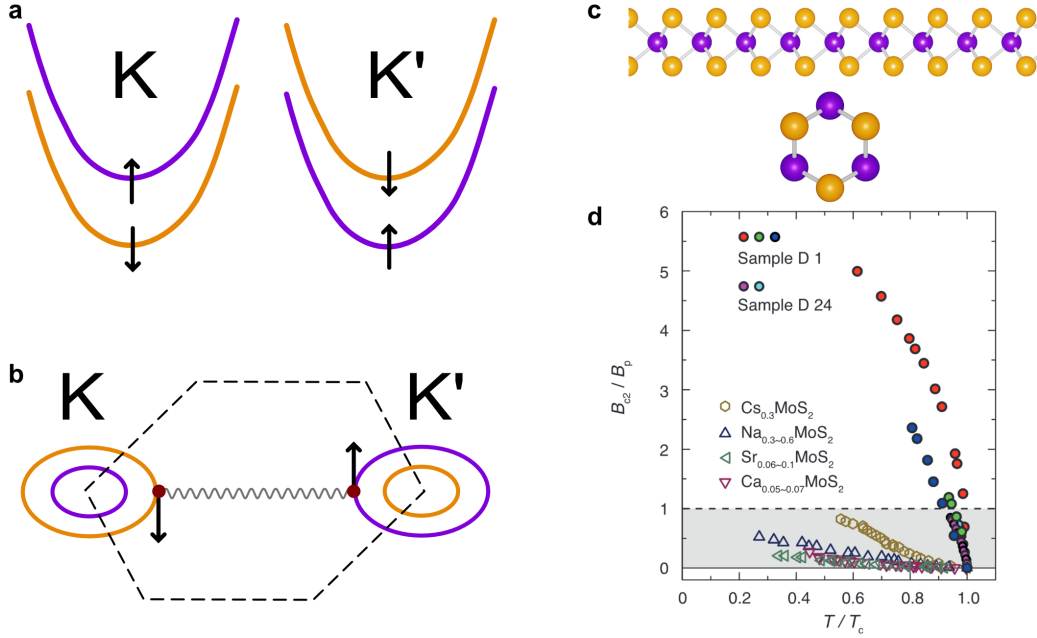


Figure 1.17: Ising superconductivity. (a) Ising SOC band splitting. (b) Ising pairing across K and K' valley. (c) Side view and top view of monolayer transition metal dichalcogenides. (d) In-plane field dependence of Ising superconductivity showing Pauli-limited violation. Reprinted from Ref. [100], with permission from The American Association for the Advancement of Science.

of the temperature for gated MoS_2 thin films. For different devices, $B_{c2\parallel}$ all exceeds the Pauli limit just slightly below T_c . The Pauli-limit violation ratio exceeds six at lowest temperature of certain parameters. The eventual in-plane critical field is complicated by other parameters, such as Rashba SOC, spin-orbit scattering, etc., depending on system details.

Normally, superconducting states are either classified as singlet or triplet depending on whether the total spin quantum number of the Cooper pair is 0 or 1. One interesting consequence of the Ising superconductivity in the single monolayer TMDs is that the superconducting state is neither singlet nor triplet but a combination of singlet and triplet. The probability amplitude of the Cooper pair to be in a state $|K \uparrow; K' \downarrow\rangle$ differs for the corresponding amplitude for the state $|K \downarrow; K' \uparrow\rangle$. Alternatively, the parity-even singlets $|\Psi_s\rangle \propto |K \uparrow; K' \downarrow\rangle - |K \downarrow; K' \uparrow\rangle$ and parity-odd triplets $|\Psi_t\rangle \propto |K \uparrow; K' \downarrow\rangle + |K \downarrow; K' \uparrow\rangle$ coexist [102, 103]. Additionally, because of the strong resilience to in-plane magnetic field, the in-plane field may introduce extra field-induced triplet pairing channel as $|\Psi_{tB\parallel}\rangle \propto |K \uparrow; K' \uparrow\rangle + |K \downarrow; K' \downarrow\rangle$ that couples to the singlet states $|\Psi_s\rangle$ [104–106]. Experimental progress [107] is working

toward the identification of different pairing channels and hopefully the evolution as a function of magnetic field.

Chapter 2

DEVICE DESIGN AND CHARACTERIZATION

The dissertation largely depends on the electrical transport techniques and thermodynamic measurements of graphene vdW heterostructures. Electrical transport measurement by itself is straightforward. To get the most informative details about correlated electrons, however, we need (i) on-demand design of 2D materials heterostructure and (ii) careful measurement scheme at the lowest electron temperature. This chapter will go through details regarding vdW heterostructure fabrication, both moiré and crystalline cases, from exfoliation to flake transfer and cleanroom protocols. Second, a brief overview of our Oxford Triton dilution refrigerator, details regarding sensitive electrical measurements and beyond.

2.1 2D materials exfoliation

We are investigating graphene multilayers with proximitized spin-orbit coupling. The structure is composed of graphene or graphite, hexagonal boron nitride, and WSe₂. Graphene multilayers are the main object. TMD materials adjacent to graphene induce SOC. Hexagonal boron nitride, also called white graphene, is a perfect dielectric material. We follow the conventional exfoliation method by scotch tape to get monolayer crystalline 2D crystals.

We start with some general principles for crystal exfoliation and then go to details for each type of materials. Apply the desired crystals to scotch tape or blue tape. Fold the left half of the tape with the right part to scatter bulk crystal around. While scattering around, the main idea is to have the large big chunk of crystal spread evenly, thinly (but also not too thin) over the whole tape area. If the spread is not even, then the tape is not even thickness, which will result in gaps forming air bubbles when attached to SiO₂ surface. If the spread is too thick, there will be less sticky tape surface exposed, which will make the adhesion to SiO₂ surface weak. If the spread is too thin, the tape is too sticky and overall the bulk materials on tape are scattered into small pieces, resulting in really tiny flakes.

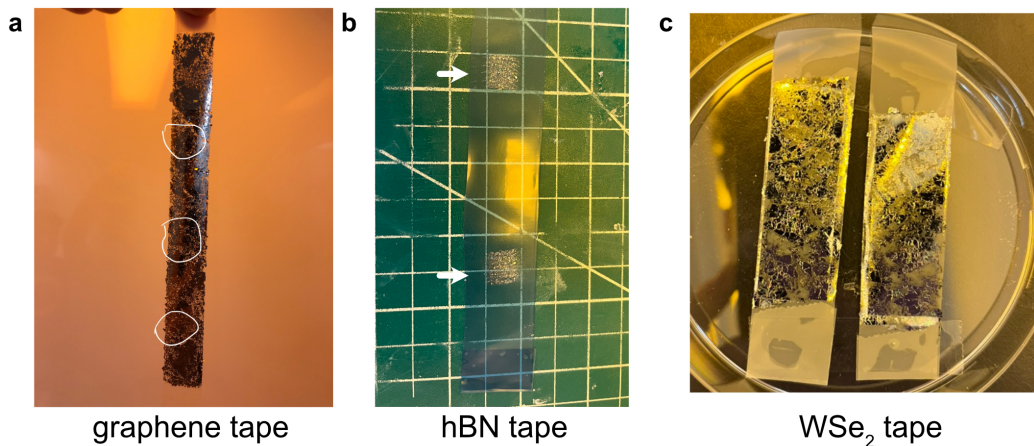


Figure 2.1: Exfoliation tapes. Different tapes with bulk crystals of graphite (a), hBN (b), and WSe₂(c).

Graphene and graphite exfoliation

1. Clean up the SiO₂/Si chip, dice the whole wafer into small pieces, roughly 2cm × 2cm for graphene exfoliation. Prepare roughly 15 chips of the same size. Blow away the small dusts by nitrogen gun. Pre-clean the plasma chamber with O₂ plasma for 10 minutes. Put four to five chips into the plasma chamber and then clean them with power of 100W, flow rate is 15 cc/min, and the outlet gauge of the regulator reads 15 ± 5 psi.
2. Prepare a scotch tape that is roughly 15-20 cm long (Fig. 2.1a); fold the two ends to form two small handles; remember to keep the tape surface clean. Select a good bulk graphite crystal from the bag. The principle is that the surface of the bulk graphite being large, flat, and smooth, both sides. Put the bulk crystal on one end of the scotch tape and fold the tape to overlap the other end. Have the bulk graphite surface scatters over several areas, not the whole tape surface.
3. Remove the remaining bulk crystal if it is too thick. With those several flat areas of graphite on the tape, overlap the two sides of the tape two or three times to have most area of the tape covered by graphite. Selectively cover the empty area with thicker graphite area, just to have the whole tape being uniform with thin flat graphite area (see circled areas in Fig. 2.1a). The best is to have some grey semi-transparent graphite, they are sticky yet big as a whole, flat, and thin. If the tape is still too thick, prepare a son tape of the

same length and overlap with the mother tape. Repeat until the thickness of graphite on the tape is ideal.

4. The surface with graphite up, fix the scotch tape on the table at the two ends by additional scotch tapes. Take out the plasma-cleaned chip immediately. With the SiO₂ surface down, put the chips onto the good areas. The good areas are those grey, semi-transparent, thin, flat area. Have Kimwipes wrapping around by thumb, press down the chips as hard as one can. Flip the whole tape with chips down. Put extra tapes on top of the areas with chips, fix the chips on the table tightly by the extra tapes. Press down the chips as hard as one can. Repeat the same for all the chips. Have heavy books on top of the tape and chips to firm the contact between tape and chips. Wait for 15 to 30 minutes.
5. Heat up the hot plate and set it to 110°C. Remove the books and use a razor blade to cut the graphite scotch tape. Gently remove the tape from the table. During the removal, keep the firm adhesion between chips and tape. Put the tape on hot plate. Wipe down the tape with Kimwipe to ensure flat surface of tape on hot plate; mainly to remove bubbles at the interface between tape and chips. Heat the tape for 5 minutes.
6. Remove the tape from the hot plates and wait for 5 minutes to cool down. Slowly and gently remove the chips from the tape.

hBN exfoliation

1. Clean up the SiO₂/Si chip, dice the whole wafer into small pieces, roughly 2cm × 2cm for hBN exfoliation. Prepare roughly 16 chips of the same size. Blow away the small dusts by nitrogen gun. Put the chips on hot plate to heat at 500°C for an hour or longer.
2. Prepare a narrow blue tape that is roughly 15 cm long (Fig. 2.1b); fold the two ends to form two small handles; remember to keep the tape surface clean. Select three or four hBN bulk crystals from Japan and align them in a line; again keep them flat. Put these crystals at the position roughly one fourth of the tape length and fold the tape to overlap the other end. Have the bulk hBN scatters along one line that is perpendicular to the tape length direction, the length of the bulk hBN line should be roughly the width of SiO₂ chips.
3. Then scatter the hBN line along the direction of the tape length. Fold the tape so that forming two areas at two sides of the blue tape that are roughly

the same area of the SiO₂/Si chips. Then align the two hBN areas, fold and separate for three times to make hBN denser in the two areas. The two areas are now the two mother tapes. Cut the tape into half.

4. The two blue tapes are now mother tape. Prepare some scotch tapes that are the same length as the two mother tapes. Overlap with the mother tapes and remove so that there are hBN bulk crystal on the son scotch tape.
5. Remove one chip from the hot plate and put on the table for cooling 10 seconds. Put the son scotch tape over the clean chip. Scratch the surface with soft-tip tweezers to form good contact and also remove all the air in between the interface. Scratch for three times. Finally, remove the scotch tape as slow as possible.
6. Each mother tape can be peeled for seven or eight times by scotch tapes. Each time the yield of hBN has different thicknesses. The later ones overall have thinner thickness.

WSe₂ exfoliation

1. Clean up the SiO₂/Si chip, dice two long pieces, each has the width of scotch tape and the length that is twice the width. Blow away the small dusts by nitrogen gun. Pre-clean the plasma chamber with O₂ plasma for 10 minutes. Put one long chip at a time into the plasma chamber and then clean it with power of 100W, flow rate is 15 cc/min, and the outlet gauge of the regulator reads 15 ± 5 psi.
2. We prepare one scotch tape that is the same length as the chip (Fig. 2.1c). Fold the two ends to form two small handles; remember to keep the tape surface clean. Select a good large flat shining WSe₂ crystal (from HQ graphene) from our glovebox. The commercial ones are quite big with diameter being roughly 1 cm and surface being shining and flat. Put the bulk crystal on the tape. Similar to graphene, have some relatively thick layers spread over the scotch tape.
3. Remove the remaining bulk crystal. With those several flat areas of WSe₂ bulk on the tape, selectively cover the empty area with thick WSe₂ area, just to have the whole tape being uniform with thin flat WSe₂ bulk. After being uniform, attach another scotch tape that is the same size as the previous one,

overlap them to have two tapes with equal amount of WSe₂ flakes. The best is to have grey semi-transparent WSe₂ bulk; they are sticky yet big as a whole, flat, and thin. If the tape is still too thick, prepare a son tape of the same length and overlap with the mother tape. Repeat until the thickness on the tape is ideal.

4. Take out the plasma-cleaned chip immediately. Put the chip onto a glass slide. Align the scotch tape with substrate and put it down. similar to hBN, scratch the surface with a soft-tip tweezers to remove all the air bubbles in between. Scratch for three times or so; sometimes can press down with thumb.
5. Heat up the hot plate and set it to 110°C. Put the tape together with glass slides on the hot plate. Wipe down the tape with Kimwipe to ensure flat surface of tape on hot plate; mainly to remove bubbles at the interface between tape and chips. Heat the tape for 5 minutes.
6. Remove the tape from the hot plates and wait for 5 minutes to cool down. Slowly and gently remove the chips from the tape.

Inspect the flakes under the microscope. Some typical images of graphene, graphite, hBN, and WSe₂ are shown in Fig. 2.2. For the microscope in Nadj-Perge lab and SiO₂ thickness being 300nm, monolayer graphene would look purple. Thicker graphene layers look more dark purple. One can identify the thickness through RGB contrast relative to the bare SiO₂. The red scales linearly with thickness. Similarly, WSe₂ thickness linearly scales in red or blue. We typically do not need monolayer hBN. The color of hBN follows: thinnest (10nm or so) are blue, then blue green for 10-20 nm, then green 20-30 nm, green yellow for 30-40 nm, and yellow for more than 40 nm, then to dark yellow. Typically we use hBN that is below 60 nm or so. For the identification of rhombohedral versus Bernal-stacked graphene multilayers, optical images solely are not enough. We identify the stacking order by Raman spectroscopy [108–111]. There are two Raman peaks that are mostly relevant for graphene multilayers. One of them is at around 1580 cm⁻¹, usually named the “G-band”. The other is at around 2750 cm⁻¹, named “G-band” or “2D-band”. The 2D-band is the most relevant for us. It is a second-order process that is contributed by a combination of the transverse optical mode and an inter-valley scattering. The 2D-band contains multiple peaks that have similar energy. In multilayer graphene, the relative intensity of these peaks is affected by the stacking order. To identify these domains, a spatial map of the Raman spectrum is necessary. The peak width

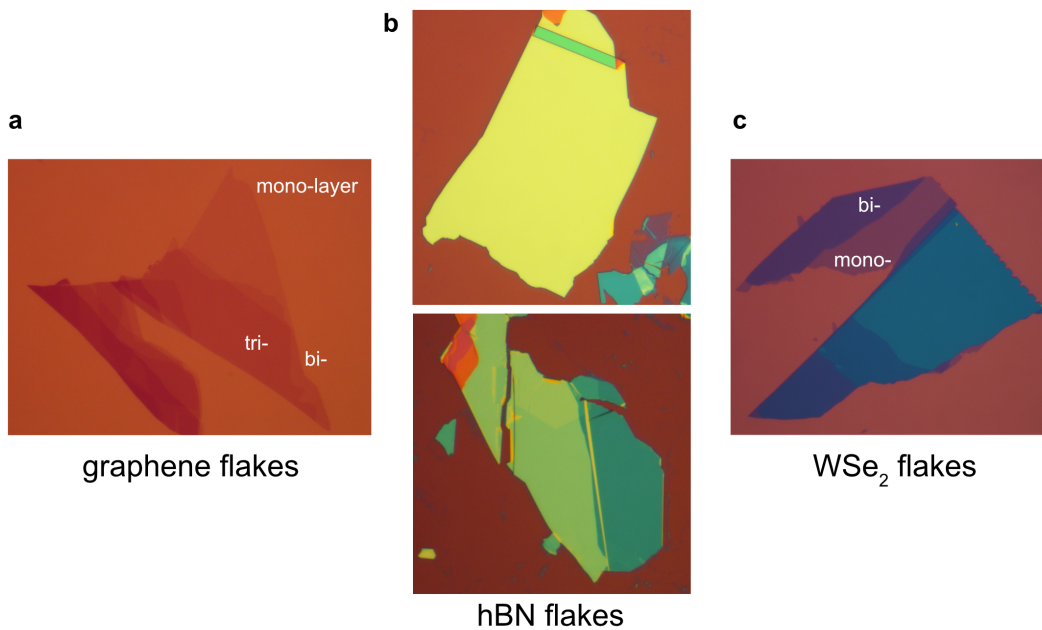


Figure 2.2: Different 2D materials flakes. Optical images of graphene multilayers (a), thick (top) and thin (bottom) hBN (b), and WSe₂ layers (c).

of the 2D band is extracted for each point, and the corresponding width map is shown in Fig. 2.3b. The brighter part corresponds to the rhombohedral area with larger width and is later separated by atomic force microscope (AFM) cutting.

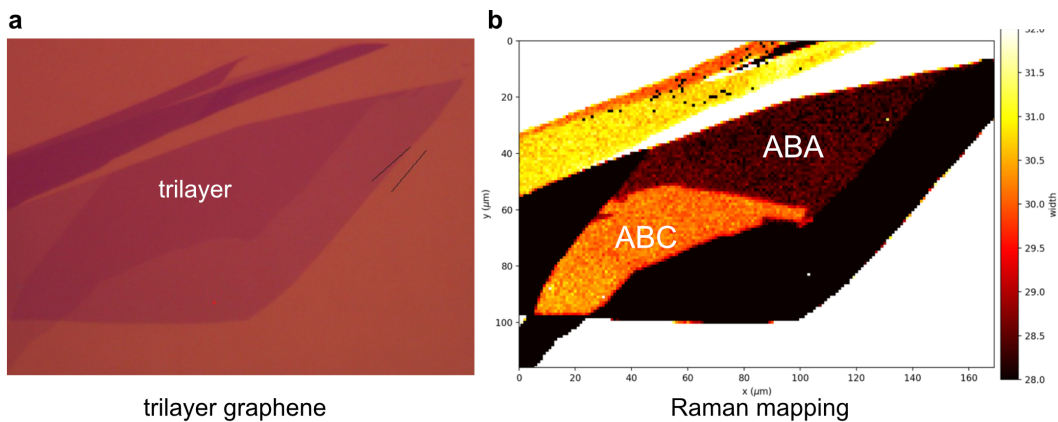


Figure 2.3: Raman spectroscopy mapping of trilayer graphene. (a) An optical image of trilayer graphene multilayers. (b) Raman spectroscopy 2D peak width mapping of the trilayer graphene area. The rhombohedral (ABC-) trilayer area has a wider 2D Raman peak in comparison to the Bernal (ABA-) stacked area.

2.2 Van der Waals heterostructure assembly

Dry transfer polymer preparation



Figure 2.4: PC/PDMS stamps. Optical images of PC/PDMS stamps. From left to right are PC on flat PDMS stamp, PC on domed PDMS stamp, and also polypropylene carbonate (PPC) on domed PDMS stamp.

To manipulate flakes, we want a supporting structure that can pick up different 2D materials one by one. Empirically, the first layer of 2D materials to be picked is hBN, which can serve as both dielectric and supporting layer. The polymer pickup technique requires a polymer that will reliably pick up the first hBN flake (soft, sticky to hBN) but will melt at reasonable low temperatures. A thin film of poly(bisphenol A carbonate) (PC) is supported by polydimethylsiloxane (PDMS) on a glass slide; see Fig. 2.4. The PDMS is homemade, simply mixing the A and B parts (Sylgard 184 silicone elastomer kit) together with a weight ratio 10:1; typically weight is 3g:0.3g in an one-time petri dish. Mix them together evenly for 5 minutes and let them dry overnight, typically resulting in a thickness ~ 1 mm or so. A PC thin film is produced by dissolving the polymer into a solvent, such as chloroform until forms a viscous liquid (weight ratio is 6%). The PC/PDMS slides assembly is as following:

1. Clean a glass slide with acetone and Isopropyl alcohol (IPA), blow dry with a nitrogen gun. Cut a small piece of PDMS with diameter $2\text{mm} \times 3\text{mm}$ and put it on the glass slide. Punch a hole on double-side tape and put the double side tape around the PDMS.
2. Prepare two clean glass slides. Put several droplets of PC/chloroform solvent

onto one of them, slipping another slide across the first slide, and letting the two slides dry; PC forms a dry thin film.

3. Punch a hole through a scotch tape and put the tape on the glass slide with PC film. Cut the edges of scotch tape with razor blade so that when removing the scotch tape, PC films can be picked. Put the scotch tape supporting PC on the PDMS piece. Press hard around the edge of PC so that it is fixed well onto double side tape; stretching the PC over the PDMS stamp.
4. After a curing step at 104°C for 9 minutes and wait for half a day or so, we can use the polymer stamp to pick up the hBN flake.



Figure 2.5: A transfer setup used to make van der Waals heterostructure stacks.

The degrees of freedom required for the assembly are: x-, y-, and z-axis control of the substrate relative to the polymer stamp slide, independent tuning of the microscope focus, accurate twist control of the substrate, and (optional but convenient) x- and y-axis control of the polymer stamp slide. The substrate holder also needs to have

temperature control up to 180°C. We used a commercially produced transfer stage (HQ Graphene), shown in Fig. 2.5. By clapping the glass slide, the slide forms a small tilted angle relative to the substrate holder. When approaching the slide to the substrate, a small touching point touches first. By further approaching, the interface between PC and substrate moves. The polymer stamp is used to subsequently pick up the top hBN (sometimes also top graphite gates and extra top hBN for dielectric), followed by monolayer WSe₂, the two twisted graphene flakes (or multilayer crystalline graphene flakes), and a bottom hBN flake (30–70 nm thick to avoid over-etching in further steps) and then back graphite gates depending on the structure; as shown in Fig. 2.6. As the polymer stamp is lowered over each van der Waals flake, the polymer contact to the substrate forms a line that propagates as the polymer stamp is raised or lowered. When the line propagates across the flake and then retracts, the flake is picked up and added to the stack that adheres to the bottom of the polymer stamp. Here are the temperatures and other details regarding different heterostructure transferring:

Moiré graphene transfer procedures

1. Picking up top hBN: glass slide approaches the substrate surface at 30°C. Increase the temperature to 80°C while keep retracting the interface (due to thermal expansion) to keep the interface at the same position. Stable the temperature at 80°C and retract glass slide slowly with hand.
2. WSe₂ picking up: set the stage temperature at 40°C and approach, raise the temperature to 80°C and retract with hand.
3. Picking up graphene: set the temperature stable at 40-50°C, approach with hand or slightly increase the temperature. For TBG, first the top flake of graphene is picked up. Then the substrate is rotated to about 1.1-1.3° (overshooting the target angle slightly to allow for relaxation), and the second flake is picked up at the same temperature with the same procedure.
4. Bottom hBN approaches at 40°C. Likely, there are air bubbles or dirty blisters trapped in between during the encapsulation procedure. Increase temperature to 90°C. Sometimes the bubbles may spontaneously be pushed away during the process, resulting in clean moiré area. Do *not* aggressively move bubbles since it may likely mess up the angle.

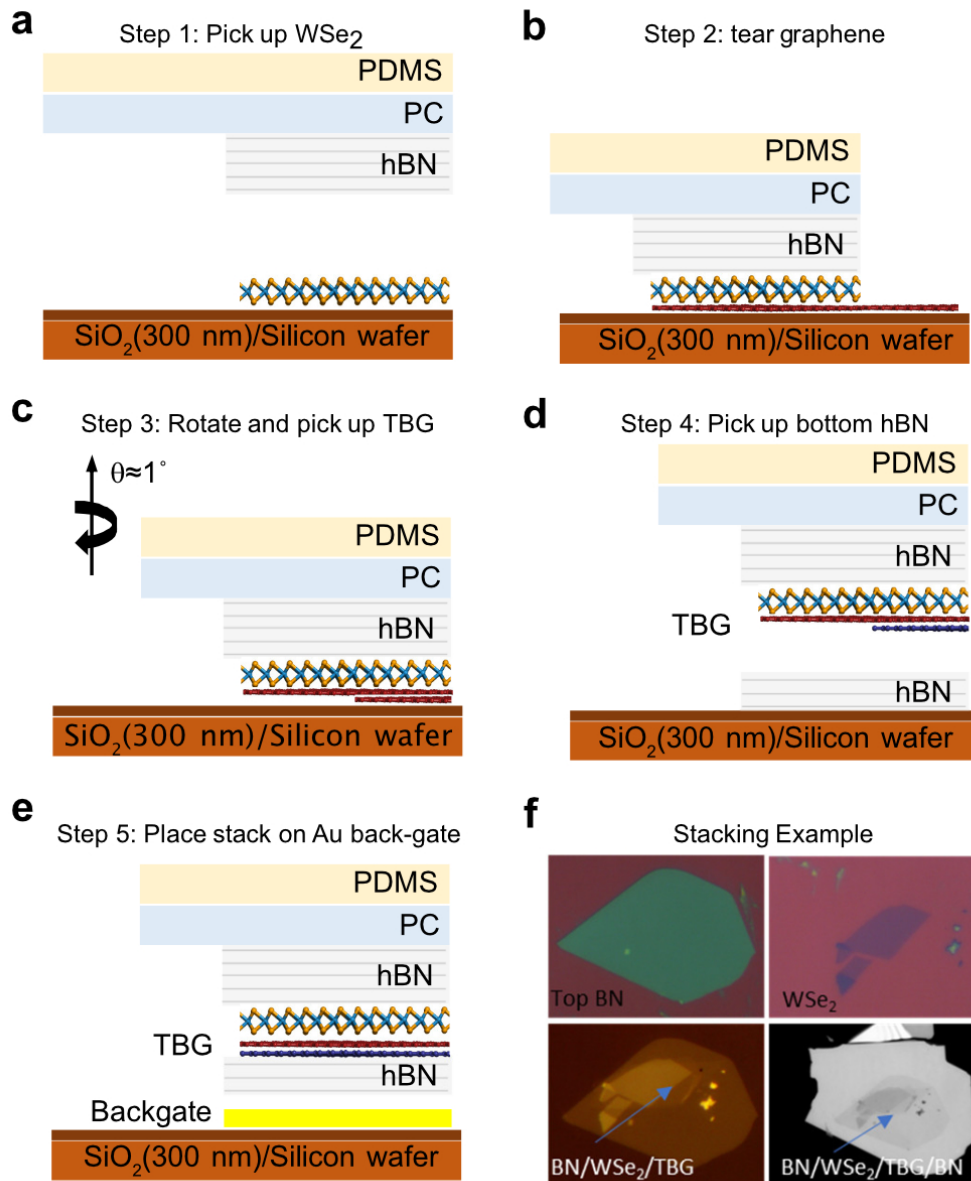


Figure 2.6: Dry flake transfer process with PC/PDMS stamp. (a)–(e), Critical steps in the stacking process. (f) Optical images of a typical flake and stacks at different stages of the fabrication.

- Finally, to complete the stacking, the stamp containing the finished stamp is lowered onto a substrate, a doped Si/SiO₂ chip pre-patterned with Au lithography markers for optically designing devices and with a Au gate (2nm Ti/20nm Au). While lower the stack onto the substrate, the temperature is set to 150°C. Then, the temperature is raised to 170°C to melt the PC, and the stamp is lifted. Leftover polymer residue can be removed in a 10-minute

Nmethyl-2-pyrrolidinone (NMP) bath, 10-minute Acetone bath and 10-minute Isopropyl alcohol (IPA) bath.

BLG-WSe₂ flake transfer procedures

1. Picking up top hBN: glass slide approaches the substrate surface at 40-50°C. Increase the temperature to 80°C while keep retracting the interface (due to thermal expansion) to keep the interface at the same position. Stable the temperature at 80°C and retract glass slide slowly with hand.
2. Top graphite gate and top hBN dielectric picking up: set the stage temperature at 50°C and approach, raise the temperature to 95°C and retract with hand. Squeeze to move air bubbles, can result in ultra clean interfaces.
3. WSe₂ picking up: set the stage temperature at 50°C and approach, raise the temperature to 80°C and retract with hand.
4. BLG, graphite contact, and bottom hBN pick up: set the temperature stable at 50°C, approach with hand or slightly increase the temperature. Then all the way increase temperature to 95-100°C, simply because higher temperature will reduce the bubbles and move them more flexibly. Squeeze bubbles forward and backward at high temperature. If last BN encapsulation has bubbles, consider to pick up graphite back gate at 102°C or so and move bubbles slowly when retracting.
5. Finally, the stamp is lowered onto a substrate, an undoped Si/SiO₂ chip (for capacitance measurement) pre-patterned with Au lithography markers for optically designing devices. While lower the stack onto the substrate, the temperature is set to 150°C. Then, the temperature is raised to 180°C to melt the PC, and the stamp is lifted. Leftover polymer residue can be removed in a 10-minute NMP bath, 10-minute Acetone bath and 10-minute IPA bath.

Interfacial twist BLG-WSe₂ flake transfer

The basic idea follows the same as BLG-WSe₂ flake transfer. Main difference is that here we use curved (dome-shaped) PDMS to slow down the flake transfer processes. Making curved PDMS is simple: after cutting a small PDMS square and putting on the glass slide, mix some new PDMS and put a small droplet of PDMS liquid onto the PDMS square. The droplet dries in a day or so, and it is a dome shape. The first top hBN is picked at 40°C and increase the temperature to

80°C and disengage. The following flakes (except BLG) approach at 70°C or so. Because of the curving PDMS, the relatively slow moving results in spontaneous jump of flake onto the stack (because of van der Waals force). Typically, this results in an ultra-clean interface but the drawback is that the final position of the flake is sometimes not under control. For BLG picking up, they are cut into several small pieces by atomic force microscope (AFM) cutting (see below). The picking up is at 50°C and increasing temperature really slow to control the interface moving. When barely cover the BLG to pick, disengage immediately with hand to avoid the pick of second flake, so on and so forth. The drop-off process follows the same but can increase temperature to 180°C to ensure melting of PC (the dropping with curved PC/PDMS is sometimes tricky; be careful).

Atomic force microscope cutting

As mentioned before, the graphene flakes are separated into pieces, either for moiré graphene devices or twisting the interface of BLG/WSe₂. Additionally, one wants to separate meta-stable rhombohedral-stacked graphene multilayers from the surrounding Bernal-stacked area for manipulation. Samples with domain walls are more likely to relax to the stable ABA-phase during the fabrication process.

We use a lithography free approach: cut the flake with an atomic force microscope (AFM) probe. Previously, d.c. voltage is applied between graphene and AFM probe, which requires electrical contacts to graphene [112–115]. An alternative techniques have recently been developed to solve this problem, which is to replace the d.c. voltage with an a.c. voltage [116]. Since the graphene is capacitively coupled to the doped-silicon substrate, a current can go through the graphene even no electrical connection is directly made to the graphene flake (Fig. 2.7a).

The actual experiment was performed on a Bruker dimension Icon AFM with probes from NANO WORLD ARROW-NCPT-20. The front side of the probe is coated with a platinum/iridium alloy coating layer which is electrically conductive. When cutting the sample, the tip is engaged to the sample in contact AFM mode. An a.c. voltage with 10V amplitude and 100kHz frequency is applied on the tip. The a.c. voltage is generated by an internal oscillator of the AFM controller, but may also be generated by an external instrument. Since the reaction is between graphene and water absorbed on the probe apex. A humidity control is optimal; the cleanroom environment works even without additional control. Usually, higher humidity gives better results. While cutting, the tip is moving at a speed of 300 nm/s. Although

the trench can be made with higher speed ($> 1\mu\text{m/s}$), it may increase the chance for relaxation. The width of the trench made is usually 50 nm to 100 nm wide. A representative cutting image is shown in Fig. 2.7b.

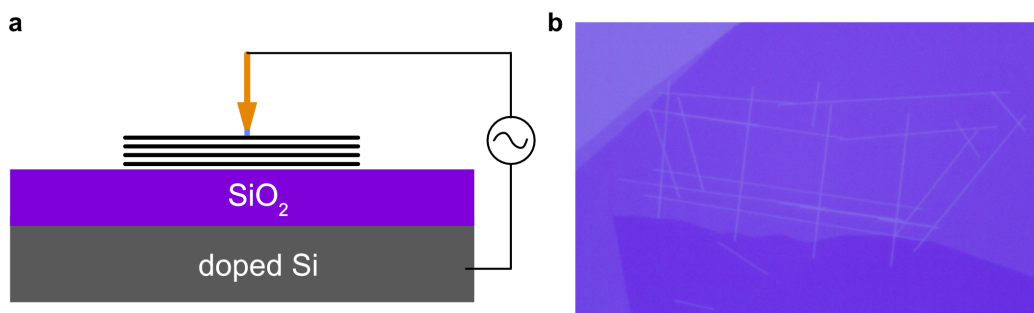


Figure 2.7: AFM cutting. (a) Schematic showing d.c. AFM cutting. (b) Optical image of graphene multilayers by AFM cutting.

2.3 Cleanroom processes

With finished stacks on the Si/SiO₂ chips, we take extra images of the stacks for electrode design and etching processes, using AutoCAD. The typical stacks go through e-beam lithography process, etching through hBN, metal electrode deposition, lift off, e-beam lithography process forming device geometry, and etching the area. The steps involve the use of nano-fabrication tools available in the Kavli Nanoscience Institute (KNI).

1. Electron-beam lithography

Each lithography step starts with first preparing spin-coating polymethyl methacrylate (PMMA, 950PMMA A4) at 1400 rpm followed by a low-temperature bake of 110°C for 90 s. When requiring aggressive etching process, use thicker PMMA layers; say 500nm. We use dedicated electron-beam lithography machines (Raith EBPG 5000+ or 5200) at 100 kV, beam currents is either 3 nA or 100 nA, and a dosage of 700–1300 $\mu\text{C}/\text{cm}^2$, depending on the substrate and the feature sizes. fine features use small current. Undoped silicon substrate uses less writing dosage. We construct our lithography patterns to avoid feature sizes $\lesssim 0.6\mu\text{m}$ and fillet edges to avoid sharp corners, which reduces cracks in the PMMA. After lithography, we use a methyl isobutyl ketone (MIBK)/isopropyl alcohol (IPA) solution to develop the patterns and remove the PMMA from the exposed area. Additional way to prevent cracks is by developing using cold mixture of IPA and distilled water

in the volume ratio 3:1. In IPA:DI water for 30s and then in MIBK/IPA for 60s and finally in IPA:DI water for 30s. In the first lithography step, we set up a pattern for the contacts and contact pads.

2. Etching

We use an RF reactive ion plasma etch system (Plasmatherm RIE) to etch our devices made of van der Waals materials since it has a controllable etch rate, roughly 30nm/minute for hBN. We first use a light O₂ etch (30 W, 20 sccm O₂ flow rate, 50 mTorr chamber pressure for 30s) to clean off PMMA residual from the contact area. Then, a CHF₃/O₂ etch step is used (60 W, 40 sccm CHF₃ / 4 sccm O₂, 40 mTorr) to remove the top hBN, graphene, and a little of the bottom hBN from the contact area. We found hBN to etch at a rate of approximately 30 nm/minute, with graphene and WSe₂ areas etching at a slightly slower rate. We optically checked the etch (every 30s or every 1 minute) to avoid over-etching. Sometimes we only want to etch hBN layers and stop the etching at graphite layer. Use SF₆ plasma at the power 60 W, 15 sccm, 40 mTorr. The etch is really fast in terms of hBN but immediately stops at carbon-based layers.

3. E-beam evaporation for metal contacts

Immediately after the etching process, we put the stack into our electron-beam evaporator for metal contacts deposition, which allows for reliable effective one-dimensional contacts to graphene [13]. As opposed to Ref. [13], we achieve contacts in one lithography step. This avoids unnecessary lithography steps and possible solvent-based contamination of the contacts. We use a Kurt J. Lesker Labline electron-beam evaporator to evaporate metals for contacts and gates. We deposit 5 nm Ti immediately followed by usually 100 nm of Au. We found more reliable contacts by depositing only after achieving base pressures $\sim 5 \times 10^{-8}$ torr; achieved by deposit some Ti in the chamber before the formal disposition.

4. Device geometry etch

After the contacts are deposited, we go through electron-beam lithography again, shape the device into the desired geometry, e.g., see Fig. 2.8 for two different devices after the contact deposition and geometry etch steps. Note that the Hall bar for moiré device is defined in a bubble-free region. After lithography, both devices are etched using the same CHF₃/O₂ etch recipe as before, but for longer to etch down to the SiO₂, even longer time for devices

with all crystalline component since they have thick graphite areas with lower etching rate.

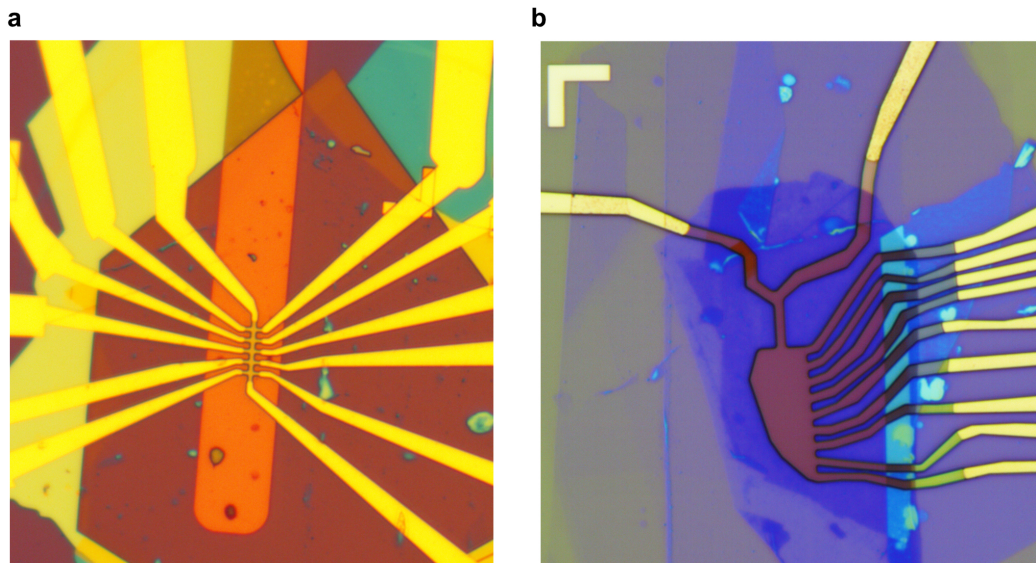


Figure 2.8: Optical images of different devices. (a) An optical image showing twisted bilayer graphene with WSe₂ Hall bar geometry. (b) An optical image showing Bernal bilayer graphene with WSe₂ dual-gated device in R_{xx} geometry.

2.4 Electrical transport measurement

Two types of measurements are applied to the characterization of graphene multilayers with proximitized SOC. The main one is electrical transport measurement and the other one is penetration field capacitance measurement (briefly in Section 2.5). The advantage of transport measurement is its simple instrument setup (a lock-in, a voltage source for gating, and a fridge for cooling). Minimal perturbation around the Fermi level enables the observation of physical phenomena at the lowest electron temperature, such as sub-100 mK superconductivity. Only a tiny a.c. current (as low as 0.5 nA) with low frequency (<50Hz) is driven through the sample and aggressive low pass filtering can be applied to reduce the electron temperature. This allows phenomena with very small energy scale to be detected.

The downside of transport measurement is double aspects. First, interpretation of resistance data is hard. Two condensed matter phenomena are the easiest to access and explained through transport. One is superconductivity and the other is quantum Hall effect. Other than that, physical quantities that are directly calculated by theory, such as density of states, are hard to directly inferred from resistance data.

There are other ways to indirectly obtain symmetry-breaking features. The second drawback is that transport is after all a global measurement. Experimental signals are averaged over the device size, thus render some subtle experimental signatures when disorders are relevant. Especially in the case of moiré materials, the twist angle inhomogeneity more or less exists [117]. In that sense, local probe techniques can easily overcome the problem [118–121].

Transport measurement is performed following the conventional technique: we use a four-wire configuration to remove the contact resistance. A Stanford SR865A lock-in amplifier is used to apply small a.c. excitation and acts as a voltmeter. A Stanford SR560 voltage preamplifier is used to preamplify the voltage signal. The frequency range used is from 13Hz to 50Hz, usually chosen based on the noise minimized at the frequency. We normally excite the sample with a constant current, amplitude of which varies from 0.5nA to 10nA depending on the measurement.

Hall bar device and irregular device shape

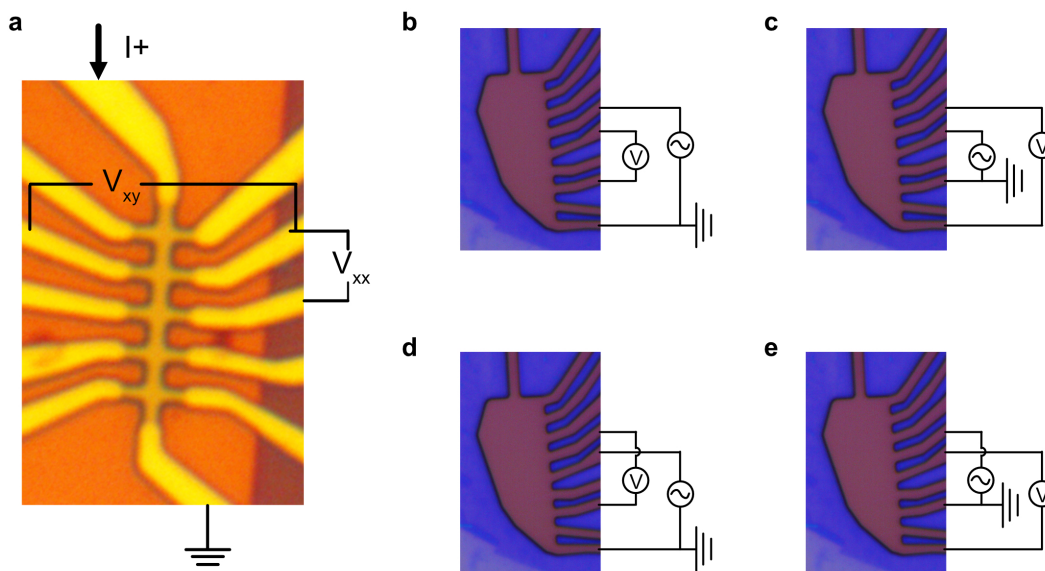


Figure 2.9: Transport measurement geometry. (a) A Hall bar geometry. (b)-(e) The combination of the four configurations can give V_{xx} and V_{xy} components.

The typical transport geometry Hall bar (Fig. 2.9a) is the easiest to obtain longitudinal and transverse resistance information. This is done by supplying a current I and measuring the longitudinal resistance as $R_{xx} = V_{xx}/I$. Four-point measurement is the most convenient case to measure ultra-low/zero resistance state like superconductivity, where the contact resistance does not contribute to V_{xx} . Under

an out-of-plane magnetic field, the transverse resistance is generated by B_{\perp} field, with $R_{xy} = V_{xy}/I$. R_{xy} is directly related to Hall density n_{Hall} as $n_{\text{Hall}} = \frac{B_{\perp}}{R_{xy}e}$, with B_{\perp} being low magnetic field. The Hall density measurement is a direct transport signature telling symmetry-breaking transitions in moiré graphene. R_{xy} component is also directly related to quantum Hall phases and topological orders.

For some devices, all the contacts are on one side of the device (Fig. 2.9b), which makes direct measurements of transverse component not possible. To address the problem, one can measure the voltage from the configuration Fig. 2.9d and Fig. 2.9e. Based on Onsager relation [22], R_{xy} is obtained by $R_{xy} = R_{xy}^c - R_{xy}^d$.

Quantum Hall effect

When 2D electron gas is clean enough, the electrons form cyclotron orbit and are localized. The bulk is an insulator but there are topologically protected edges that flow around the boundaries. R_{xy} measurement using contacts at the opposite side gives quantized resistance $R_{xy} = \frac{h}{\nu e^2}$, where ν is an integer number representing the topological index for integer quantum Hall system. The number of edge states depends on both magnetic field and the density of electrons in the system. Thus, integer quantum Hall effect is a good phenomenon to calibrate the carrier density.

The electrons for quadratic bands form cyclotron orbits with discrete energy levels

$$E = \hbar\omega_c(N + 1/2). \quad (2.1)$$

Here, $\omega_c = eB/m^*$, m^* is the effective mass and N is integers. In the case of monolayer graphene, the equation writes as

$$E = \hbar\omega_D \text{sgn}(N)\sqrt{|N|}, \quad (2.2)$$

where $\omega_D = v_F\sqrt{2eB/\hbar}$ is the cyclotron frequency of Dirac bands. When tuning gate voltage to change Fermi level, R_{xx} goes through oscillations and R_{xy} goes through quantized gap. Within the Landau level gap, R_{xx} is zero and R_{xy} quantized to $R_{xy} = \frac{h}{\nu e^2}$. Importantly, the carrier density is related to integer filling ν as

$$n_{2D} = \nu \frac{eB}{h}. \quad (2.3)$$

Once identifies the correct index ν , we know the carrier density at certain gate voltages and the calibration of gate capacitance is achieved. With the conversion between doping density and gate voltage, one may get the carrier density in crystalline graphene and in moiré systems. Specially in moiré graphene at the small

angle limit, twist angle is related to moiré full filling density as:

$$\theta^2 \approx \frac{\sqrt{3}a^2}{8}n_{\text{full}}. \quad (2.4)$$

Shubnikov de Haas oscillation

For crystalline graphene systems, since there are no integer fillings, we reveal the Fermi-surface degeneracy to indicate the symmetry-breaking orders. The Fermi surface degeneracy is obtained by Shubnikov de Haas (SdH) oscillation. we measure the longitudinal resistance R_{xx} as a function of out-of-plane magnetic field (B_{\perp}). The magneto resistance will show periodic patterns in $1/B_{\perp}$. Since the electrons cycle around the Fermi contours, the area A surrounded by the electron's trajectory can help to determine the size of the Fermi surface. The area A is related to the oscillation frequency f by

$$f = \frac{h}{2\pi e}A. \quad (2.5)$$

When a 2D electron gas has a simple Fermi surface, the frequency of the oscillation is proportional to the area of the Fermi surface. When complex Fermi surfaces are present, such as flavor symmetry-breaking orders, the oscillation of magneto resistance will be a combination of multiple oscillation frequencies. Analyzing the oscillation components in frequency space by performing Fourier transform will reveal the Fermi surface geometry.

2.5 Penetration field capacitance measurement

The complex origin of resistance data makes it difficult to directly link to calculated theoretical models. Penetration field capacitance can be linked to theoretical calculated quantities by a simple relation

$$C_p = \frac{1}{2c_0} \frac{\partial \mu}{\partial n} = \frac{1}{2c_0} \kappa \quad (2.6)$$

where κ is the inverse electronic compressibility. κ characterizes how much chemical potential changes when unit area of electrons are added into the system. In the non-interactive picture, κ is the inverse of density of states at the Fermi level ($1/\text{DOS}$), which can be directly calculated from theory. Additionally, when first or second order phase transitions happened as a function of gate voltage, measured penetration field capacitance typically reflects a strong signature, due to strong Fermi surface reconstruction imprinted to $\frac{\partial \mu}{\partial n}$. The constant c_0 here is the averaged geometric capacitance factor

$$c_0 = (c_t + c_b)/2 \quad (2.7)$$

where c_t and c_b are the top and bottom gate capacitance, respectively.

The capacitance of the sample is usually orders of magnitude smaller than the parasitic capacitance of the measurement scheme, making it challenging to detect. To address the problem, the capacitance is measured with an a.c. capacitance bridge circuit implemented with an *in situ* amplifier serving as an impedance transformer. The circuit diagram for capacitance measurement is shown in Fig. 2.10a. One

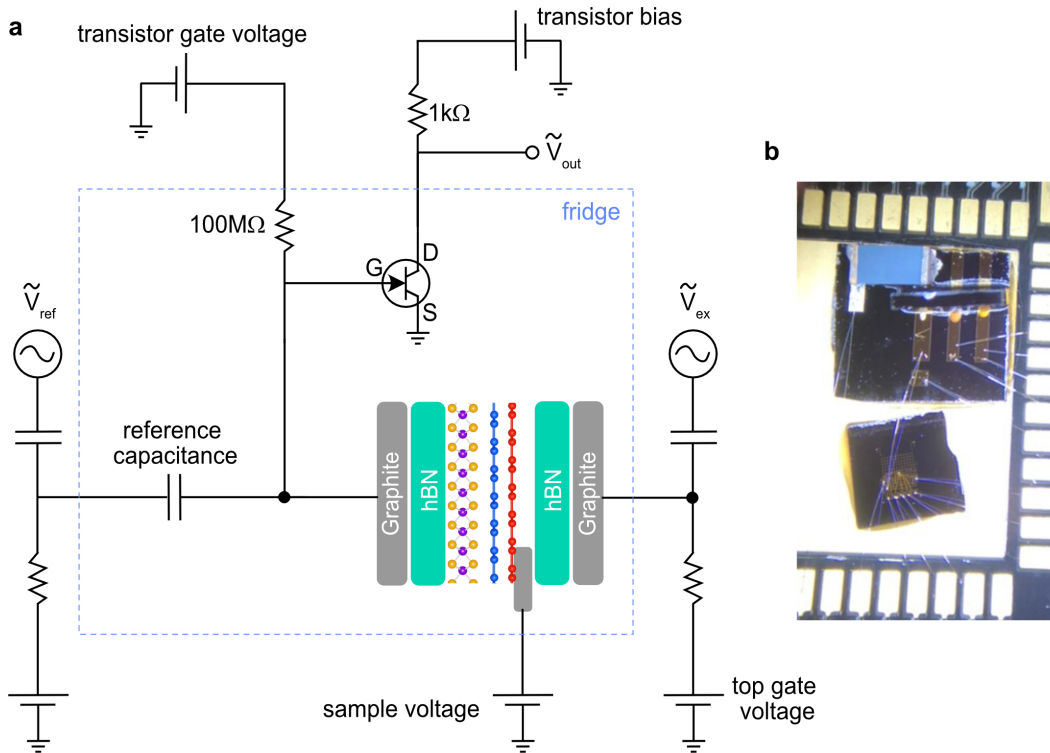


Figure 2.10: Penetration field capacitance measurement. (a) Electrical circuit of penetration field capacitance measurement. (b) an optical image of vertical HEMT mount.

of the gates of the device is connected to one electrode of a reference capacitor whose capacitance is a constant. Two a.c. voltages with the same frequency and relative phase locked are applied on the other gate of the sample as well as the other electrode of the reference capacitor; denoted \tilde{V}_{ex} and \tilde{V}_{ref} , respectively. The voltage between the sample and the reference capacitor is monitored. The module needs to be separated from external wires with large impedance so that the parasitic capacitance is minimized. A high electron mobility transistor (HEMT) is mounted close to the sample to monitor the capacitance bridge without low impedance wires. The transistor gate voltage is applied through a 100MΩ resistor to again increase the impedance. In order to drive the HEMT, a source drain bias voltage, 50mV

to 100mV, is also required. This current contributes a significant amount of Joule heating, limiting the electron temperature. A slightly different configuration enables lower electron temperature [122].

The quantity directly measured is $M = \frac{c_p + c_{\text{parasitic}}}{c_{\text{ref}}}$. The inverse compressibility κ is related to c_p as $c_p = \frac{c_t c_b}{c_t + c_b + \kappa^{-1}} \approx \kappa c_t c_b$ [64, 123]. To obtain κ , M is obtained at two extremes, denoted M_0 and M_∞ . M_∞ corresponds to when device is a good metal and simply the partial filling of a Landau level. While M_0 corresponds to an incompressible state and is achieved by go to certain band gap. In the case of M_∞ , $c_p = 0$ and therefore $M_\infty = \frac{c_{\text{parasitic}}}{c_{\text{ref}}}$. In the case of M_0 , $c_p = (M_0 - M_\infty)c_{\text{ref}} = \frac{c_t c_b}{c_t + c_b}$. Then we obtained $\kappa = \frac{1}{2c} \frac{M - M_0}{M_0 - M_\infty}$.

2.6 Dilution refrigerator setup

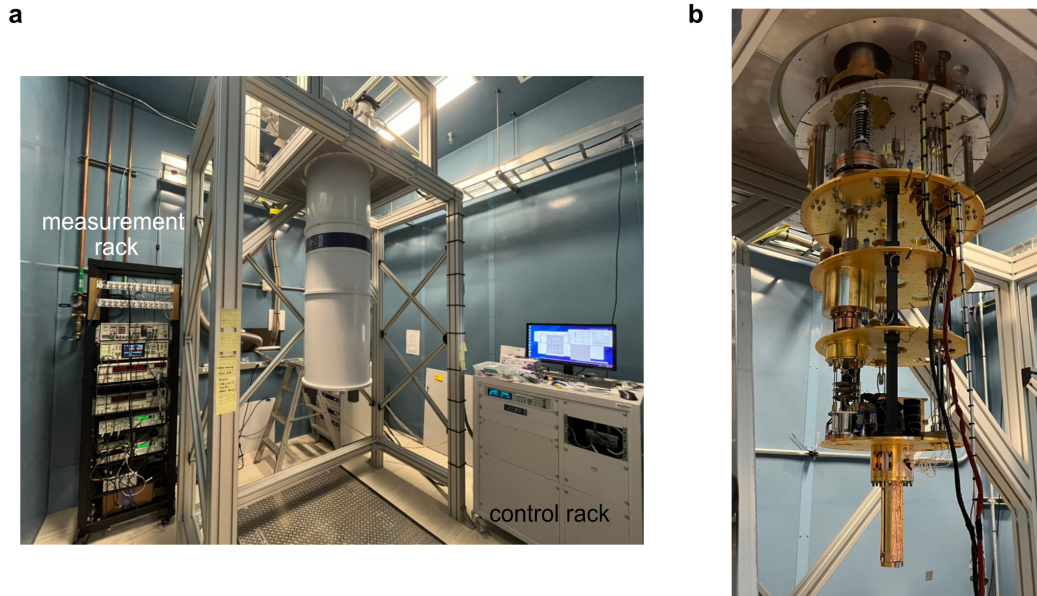


Figure 2.11: Dilution refrigerator setup. (a) Oxford Triton dilution refrigerator setup; here showing the fridge, measurement rack, gas handling rack, and magnet power supply. (b) Inside dilution fridge; from top to bottom are PT1 plate, PT2 plate, still plate, cold plate, and mixing chamber plate with sample loading at the bottom.

Most of the measurements in the dissertation were performed in our bottom-loading Oxford Triton dilution fridge (Fig. 2.11). The dilution fridge is a dry system with multi-stage cooling. The temperature from top to bottom are roughly 50K, 4K, 0.9K, 60mK and base temperature. The final stage utilizing a pumping action on a mixture of He3 and He4 isotopes to reach a base temperature of about 20–25

mK. The plate containing the mixture, and thus the lowest temperature stage, is the mixing chamber plate. The fridge is equipped with 48 DC lines and a vector magnet that can reach up to 9 T in Z direction and 1T in X and Y direction. Data presented here are generally taken at the base temperature unless otherwise stated.

Our dilution fridge uses multiple temperature stages, with fully-encapsulating shields thermally anchored to each stage, to minimize heat transfer through thermal radiation. However, one source of radiation still needs to be suppressed: transmission through the wires to the device [124]. Unless filtering is applied, the electron temperature will be significantly higher than the base temperature of the fridge, which is really detrimental for fragile states such as superconductivity with critical temperature below 100mK. For d.c. measurements, the general approach involves repeated thermalization steps and low-temperature passive filtering of frequencies outside of the range used.

The exact details of filtering are described in Ref. [125]. Our setup has been thermalized by first installing an extra 5m of constantan (a copper-nickel alloy with low thermal conductivity) twisted pair cables (in addition to ~ 2 m already installed), which is wound around and glued with GE varnish onto oxygen-free copper cylinders that are bolted to each stage of the fridge. The slightly resistive nature of the constantan wires ($\sim 66\Omega/\text{m}$) causes a small amount of attenuation at each stage. For high-frequency filtering, we first used three different passive π filters in series, which filter out bands of 200 MHz–4 GHz, 2–7 GHz, and 7–18 GHz. We included two π filters of that range for each line. Then, we used a two-pole RC filter, consisting of 1 k Ω resistors and 1–10 nF ceramic capacitors. Additional VLFX-80+ π filters were added between the room-temperature electronics and the fridge for further filtering.

To get the lowest electron temperature, additional care is needed when doing measurement. We use uninterruptible power supply for the measurement instruments to ensure a cleaner power source. The ground configuration is optimized to reduce the electronic noise. When doing the measurements at the lowest temperature, all temperature sensors are electrically disconnected to ensure the lowest excitation. The amount of instruments that are connected to power plugs is minimized to reduce additional noise introduced.

The sample printed circuit board is loaded into an encapsulated puck, shown in Fig. 2.12. The main frame is made of oxygen-free copper and coated with gold to thermalize the sample and position it such that an out-of-plane magnetic field can be

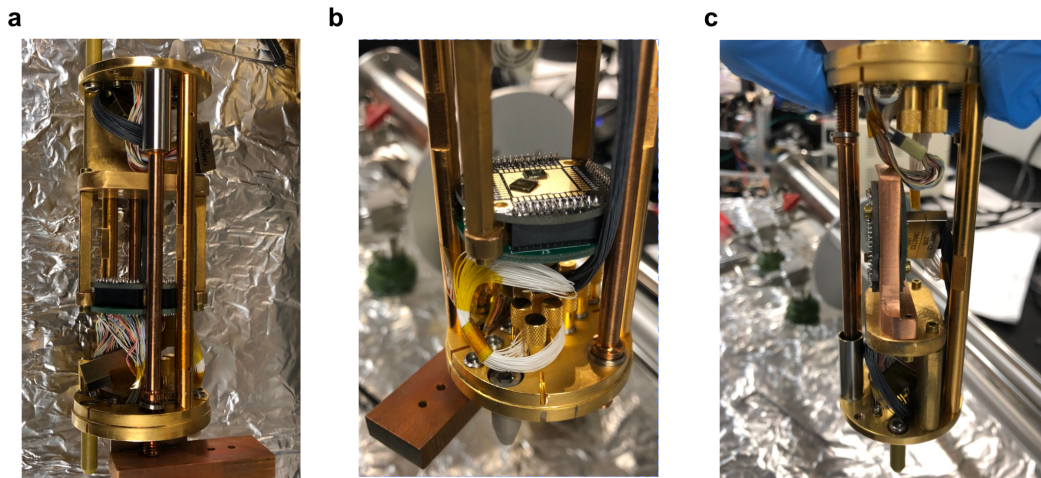


Figure 2.12: Sample puck. (a),(b) Configuration for out-of-plane magnetic field measurements. (c) Configuration for large in-plane magnetic field measurements.

applied (Fig. 2.12a,b). An additional piece was constructed for holding the sample in an in-plane magnetic field orientation (Fig. 2.12c) so that large in-plane magnetic field can be accessed.

SUPERCONDUCTIVITY IN METALLIC TWISTED BILAYER GRAPHENE STABILIZED BY WSe_2

The small angle rotation between two single-sheet of graphene forms moiré superlattices that feature flat electronic bands at the magic angle 1.1° (Chapter 1.4). At the magic angle, Coulomb energy dominates over kinetic energy. The spontaneous symmetry breaking drives correlated insulators and superconductivity in the system, and in principle would be highly susceptible to additional explicit symmetry-breaking perturbations. The reminiscence of TBG phase diagram compared to high-temperature superconductor naturally raises the question: How important the correlated insulating state is with respect to the occurrence of superconductivity? Are we able to modify the phase diagram to disentangle the relation between different correlated states?

3.1 Adding WSe_2

There are several reasons why we want to introduce SOC to TBG and why to use WSe_2 . Superconductivity with reduced symmetry often leads to unconventional pairing, e.g., combining SOC with time-reversal symmetry breaking by magnetic field. While graphene is the easiest 2D material to work with, its intrinsic spin-orbit interactions are considerably small [66–68]. Monolayer transition metal dichalco-

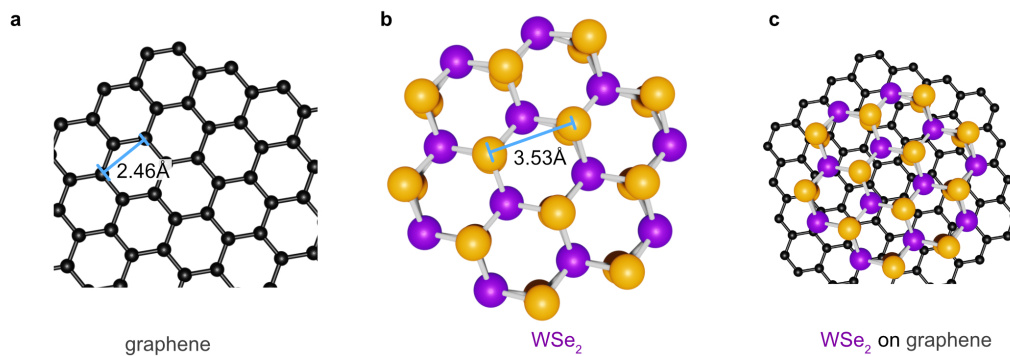


Figure 3.1: The lattice constant of graphene (a) and WSe_2 (b). Stacking them together introduces proximitized SOC to graphene (c).

genides (WSe_2 , WS_2 , MoS_2 , and MoSe_2) are direct band gap semiconductors that host intrinsic Ising SOC on the order of $\sim 500\text{meV}$. They are perfect dielectric materi-

als [126, 127] and at the same time can introduce proximitized SOC (Fig. 3.1c) [128–131]. Second, unlike hBN, WSe₂ and graphene lattice constants differ significantly (Fig. 3.1a,b; 0.353 nm for WSe₂ and 0.246 nm for graphene). The mismatch implies that the moiré pattern formed between TBG and WSe₂ has a maximum lattice constant ~ 1 nm when angle-aligned—much smaller than that formed in small-angle TBG (> 10 nm). Finally, due to hybridization effects, WSe₂ may also change both the Fermi velocity of the proximitized graphene sheet and the system’s phonon spectrum.

3.2 TBG-WSe₂ devices under study

We have studied more than ten TBG-WSe₂ devices with twist angles mostly away from the magic angle to fully map out the correlated phase diagram. The schematic in Fig. 3.2a well presents the typical structure. A top layer of WSe₂ monolayer is put adjacent to TBG with a twist angle θ . Both graphene and WSe₂ are encapsulated between two hBN crystals (which serve as dielectric) to ensure high quality of the van der Waals interfaces. The bottom hBN has thickness ranging from $\sim 40 - 60$ nm while the top hBN has thickness ranging from $\sim 10 - 30$ nm. All the devices were stacked by PDMS/PC stamps and then were placed on pre-defined Au back gates. A representative device image is shown in Fig. 3.2b (right inset), the yellow area corresponds to gold electrodes and the gold top gate covering the stack. Orange region is the thin gold back gate. Surprisingly, we find robust superconductivity in all the studied TBG-WSe₂ structures, as long as some correlated effects are shown. Additionally by adding WSe₂, these TBG devices typically show high twist-angle homogeneity. For example, the data shown in Fig. 3.2b are R_{xx} versus filling factor ν measured from four pairs of contacts from the same device; the contact pairs are marked by the corresponding colored bar in the device image. These four gate curves are almost on top of each other, not only the resistance value but also the correlated features. The results suggest a highly uniform moiré twist angle in the area. The uniformity achieved here is not well understood yet, presumably because of larger friction between the interface of graphene and WSe₂ that helps to lock the local twist angle while going through the flake transfer processes.

3.3 Twist-angle dependent phase diagram

We mainly focus on four superconducting devices; the twist angle of which are $\theta = 1.1^\circ$, $\theta = 0.97^\circ$, $\theta = 0.87^\circ$, and $\theta = 0.79^\circ$, respectively (Fig. 3.3). We find robust superconductivity in all studied TBG-WSe₂ structures even for twist angles

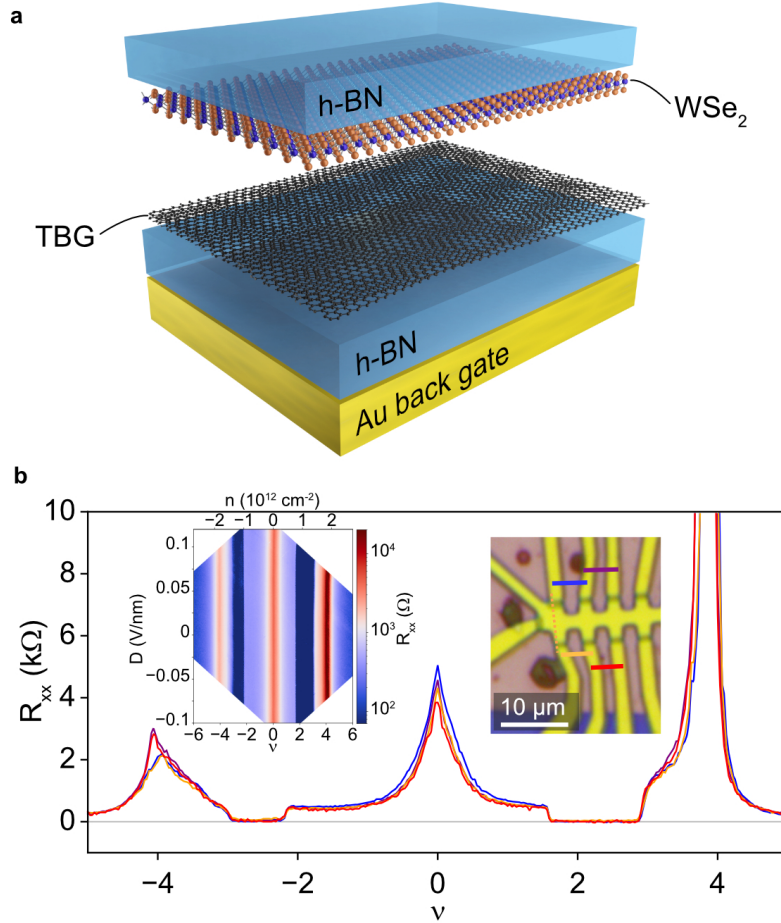


Figure 3.2: Bottom-gated WSe₂-TBG devices. (a) the typical geometry for TBG-WSe₂ devices, including WSe₂ and TBG in between two hBN and a globe gold gate. (b) R_{xx} versus filling factor ν measured from different contacts with uniform twist angle $\theta = 0.88^\circ$. right inset shows the optical image of the device and left inset shows the gate curve as a function of displacement field.

far away from the magic angle (Fig. 3.3). The twist angle was measured using the Landau fan diagram, from which we obtain the back gate voltage at charge neutrality as well as full-filling voltage. Combining with the fact that the slope of the Landau fan is directly proportional to the capacitance, the electron density at full filling (n_{full}) can be obtained. From the density, the twist angle is calculated using the low-angle approximation

$$\theta^2 \approx \sqrt{3}a^2 n_{\text{full}}/8, \quad (3.1)$$

where $a = 0.246$ nm is the lattice constant of graphene. The electron (hole) full-filling voltage corresponds to $\nu = +(-)4$, and accordingly half and quarter filling are at $\nu = +(-)2$ and $\nu = +(-)1$, respectively.

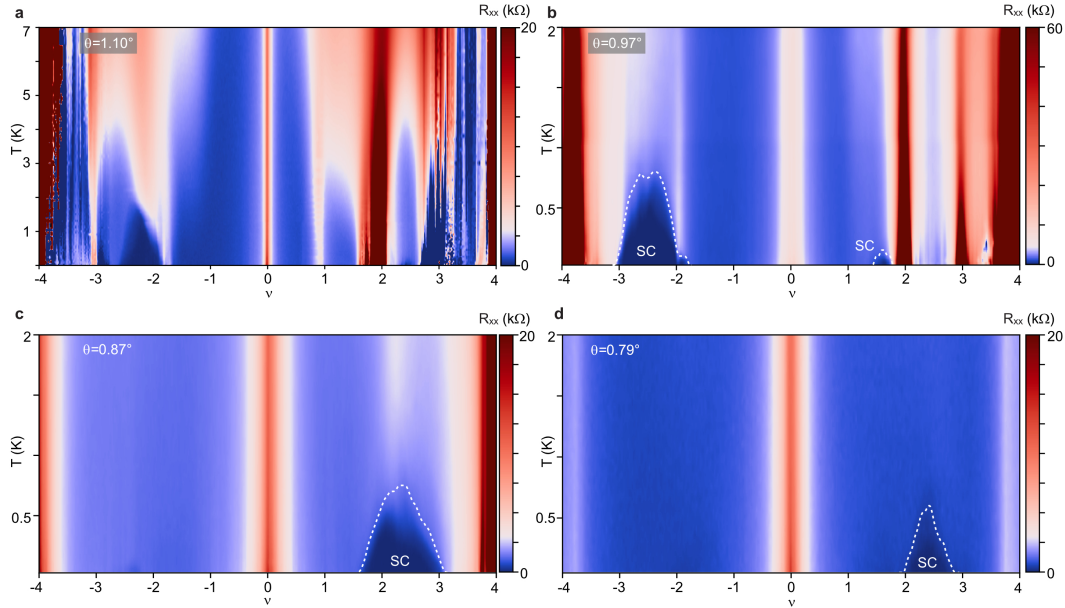


Figure 3.3: R_{xx} versus temperature and filling factor ν for TBG-WSe₂ devices with twist angle $\theta = 1.10^\circ$ (a), 0.97° (b), 0.87° (c), and 0.79° (d), respectively.

The existence of superconductivity is independently confirmed by Fraunhofer interference pattern that suggests the superconducting phase coherence. Fig. 3.4 shows the critical current as a function of out-of-plane magnetic field B_{\perp} . It is clear that the supercurrent for all the devices shows pronounced oscillations versus magnetic field. This is the consequence of Josephson junctions in the system, where at certain filling factors, part of the system is not superconducting due to moiré disorder [117] (possibly some metallic or insulating states). In these devices, we typically see periodicity of 1.5-3 mT that, interpreted as the effective junction area $S \sim 0.67\text{--}1.33 \mu\text{m}^2$, are consistent with the device geometry.

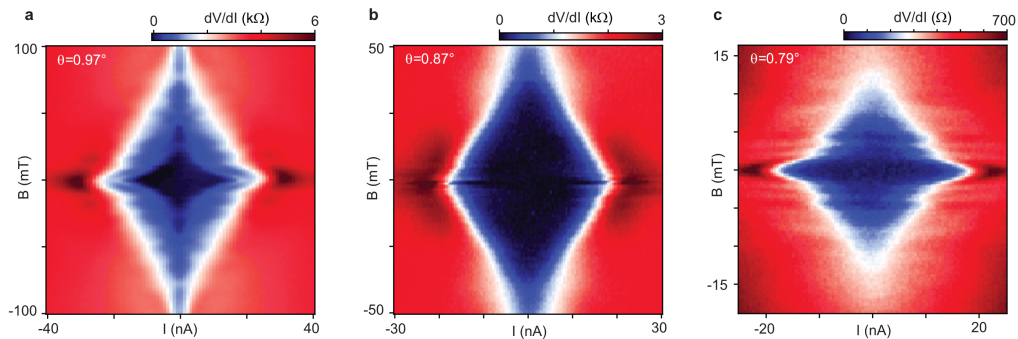


Figure 3.4: Superconducting Fraunhofer pattern measured from devices with twist angle $\theta = 0.97^\circ$ (a), 0.87° (b), and 0.79° (c), respectively.

We start to look at the phase diagram of a magic-angle device at $\theta = 1.10^\circ$. The device exhibits clear R_{xx} peaks at every integer filling $0 < |\nu| < 4$ (Fig. 3.3a); including a correlated insulator (CI) develops near $\nu = +2$. At hole side around half filling $\nu = -2$, superconductivity features a maximal transition temperature of $T_c \approx 1.6$ K. The observations are in line with previously reported hBN-encapsulated, high-quality magic-angle TBG devices and also suggest that the magic-angle condition is not dramatically changed by adding WSe₂, i.e., 1.1° remains strong correlation regime.

Tuning away from the magic angle by reducing the twist angle, the impact of correlation is strongly reduced: the bandwidth increases rapidly and moreover, the characteristic correlation energy scale $U = e^2/4\pi\epsilon L_m$ also diminishes due to an increase in the moiré periodicity $L_m = a/\sin(\theta/2)$ [18, 59, 118–121]. Coulomb interaction (U) is reduced while moiré band bandwidth (W) is broaden; reducing the ratio U/W between them. The phase diagram qualitatively changes.

Figure 3.3b shows the temperature dependence of resistance at the twist angle slightly away from the magic angle $\theta = 0.97^\circ$. A superconducting pocket emerges on the hole side near $\nu = -2$ with a maximal transition temperature $T_c \approx 0.8$ K and another weak superconductivity pocket develops close to $\nu = +2$. Despite being away from the magic angle by 0.1° , the observed phase diagram resembles that of magic angle case except reduced T_c and reduced correlated insulating behavior. For filling factors $\nu = +2, +3$, the activation gaps are $\Delta_{+2} = 0.68$ meV and $\Delta_{+3} = 0.08$ meV, respectively (Fig. 3.5). Here, we get the activation gap through the activation fitting (green lines; $\sigma_{xx} \propto e^{-\Delta/2k_B T}$).

3.4 Disappearing insulating gaps

Next, we focus on two devices that are far away from the magic angle, where correlation effect is significantly reduced. At the twist angle $\theta = 0.87^\circ$, the correlated insulating behavior totally disappeared for the ν - T diagram below 2K, as show in Fig. 3.3c. However, when raising the temperature to 1K or so, signatures of correlations do emerge. In Fig. 3.3c, a peak in longitudinal resistance versus density is visible around $\nu = +2$ above the superconducting transition ($T_c = 600$ – 800 mK). Data for a larger temperature range (Fig. 3.6a,b) shows that the resistance peak near $\nu = +2$ survives up to $T = 30$ K, and also reveals a new peak near $\nu = +1$ in the temperature range 10-35 K. These observations suggest that electron correlations remain strong, though the corresponding states at $\nu = +1$ and $\nu = +2$ appear to be

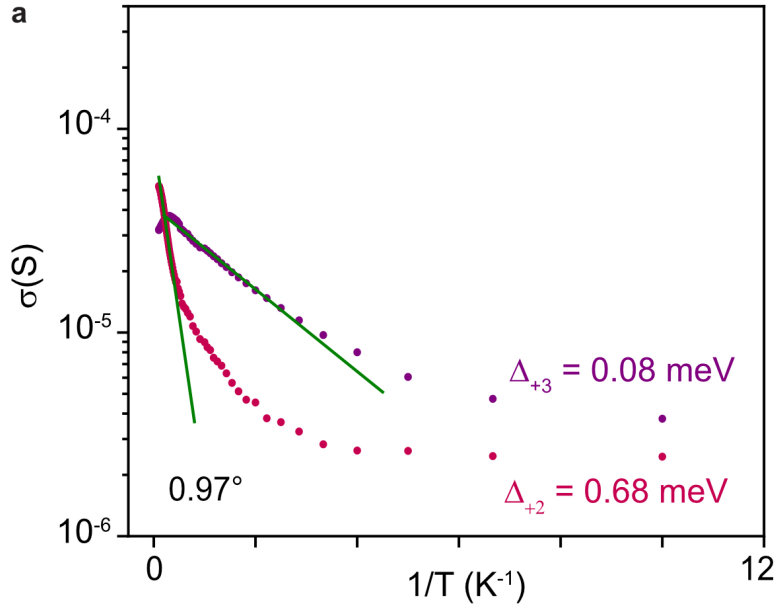


Figure 3.5: Correlated insulating states for TBG-WSe₂ device at $\theta = 0.97^\circ$. $\nu = +2$ and $\nu = +3$ show activating behavior.

metallic as the overall resistance increases with temperature (Fig. 3.6f). For this angle, we measure activation gaps at full filling (i.e., at $\nu = \pm 4$) of $\Delta_{+4} = 8.3$ meV and $\Delta_{-4} = 2.8$ meV (Fig. 3.6e)—far smaller than the gaps around the magic angle.

Importantly at the smallest twist angle, the temperature dependence of R_{xx} strongly suggests the independence between superconductivity and insulating behavior. At the smallest angle $\theta = 0.79^\circ$, not only insulating behavior is absent in the partial filling of moiré flat bands, the resistance at full filling is even more reduced (Fig. 3.6c,d). The relatively low resistances < 2 k Ω , measured at full filling—which are less than 15% of the resistance at the charge neutrality point (CNP)—suggest a semi-metallic band structure around full filling, consistent with theoretical expectations for TBG at $\theta = 0.79^\circ$ [132] and the resistivity of a dilute 2D electron gas [133]. Surprisingly, despite the complete absence of both full-filling band gaps and correlated insulators, the superconducting zero-resistance pocket near $\nu = +2$ is clearly resolved (Fig. 3.3d). The behavior has been well reproduced in another device at similar twist angle, where TBG is encapsulated between two WSe₂ on both sides (Fig. 3.7).

Our observations strongly suggest correlated insulator and superconductivity are likely having different origins [51, 52]. Note also that the close proximity of the dispersive bands does not seem to have a major impact on the superconducting phase. Our findings of superconductivity in TBG with metallic band structure put

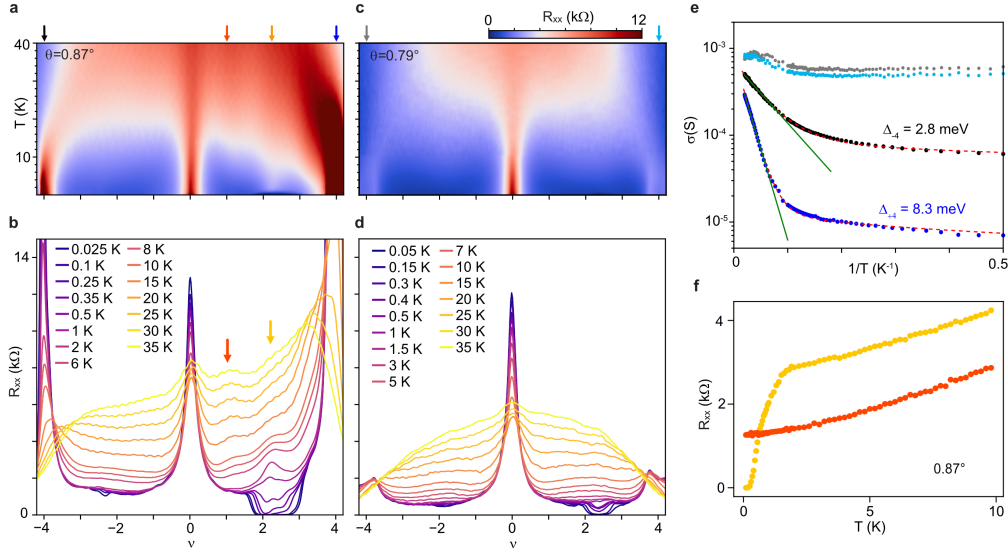


Figure 3.6: Large temperature range R_{xx} for $\theta = 0.87^\circ$ (a) and $\theta = 0.79^\circ$ (c) devices. Selective gate curves at different temperatures are shown in (b) and (d). (e) shows temperature dependence of conductance measured at the filling factors marked by the corresponding colored arrows in (a) and (c). The green lines correspond to activation fit. (f) shows metallic behavior around $\nu = +1$ and $\nu = +2$ for the $\theta = 0.87^\circ$ devices.

constraints on the proposed theoretical explanations and are the main result of this chapter. For example, the observations are in contrast with scenarios wherein superconductivity descends from a Mott-like insulating state as in high-temperature superconductors [78]. We emphasize, however, that electron correlations may still prove important for the development of superconductivity. For instance, even for the smallest angle of $\theta = 0.79^\circ$, the superconducting pocket is seemingly pinned to the vicinity of $\nu = 2$. Additionally, as shown in Fig. 3.6c,d, at higher temperatures residual R_{xx} peaks can still appear around half filling despite the absence of gapped correlated insulating states. It is thus hard to rule out the possibility that superconductivity arises from correlated metallic states that may be present at smaller angles and near integer values of ν in analogy to other exotic superconducting systems [79, 80, 134].

3.5 Evidence for spin-orbit interactions

The complex band structure of TBG makes it intrinsically hard to precisely quantify the type (Rashba, Ising, Kane-Mele SOC) and the size of spin-orbit interaction by mapping to single-particle band structure calculations. However, the measurement

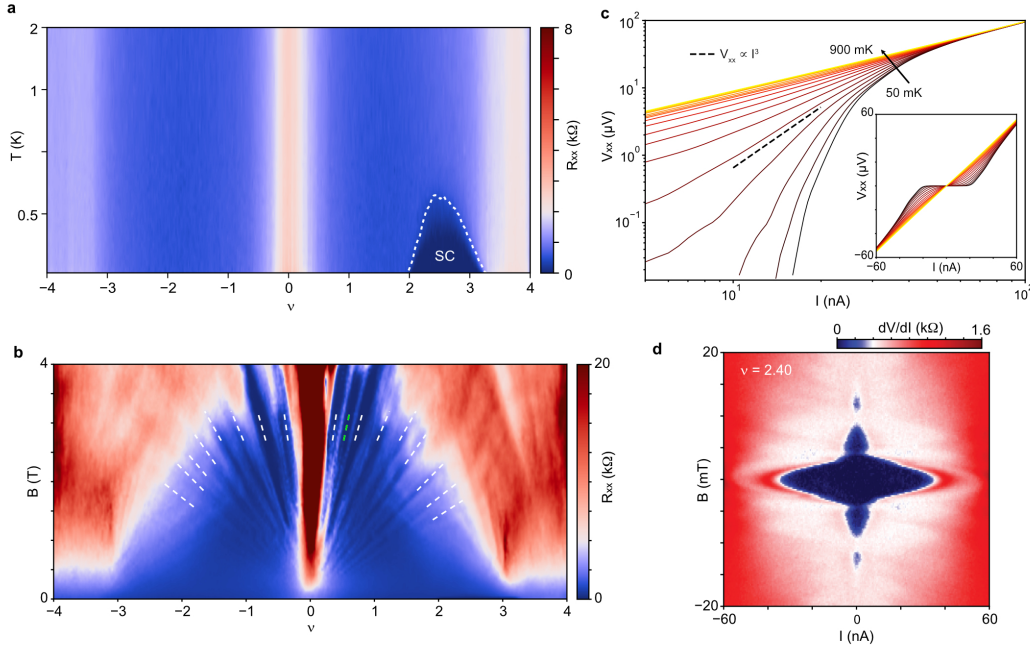


Figure 3.7: Characterizations for a second TBG-WSe₂ device at $\theta = 0.8^\circ$. (a) R_{xx} measured as a function of ν and temperature for a second TBG-WSe₂ device at $\theta = 0.8^\circ$. (b) Landau Fan diagram for the same device. (c) $I - V$ characteristic at different temperature showing a superconducting transition for Berezinskii–Kosterlitz–Thouless extraction. (d) Fraunhofer pattern measured from the device confirming the superconducting phase coherence.

of weak antilocalization serves as a direct evidence of the presence of SOC.

In small out-of-plane magnetic fields, we observe a conductance peak at $B_\perp = 0$ mT; the signal comes from weak antilocalization (WAL) and consequently the presence of strong SOI (Fig. 3.8). In a system with SOC, the spins of electrons are coupled to the momentum. The spins rotate as the electrons go around a self-intersecting path, and the direction of the rotation is opposite for the two directions about the loop. Because of this, the two paths along the loop interfere destructively, leading to a lower net resistivity at zero magnetic field.

Previous works established that TMDs can induce large SOC into monolayer/bilayer graphene [128, 129, 131], and hence the generation of SOI in the proximitized layer of TBG is expected. In Fig. 3.8b,e show the conductance variation $\Delta\sigma$ measured as a function of gate voltage from both morié flat bands and higher dispersive bands. It is obvious that conductance maximum persists regardless of gate voltages, consistent with the signature of weak antilocalization. The WAL peak developed at temperature from 700 mK to 25 mK. Here the data shown in Fig. 3.8c,d (dots) are

averaged over the density range because at low temperature noise mechanism such as universal conductance fluctuations [135] can be pronounced. Each peak is taken by averaging over a small range of gate voltages, which averages out the noise due to mechanisms such as universal conductance fluctuations [135]. However, at higher temperature ~ 900 mK, the weak antilocalization peaks disappear, therefore, we use the data at the temperature as background for subtraction. Data are symmetrized relative to 0 mT for a better fit to formula.

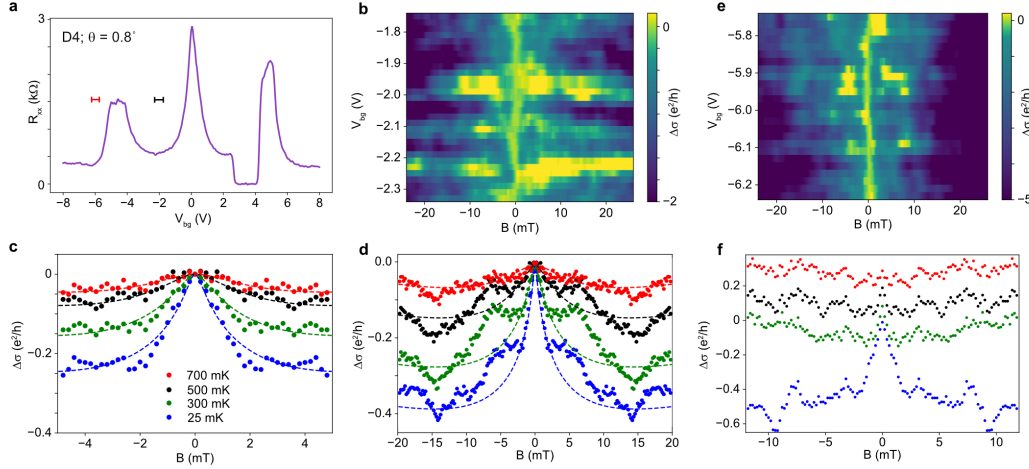


Figure 3.8: Weak antilocalization signatures. (a) R_{xx} versus backgate voltage for the $\theta = 0.8^\circ$ device. (b),(e) Conductance change, relative to the 0 mT value, versus out-of-plane magnetic field and backgate voltages. (c),(d) Averaged data from (b) for different field ranges. The dashed lines are comparison to the weak antilocalization model used for monolayer graphene/TMD.

We adapted the WAL theory from monolayer graphene on TMDs because here for TBG, Dirac cone is still a good approximation around the low energy. only modification probably needed is just reducing Fermi velocity due to heavier mass from moiré flat band. The WAL equation is:

$$\Delta\sigma(B) = -\frac{e^2}{2\pi h} \left[F\left(\frac{\tau_B^{-1}}{\tau_\phi^{-1}}\right) - F\left(\frac{\tau_B^{-1}}{\tau_\phi^{-1} + 2\tau_{asy}^{-1}}\right) - 2F\left(\frac{\tau_B^{-1}}{\tau_\phi^{-1} + \tau_{so}^{-1}}\right) \right] \quad (3.2)$$

where $F(x) = \ln(x) + \psi(0.5 + x)$, ψ is the digamma function, and $\tau_B = 4eDB/\hbar$. $D = v_F^2\tau/2$ is the diffusion constant, which is determined by Fermi velocity; here $v_F \approx 10^5$ m/s is used instead of $v_F \sim 10^6$ m/s due to the flat band condition. The Drude scattering time $\tau = \frac{\mu m^*}{e} = \frac{\hbar\sigma}{v_F e^2} \sqrt{\frac{\pi}{|n|}}$, here the effective mass $m^* = \hbar\sqrt{\pi|n|}/v_F$

and the mobility estimated from $\mu = \sigma/|n|e \sim 1.5$ ps. Therefore, the only free parameters left are $\tau_\phi, \tau_{asy}, \tau_{so}$. Here, τ_{asy} comes from Ising SOC while τ_{so} is the combination of symmetric and asymmetric components $\tau_{so}^{-1} = (\tau_{sym}^{-1} + \tau_{asy}^{-1})$ does not change with temperature. The τ_ϕ dephasing term, however, is temperature dependent. Thus, the temperature dependence here puts constraint on the τ_ϕ term.

Given the three parameters, it is relatively hard to get a precise estimation of SOC values, while order-of-magnitude precision can be achieved. For the low-field-range data Fig. 3.8c, the total spin-orbit scattering time $\tau_{so} \approx 10$ ps can reproduce the data. Going to higher field range (Fig. 3.8d), $\tau_{so} \approx 1 - 3$ ps capture the saturation trend at high field with the asymmetric versus symmetric term ratio (τ_{asy}/τ_{sym}) being around 0.3-3. Importantly, the τ_{so} obtained from various fitting is in the range of 0.5 - 1 meV, matches some of the previous studies and also the values from BLG-WSe₂ cases (see Chapters 5 and 6). However, to well capture the WAL analysis in the case of TBG, a better model taking into account correlation effects, etc. is necessary. Regardless, the WAL measurement serves as a smoking gun evidence of the presence of SOC in TBG coupled to WSe₂.

Additional experimental evidences that are compatible with SOC is from Landau Fan diagram (Fig. 3.9). For the low angle devices $0.79^\circ - 0.97^\circ$ we focus on here, we find the Landau level gaps are well developed at $B_\perp \sim 1$ T. Also, the main Landau level sequences are $\pm 2, \pm 4, \pm 6$, etc., consistent with a broken four-fold spin-valley flavor symmetry. In comparison, the previous hBN-encapsulated TBG normally shows Landau level sequences $\pm 4, \pm 8, \pm 12$, etc. [16, 19, 20, 51, 52, 117]. In addition to the four-fold degeneracy breaking in R_{xx} , we also observed well quantized quantum Hall plateaus (Fig. 3.9d,e), indicating the high quality of our devices. Indeed, for all the TBG coupled to WSe₂ studied over the years, we found high success rate hitting around the magic angle with devices demonstrating high twist-angle uniformity.

3.6 Theory of spin-orbit coupling in TBG

For the vanilla TBG without SOC, the model Hamiltonian may be expressed as

$$H_{\text{cont}} = H_t + H_b + H_{\text{tun}}. \quad (3.3)$$

The first two terms on the right-hand side denote the Dirac Hamiltonian of the top and bottom layers, respectively, in the absence of interlayer tunneling, while the third term corresponds to interlayer tunneling.

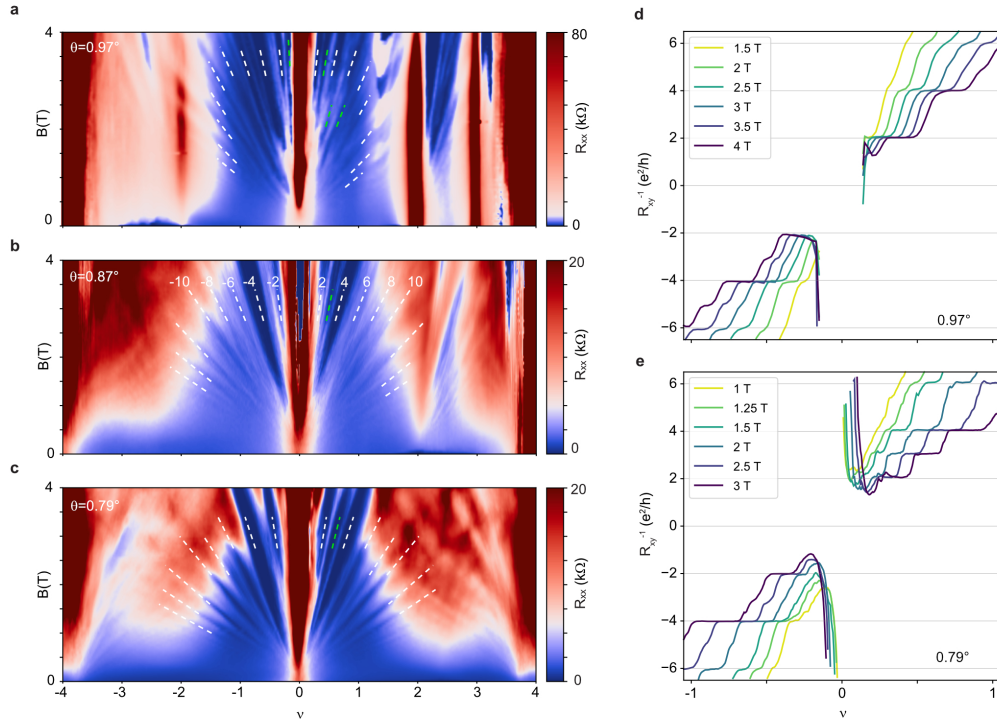


Figure 3.9: Landau fan diagrams for TBG-WSe₂. (a)-(c) Landau fan diagrams for three devices with $\theta = 0.97^\circ$, 0.87° , and 0.79° , respectively. The main Landau level sequences are ± 2 , ± 4 , ± 6 , etc. that break four-fold degeneracy, consistent with the existence of SOC. (d),(e) quantum Hall conductance measured at different magnetic field showing quantized plateaus at ± 2 , ± 4 , $\pm 6e^2/h$, suggesting high quality of our devices.

We consider the effect of adding SOC to TBG. Assuming that TMD resides adjacent to the top-layer graphene of TBG, the primary modification to the continuum model presented in Eq. (3.3) then occurs in H_t :

$$H_t = \int_{\mathbf{k}} \psi_t^\dagger(\mathbf{k}) (h_t(\mathbf{k}) + h_{t,\text{SO}}) \psi_t(\mathbf{k}). \quad (3.4)$$

Here, $h_{t,\text{SO}}$ represents the appropriately rotated projection of H_{SO} (monolayer graphene including SOC) onto the $+\mathbf{K}$ valley:

$$h_{t,\text{SO}} = e^{i\theta\sigma^z/4} \left(\frac{\lambda_I}{2} s^z + \frac{\lambda_R}{2} (\sigma^x s^y - \sigma^y s^x) + \frac{\lambda_{\text{KM}}}{2} \sigma^z s^z \right) e^{-i\theta\sigma^z/4}. \quad (3.5)$$

The spin-orbit parameters used here Ising (λ_I), Rashba (λ_R) and Kane-Mele (λ_{KM}) ranges from below 1meV to 10meV depending on the previous literatures; the results of which ranging from $\lambda_I \sim 1 - 5$ meV and $\lambda_R \sim 1 - 15$ meV. Additionally, Ising and Kane-Mele contribute symmetric type SOC while Rashba contribute asymmetric

SOC. Although there was no previous experience on proximitized SOC to TBG, the results should be relatively similar to monolayer graphene adjacent to TMDs. We calculate band structures using the various SOC strengths reported before. Fig. 3.10 shows the band structure calculation using $\lambda_I = 3$ meV and $\lambda_R = 4$ meV. At the two twist angles $\theta = 0.87^\circ$ and 0.79° , the correlation effect Hartree correction is not significant. We can clearly observe the breaking of four-fold spin-valley symmetry by SOC here.

The out-of-plane projection is largely constant along these surfaces, as can be seen in Figs. 3.10a,d. The large spin-orbit-induced Fermi-surface deformation visible here reflects the flatness of the bands near the Fermi energy. We note that the apparent electron-hole symmetry in the band structure is a consequence of twist angle being well below the magic-angle value.

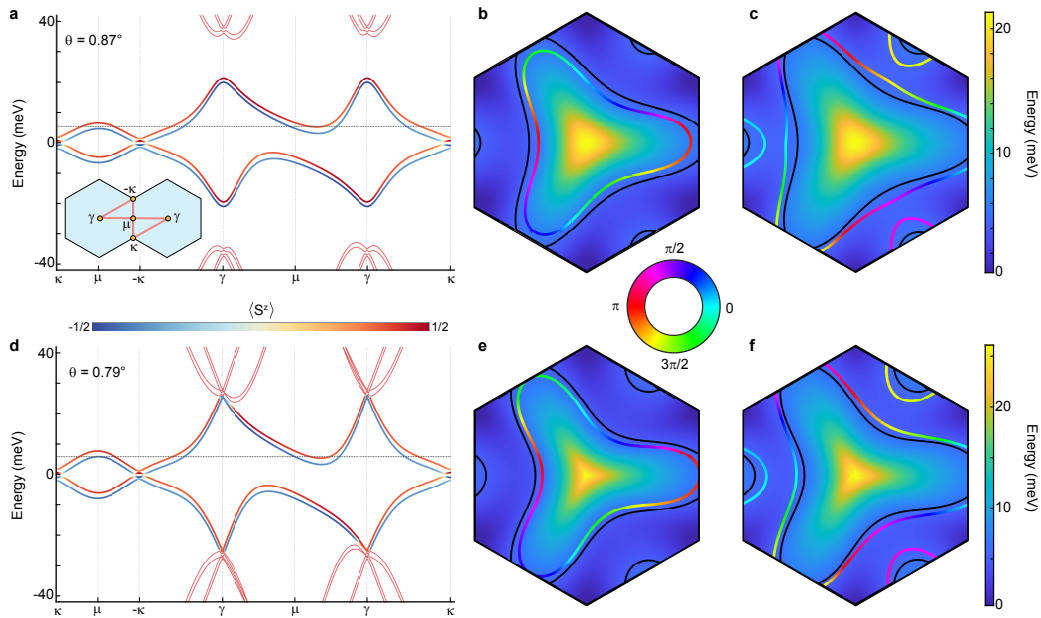


Figure 3.10: Spin-orbit effect on TBG band structure. (a)–(f), Continuum-model results for valley K that include Ising and Rashba spin-orbit coupling at twist angles of 0.87° (a)–(c) and 0.79° (d)–(f). (a),(d) Band structure along the high-symmetry directions of the Brillouin zone. The color represents the out-of-plane spin projection, $\langle S_z \rangle$, and the dotted line denotes the chemical potential at $\nu = +2$. (b),(c),(e),(f) Energy of the conduction flat bands with spin-orbit coupling. Colored line indicates the in-plane spin projection. Black line corresponds to SOC-free case.

Induced SOI can additionally constrain the nature of the TBG phase diagram. Regardless of the details of the SOC, an SOI acts as an explicit symmetry-breaking field that further promotes instabilities favoring compatible symmetry-breaking patterns

and suppressing those that do not. For example, the relative robustness of the half-filling correlated insulator in our $\theta = 0.97^\circ$ device suggests that interactions favor re-populating bands [23, 24] in a manner that also satisfies the spin-orbit energy. Furthermore, the survival of superconductivity with SOI constrains the plausible pairing channels—particularly given the dramatic spin-orbit-coupling-induced Fermi-surface deformations that occur at $\nu = +2$. Superconductivity in our low-twist-angle devices, for instance, is consistent with Cooper pairing of time-reversed partners that remain resonant with the SOI. Thus the stability of candidate insulating and superconducting phases with the added SOI provides additional nontrivial constraints for theory [136–140]. The integration of monolayer WSe₂ demonstrates the impact of the van der Waals environment and proximity effects on the rich phase diagram of TBG. In a broader context, this approach opens future prospects for controlling the range of correlated phases available in TBG and similar structures by carefully engineering the surrounding layers, and it highlights a key tool for disentangling the mechanisms driving the different correlated states.

3.7 Connection between superconductivity and Fermi-surface reconstruction

TBG-WSe₂ provides an invaluable opportunity for detailed mapping of various correlated ground states, especially the robustness of superconductivity compared to other symmetry-breaking phases. The detailed characterization of multiple devices with twist angles ranging from $\theta = 0.79^\circ$ to 1.23° reveals a hierarchy of different phases. Here, the twist angle serves as a tuning knob to modify the Coulomb interactions as we discussed previously. At the magic-angle condition, other than the strongest superconductivity, there are also correlated insulators, anomalous Hall effect [141], cascade of symmetry-breaking transition, pommeranchuk effect, strange metal behavior, etc. By tuning away from the magic angle, we found that superconductivity is the most robust phase that remains, together with the Fermi-surface reconstruction around the half filling.

Start with the phase diagram at the magic angle. We observed an abundance of correlated phases around the magic angle, including but not limited to correlated insulating states at $\nu = \pm 2$ and ± 3 , anomalous Hall effect/ferromagnetism around $\nu = +1$. Among them, $\nu = +1$ ferromagnetism is most sensitive to twist angle that only emerges for $\theta = 1.05^\circ \pm 0.05^\circ$ (Fig. 3.11). Correlated insulating states that have clear activating gapped behavior also exist in a relatively narrow angle range $\theta = 0.97^\circ$ - 1.15° , indicating adding WSe₂ primarily does not change the magic-angle condition.

The cascade of high temperature symmetry-breaking transitions and superconductivity near $\nu = \pm 2$ persist over a much wider range of twist angles (see Fig. A.1 for temperature dependence for a range of devices at different twist angles). While all devices exhibit pronounced electron-hole asymmetry and a peak T_c on the electron (hole) side which is shifted toward lower (higher) angles, superconductivity can be found well above ($\theta = 1.23^\circ$) and below ($\theta = 0.88^\circ$) the magic angle for both negative and positive filling factors. To the best of our knowledge, this is the largest reported range of twist angles exhibiting superconductivity for both electron and hole doping.

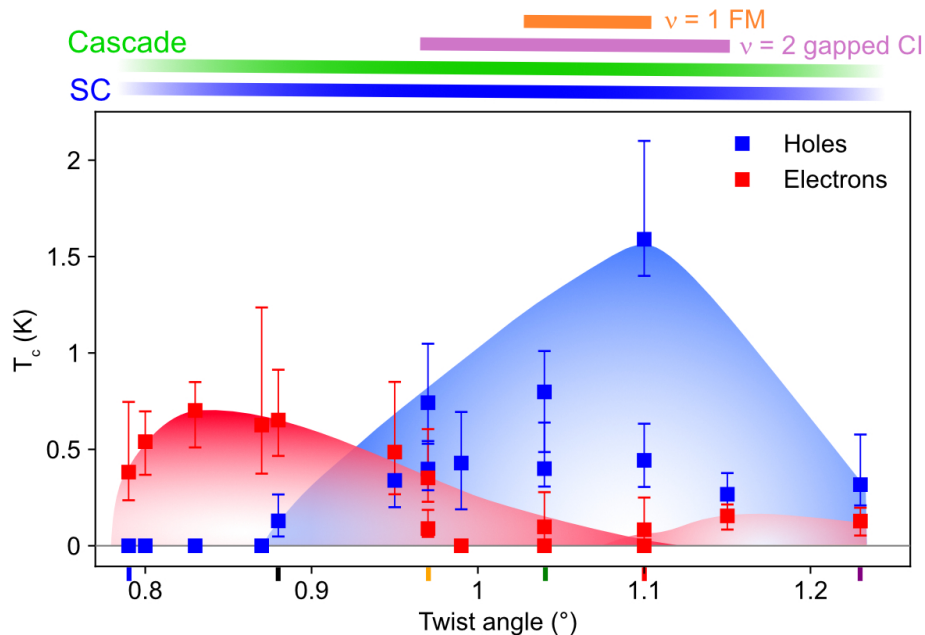


Figure 3.11: Phase diagram of various correlated phases focusing on superconductivity. The main panel plots critical temperature T_c as a function of twist angle; electron side (red dots) and hole side (blue dots). For hole side, T_c peaks around the magic angle, and for electron side T_c is somewhat suppressed at the magic angle due to the competition with correlated insulator at $\nu = +2$. When tuning away, electron-side T_c increases. On top, we show the rough ranges of various correlated phases, among which correlated insulator and ferromagnetism only appear around the magic angle. Ultimately, tuning away from the magic angle both electron and hole side superconductivity diminished together with the cascade of symmetry-broken transition around the half filling.

Importantly, the occurrence of superconductivity is consistently accompanied by Fermi surface reconstructions around $\nu = \pm 2$, as manifested by a low-temperature reset in the Hall density marked by arrows in Fig. 3.12. We focus on the devices

angle far away from the magic angle, where superconductivity T_c is much lower (blue and black curves). For 0.88° , hole-side superconductivity around $\nu = -2$ has $T_c = 130$ mK and is accompanied by the formation of a kink in the Hall density (black arrow), which is separate from the van Hove singularity. At larger twist angles, the kink becomes a fully-developed Hall density reset to zero (marked by colored arrows), corresponding to a more complete flavor symmetry breaking induced Fermi-surface reconstruction. In contrast, the device with lowest twist angle 0.79° reveals a linear Hall density on the hole side that extends well beyond $\nu = -2$, ultimately reaching a van Hove singularity [142]. This signals the absence of an interaction-driven Fermi surface reconstruction. Interestingly, we also no longer find hole-side superconductivity for this twist angle. On the electron side, both twist angles exhibit superconductivity and a kink in the Hall density due to Fermi surface reconstructions.

Our observations indicate that a fully symmetric (equally populated) spin-valley flavor state strongly disfavors the formation of superconductivity and thus rules out the simplest scenario of electron-phonon mechanisms which only rely on the local density of states [143]. In this context, our results are more in line with spin (or valley) fluctuation [138] driven superconductivity but other mechanisms such as the Kohn-Luttinger mechanism [144] may also be relevant. Alternatively, and independently of the pairing mechanism, in a case of multiflavor (multi-component) pairing, superconductivity and magnetism (i.e. flavor polarization) can be inherently connected. The physical manifestation of this connection is through a $\Delta^2 M$ term, where Δ is superconducting gap and M describes degree of polarization, in the free energy which is allowed by a $U(N)$ symmetry, as well as lower symmetries. The interplay implies that strong flavor polarization will generally increase the T_c of a multi-flavor superconductor, and, furthermore, that a finite superconducting order parameter could even induce polarization.

Our results strongly indicate that TBG phases can be roughly divided into two categories in respect to their robustness on twist angle deviations from the magic-angle value. The phases exhibiting superconductivity, linear-in- T dependence, and Pomeranchuk-like effects generically emerge from interaction-driven symmetry breaking alone that is robust for a wide range of twist angles. In contrast, correlated insulating states and orbital ferromagnetism require a more subtle interplay between strong interaction effects, kinetic energy scales, and possibly breaking of spatial symmetries. The sensitivity of these phases result in their appearance only in the

near vicinity of the magic angle, and the close competition of phases can result in differing behavior between devices at the same twist angle. This hierarchy between different phases will hopefully guide future theoretical frameworks aiming to explain the rich phenomenology of TBG and related structures.

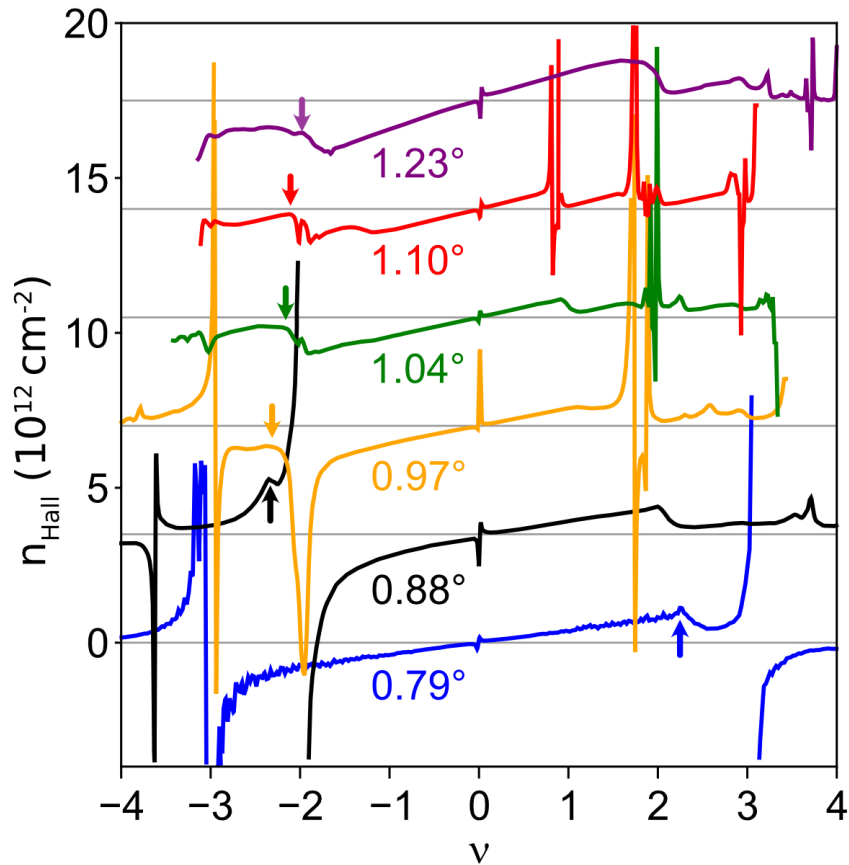


Figure 3.12: Hall density reset at different twist angles. Hall density (n_{Hall}) versus filling factor ν for TBG-WSe₂ devices with angle $\theta = 0.79^\circ, 0.88^\circ, 0.97^\circ, 1.04^\circ, 1.1^\circ, 1.23^\circ$, respectively. The respect offset Hall density values are indicated by gray horizontal solid lines.

Chapter 4

PROMOTION OF SUPERCONDUCTIVITY IN MAGIC-ANGLE GRAPHENE MULTILAYERS

The previous chapter studied the electronic properties of TBG coupled to WSe_2 and its twist-angle-dependent correlated phase diagram. In the moiré category, TBG is not the only one that demonstrates robust superconductivity. When three layers of graphene are twisted in an alternating sequence, so called twisted trilayer graphene (TTG), and at its corresponding magic angle, TTG also hosts robust superconductivity that is close to strongly coupled regime [45]. Additionally, it is highly tunable with displacement fields [44, 45]. Here, we generalized the alternating twisted graphene to four layers (quadrilayer; TQG) and five layers (pentalayer; TPG). All of them show flavor symmetry-breaking transitions and robust superconductivity with $T_c = 1 - 2$ K. Despite the coexistence of dispersive bands with the flat bands, we observed half-filling correlated insulating states in TTG and also single-particle band gap in TQG. As the number of layers increases, superconductivity emerges over an enhanced filling-factor range, and in the pentalayer it extends well beyond the filling of four electrons per moiré unit cell. Our results highlight the role of the interplay between flat and more dispersive bands in extending superconducting regions in graphene moiré superlattices.

4.1 Alternating twisted graphene multilayers

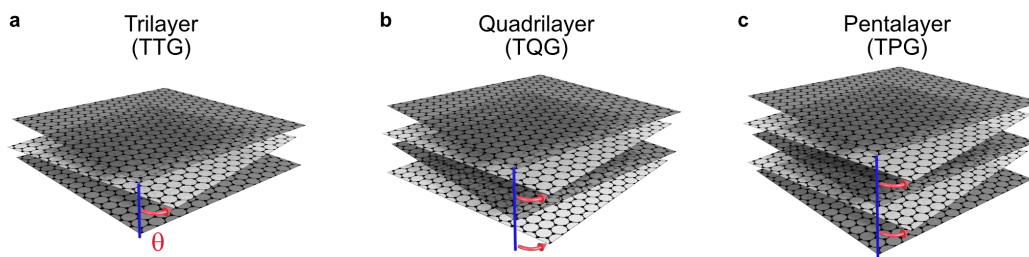


Figure 4.1: Schematics of the alternating twisted graphene multilayers. (a)-(c) schematics of alternating twisted trilayer (a), quadrilayer (b), and pentalayer (c) graphene, where each successive layer is twisted by an angle $\pm\theta$ relative to the previous one in an alternating sequence.

We investigate twisted graphene multilayers where each successive layer is twisted

by an angle $\pm\theta$ relative to the previous one in an alternating sequence (Fig. 4.1). For these structures with multiple alternating twists, the system can be viewed as several TBG-like subsystems with the addition of monolayer graphene-like (MLG-like) subsystem (depending on the layer number). For an even number n of layers, the spectrum at zero displacement field D is expected to separate into $n/2$ independent TBG-like bands, each characterized by a different effective twist angle. When the number of layers n is odd, in addition to $(n - 1)/2$ TBG-like bands, one MLG-like band (essentially a Dirac cone) is expected (see left column of Fig. 4.2 for examples when n is 3, 4, and 5) [145].

We now comment on the Hamiltonian of the twisted graphene multilayers. The relevant consideration is the stacking order between different layers. In TTG, it has been numerically and experimentally shown that all odd (even) layers are AA stacked, i.e., stacked directly on top of one another to lower the system's energy [40]. Starting from a bilayer system, the moiré superlattice is manifest on the microscopic lattice scale as the periodic variation of the relative interlayer stacking: one has AA regions at the moiré hexagon centres, while AB and BA stacking regions represent the moiré hexagon vertices. The AA regions have a relatively high energy compared to the Bernal-like region and the lattice accordingly responds by relaxing to minimize their area. Adding a third layer will in principle generate another set of moiré pattern that is offset from the previous one. However, only when the first and third layers are aligned will the AA region occur at the same locations and only then can the system optimize its energy through relaxation.

Given the assumption of AA stacking order, the total Hamiltonian may be written in matrix form as

$$H_{Tn_{\text{layer}}G} = H_D + H_{\text{tun}} = \sum_{\ell, \ell'=1}^{n_{\text{layer}}} \int d^2\mathbf{r} \psi_{\ell}^{\dagger}(\mathbf{r}) [h_{\text{cont}}(\mathbf{r})]_{\ell, \ell'} \psi_{\ell'}(\mathbf{r})$$

$$h_{Tn_{\text{layer}}G}(\mathbf{r}) = \begin{pmatrix} h_{D,1}(\mathbf{r}) & T_{1,2}(\mathbf{r}) & 0 & \dots \\ T_{1,2}^{\dagger}(\mathbf{r}) & h_{D,2}(\mathbf{r}) & T_{2,3}(\mathbf{r}) & \dots \\ 0 & T_{2,3}^{\dagger}(\mathbf{r}) & h_{D,3}(\mathbf{r}) & \dots \\ \vdots & \vdots & \vdots & \ddots \end{pmatrix}. \quad (4.1)$$

Here H_D is the intralayer Dirac term and H_{tun} is the tunneling that occurs between adjacent layers. As currently written, the diagonal Dirac terms, $h_{D,\ell}(\mathbf{r})$, as well as the off-diagonal tunneling terms, $T_{\ell, \ell'}(\mathbf{r})$, depend only on whether ℓ is even or odd. We can thus simplify the above expression by writing the Dirac terms as

$h_{D,2\ell-1}(\mathbf{r}) = h_{D,1}(\mathbf{r})$, $h_{D,2\ell}(\mathbf{r}) = h_{D,2}(\mathbf{r})$ and the tunneling terms as $T_{2\ell-1,2\ell}(\mathbf{r}) = T(\mathbf{r})$, $T_{2\ell,2\ell+1}(\mathbf{r}) = T^\dagger(\mathbf{r})$.

Providing that the simplest TBG Hamiltonian takes the form:

$$h_{\alpha,\eta,\theta}(\mathbf{r}) \equiv h_{\text{TBG}}(\mathbf{r}) = \begin{pmatrix} h_{D,1}(\mathbf{r}) & T(\mathbf{r}) \\ T^\dagger(\mathbf{r}) & h_{D,2}(\mathbf{r}) \end{pmatrix}, \quad (4.2)$$

we can consider the most complicated structure twisted pentalayer graphene structure. In the original layer basis, the Hamiltonian is

$$h_{\text{TPG}}(\mathbf{r}) = \begin{pmatrix} h_{D,1}(\mathbf{r}) & T(\mathbf{r}) & 0 & 0 & 0 \\ T^\dagger(\mathbf{r}) & h_{D,2}(\mathbf{r}) & T^\dagger(\mathbf{r}) & 0 & 0 \\ 0 & T(\mathbf{r}) & h_{D,1}(\mathbf{r}) & T(\mathbf{r}) & 0 \\ 0 & 0 & T^\dagger(\mathbf{r}) & h_{D,2}(\mathbf{r}) & T^\dagger(\mathbf{r}) \\ 0 & 0 & 0 & T(\mathbf{r}) & h_{D,1}(\mathbf{r}) \end{pmatrix}. \quad (4.3)$$

Independent, co-existing TBG- and MLG-like subsystems are revealed with the appropriate change of basis:

$$\tilde{h}_{\text{TPG}}(\mathbf{r}) = V_{\text{TPG}}^\dagger h_{\text{TPG}}(\mathbf{r}) V_{\text{TPG}} = \begin{pmatrix} h_{\sqrt{3}\alpha,\eta,\theta}(\mathbf{r}) & & \\ & h_{D,1}(\mathbf{r}) & \\ & & h_{\alpha,\eta,\theta}(\mathbf{r}) \end{pmatrix}$$

$$V_{\text{TPG}} = \frac{1}{\sqrt{6}} \begin{pmatrix} 1 & 0 & \sqrt{2} & \sqrt{3} & 0 \\ 0 & \sqrt{3} & 0 & 0 & \sqrt{3} \\ 2 & 0 & -\sqrt{2} & 0 & 0 \\ 0 & \sqrt{3} & 0 & 0 & -\sqrt{3} \\ 1 & 0 & \sqrt{2} & -\sqrt{3} & 0 \end{pmatrix}. \quad (4.4)$$

There are now *two* independent TBG-like bands characterized by effective twist angles $\theta/\sqrt{3}$ and θ in addition to a MLG-like Dirac cone.

Applying the same principle to TTG and TQG systems, the band structures of all the three are shown in Fig. 4.2 left column. The band structure of TTG consists of one set of TBG-like bands and a MLG-like cone; TQG consists of two sets of TBG-like bands; TPG consists of two sets of TBG-like bands and a MLG-like cone. The system may be conveniently modified through the application of a displacement field D , which controllably hybridizes the different subsystems (Fig. 4.2 right column).

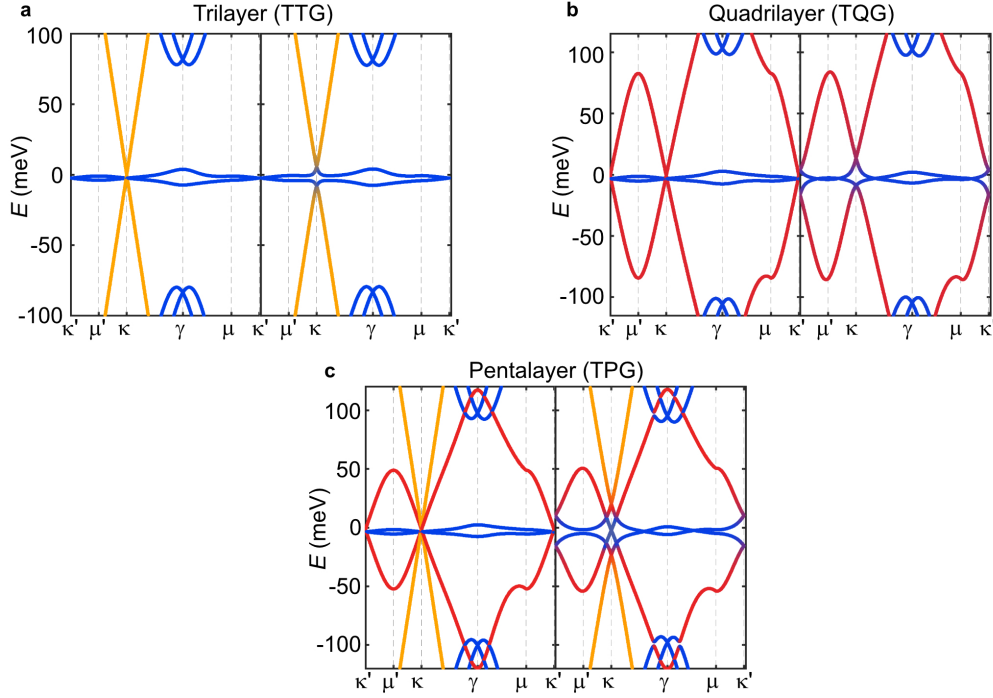


Figure 4.2: Band structure of twisted trilayer (a), quadrilayer (b), and pentalayer (c) graphene for angles close to the respective theoretical magic angle at zero D field (left) and $D/\epsilon_0 \approx 0.4 \text{ V nm}^{-1}$ (right) for valley K .

Magic-angle condition relies on the one set of the flat bands being at the magic-angle condition, say for the case of TPG, one of the effective twist angle is $\theta/\sqrt{3}$. Given the magic angle of TBG is $\theta_{\text{TBG}}^{\text{magic}} = 1.08^\circ$, one of the TPG magic angle is at $\theta_{\text{TPG}}^{\text{magic}} = \sqrt{3}\theta_{\text{TBG}}^{\text{magic}} \approx 1.87^\circ$. The twist angles lie close to the theoretically predicted “magic” values needed to obtain one set of flat TBG-like bands are $\theta_{\text{TTG}}^{\text{magic}} = \sqrt{2}\theta_{\text{TBG}}^{\text{magic}} \approx 1.53^\circ$, $\theta_{\text{TQG}}^{\text{magic}} = (\sqrt{5} + 1)\theta_{\text{TBG}}^{\text{magic}}/2 \approx 1.75^\circ$. The exact magic-angle value is essentially determined by the velocity of monolayer graphene v_0 and the interlayer tunneling amplitude w , which maybe renormalized by lattice relaxation etc., resulting in slightly deviated magic angle value.

4.2 TTG, TQG, and TPG devices under study

Here, we explore properties of alternating twisted trilayer, quadrilayer, and pentalayer graphene (TTG, TQG, TPG) structures with $\theta = 1.52 \pm 0.02^\circ$ (device D1, trilayer), $\theta = 1.80 \pm 0.04^\circ$ (D2, quadrilayer), and $\theta = 1.82 \pm 0.05^\circ$ (D3, pentalayer), respectively. These angles are all close to the theoretically predicted “magic” values mentioned above to obtain one set of flat TBG-like bands.

Importantly, we find that the TTG, TQG, and TPG devices all exhibit hallmark

signatures of strong correlations (Fig. 4.3), including robust superconductivity at base temperature (zero resistance region) and flavor symmetry breaking as revealed by pronounced resistance peaks around certain integer filling factors ν (number of electrons per moiré site) at elevated temperature.

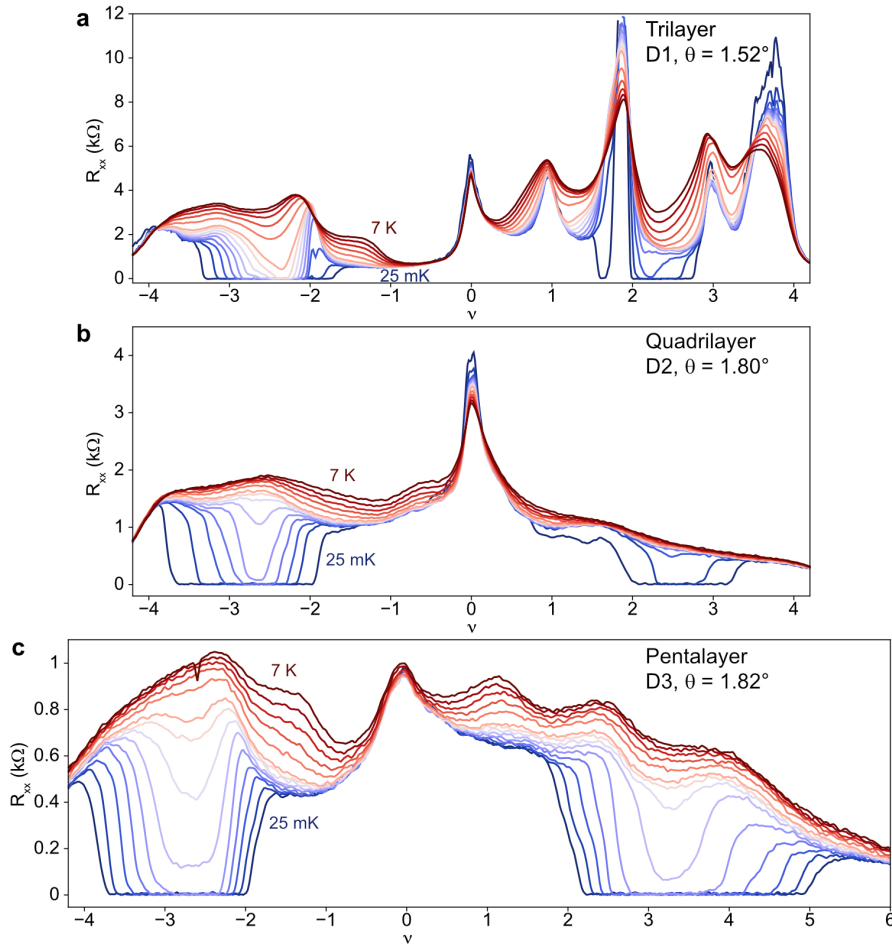


Figure 4.3: Line cuts of R_{xx} versus filling factor ν for a range of temperatures (shown are traces taken first at 25 mK, then every 0.25 K from 0.25 K to 2 K, followed by every 1 K from 3 K to 7 K), from top to bottom measured at $D/\epsilon_0 = 0.22 \text{ V nm}^{-1}$ (a), -0.15 V nm^{-1} (b), and 0 V nm^{-1} (c), respectively.

The superconducting regions in all three structures extend over significantly larger filling factor ranges in comparison to TBG [16, 20, 50, 51] where superconductivity is typically observed within $2 < |\nu| < 3$. Moreover, superconductivity is “ascendant” as the layer number is increased, in the sense that it emerges over successively broader regions of phase space, reaching $\nu \approx +5$ on the electron side for TPG (Fig. 4.3). Along with a zero longitudinal resistance R_{xx} observed in the characteristic ν vs. T dome (Fig. 4.4), the high critical perpendicular magnetic fields

B_c (typically ~ 0.8 T) indicate that the corresponding Ginzburg–Landau coherence lengths ξ_{GL} (magenta dots in Fig. 4.4; approximately 10 – 30 nm) are significantly smaller than those observed in TBG and deviate from the weak-coupling prediction, $\xi_{GL} \approx \hbar v_F / \pi \Delta$ with $\Delta \approx 1.76 k_B T_c$ —suggesting a strong-coupling origin of superconductivity [44, 45]. When combined with other experiments [39, 40, 146], these observations affirm the unconventional nature of superconductivity within the entire class of graphene moiré systems. Further, the measurements on three to five layers indicate that the addition of layers promotes superconductivity over a broader filling window.

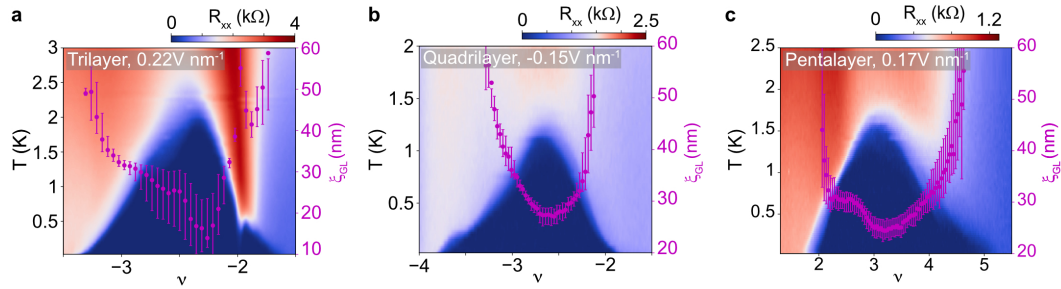


Figure 4.4: R_{xx} versus temperature and ν around half filling, showing superconducting domes around $|\nu| = 2$ in TTG, TQG, and TPG, respectively. Ginzburg–Landau coherence lengths ξ_{GL} versus ν for all three devices are superimposed on the R_{xx} versus T and ν plots.

All the devices investigated here show a high degree of twist angle homogeneity as characterized by four-point measurements between different pairs of contacts. Fig. 4.5 shows R_{xx} versus carrier density with fixed top-gate voltage ($V_{tg} = 0$ V), revealing that almost every pair of contacts shows superconductivity. More importantly, superconducting pockets from different pairs significantly overlap in the filling range, and resistance peaks at $|\nu| = 4$ appear at the same density. Moreover, all findings related to the extent of the superconducting phase and the occurrence of the symmetry-breaking transitions in the ν - D phase diagram are highly reproducible.

We attribute the low level of disorder to the use of monolayer WSe₂ during device stacking, presumably originating from the increased lateral friction between WSe₂ and graphene, as mentioned before. We note that this additional layer does not change the magic-angle condition [27, 50], and the induced spin-orbit interaction energy scale is ~ 1 meV in twisted bilayers. Therefore, SOI is likely too small to significantly affect the overall band structure and directly impact the cascade physics at the magic angle (though may play a more important role for stabilizing

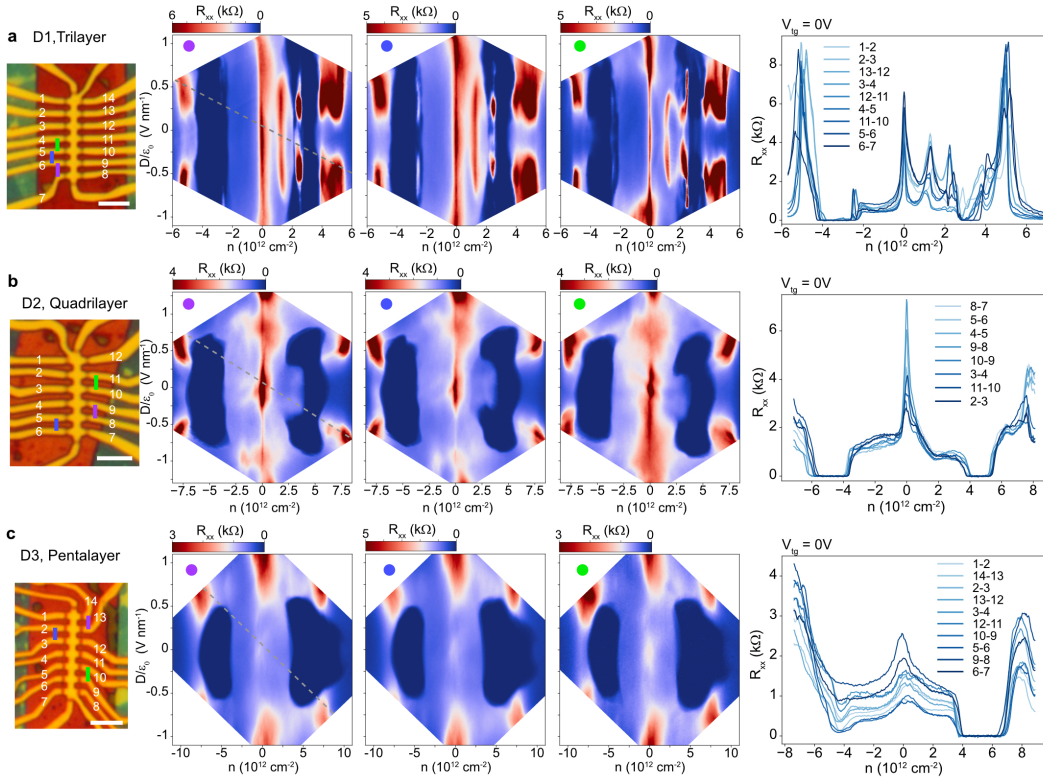


Figure 4.5: Twisted graphene multilayers sample uniformity. (a)-(c) Leftmost optical images of the three twisted graphene multilayers. The scale bar in each panel corresponds to $5 \mu\text{m}$. R_{xx} versus density and displacement field (n - D) plots shown in the middle are obtained from electrodes marked with the corresponding colored lines. Rightmost plots are R_{xx} versus carrier density with top-gate voltage fixed at $V_{tg} = 0 \text{ V}$ (gate sweeps are along the grey dashed lines in the n - D plots). All the three devices have a high degree of homogeneity in twist angle with the same superconducting filling range and $|\nu| = 4$ carrier density for multiple contacts. The behavior of superconductivity and other symmetry-breaking features is highly reproducible for different contacts.

superconductivity far away from the magic angle [50]). Finally, we note that, in general, SOI is expected to manifest differently when the sign of D field is reversed, a feature that has not been observed in the experiment. The absence of D -field asymmetry is probably due to the small energy scale of SOI compared to the interactions and the weak tendency to polarize wavefunctions with D field in magic-angle graphene multilayers.

4.3 Insulators in TTG and TQG

Looking at the half filling of TTG (Fig. 4.3a), the resistance increases when temperature goes down, suggesting activating behavior. Assignment as an insulator is based on the activating behavior reflected in exponential suppression of conductance with $1/T$ (Fig. 4.6c), which is not expected from a Dirac semimetal; see Fig. 4.6 for detailed D and ν dependence. The two-temperature scale in conductance is in line with the behavior of TBG correlated insulator where transport at higher temperature and lower temperature is governed by activation and variable-range hopping, respectively [147] (see blue dashed line in Fig. 4.6c).

Also, the insulating behavior is suppressed by an out-of-plane B field of $B_{\perp} > 0.4$ T but is mostly insensitive to the in-plane B field (the weak suppression by the in-plane B field could possibly originate from a non-ideal in-plane-field alignment of the sample). These experimental observations are highly indicative of a gap that originates from strong interactions in TTG. We note, however, that formation of the fully gapped states in TTG requires a mechanism that additionally gaps out the MLG-like band, which may explain the presence of the gap only at finite D fields. Moreover, suppression of the gap with an out-of-plane magnetic field is at odds with the C_2 breaking scenario [21, 22] and is more in line with incommensurate Kekulé spiral [148] or inter-valley-coherent [149–152] orders in the flat bands. The insensitivity to in-plane field is suggestive of a spin-polarized insulator or otherwise insensitive to in-plane magnetic field. Finally, we can not rule out that the gap originates from induced SOI, since it is still possible that SOI promotes instabilities that favor the formation for certain $\nu = +2$ insulating states in TTG.

Fig. 4.7 shows the charge-neutrality gap of TQG as a function of D field or potential difference U (between the top and the bottom graphene layer). From the continuum model, a gap in TQG is expected when finite D field is applied. However, the details of the gap evolution depend on the precise twist angle. When the twist angle is below the magic-angle value, a charge-neutrality gap opens as soon as a finite D field is applied. On the other hand, when the twist angle is above the magic-angle value, a gap opens only at much higher D fields. The gap opening at $D/\epsilon_0 \approx 1.1$ V nm⁻¹ in our TQG structure is consistent with the device being slightly above the magic angle. Note that the charge-neutrality gap is a good reference for matching the experimental D field with the potential difference U used in calculations since the interaction-driven Hartree correction vanishes at CNP. A good match between the experimental and the calculated gap is found when converting D into U with an

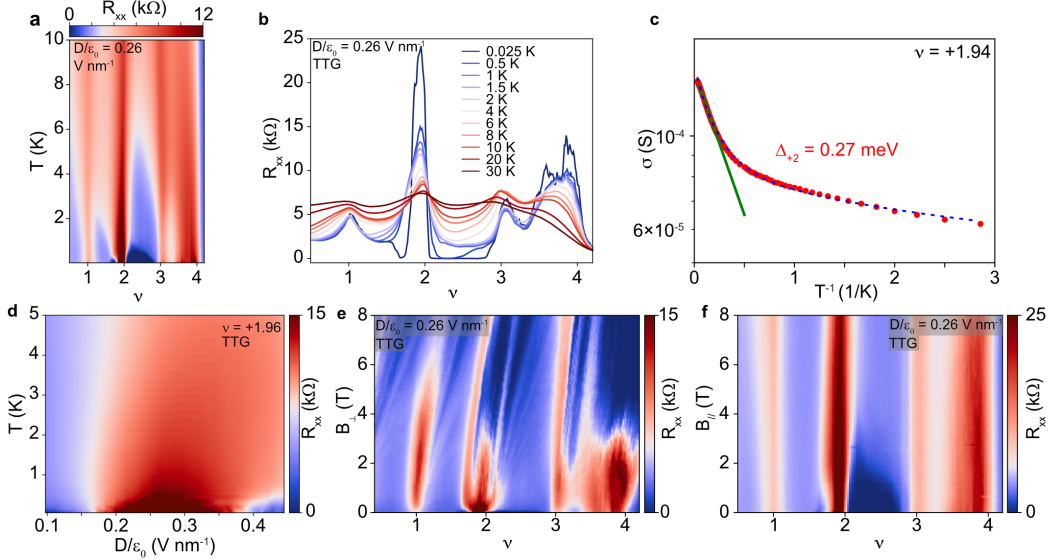


Figure 4.6: Half-filling correlated insulating state in TTG. (a) R_{xx} versus temperature and ν for the trilayer focusing around $\nu = +2$ at $D/\epsilon_0 = 0.26 \text{ V nm}^{-1}$. (b) Line cuts of R_{xx} versus ν for a range of temperatures on the electron side for TTG. (c) Conductance versus T^{-1} for TTG showing thermal activation behavior. (d) R_{xx} versus D and temperature at $\nu = +1.96$ in TTG. Out-of-plane (e) and in-plane (f) magnetic field dependence of R_{xx} versus ν in TTG.

empirical factor: $U = 0.1 \times (n - 1) \times 0.33 \text{ nm} \times eD$, where e is the electron charge and $n - 1$ is the number of graphene interfaces.

4.4 Electric-field tunable superconductivity

In addition to the pronounced ν dependence, the observed superconducting pockets are highly tunable with electric displacement field D (Fig. 4.8). A comparison of the three structures reveals that TQG and TPG are more tunable than TTG. This is apparent both in the D -dependent evolution of the filling range where superconductivity is measured (Fig. 4.8) as well as in the critical temperature T_c (Fig. 4.9a-c). Notably, superconductivity in TQG and TPG is fully quenched for all fillings at $D/\epsilon_0 = 0.75 \text{ V nm}^{-1}$ and $D/\epsilon_0 = 0.6 \text{ V nm}^{-1}$, respectively. In the case of TTG, however, superconductivity is present up to the maximum accessible electric field $D/\epsilon_0 = 1 \text{ V nm}^{-1}$.

Nevertheless, R_{xx} versus D and temperature measurements do show that superconductivity is suppressed at optimal doping in all three structures; further, they reveal that T_c forms a D symmetric dome maximized at small finite D fields (Fig. 4.9a to c). We also note that TTG, TQG, and TPG all exhibit a similar variation of T_c

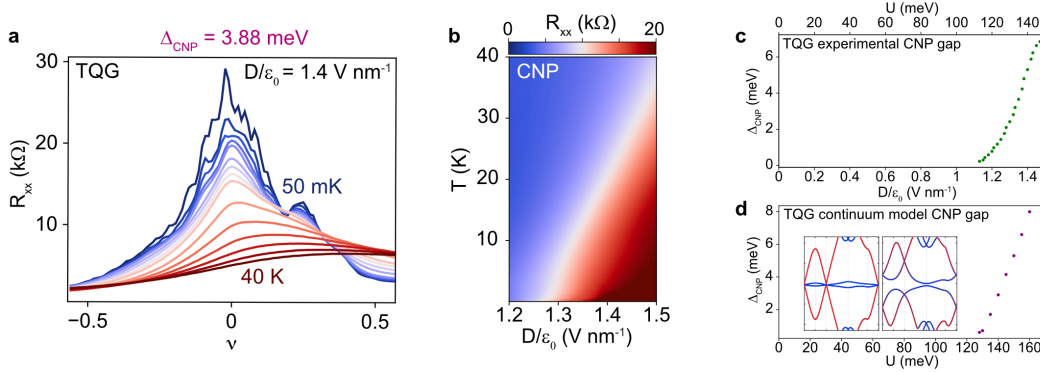


Figure 4.7: Charge-neutrality insulating state in TQG. (a) Line cuts of R_{xx} versus ν for a range of temperatures around charge-neutrality point. (b) R_{xx} versus D and temperature around CNP in TQG. (c) Experimental charge-neutrality gap of TQG as a function of D field. (d) The continuum-model gap as a function of potential difference U . Inset, single-particle band structure of TQG (slightly above the magic angle) at $U = 0$ meV and 150 meV, respectively.

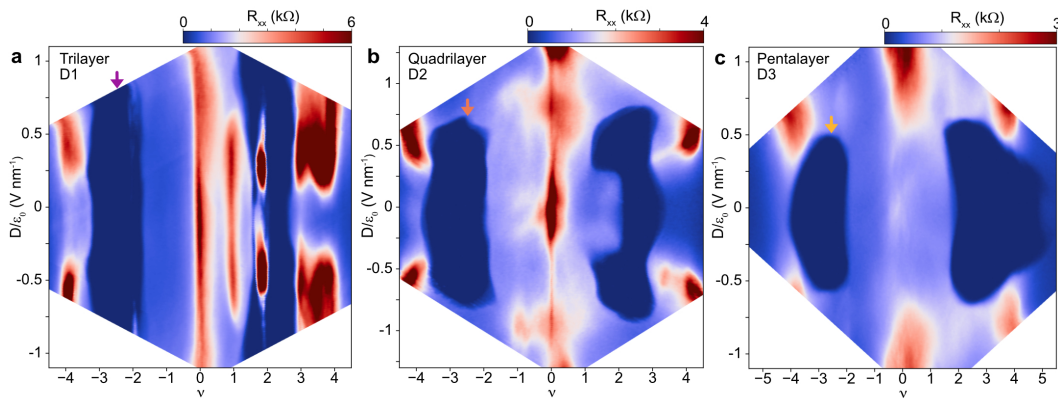


Figure 4.8: TTG, TQG, and TPG n - D phase diagrams. (a)-(c) R_{xx} versus filling factor ν and displacement field D for twisted trilayer (a), quadrilayer (b), and pentalayer (c) graphene, respectively. All data are taken at 25 mK, and the dark blue regions signal superconductivity. For electron-doped TTG and TQG, superconducting regions extend toward $\nu = +1$ at intermediate D field.

when viewed as a function of the potential difference U between the top and bottom layers (Fig. 4.9d). This layer-number invariance is consistent with non-interacting continuum-model calculations tracking the evolution of the inverse of the flat-band bandwidth with U (Fig. 4.9f). The dependence of T_c on D in all the devices qualitatively matches the predictions of Ref. [153] for TTG with one marked exception: the observed vanishing of superconductivity and the decay of T_c appears to be linear in D (Fig. 4.9a-c), in line with predictions for multilayer graphene with rhombohedral

stacking [154] and in contrast to the exponential “tail” typically expected from the weak-coupling theory (and seen in the model of Ref. [153]).

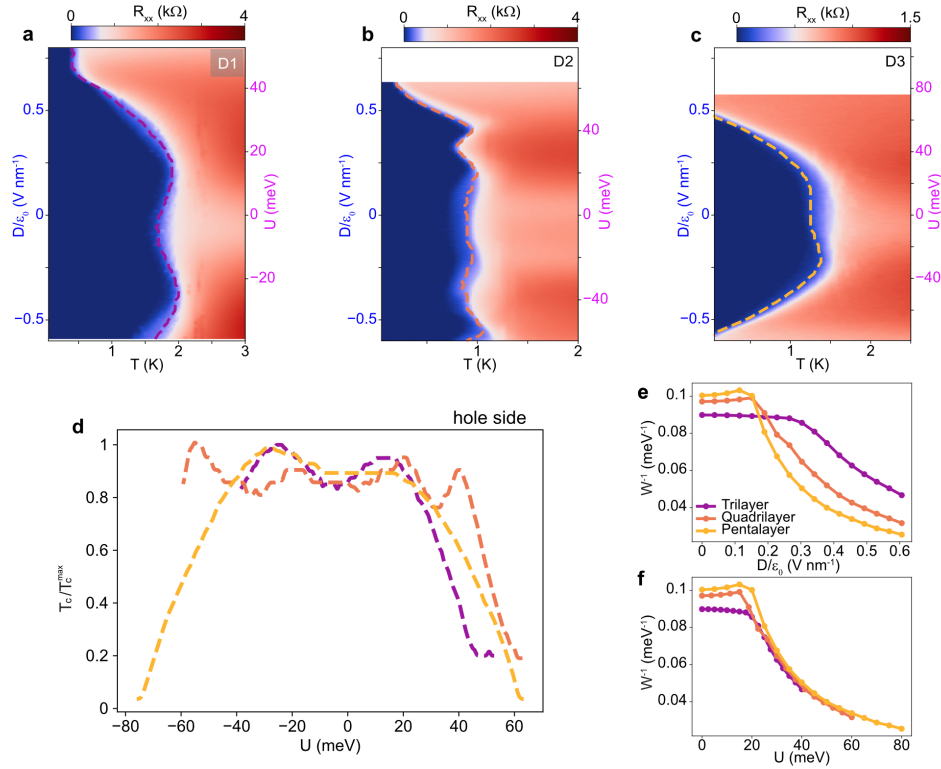


Figure 4.9: D -tuned superconductivity in the three structures. (a)-(c) R_{xx} versus temperature and D (or equivalent potential difference U between layers) for the filling factors indicated by arrows in Fig. 4.8. Critical temperature T_c is indicated by a dashed line that delineates 10% of the normal state resistance. T_c is maximized at finite D fields. Overall, superconductivity is suppressed more easily with D as the layer number is increased. (e),(f) Theoretical calculations of the inverse of the flat-band bandwidth for twisted trilayer, quadrilayer, and pentalayer graphene as a function of D/ϵ_0 (e) and potential difference U (f). For a fixed D , the bandwidth of the flat bands is larger for systems with more layers, but when expressed as a function of U , the flat-band broadening follows a similar trend across the different structures.

4.5 Interplay between superconductivity, flavor symmetry-breaking transitions, and van Hove singularities

Comparing the location of the superconducting regions with the evolution of the Hall density as a function of D and ν in TTG, TQG, and TPG provides further insight into the intricate relationship between the superconducting phase and the correlation-modified Fermi surface (Fig. 4.10 and Fig. 4.11). As in previous TBG and TTG measurements, we observe symmetry-breaking electronic transitions (a

“cascade” of transitions) that are signalled by sudden drops in the Hall density magnitude (a “reset”) without a change in sign. These resets (see dashed lines in Fig. 4.10) indicate a rearrangement of spin/valley sub-bands and typically occur near integer fillings of the flat bands [23, 24]. At low D fields, superconducting pockets onset around the $|\nu| = 2$ resets (purple dashed line), and the filling extent of superconductivity varies depending on the presence or absence of a $|\nu| = 3$ flavor symmetry-breaking transition (grey dashed line). For electron- and hole-doped TTG as well as for electron-doped TQG (Fig. 4.10a,b,d), a flavor symmetry-breaking transition appears around $|\nu| = 3$ and superconductivity accordingly terminates, as previously noted in TTG [45]. By contrast, when signatures of the $|\nu| = 3$ reset are completely absent (for example in hole-doped TQG, Fig. 4.10c, or in TPG), superconductivity extends much further. Combined, these observations suggest that superconductivity is favored when only two out of the four flavors are predominantly populated ($|\nu| = 2$ cascade) and suppressed beyond $|\nu| = 3$ resets. This behavior can be understood within the simplest iteration of the cascade scenario: resets associated with $|\nu| = 3$ produce spin- and valley-polarized bands [155] and naturally disfavor Cooper pairing of time-reversed partners.

At high D fields, signatures of the cascade vanish and instead van Hove singularities (vHs) become more prominent, reflecting qualitative changes in the band structure (see yellow lines in Fig. 4.10). Consistent with previous TTG measurements [44, 45], the vHs in our TTG sample (as well as in TPG, Fig. 4.11) crudely bound the superconducting regions. By contrast, the vHs in TQG cross well into the superconducting pockets—in fact, for electron doping, T_c reaches its maximum exactly at the position of the vHs (Fig. 4.10d, orange dot). The interplay between the vHs and superconducting boundaries, as revealed by Hall density measurements, is complex: T_c can be both enhanced and suppressed at the vHs depending on the layer number and possibly other details such as the precise twist angle.

Pentalayer measurements provide additional signatures that point toward a close relation between superconductivity and flavor symmetry-breaking cascades (Fig. 4.11). In contrast to TTG, in TPG we can access D fields that are large enough to stifle superconductivity—which occurs simultaneously with the onset of the vHs and the apparent suppression of the cascade transitions (see red and light blue lines in Fig. 4.11b that mark the superconducting boundaries and the cascade transitions, respectively). For example, at low D fields ($|D|/\epsilon_0 < 0.6 \text{ V nm}^{-1}$) around $\nu = +2$, the Hall density resets close to zero, in line with a nearly complete flavor symmetry-

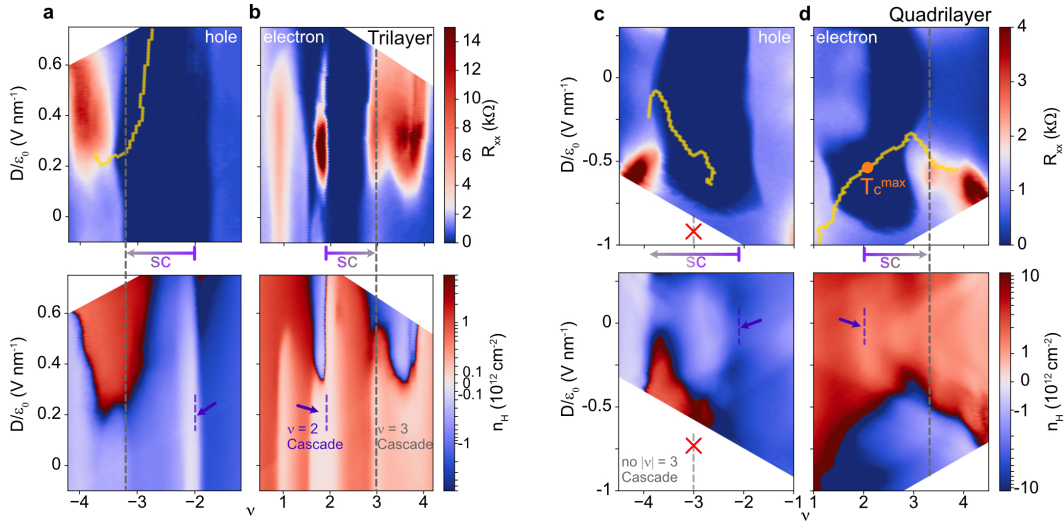


Figure 4.10: Interplay between superconductivity, flavor symmetry-breaking transitions and van Hove singularities in TTG and TQG. (a),(b) D field and ν dependence of R_{xx} (top) and Hall density (bottom, measured at $B = 0.9$ T) for TTG. Purple and grey dashed lines mark the filling factors where flavor symmetry-breaking transitions associated with $|\nu| = 2$ and $|\nu| = 3$ happen, respectively. The yellow line in (a) delineates the evolution of the vHs. (c),(d) D field and ν dependence of R_{xx} (top) and Hall density (bottom, measured at $B = 1.5$ T) for TQG. Superconducting T_c reaches its maximum (orange dot in (d)) exactly at the position of the vHs. When present, flavor symmetry-breaking transitions around $|\nu| \approx 3$ coincide with the termination of superconductivity ((a), (b), (d)). By contrast, superconductivity extends much further in the absence of a $|\nu| \approx 3$ reset (c).

breaking polarization. However, at higher D fields ($|D|/\epsilon_0 > 0.6$ V nm $^{-1}$), the Hall density is dominated by a vHs around $\nu = +2$, while the cascade signatures are diminished. Superconductivity accordingly also vanishes. For hole doping, the disappearance of superconductivity similarly coincides with the weakening of the cascade. This on/off correspondence between the two phenomena suggests that they either share a common origin, such as a large DOS, or that the cascade serves as a prerequisite for robust superconductivity in graphene moiré superlattices.

4.6 Extended superconducting pockets to $\nu \approx +5$ in TPG

One remaining puzzle is the unprecedented large superconducting pockets on the electron side of TPG. As mentioned above, for low D fields in TPG, the superconducting pockets are extraordinarily large, spanning $-4 \lesssim \nu < -2$ for hole doping and $+2 \lesssim \nu \lesssim +5$ for electron doping (Fig. 4.12 and Fig. 4.13a). In particular, the electron-side range corresponds roughly to a density window of 6×10^{12} cm $^{-2}$,

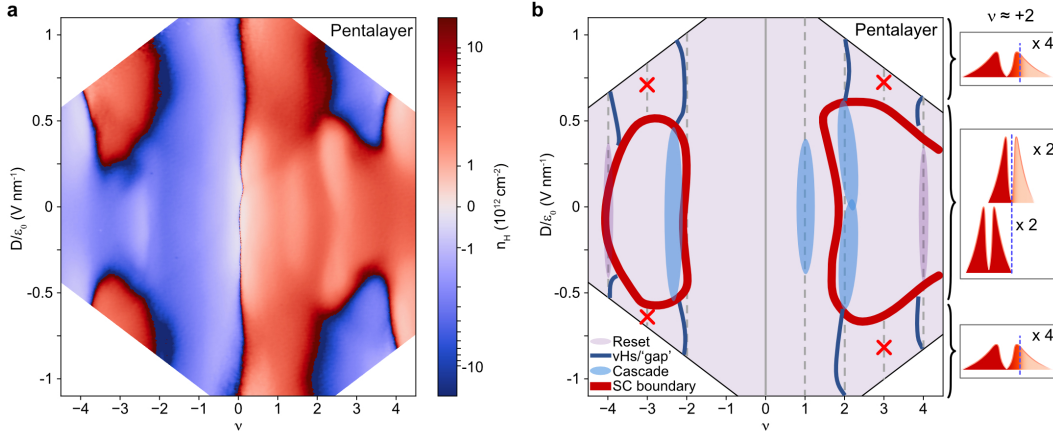


Figure 4.11: Interplay between superconductivity, flavor symmetry-breaking transitions and van Hove singularities in TPG. (a) D field and ν dependence of Hall density for TPG measured at $B = 1.5$ T. (b) Schematic of Hall density (a) and R_{xx} (Fig. 4.8c) features for the pentalayer, including the boundary of the superconducting region (red), vHs/“gap” (dark blue), cascade (light blue), and $|\nu_{\text{flat}}| = 4$ Hall density reset (light purple). Sketches of the DOS around $\nu = +2$ for different D fields are shown on the right. The middle panel illustrates the flavor symmetry polarization observed in regions that support superconductivity. Flavor symmetry is preserved at higher D fields, as shown in the top and bottom panels.

which is the largest filling range so far reported in a graphene-based superconductor. The observed superconductivity exhibits similar values of T_c and B_c as the trilayer and quadrilayer samples and is likewise accompanied by a weak oscillating pattern of critical current (Fig. 4.13c), confirming superconducting phase coherence. We emphasize that the unprecedented persistence of superconductivity across a large filling factor range in TPG (and also TQG in comparison to TTG or TBG) cannot be explained in a minimal framework of alternating twisted graphene multilayers [145, 156] without invoking the non-trivial role of the additional bands.

The role of the additional bands in TPG deserves careful consideration due to the implications for the strength of interactions, such as Hartree effects, and the types of superconductivity the bands can plausibly support. Explanations for the enlarged superconducting intervals can generically be organized into three scenarios depending on the filling of the flat TBG-like bands ν_{flat} , relative to the total filling ν_{max} at which superconductivity terminates ($\nu_{\text{max}} = +5$ for electron-doped TPG and $|\nu_{\text{max}}| = 4$ for TQG and hole-doped TPG).

We present the three scenarios in detail (see also Appendix B). In scenario (i), ν_{max} corresponds to $\nu_{\text{flat}} \approx +3$, the flat-band filling at which superconductivity is

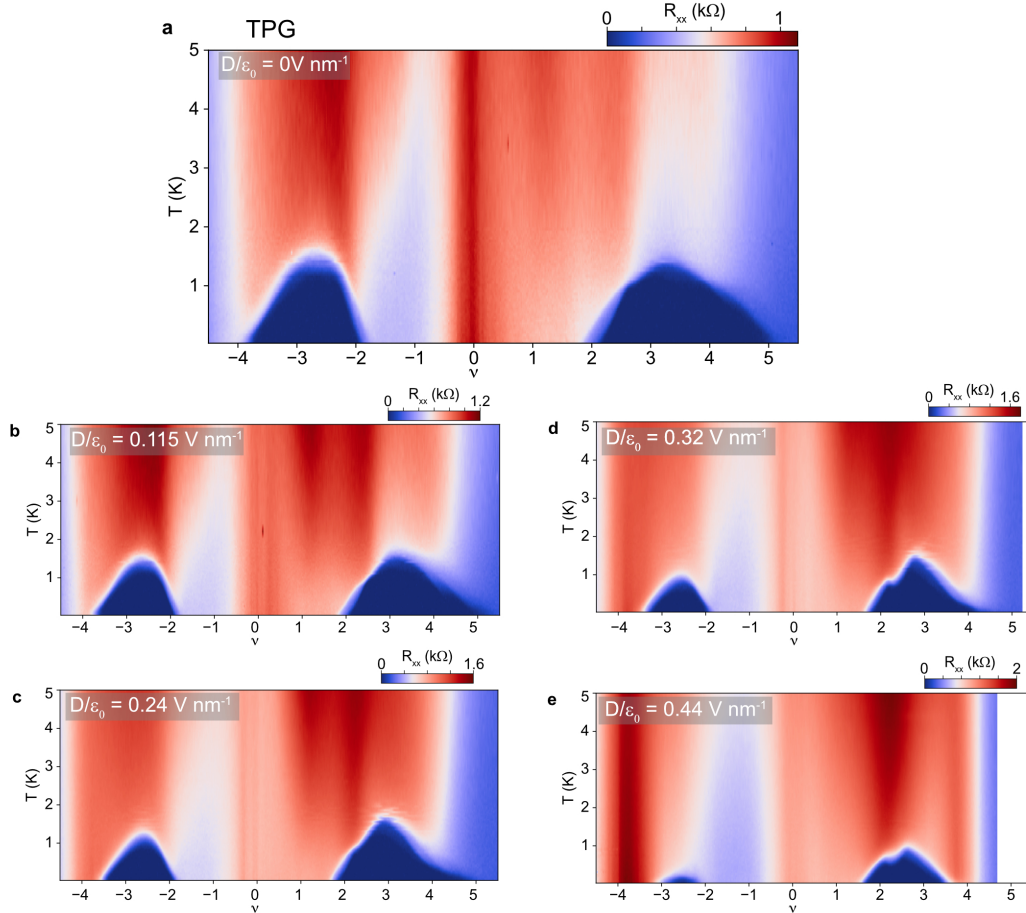


Figure 4.12: Temperature dependence of TPG measured at different D fields. (a)-(e) R_{xx} versus filling factor ν and temperature measured at $D/\epsilon_0 = 0$ (a), 0.115 (b), 0.24 (c), 0.32 (d) and 0.44 V nm^{-1} (e), respectively.

typically suppressed in TBG, suggesting that the superconducting phase space is largely the same for different multilayer magic-angle structures when considering just the flattest TBG-like bands. In scenario (ii), ν_{max} coincides with $\nu_{\text{flat}} \approx +4$, precluding any simple analogy with TBG, although superconductivity can still be attributed to the flat bands. Finally, scenario (iii) assumes full filling of the flat bands *before* superconductivity is suppressed at ν_{max} . This scenario includes the possibility that the distinction between the different TBG- and MLG-like bands breaks down even at $D = 0$ due to hybridization as well as potential multi-band superconductivity [157–160]. In this case, superconductivity in TPG is a more general phenomenon than in TBG since it occurs in either mixed bands or new, more dispersive bands.

From the perspective of the non-interacting band structure, the three scenarios all

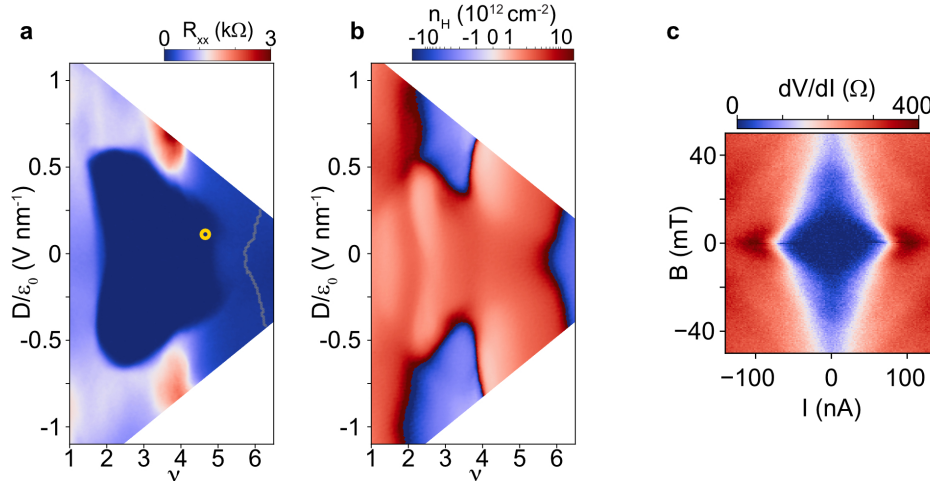


Figure 4.13: Superconductivity at extended filling factors in TPG. (a),(b) D field and ν dependence of R_{xx} (a) and Hall density (b), showing the region around the electron-side superconducting pocket. The grey line in (a) marks the ν Hs originating from the dispersive TBG-like bands. (c) The evolution of dV/dI as a function of I and B_{\perp} measured at $\nu = +4.6$, $D/\epsilon_0 = 0.12\text{ V nm}^{-1}$ (marked by a yellow dot in (a)), confirming the robustness of superconductivity above $\nu = +4$.

seem implausible, therefore interactions must play a crucial role. In particular, although the presence of the dispersive bands implies that $|\nu| - |\nu_{\text{flat}}| > 0$, this effect is much smaller than needed for either scenario (i) or (ii). Coulomb interactions can significantly enhance $|\nu| - |\nu_{\text{flat}}|$, either by evening out the spatial charge distribution [137, 161–164] or symmetry breaking [165].

We model the interactions by incorporating three types of corrections: (a) an in-plane Hartree correction; (b) a two-parameter effective model mimicking generic Hartree-Fock modifications of band structure; (c) an out-of-plane Hartree correction allowing for inhomogeneous charge distribution between the layers. The model suggests a minimal flat-band occupation $\nu_{\text{flat}} \gtrsim +3.8$ at $\nu \approx +5$ (Fig. 4.14g,h), diminishing the plausibility of scenario (i) for electron-doped TPG which has $\nu_{\text{max}} \approx +5$.

The relevance of this scenario is further undermined with the following experimental observations. For TBG and TTG, the strongest superconducting pockets normally start from $|\nu| = 2$ and end around $|\nu| = 3$. Therefore, the scenario would suggest that TPG could behave in a similar way, i.e., flat TBG-like bands are filled to $\nu_{\text{flat}} = +3$ when superconductivity is diminished at $\nu = +5$. This scenario implies that the additional two electrons per moiré site are distributed in the dispersive TBG- and MLG-like bands due to the interaction effects discussed, with a large

portion of the charge carriers being hosted by the dispersive TBG-like bands. Since vHs of the dispersive TBG-like bands are normally found around half filling, the corresponding Hall density signatures are expected to occur at the same filling, i.e., $\nu = +5$ in this scenario. However, in the experiment we observe vHs signatures originating from the dispersive TBG-like bands near $\nu \approx +6$ instead (see Fig. 4.15). This line of reasoning allows us to rule out scenario (i), therefore, we conclude that superconductivity exceeds flat-band filling $\nu_{\text{flat}} = +3$ for electron-doped TPG.

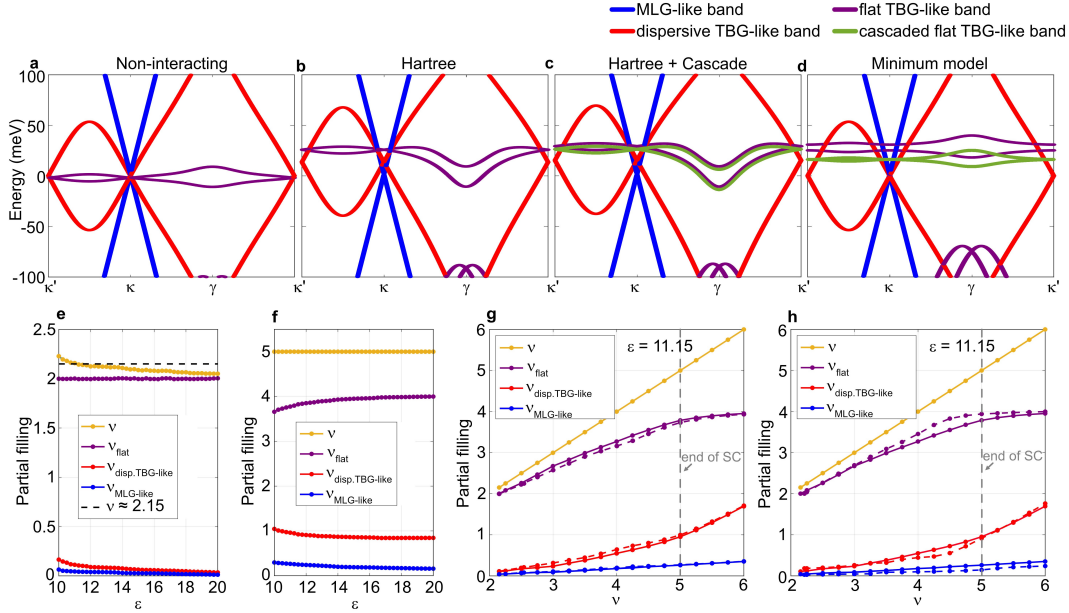


Figure 4.14: Hartree corrections in TPG. (a)-(d) Depiction of different approximation schemes used to understand the role of interactions in TPG. The Hartree correction shifts the flat band (purple) up in energy. Cascaded bands in (c) and (d) are shown in green. (d) corresponds to a minimum model of Hartree and Fock effects characterized by a Hartree shift and a Fock gap. (e),(f) Partial filling of each subsystem versus dielectric constant ϵ for a fixed flat-band filling $\nu_{\text{flat}} = +2$ (e) and a fixed total filling $\nu = +5$ (f), respectively. (g) Partial filling of each subsystem versus total filling ν for a fixed dielectric constant $\epsilon = 11.15$. Here, solid (dashed) lines correspond to a cascaded (uncascaded) solution with the cascade solution enabling higher filling of the flat-band subsystem. (h) Similar to (g) but the solid (dashed) lines correspond to a solution at potential difference $U = 0$ meV ($U = 34$ meV).

Both scenarios (ii) and (iii) are indicative of the non-trivial role of additional bands in stabilizing superconductivity. Assuming well-defined flat and dispersive bands, in scenario (iii) the former bands are completely filled, and superconductivity is supported fully by the latter non-flat bands. This assertion is at odds with the large dispersion of the remaining TBG- and MLG-like bands. However, while the

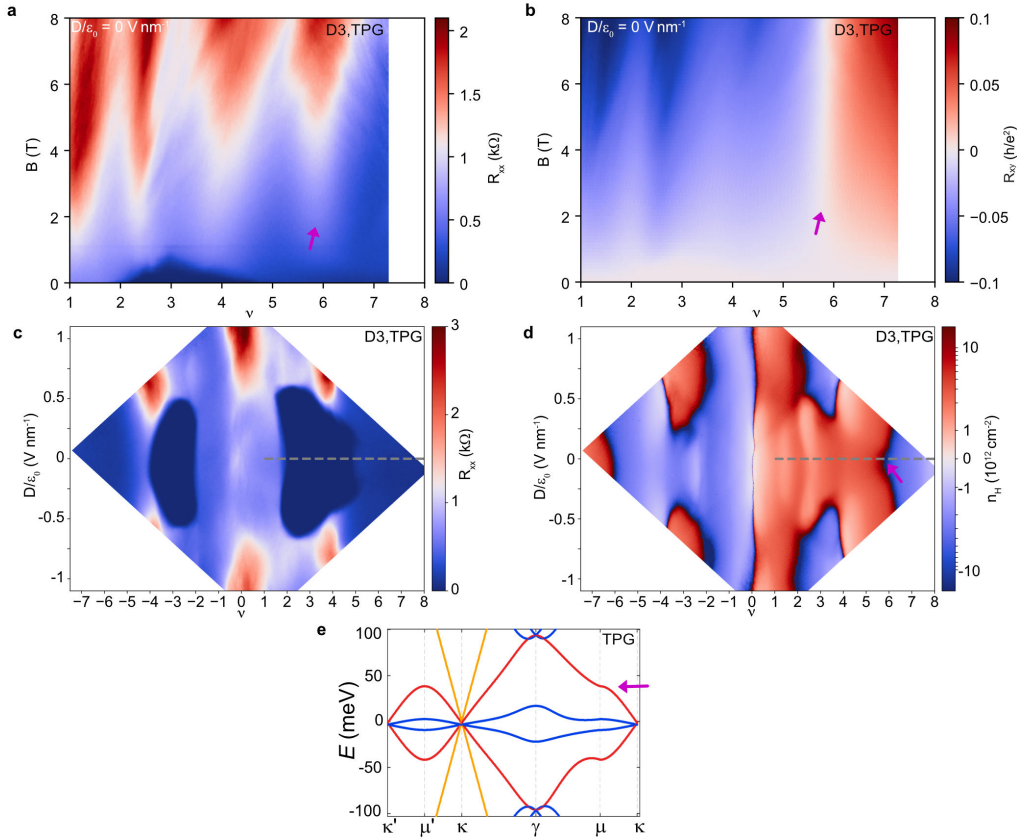


Figure 4.15: Van Hove singularities around $\nu = +6$ in TPG. (a),(b) R_{xx} and R_{xy} as a function of ν and B field measured at zero D field for TPG. The sign change in R_{xy} around $\nu = +6$ (marked by arrows in (a) and (b)) indicates vHs. (c),(d) R_{xx} (c) and Hall density (d) as a function of D and ν with gray dashed lines indicating ν linecuts (at $D = 0$) where plots in (a) and (b) were taken. (e) Band structure of TPG calculated using non-interacting model. Arrow indicates the position where vHs from dispersive TBG-like bands is expected.

exact mechanism underlying scenario (iii) is difficult to pin down, it is not without experimental support. For instance, a natural interpretation of the Hall density minimum around $\nu \approx +4$ for $|D| \lesssim 0.4 \text{ V nm}^{-1}$ is that it marks the complete filling of the flat bands, $\nu_{\text{flat}} \approx +4$ (Fig. 4.16).

One possible realization of scenario (iii) consistent with the experimental observations is that the division of the electronic states into simple TBG- and MLG-like bands fails—obviating our very definition of ν_{flat} and potentially allowing flavor polarization, and accompanying superconductivity, to persist well beyond $\nu = +4$. While such hybridization is expected for finite D fields, mixing between flat, dispersive TBG- and MLG-like bands for $|\nu| < |\nu_{\text{max}}|$ may occur even at $D = 0$ due to, for

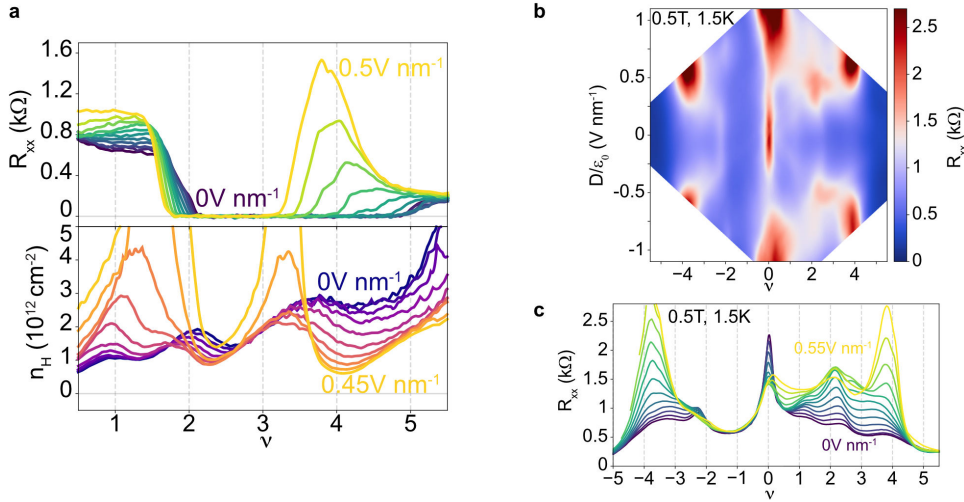


Figure 4.16: Reset at $\nu \approx +4$ in TPG. (a) Line cuts of R_{xx} (top) and Hall density (bottom, measured at $T = 1.5 \text{ K}$, $B = 0.5 \text{ T}$) versus ν for a range of D fields (traces are shown for every 0.05 V nm^{-1} for both R_{xx} and Hall density). Both the presence of Hall density resets around $\nu = +4$ and the development of superconductivity extending from $\nu = +2$ to $+5$ are shown to persist for a wide range of D fields. (b) R_{xx} versus D and ν measured at $T = 1.5 \text{ K}$, $B = 0.5 \text{ T}$ (line cuts are shown in (c)). From all the above line cuts, Hall density resets and R_{xx} resistive features consistently exist around $\nu = +4$.

example, proximity to WSe_2 , layer-to-layer charge inhomogeneity or distant-layer coupling.

Our measurements demonstrate the increasing predominance of superconductivity in twisted graphene multilayer structures as the number of layers is increased from three to five and highlight the close relationship between the flavor symmetry-breaking transitions and superconductivity. Moreover, our findings suggest a scenario in which the symmetry-broken $\nu = \pm 2$ state strongly favors the formation of the superconducting state while the cascade corresponding to $\nu = \pm 3$ suppresses it. Interestingly, this scenario is consistent not only with previous TBG [16, 20, 50–52, 141] and TTG [44, 45, 166] observations but also in part with the ABC trilayers [54] and Bernal bilayers without [55] and with a WSe_2 substrate [56] where superconductivity is observed near or within phases in which two out of four flavors are predominantly filled. These common observations suggest that symmetry-broken states with similar types of polarization underlie superconductivity in all these graphene-based superconductors. In this context, the discovery of superconductivity in TQG and TPG together with untwisted bi- and trilayers dramatically expands the scope

of graphene-based superconductors. This expansion holds promise for resolving important questions related to the nature of the pairing mechanism in these systems and provides guidance for developing novel graphene-based superconductors and their applications.

4.7 Conclusion

In this chapter, we demonstrated that moiré graphene multilayers (twisted relative to each other in an alternating sequence) all exhibit robust superconductivity with T_c similar to the TBG case. With increasing number of layers, superconductivity occupies a significantly larger phase space, especially in the pentalayer case reaching $\nu = +5$. Despite the coexistence of dispersive bands with moiré flat bands, we observed correlation-driven half-filling insulating state in TTG and single-particle charge-neutrality gap in TQG. The D -field hybridization between dispersive and flat bands makes the superconductivity in twisted graphene multilayers highly tunable. Among all three structures and also TBG, superconductivity shows intimate relation with $\nu = +2$ symmetry-breaking transitions, establishing an universal rule. We discussed the occurrence of unprecedented $\nu = +5$ superconductivity in TPG in three different scenarios. Combined with theoretical calculations including interaction effects, we confirm the abundance of superconductivity in the moiré flat bands in the pentalayer case.

ENHANCED SUPERCONDUCTIVITY IN SPIN-ORBIT PROXIMITIZED BILAYER GRAPHENE

In Chapter 3, we discussed that by adding WSe₂ to twisted bilayer graphene, superconductivity is stabilized to twist angles much far away from the magic angle. The results serve as an important tuning knob to disentangle the relevance of various symmetry-breaking phases. Half-filling flavor symmetry-breaking transition seems tightly related the occurrence of superconductivity. However, given the complicated band structure of moiré graphene as well as twist angle inhomogeneity, the exact role of WSe₂ and the type (strength) of induced SOC are hard to quantify. Superconducting state at the magic-angle condition seems not modified, i.e., the critical temperature is not affected by the addition of WSe₂.

In this chapter, we couple WSe₂ to crystalline graphene: Bernal-stacked bilayer graphene (BLG). Surprisingly, placing monolayer WSe₂ on BLG promotes Cooper pairing to an extraordinary degree: superconductivity appears at zero magnetic field, exhibits an order of magnitude enhancement in T_c , and occurs over a density range that is wider by a factor of eight. By mapping quantum oscillations in BLG-WSe₂ as a function of electric field and doping, we establish that superconductivity emerges throughout a region whose normal state is polarized, with two out of four spin-valley flavors predominantly populated. In-plane magnetic field measurements further reveal that superconductivity in BLG-WSe₂ can exhibit striking dependence of the critical field on doping, with the Chandrasekhar-Clogston (Pauli) limit roughly obeyed on one end of the superconducting dome yet sharply violated on the other. Moreover, the superconductivity arises only for perpendicular electric fields that push BLG hole wavefunctions toward WSe₂—suggesting that proximity-induced Ising spin-orbit coupling plays a key role in stabilizing the pairing. Our results pave the way for engineering robust, highly tunable, and ultra-clean graphene-based superconductors.

5.1 The advantages of Bernal bilayer graphene coupled to WSe₂

We start with the correlated phenomena in vanilla Bernal bilayer graphene. The flat electronic bands are enabled by electrical displacement fields (D fields), which open a band gap around charge neutrality point and push conduction and valence bands

edges up and down. The band edges flat, featuring van Hove singularities and high density of states (Fig. 5.1b). Eventually Coulomb interactions dominate. Measuring longitudinal resistance and quantum oscillations show resistance peaks and frequencies that suggest the breaking of flavor symmetry [55]. However, superconductivity is absent at zero magnetic field (Fig. 5.1c), in sharp contrast to the rhombohedral trilayer graphene, within which superconductivity emerges at $B = 0$ T [54]. Surprisingly, superconductivity in Bernal bilayer graphene shows up when an in-plane magnetic field is applied (Fig. 5.1d,e). The critical temperature is $T_c \approx 30$ mK (Fig. 5.1f inset).

Superconductivity that only emerges when an in-plane field is applied in BLG suggests the spin-polarized nature. Given its susceptibility to spin polarization, one nature question to ask: how will the system react to other spin perturbations, such as spin-orbit coupling? Spin-orbit coupling after all is an effectively symmetry-breaking magnetic field that couples to momentum (valley) degree of freedom. This is the motivation of coupling BLG to WSe₂.

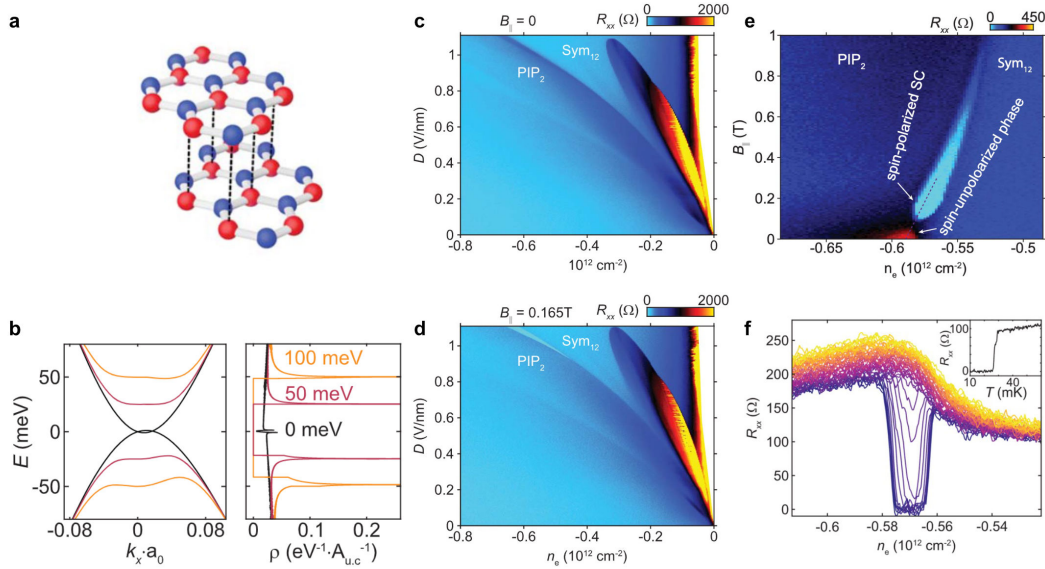


Figure 5.1: Spin-polarized superconductivity in intrinsic Bernal bilayer graphene. (a) Lattice structure of Bernal bilayer graphene. (b) Band structure calculated within a tight-binding model near the Brillouin zone corner. (c),(d) R_{xx} measured at fixed $B_{||} = 0$ (c) and 165 mT (d) at a nominal temperature of 10 mK. (e) $B_{||}$ dependence of linear response resistivity measured at $D/\epsilon_0 = 1.02$ V/nm. (f) Doping dependence of R_{xx} measured at fixed $D/\epsilon_0 = 1.02$ V/nm and $B_{||} = 165$ mT and variable temperatures. Inset measured at doping $n = -0.57 \times 10^{12}$ cm $^{-2}$ and the same D field. Reprinted from Ref. [55]; permission from The American Association for the Advancement of Science.

Fig. 5.2a shows the BLG-WSe₂ stack and all the devices have a dual-graphite gate structure with graphite electrodes (Fig. 5.2b) such that we can tune the doping density n and displacement field independently, simply by changing the top and bottom gate voltages. The device is entirely made of crystalline 2D material components including the BLG-WSe₂ channel, the hBN dielectric, graphite gates, graphite electrodes. Optical image of a typical device is shown in Fig. 5.2c.

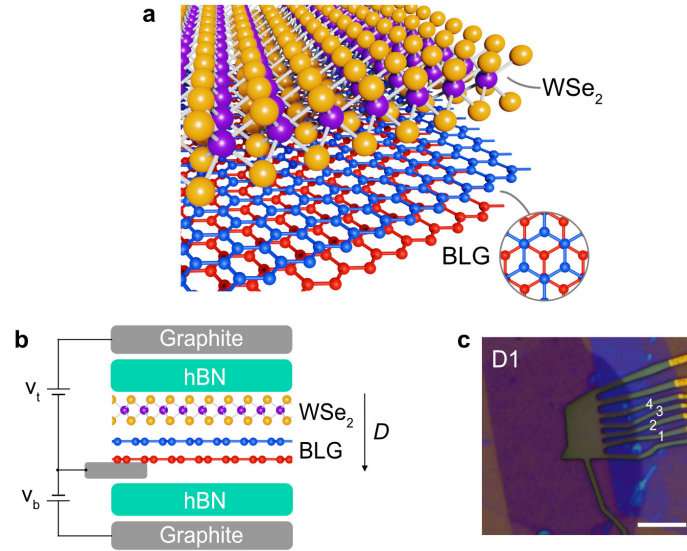


Figure 5.2: BLG-WSe₂ device structure. (a) Schematic of a BLG-WSe₂ structure showing the crystal lattice of Bernal-stacked bilayer graphene (blue and red) and a WSe₂ monolayer (yellow and purple) on top. (b) Schematic of a dual-gated device. Doping density n and D field are controlled by tuning top and bottom gate voltage v_t and v_b . (c) Optical image of the investigated device. The scale bar in the panel corresponds to 10 μm .

We shall start with the band structure of Bernal bilayer graphene, just to ask where the correlation effect comes from and why it is better for figuring out the details of SOC in comparison to TBG. Unlike monolayer graphene, the low-energy band structure of which is described by Dirac cones, the low-energy spectrum of Bernal bilayer graphene is well approximated by quadratic band touching at zero displacement field. In a finite D field, BLG features a band gap at charge neutrality [167, 168], trigonal warping [62] and prominent van Hove singularities (vHs) near the weakly dispersive band edge (Fig. 5.3). Due to the large density of states, interactions between electrons are greatly amplified when the chemical potential crosses the vHs. The details are below.

Considering the low-energy continuum model commonly used to describe Bernal-

stacked bilayer graphene [62], a perpendicular displacement field D generates a potential difference $u = -d_{\perp}D/\epsilon_{\text{BLG}}$ between the top and bottom layers. Here $d_{\perp} = 0.33$ nm is the interlayer distance and $\epsilon_{\text{BLG}} \sim 4.3$ is the relative permittivity of BLG. A continuum approximation of the band structure returns a Hamiltonian of the form

$$H_0 = \sum_{\xi=\pm} \sum_{\mathbf{k}} \psi_{\xi}^{\dagger}(\mathbf{k}) h_{0,\xi}(\mathbf{k}) \psi_{\xi}(\mathbf{k}),$$

$$h_{0,\xi}(\mathbf{k}) = \begin{pmatrix} u/2 & v_0\Pi^{\dagger} & -v_4\Pi^{\dagger} & -v_3\Pi \\ v_0\Pi & \Delta' + u/2 & \gamma_1 & -v_4\Pi^{\dagger} \\ -v_4\Pi & \gamma_1 & \Delta' - u/2 & v_0\Pi^{\dagger} \\ -v_3\Pi^{\dagger} & -v_4\Pi & v_0\Pi & -u/2 \end{pmatrix} \quad (5.1)$$

where $\Pi = (\xi k_x + i k_y)$ and $v_i \equiv \frac{\sqrt{3}a}{2}\gamma_i$. Here, $\xi = \pm 1$ indicates the valley that has been expanded about: $\mathbf{K}, \mathbf{K}' = (\xi 4\pi/3a, 0)$ with $a = 0.246$ nm the lattice constant of monolayer graphene. The 4×4 matrix $h_{\xi}(\mathbf{k})$ is expressed in the sublattice/layer basis corresponding to creation/annihilation operators of the form $\psi_{\xi}(\mathbf{k}) = (\psi_{\xi,A1}(\mathbf{k}), \psi_{\xi,B1}(\mathbf{k}), \psi_{\xi,A2}(\mathbf{k}), \psi_{\xi,B2}(\mathbf{k}))^T$, where A/B indicate the sublattice, 1, 2 indicate the layer, and the momentum \mathbf{k} is measured relative to \mathbf{K}_{ξ} (indices denoting the spin degrees of freedom have been suppressed). The values for the parameters entering into Eq. (5.1) are $\gamma_0 = 2.61$ eV (intralayer nearest-neighbor tunneling), $\gamma_1 = 361$ meV (leading interlayer tunneling), $\gamma_3 = 283$ meV (also known as trigonal warping term), $\gamma_4 = 138$ meV, and $\Delta' = 15$ meV (potential difference between dimer and non-dimer sites) [63].

In the absence of SOC and an applied displacement field with $v_3 = v_4 = 0$, two bands touch quadratically at charge neutrality. Two remaining bands are at significantly higher and lower energies; their wavefunction are dominated by the ‘‘dimer sites’’, i.e., the A2 and B1 which sit immediately on top of one another in the bilayer and hybridize strongly through the onsite tunneling parameter γ_1 . Trigonal warping introduced by the v_3, v_4 associated hoppings in Eq. (5.1) splits the quadratic band touching at charge neutrality into four distinct Dirac cones separated by van Hove singularities: one Dirac cone remains at $\mathbf{k} = 0$, while the other three are located at C_3 -related momenta slightly away from the Dirac point. Turning on a displacement field D , a gap opens at charge neutrality and the vHs move apart in energy. Further, by flattening the band bottom, the applied D field also amplifies divergence of the DOS close to the vHs.

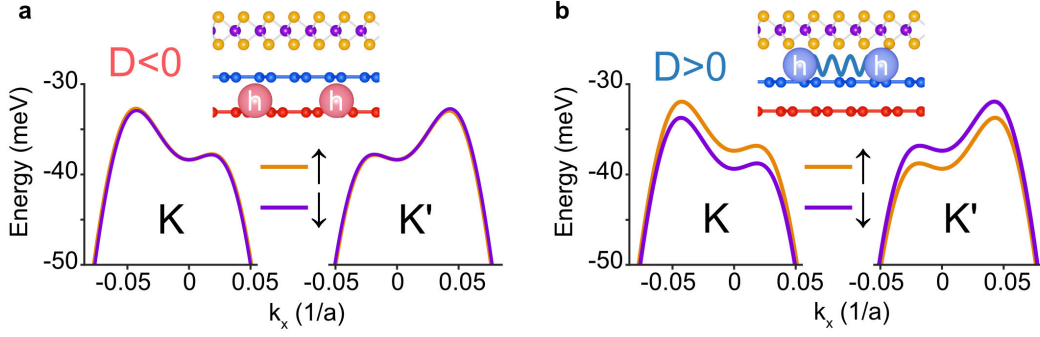


Figure 5.3: Non-interacting valence bands of BLG-WSe₂. Non-interacting valence bands near the K and K' points of the Brillouin zone for $D/\epsilon_0 = -1$ V/nm (a) and 1 V/nm (b), calculated by including an Ising SOC ($\lambda_I = 1$ meV) on the top layer. Schematics show that when BLG is hole-doped, electronic wavefunctions are polarized toward the top layer for $D > 0$, and toward the bottom layer for $D < 0$.

Importantly, The low-energy states near K and K' become strongly layer- and sublattice-polarized; e.g., on $A1$ sites for the valence band and $B2$ sites for the conduction band, or vice versa for the other sign of D . That is, the low-energy wavefunctions near charge neutrality and under a large D field are strongly localized on the “non-dimer sites” of BLG.

A WSe₂ monolayer adjacent to the graphene is known to induce SOC via virtual tunneling [129, 169, 170]:

$$H_{\text{SOC}} = \sum_{\xi=\pm} \sum_{\mathbf{k}} \psi_{\xi}^{\dagger}(\mathbf{k}) h_{\text{SOC},\xi} \psi_{\xi}(\mathbf{k}),$$

$$h_{\text{SOC},\xi}(\mathbf{k}) = \mathcal{P}_1 \left[\frac{\lambda_I}{2} \xi s^z + \frac{\lambda_R}{2} (\xi \sigma^x s^y - \sigma^y s^x) \right], \quad (5.2)$$

where the Pauli matrices σ^i and s^i , $i = x, y, z$, respectively act on sublattice and spin degrees of freedom. The operator \mathcal{P}_1 projects onto the top graphene sheet, i.e., only the sites $A1$ and $B1$: $\mathcal{P}_1 = \text{diag}(\mathbb{1}_{2 \times 2}, \mathbb{0}_{2 \times 2})$ in the layer/sublattice basis used to express $h_{0,\xi}(\mathbf{k})$ in (5.1). The parameters λ_I and λ_R quantify the strength of the Ising (also called “valley-Zeeman”) and Rashba SOC. Ab initio-type numerics and experimental estimates find a range of values $\lambda_I \sim 0-5$ meV and $\lambda_R \sim 0-15$ meV for the SOC parameters [169–176], which are also predicted to be strongly twist-angle dependent [173–175].

The layer- and sublattice polarization of the low-energy wavefunctions near the K , K' points has important consequences for SOC induced by the TMD. Indeed, Rashba

SOC does not act effectively in the low-energy theory because it is off-diagonal in the sublattice degree of freedom. It therefore induces a splitting only at second order in degenerate perturbation theory, with $\lambda_R^{\text{eff}} \sim (\lambda_R v_0 k)^2 / (\gamma_1^2 u)$ with u the interlayer potential [177]. By contrast, the Ising SOC acts effectively in the subspace of sublattice- and layer-polarized wavefunctions.

5.2 Asymmetry with electrical displacement field

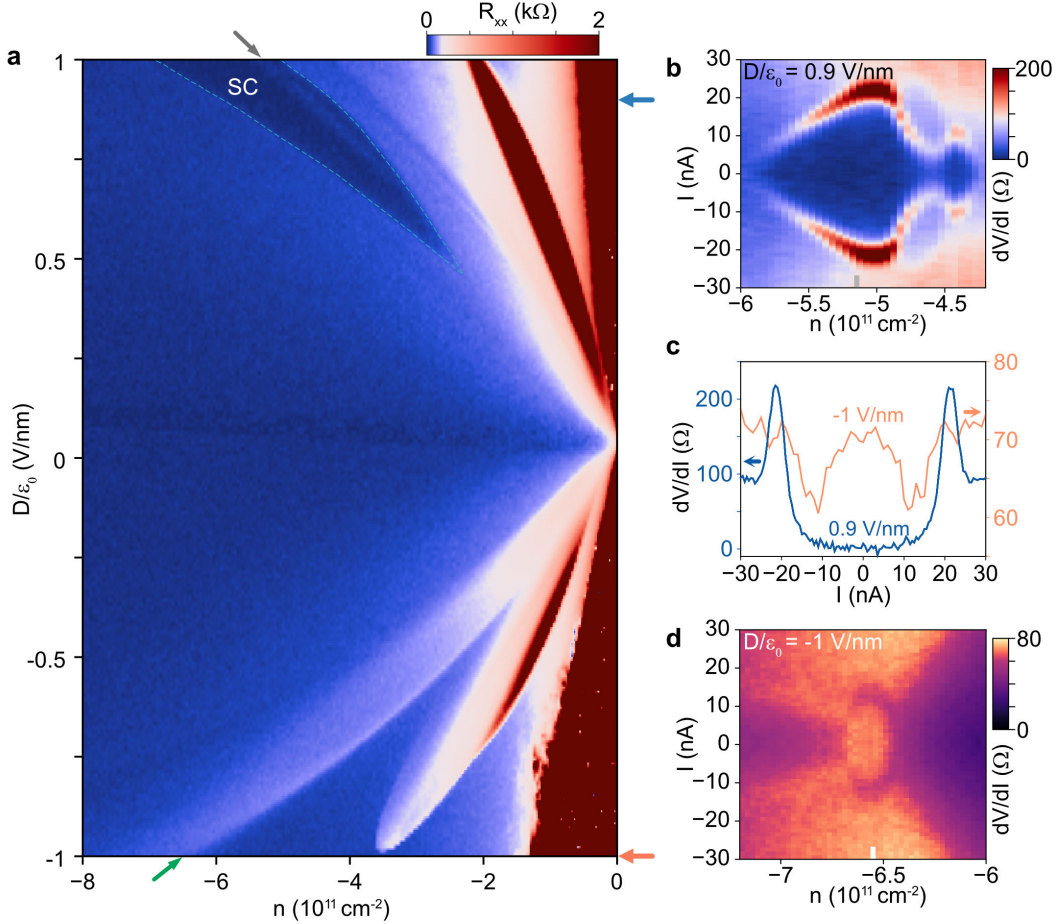


Figure 5.4: Asymmetric n - D phase diagram of BLG-WSe₂. (a) R_{xx} versus doping density n and displacement field D measured at zero magnetic field. Flavor-polarized states show strong asymmetry with respect to the sign of D field. Superconductivity (delineated by a dashed line) spans across wide doping and D ranges at positive D fields (wavefunctions are strongly polarized toward the WSe₂). A competing resistive phase appears in the middle of the superconducting region, as marked by the grey arrow. (b),(d) dV/dI versus n and bias current I measured at $D/\epsilon_0 = 0.9$ V/nm (b) and -1 V/nm (d), respectively. (c) Blue and orange curves are line cuts from (b) and (d), respectively, with the densities marked by the colored bars.

Longitudinal resistance R_{xx} measured as a function of carrier density n and D at zero magnetic field shows peaks or dips that emerge and separate from each other as $|D|$ is increased (Fig. 5.4a). These features can be associated with an interplay of Lifshitz transitions and breaking of spin and valley symmetries, similar to the case of hBN-encapsulated BLG [55]. Importantly, the resulting phase diagram is strongly asymmetric with respect to the sign of D field. Focusing on hole doping, for both signs of D , the largest resistance peaks (red diagonal regions in Fig. 5.4a) correspond to phases that possess a single spin-valley flavor-polarized Fermi surface, which we denote as $\text{FP}(1)_{\pm}$ ($\text{FP}(n)$ denotes a flavor-polarized phase with n degenerate Fermi pockets and \pm denotes the sign of D ; see section 5.5 for the identification of spin-valley degeneracy). For positive D , this resistive feature spans beyond $D/\epsilon_0 = +1$ V/nm but is suppressed by $D/\epsilon_0 = -0.75$ V/nm for negative D .

The most striking difference in the BLG-WSe₂ phase diagram between positive and negative D fields is the emergence of a broad zero-resistance region corresponding to superconductivity at $D > 0$. No analogous region has been observed in hBN-encapsulated BLG, where superconductivity only appears in a finite in-plane magnetic field [55].

The pronounced $\pm D$ asymmetry highlights the role of Ising SOC in defining the phase diagram of BLG-WSe₂. Theoretical calculations [170, 178] (Fig. 5.3b) confirm that Ising SOC is induced only on the top layer proximate to WSe₂ and that, correspondingly, the SOC-induced spin splitting in the valence band is largely restricted to $D > 0$ —consistent with the D -asymmetric experimental data (Fig. 5.4a). In contrast, Rashba SOC is expected to produce splittings that are largely independent of the sign of D , and thus cannot account for the pronounced $\pm D$ asymmetry.

5.3 Estimating SOC strength

In the Sections 5.1 and 5.2, both the theory of proximitized SOC in BLG and the asymmetric n - D phase diagram already provide strong evidence of the important role of Ising SOC. Here, we try to estimate Ising and Rashba SOC quantitatively.

Quantum Hall measurements around $D = 0$ further support the existence of Ising SOC (Fig. 5.5a-e). To quantify WSe₂-induced Ising SOC, we probe the octet zeroth Landau level (LL) in BLG, since few-meV-scale Ising SOC can rearrange the energies of these states. Note that these LL energies are not sensitive to Rashba SOC [179]. Previous experiments [128, 129] have shown that one can quantify the Ising SOC $H_I = \frac{1}{2}\lambda_I\tau_zs_z$ (λ_I is the Ising SOC strength) with LLs on opposite

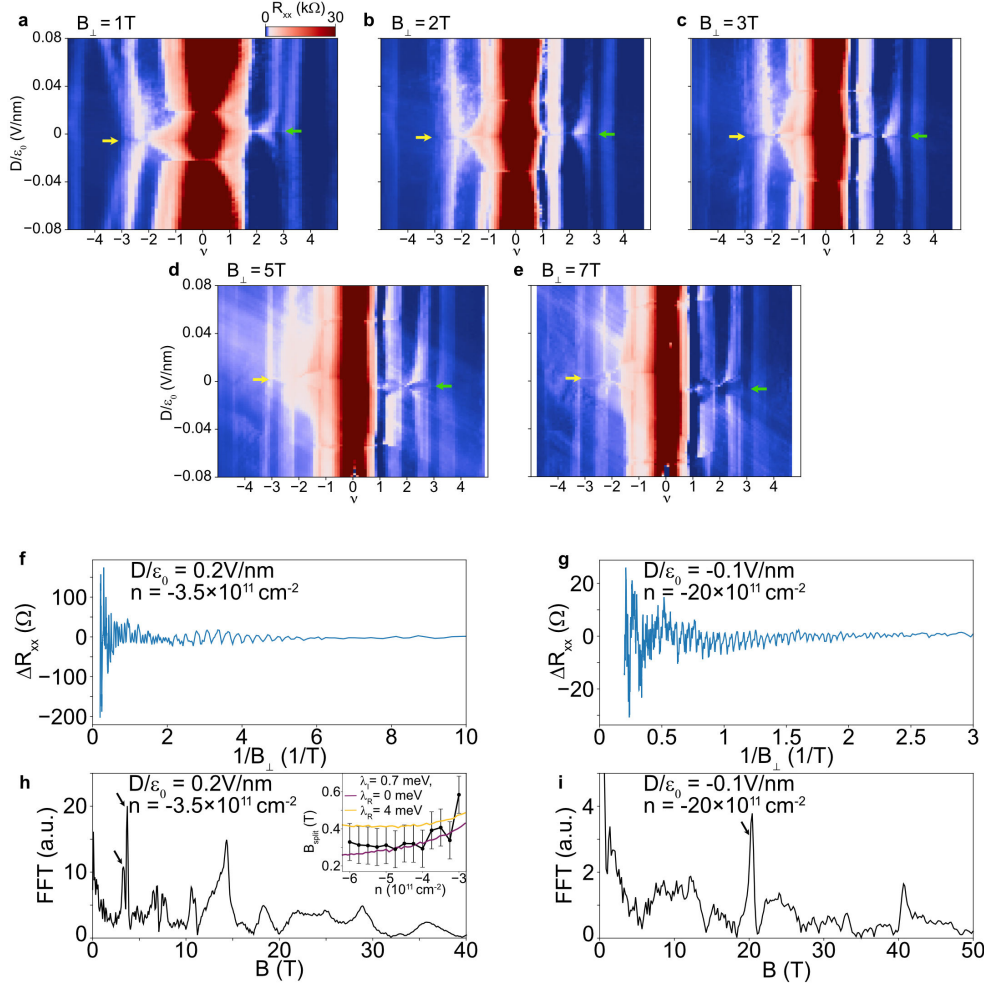


Figure 5.5: Estimating different SOC strengths through quantum Hall effect and quantum oscillations. (a)-(e) R_{xx} versus $\nu = 2\pi\ell_B^2 n$ (ℓ_B is the Landau magnetic length) and D field at $B_{\perp} = 1$ T, 2 T, 3 T, 5 T, and 7 T, respectively. Arrows mark the transition of $|\nu| = 3$ quantum Hall states with D field. (f),(g) ΔR_{xx} versus $1/B_{\perp}$ (measured up to $B_{\perp} = 5$ T) at $D/\epsilon_0 = 0.2$ V/nm, $n = -3.5 \times 10^{11}$ cm $^{-2}$ (f) and $D/\epsilon_0 = -0.1$ V/nm, $n = -20 \times 10^{11}$ cm $^{-2}$ (g), respectively. The corresponding FFT data are shown in (h) and (i). Inset of (h) shows the FFT splitting B_{split} (marked by black arrows in the main panel) versus doping density n measured at $D/\epsilon_0 = 0.2$ V/nm. Colored lines show the FFT splitting predicted from band structure calculations for the same D field, using Ising SOC $\lambda_I = 0.7$ meV with Rashba SOC $\lambda_R = 0$ meV (purple line) and $\lambda_R = 4$ meV (yellow line).

graphene layers: The sets of two Landau levels that cross at $\nu = \pm 3$ filling factors have opposite layer polarization, such that their energy difference (at zero D field) is given by $\Delta E = E_Z \pm \lambda_I/2$ (E_Z is the Zeeman gap between spin-up and spin-down LLs)—only one of the two Landau levels (with layer polarization close to the WSe $_2$)

is affected by the Ising SOC. Therefore, the critical field B_{\perp}^* that makes ΔE vanish is $2E_Z = 2g\mu_B B_{\perp}^* = \lambda_I$. In Fig. 5.5a-e, $B_{\perp}^* \approx 3$ T is the magnetic field at which yellow and green arrows level at the same D field, yielding $\lambda_I \approx 0.7$ meV.

Independently, λ_I can also be extracted from the doping-dependent FFT splitting of quantum oscillations. Fig. 5.5h inset shows the FFT splitting B_{split} as a function of doping at $D/\epsilon_0 = 0.2$ V/nm. Ising-type splitting is suppressed with increasing $|n|$, in contrast to Rashba-type splitting which increases with increasing $|n|$. The observed splitting is consistent with the value of $\lambda_I \approx 0.7$ meV extracted from the quantum Hall measurements, as shown in the Fig. 5.5h inset by comparing to the band splitting predicted from the band structure calculations at the same D field. In the Section 5.5, the Fermi-surface structures additionally support explicit symmetry breaking by Ising SOC.

The effect of Rashba SOC is more subtle in the experiment. Quantum oscillations at higher B_{\perp} field provide an upper bound for the magnitude of Rashba SOC. Fig. 5.5f-i shows ΔR_{xx} versus $1/B_{\perp}$ and corresponding FFT measured at $D/\epsilon_0 = 0.2$ V/nm and -0.1 V/nm, respectively. At $D > 0$ (Fig. 5.5h), FFT reveals a frequency splitting while at $D < 0$ the splitting is absent (Fig. 5.5i). These observations are consistent with the interpretation that at $D > 0$, the splitting is mainly caused by Ising SOC; however at $D < 0$, the Ising effect is strongly diminished and Rashba SOC strength λ_R is not big enough to induce an observable splitting. The FFT peak at $D < 0$ (Fig. 5.5i) has a full width at half maximum around 0.8 T, which translates to an upper bound for the bare Rashba SOC strength $\lambda_R \lesssim 5$ meV by comparing to the spin splitting predicted from band structure calculations at the same density $n = -2 \times 10^{12}$ cm $^{-2}$ and displacement field $D/\epsilon_0 = -0.1$ V/nm. An upper bound on Rashba SOC can also be extracted from the observed spin splitting at positive $D/\epsilon_0 = 0.2$ V/nm, assuming Ising SOC $\lambda_I = 0.7$ meV (Fig. 5.5h inset). From this analysis we find an upper bound $\lambda_R \lesssim 4$ meV, roughly consistent with the bound from the negative D field data.

5.4 Superconductivity at zero magnetic field

After establishing the role of Ising SOC and quantifying the magnitude, we turn to the characteristics of the broad superconducting region at $D > 0$. No analogous region has been observed in hBN-encapsulated BLG, where superconductivity only appears in a finite in-plane magnetic field [55]. The critical current of the zero-magnetic-field superconductivity in BLG-WSe $_2$ exhibits nontrivial doping dependence (Fig. 5.4b),

with two distinct maxima (the larger of which reaches 20 nA). By contrast, at $D < 0$ a different phase (Fig. 5.4c,d) exhibiting highly nonlinear current-dependent resistance is observed for similar values of n and $|D|$ (marked by a green arrow in Fig. 5.4a). This resistive phase is suppressed by small magnetic fields and is similar to the zero-magnetic-field phase that has been reported in hBN-encapsulated BLG [55].

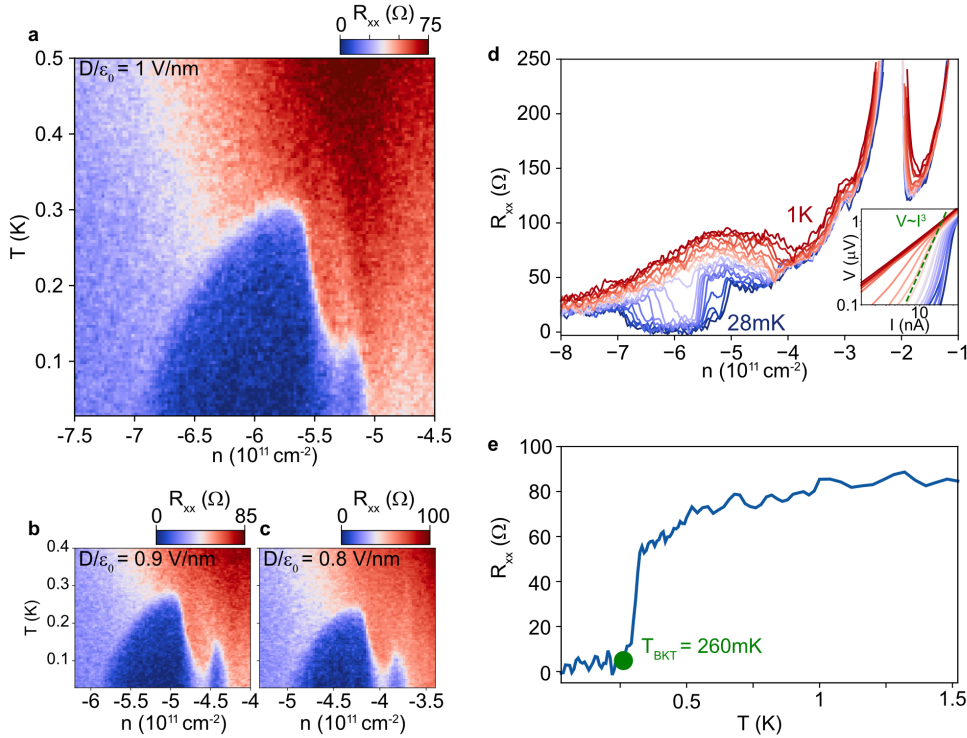


Figure 5.6: Temperature dependence of superconductivity. (a)-(c) R_{xx} versus density n and temperature for hole doping, showing superconducting domes in the FP(2, 2)₊ phase for $D/\epsilon_0 = 1 \text{ V/nm}$ (a), 0.9 V/nm (b), and 0.8 V/nm (c), respectively. A competing resistive phase intersects the superconducting domes at these D fields. (d) Line cuts of R_{xx} versus n for a range of temperatures (from 28 mK to 1 K) measured at $D/\epsilon_0 = 1 \text{ V/nm}$. The inset shows the V - I plot at $n = -5.75 \times 10^{11} \text{ cm}^{-2}$ and various temperatures. The green dashed line marks where $V \sim I^3$, from which we determine $T_{BKT} = 260 \text{ mK}$. (e) R_{xx} versus temperature measured at $n = -5.75 \times 10^{11} \text{ cm}^{-2}$ showing a superconducting transition.

The evolution of critical temperature T_c with n and D provides further insights into the superconducting phase (Fig. 5.6a-c). The superconducting dome occupies a wide range of doping ($\sim 2 \times 10^{11} \text{ cm}^{-2}$; see Fig. 5.4a) and features a maximal T_c of approximately 300 mK. Figure 5.6d shows R_{xx} line cuts at different temperatures; insets show nonlinear I - V curves at optimal doping, yielding a Berezinskii-Kosterlitz-Thouless (BKT) transition temperature $T_{BKT} \approx 260 \text{ mK}$.

(estimated by the temperature where $V \sim I^3$). We emphasize that the superconducting critical temperature observed here is an order of magnitude larger than the T_c in hBN-encapsulated BLG. Moreover, the relatively high T_c does not appear to be sensitive to minor changes of D field, further substantiating the robustness of the superconducting phase. Fig. 5.7 shows the evolution of the superconducting phase in the presence of an out-of-plane magnetic field B_\perp . The maximal critical field $B_{c\perp} \approx 15$ mT at base temperature yields a corresponding Ginzburg-Landau coherence length $\xi_{GL} = \sqrt{\Phi_0/(2\pi B_{c\perp})} \approx 150$ nm (Φ_0 is the superconductor flux quantum).

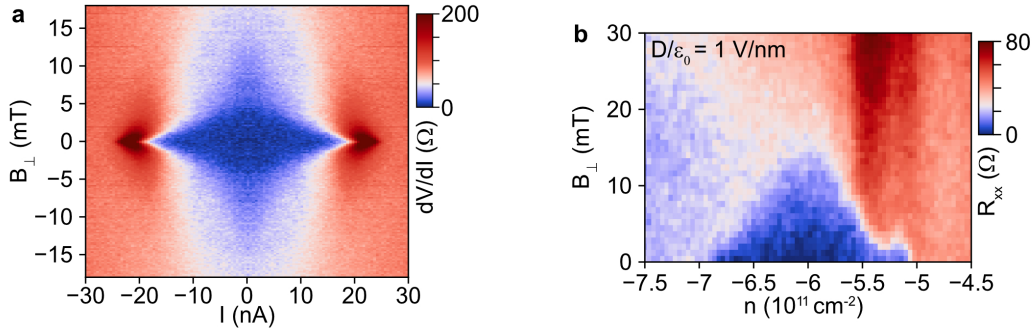


Figure 5.7: Out-of-plane magnetic field dependence of superconductivity. (a) Critical current disappearing with B_\perp field measured at $D/\epsilon_0 = 0.9$ V/nm, $n = -5.05 \times 10^{11}$ cm $^{-2}$. (b) R_{xx} versus n and B_\perp field around the superconducting region for $D/\epsilon_0 = 1$ V/nm.

We can estimate the mean free path through the magnetic focusing measurement. Fig. 5.8a shows non-local resistance R_{nl} as a function of n and B_\perp for $D/\epsilon_0 = 0.6$ V/nm measured with the configuration shown in Fig. 5.8b. Data at density $n = -7 \times 10^{11}$ cm $^{-2}$ show a pronounced feature around $B_\perp \approx 20$ mT, which suggests a transverse magnetic focusing [180] that is comparable with the electrodes separation of $5 \mu\text{m}$, and translates to a mean free path $\ell_{mf} \gtrsim \pi L/2 \approx 7.9 \mu\text{m}$. Thus, superconductivity resides deep in the clean limit, $\xi_{GL}/\ell_{mf} < 0.02$, similar to the case of hBN-encapsulated Bernal bilayer and rhombohedral trilayer graphene [54, 55].

Another prominent feature of both the T and B_\perp field dependence (Fig. 5.6a-c) is a resistive peak that intersects the superconducting dome, effectively splitting it into two regions within a certain range of D fields (note by the grey arrow in Fig. 5.4a). This peak signals the presence of another phase that appears to compete with superconductivity. Both the doping range where this state occurs

and its disappearance at relatively low magnetic fields are features shared by the resistive phase observed for $D < 0$ (see the green arrow in Fig. 5.4a) and in hBN-encapsulated BLG [55]. Moreover, both the resistive peak and superconductivity feature a broken-symmetry parent state with two large and emerging small Fermi pockets (see discussion in the Section 5.5), suggesting that transport in this region is highly sensitive to the exact details of the spin-valley ground states.

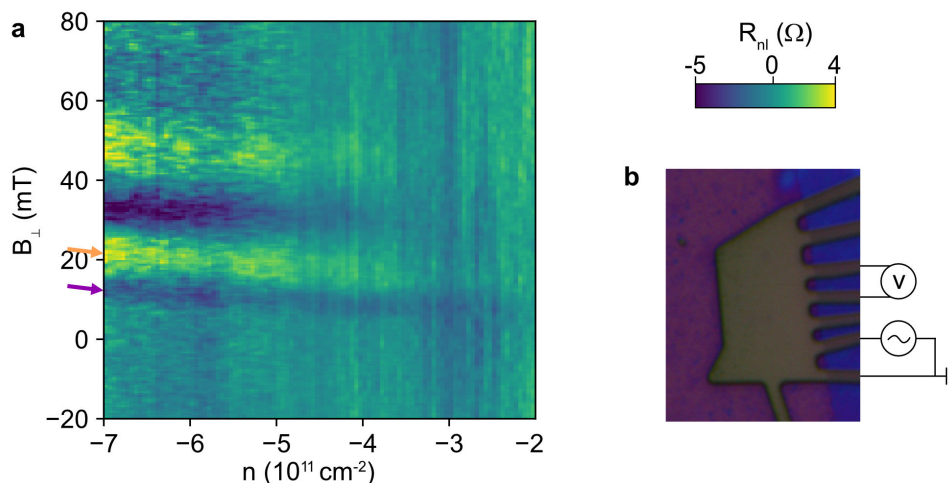


Figure 5.8: Transverse magnetic focusing with an out-of-plane magnetic field. (a) Non-local resistance R_{nl} measured as a function of n and B_{\perp} at $D/\epsilon_0 = 0.6$ V/nm with the measurement configuration shown in (b).

5.5 Fermi surfaces of the flavor-polarized states

Upon applying D fields, the top portion of the valence bands around K and K' points is quite flat (Fig. 5.9a). Coulomb interactions dominate over kinetic energy. To reduce the total energy, BLG prefers to unevenly populate different spin-valley flavors, forming spontaneous flavor-polarized states (flavor ferromagnetism). Additionally, the top of the valence bands host three trigonally warped pockets (Fig. 5.9b). To further reduce the total energy, electrons may selectively populate one or two out of the three trigonally warped pockets within certain flavors, thus forming spontaneous nematic orders [181]. The interplay between kinetic energy, strong correlations, trigonal warping, and explicit Ising SOC gives rise to a plethora of symmetry-breaking ground states as following.

The D -field asymmetry discussed in Section 5.2 is also highlighted by low field ($B_{\perp} < 1$ T) quantum oscillations measured at $D/\epsilon_0 = 1$ V/nm and -1 V/nm, which imply distinct Fermi surface structures within the superconductivity region

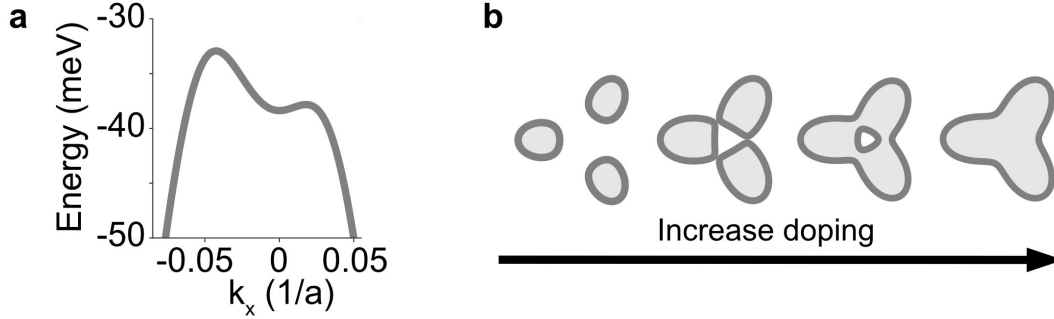


Figure 5.9: Band structure and Fermi surfaces for single spin-valley flavor. (a) Non-interacting valence bands near the K/K' point for at large displacement field featuring trigonal warped pockets and a flat portion of the band. (b) The evolution of Fermi surfaces as a function of doping for single spin-valley flavor.

for $D > 0$ (Fig. 5.11) and within the resistive phase for $D < 0$ (Fig. 5.10). The ultra-clean BLG enables high quality quantum oscillations that quantifies the size of Fermi surfaces. Fourier transforms of the oscillations—taken with respect to $1/B_{\perp}$ —reveal the phases in the relevant doping ranges. Because the crystalline graphene does not have integer filling factors, therefore, we normalize the Fermi surface sizes relative to the size of total density to see the electron polarization. The Fourier transform of $R_{xx}(1/B_{\perp})$ at low magnetic fields ($0.05 \text{ T} < B_{\perp} < 0.5 \text{ T}$ or so) is normalized by the frequency corresponding to the full doping density, $f_{\text{norm}} = n \times h/e$, so that the resulting frequency f_v reveals the fraction of the total Fermi surface area enclosed by a cyclotron orbit (Fig. 5.10b,e).

Start with the Fermi surfaces at negative D field where the effect of Ising SOC is small. At $D/\epsilon_0 = -1 \text{ V/nm}$, the resulting phase diagram is remarkably similar to that reported on hBN-encapsulated BLG without WSe₂ [55]. At the lowest electron densities ($|n| < 3 \times 10^{11} \text{ cm}^{-2}$; Fig. 5.10b), we observe a Fourier transform peak at $f_v = 1/12$ (along with its higher harmonics) corresponding to a spin-valley symmetric phase with 12 degenerate Fermi pockets produced by trigonal warping (denoted as $\text{Sym}(12)_-$; see schematics on top). Upon further doping, we observed a Fourier transform peak at $f_v = 1$ ($-4 < n < -3 \times 10^{11} \text{ cm}^{-2}$). It corresponds to a spin-valley polarized phase to one single flavor; denoted $\text{FP}(1)_-$. Then we come to the spin-valley symmetric phase $\text{Sym}(12)_-$ again ($-6.2 < n < -4 \times 10^{11} \text{ cm}^{-2}$). Further hole doping, BLG transitions into another phase with two frequency peaks at $f_v^{(1)} < 1/2$ and $f_v^{(2)} < 1/12$ such that $f_v^{(1)} + f_v^{(2)} = 1/2$. This phase can be identified as a spin-valley flavor-polarized phase—denoted $\text{FP}(2,2)_-$ —with two majority ($f_v^{(1)} < 1/2$) and two minority ($f_v^{(2)} < 1/12$) flavors. The resemblance

between our $D < 0$ data and hBN-encapsulated BLG [55] suggests that SOC does not play a major role for $D < 0$.

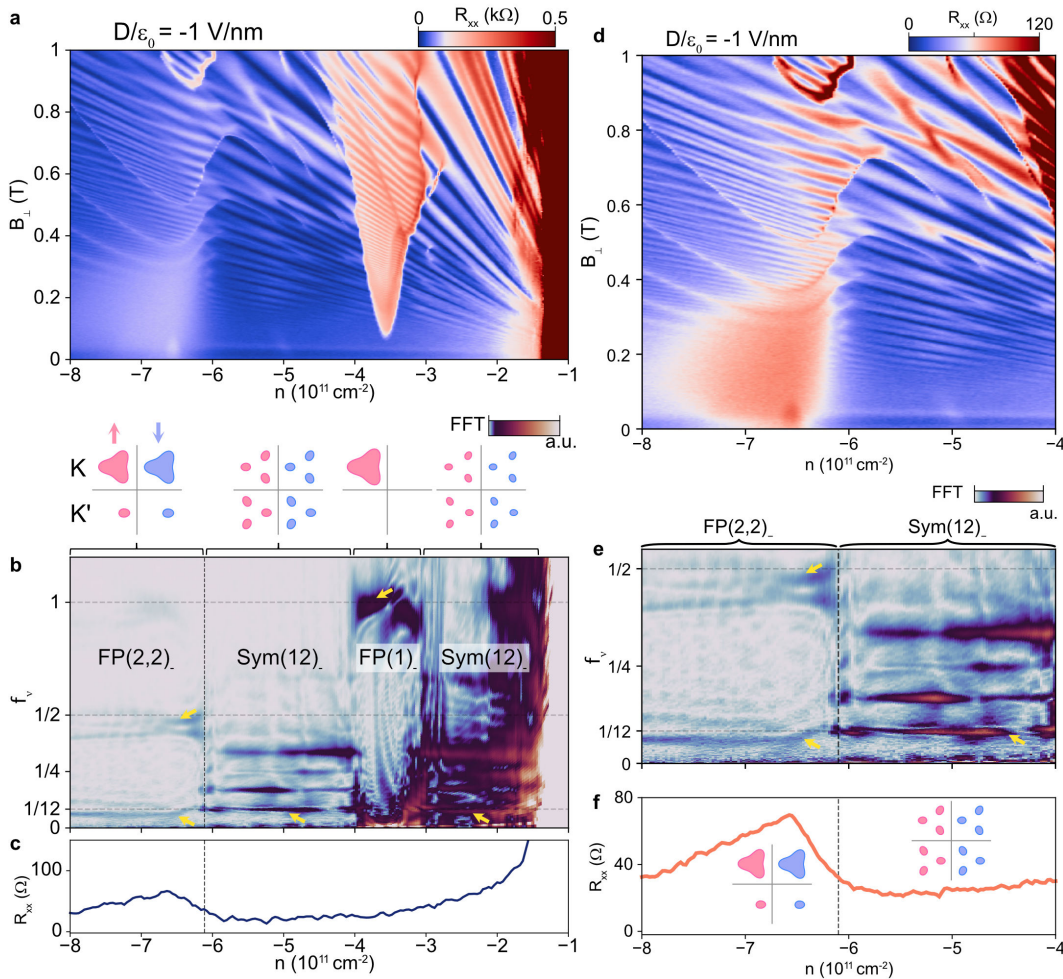


Figure 5.10: Fan diagram and Fermi surfaces at $D/\epsilon_0 = -1$ V/nm. (a) R_{xx} versus B_{\perp} and doping density n for $D/\epsilon_0 = -1$ V/nm. (b) Fourier transform of $R_{xx}(1/B_{\perp})$ versus n and f_v for $D/\epsilon_0 = -1$ V/nm. The schematics on top show the corresponding symmetry-breaking Fermi surfaces. (c) R_{xx} versus doping density n for the same density range. (d-f) The same data as the one in (a)-(c), but zoom in certain density ranges.

At $D/\epsilon_0 = 1$ V/nm (Fig. 5.11), where the wavefunctions are strongly polarized toward WSe $_2$, we see a few notable differences that suggests the presence of Ising SOC. First, at lowest densities ($-2 < n < -1 \times 10^{11}$ cm $^{-2}$), we observed a frequency peak at $f_v = 1/6$. The result is consistent with Ising-induced spin imbalance: within each valley, only three trigonally warped pockets from one flavor are filled, thus the phase in total has six small equal sized pockets, denoted FP(6) $_{+}$ (Fig. 5.11d). Second, at slightly higher densities ($-5 < n < -4.3 \times 10^{11}$ cm $^{-2}$), one of the Fourier

frequency peaks clearly appears below $f_v = 1/12$, suggesting the existence of Fermi surfaces whose occupancy is smaller relative to $\text{Sym}(12)_-$. As we can identify two independent frequencies in this region, we denote this phase as $\text{FP}(6, 6)_+$, with six bigger and six smaller Fermi pockets (Fig. 5.11e). The explicit flavor polarization here of the two phases likely originates from spin-orbit induced band splitting. Additionally, the transition between the $\text{FP}(6, 6)_+$ phase and the adjacent $\text{FP}(2, 2)_+$ phase (with two big and two small Fermi pockets) occurs at a lower hole density of $|n| = 5 \times 10^{11} \text{ cm}^{-2}$.

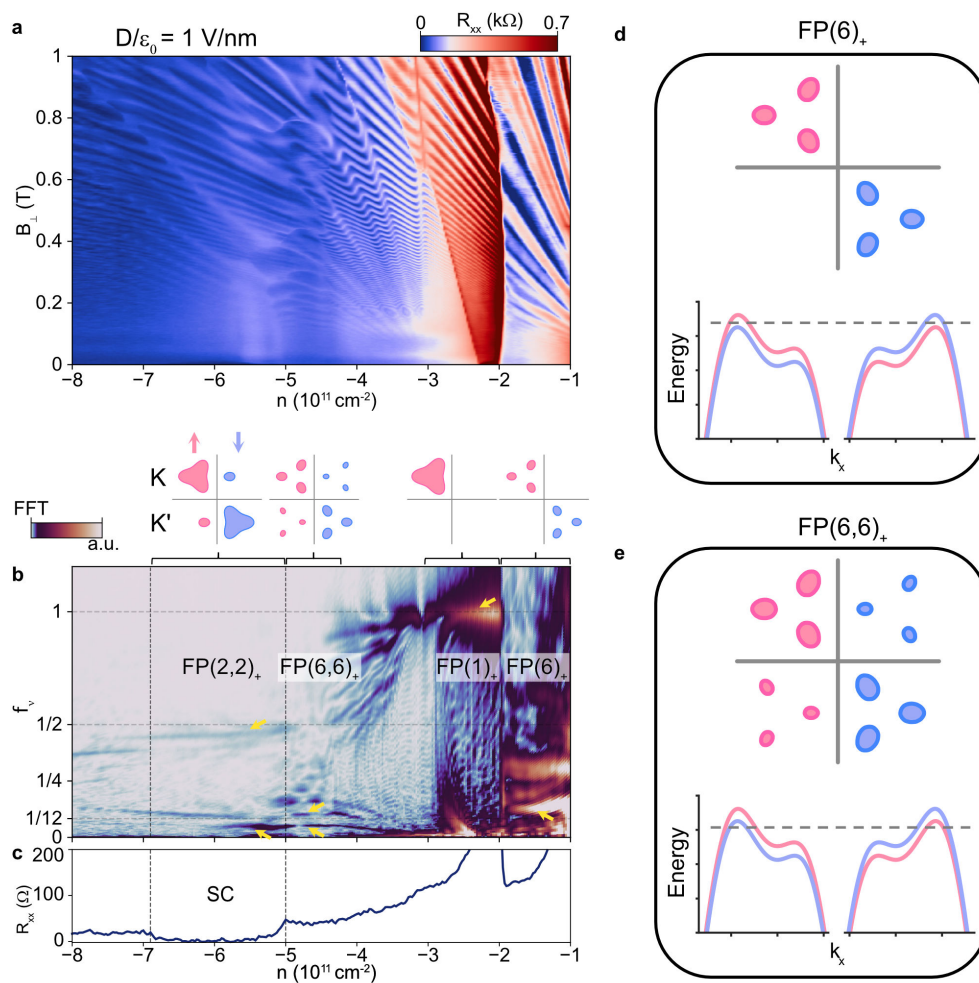


Figure 5.11: Fan diagram and Fermi surfaces at $D/\epsilon_0 = 1 \text{ V/nm}$. (a) R_{xx} versus B_{\perp} and doping density n for $D/\epsilon_0 = 1 \text{ V/nm}$. (b) Fourier transform of $R_{xx}(1/B_{\perp})$ versus n and f_v for $D/\epsilon_0 = 1 \text{ V/nm}$. The schematics on top show the corresponding symmetry-breaking Fermi surfaces. (c) R_{xx} versus doping density n for the same density range. (d),(e) Fermi level and Fermi surfaces of the $\text{FP}(6)_+$ (d) and the $\text{FP}(6, 6)_+$ (e) phase.

Finally, we observe that superconductivity is established throughout the $\text{FP}(2, 2)_+$

phase (except a small region where it competes with the resistive phase) ending on the high doping side with the onset of another complex flavor-polarized phase characterized by the occurrence of additional frequency peaks (Fig. 5.12b). Importantly, in $\text{FP}(2, 2)_+$, as for $\text{FP}(2, 2)_-$, we find that $f_v^{(1)} + f_v^{(2)} = 1/2$. Given the non-interacting band structure of Fig. 5.9, this observation implies that the carriers in each minority flavor are spontaneously polarized to one of the trigonally warped pockets—pointing toward nematic order [181, 182] (schematics in Fig. 5.12c).

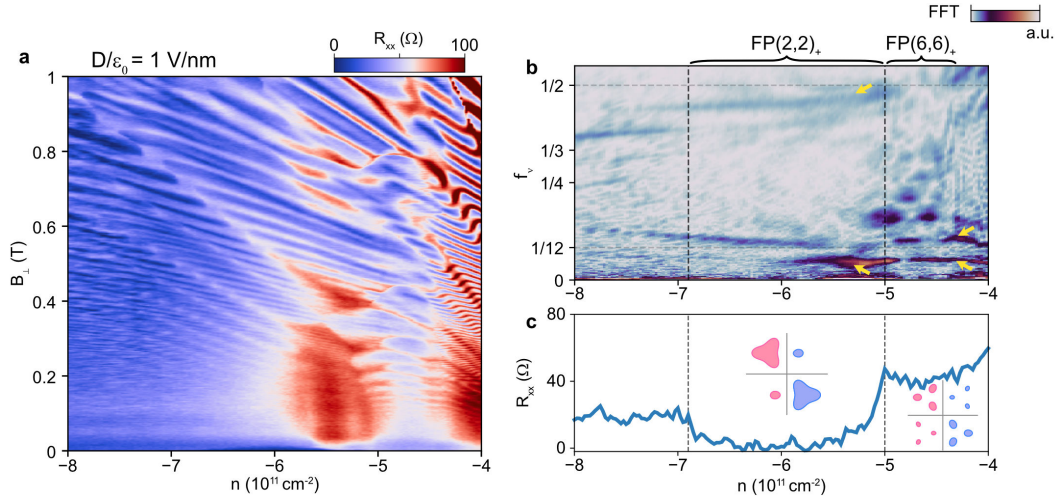


Figure 5.12: Zoomed-in Fan diagram and Fermi surfaces at $D/\epsilon_0 = 1$ V/nm. (a) R_{xx} versus B_{\perp} and doping density n for $D/\epsilon_0 = 1$ V/nm. (b) Fourier transform of $R_{xx}(1/B_{\perp})$ versus n and f_v for $D/\epsilon_0 = 1$ V/nm. (c) R_{xx} versus doping density n for the same density range. The schematics show the corresponding symmetry-breaking Fermi surfaces.

5.6 Doping-dependent Pauli-limit violation

In-plane magnetic field measurements further illuminate the unconventional nature of superconductivity in BLG-WSe₂ (Fig. 5.13). Figure 5.13a shows R_{xx} as a function of density n and in-plane magnetic field B_{\parallel} for the superconducting region (dark blue) at $D/\epsilon_0 = 1.1$ V/nm. When approaching the superconductivity from low densities $|n|$, the in-plane critical field $B_{c\parallel}$ quickly reaches a maximum near the phase boundary separating $\text{FP}(2, 2)_+$ and $\text{FP}(6, 6)_+$, and then slowly decreases with further hole doping. Conversely, the critical temperature measured at zero B_{\parallel} field, T_c^0 (red open circles), shows a more symmetric dome shape with a maximum at higher $|n|$. The interplay between $B_{c\parallel}$ and T_c^0 suggests that the violation of the Pauli limit ($B_p = 1.86 \text{ T/K} \times T_c^0$ for a weak-coupling spin-singlet BCS superconductor with g -factor $g = 2$) varies with doping.

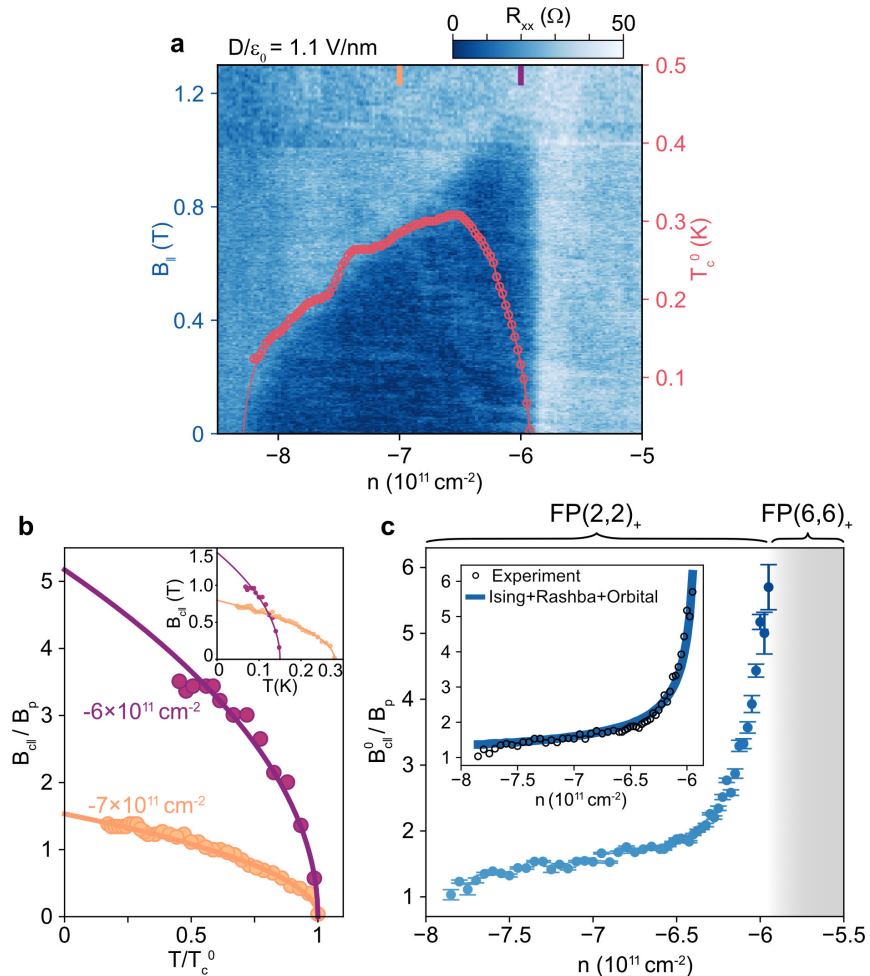


Figure 5.13: Doping-dependent Pauli-limit violation. (a) R_{xx} versus in-plane magnetic field B_{\parallel} and doping density n for $D/\epsilon_0 = 1.1$ V/nm. The red line delineates the T -dependent superconducting dome, and open circles indicate the zero-magnetic-field critical temperature T_c^0 that is defined by the temperature at which R_{xx} is 50% of the normal state resistance. (b) The ratio of in-plane critical magnetic field $B_{c\parallel}$ to the Pauli-limit field $B_p = 1.86$ T/K $\times T_c^0$ is plotted as a function of normalized temperature T/T_c^0 at two doping densities $n = -6 \times 10^{11}$ cm^{-2} and -7×10^{11} cm^{-2} . Inset: the same data as in the main panel but plotted in $B_{c\parallel}$ versus T . (c) Pauli violation ratio $B_{c\parallel}^0/B_p$ as a function of density n . The doping trend of the PVR is well captured by a model (blue line in the inset) taking into account fixed Ising SOC together with doping-dependent Rashba SOC and constant orbital depairing.

As an example, Fig. 5.13b shows $B_{c\parallel}/B_p$ as a function of temperature (T normalized to T_c^0) at two representative densities. Both curves are well-fit by the phenomenological relation $T/T_c^0 = 1 - (B_{c\parallel}/B_{c\parallel}^0)^2$ (solid lines; $B_{c\parallel}^0$ denotes the critical field at zero temperature). However, they show distinct Pauli violation ratios (PVR) $B_{c\parallel}^0/B_p$: for

high $|n|$ (orange curve, $n = -7 \times 10^{11} \text{ cm}^{-2}$), $B_{c\parallel}^0/B_p \approx 1.5$ which is close to the ratio expected from weak coupling BCS theory. The purple curve ($n = -6 \times 10^{11} \text{ cm}^{-2}$), however, shows $B_{c\parallel}^0/B_p \approx 5$, strongly violating the Pauli limit. Overall the PVR changes from roughly six to one as the doping is increased (Figure 5.13c). Note that the PVR values at the phase boundaries represent a lower limit due to possible imperfect in-plane alignment of the sample during the measurement.

The large PVR of $B_{c\parallel}/B_p \sim 6$ on the low hole doping side of the superconducting dome evokes the phenomenology of Ising superconductivity observed in transition metal dichalcogenides [9, 100, 101]. Ising superconductivity refers to a scenario in which pairing connects time-reversed states, e.g., $|\mathbf{k}, \uparrow\rangle$ and $|\mathbf{-k}, \downarrow\rangle$, with spins oriented along a fixed quantization axis selected by Ising SOC. Here $\lambda_I \approx 0.7 \text{ meV}$ —estimated in the Section 5.3—far exceeds $\Delta = 1.76k_B T_C \approx 0.02 \text{ meV}$ estimated from weak-coupling BCS scaling. The resulting Cooper pairs enjoy resilience against in-plane fields that rotate the spins away from this preferred axis, naturally leading to significant Pauli-limit violation as measured on the low hole doping side of the dome. The substantial PVR reduction for higher hole doping is more puzzling and implies that the ground state cannot evolve into a predominantly spin or spin-valley polarized phase. This reduction could emerge from a doping-dependent change in the flavor polarization of the parent $\text{FP}(2, 2)_+$ state or in-plane depairing effects (or the interplay between the two).

As proof of concept, we consider a simple model that incorporates two depairing mechanisms: Rashba SOC (which favors in-plane spin orientation) and orbital in-plane magnetic field effects—both of which compete with the Ising SOC and suppress the PVR. A final form of the a self-consistent superconducting gap equation is:

$$\ln\left(\frac{T_c}{T_c^0}\right) + \Phi(\rho_-, \tilde{\chi}_0) + \Phi(\rho_+, \tilde{\chi}_0) - \frac{\tilde{\mathbf{p}}_+ \cdot \tilde{\mathbf{p}}_-}{|\tilde{\mathbf{p}}_+||\tilde{\mathbf{p}}_-|} [\Phi(\rho_-, \tilde{\chi}_0) - \Phi(\rho_+, \tilde{\chi}_0)] = 0, \quad (5.3)$$

where $\tilde{\chi}_0 = -\tilde{g}_{\text{orb}}\mu_B B_{\parallel}/2\pi T_c$ ($\tilde{g}_{\text{orb}} \equiv g_{\text{orb}}(k_F + k_{0,y})$ denotes a characteristic scale for the orbital depairing), $\tilde{\mathbf{p}}_{\pm} = (\pm g_R k_F/2 + \mu_B B_{\parallel}, \mp g_R k_F/2, \pm g_I/2)$, and $\rho_{\pm} = (|\tilde{\mathbf{p}}_+| \pm |\tilde{\mathbf{p}}_-|)/2\pi T_c$. The function $\Phi(\rho, \tilde{\chi}_0)$ is defined in terms of the digamma function $\psi(z)$ as

$$\Phi(\rho, \tilde{\chi}_0) = \frac{1}{4} \left\{ \text{Re} \left[\psi \left(\frac{1+i\rho}{2} + i\tilde{\chi}_0 \right) - \psi \left(\frac{1}{2} \right) \right] + \text{Re} \left[\psi \left(\frac{1+i\rho}{2} - i\tilde{\chi}_0 \right) - \psi \left(\frac{1}{2} \right) \right] \right\}. \quad (5.4)$$

We plotted the solution either with only Rashba term or with only orbital depairing term in Fig. 5.14. The in-plane critical field is suppressed by either of them. The

solution to the model Eq. 5.3 can capture the observed PVR evolution (Fig. 5.13c inset) provided that the effective Rashba spin splitting increases with hole density, which may be expected if superconductivity arises from minority Fermi pockets that grow with hole doping and the Rashba term follows $g_R k_F$, with k_F increasing accordingly.

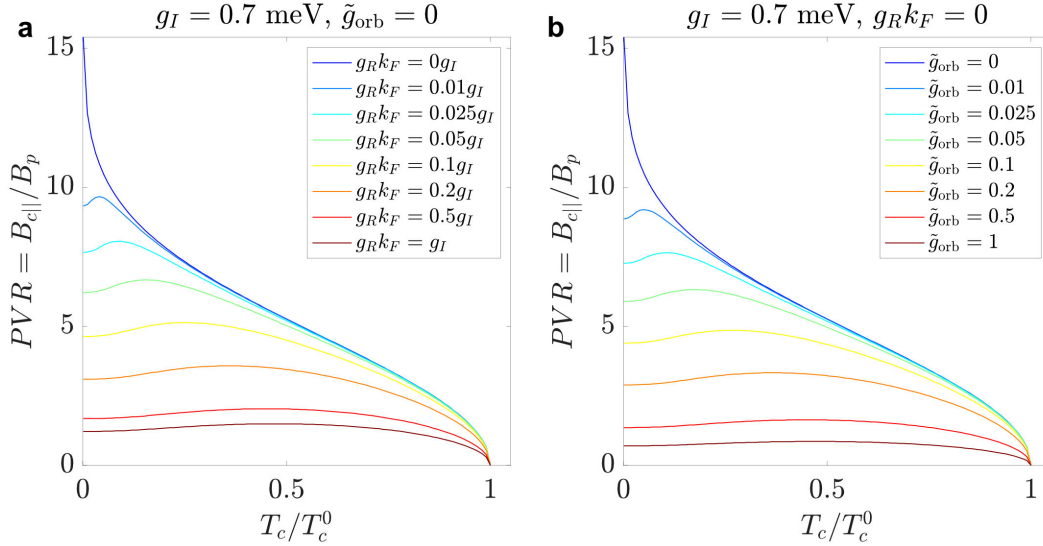


Figure 5.14: Depairing model for doping-dependent Pauli violation ratio. (a),(b) Pauli violation ratio expected in a system with: Ising g_I and Rashba $g_R k_F$ coupling (a), Ising g_I and orbital \tilde{g}_{orb} coupling (b). Note that \tilde{g}_{orb} is a dimensionless quantity: the corresponding orbital energy scale is $\tilde{g}_{\text{orb}} \mu_B B$.

5.7 Discussion

The extended superconducting phase space in BLG-WSe₂ clearly contrasts observations in hBN-encapsulated bilayer and trilayer graphene [54, 55], where superconductivity occurs only within a narrow density range around the symmetry-broken phase boundaries. Moreover, the coincidence of the doping range exhibiting superconductivity with the FP(2, 2)₊ phase (Fig. 5.12) at $D > 0$ strongly hints that (i) superconductivity descends from the latter broken-symmetry parent state and (ii) SOC plays a key role in selecting a symmetry-breaking order conducive to pairing. These observations constrain the possible mechanisms that can lead to T_c enhancement [183, 184]. Figure 5.15c depicts a phenomenologically motivated scenario wherein multiple nearly degenerate broken-symmetry orders compete. If the FP(2, 2)₊ phase is, e.g., valley polarized in the absence of SOC, then broken inversion and time-reversal symmetries would heavily disfavor pairing—consistent with

the absence of superconductivity in BLG-WSe₂ at $D < 0$ and hBN-encapsulated BLG at zero magnetic field [55]. Turning on Ising SOC could then tip the balance in favor of orders that facilitate Cooper pairing. One candidate for this parent state is a primarily spin-valley polarized phase arising due to an interaction-enhanced Ising SOC strength (Fig. 5.15a); however, superconductivity emerging from such a state would exhibit a much larger Pauli-limit violation, which would vary far less with doping. We suggest instead that Ising SOC can promote inter-valley coherent (IVC) order that is also amenable to pairing while maintaining compatibility with observed trends (Fig. 5.15b).

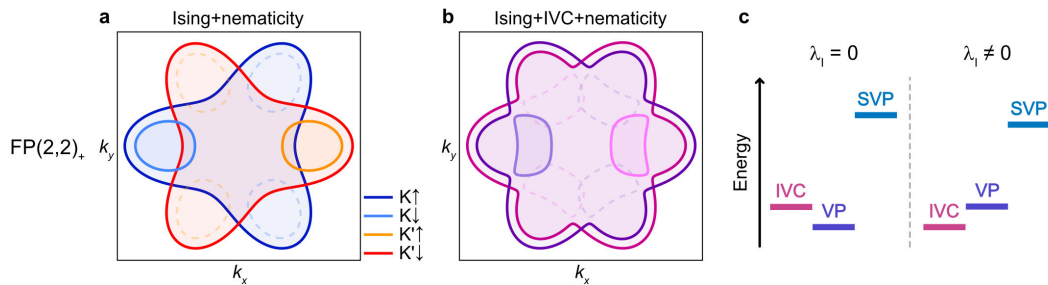


Figure 5.15: Ground state selection by Ising SOC. (a),(b) Fermi surfaces of the FP(2, 2)₊ phase with Ising SOC and nematic order (a), or allowing for inter-valley coherent order (b). Dashed Fermi pockets correspond to the condition that nematic order is absent. (c) Schematics of a proposed scenario where Ising SOC tilts the energy balance toward IVC order, within which the development of superconductivity is more favored, at the expense of a state which is not conducive to pairing, e.g., a valley polarized state.

The crystalline nature of BLG offers high reproducibility of superconductivity at zero-magnetic field. We made multiple devices showing similar behaviors, an example of which is in Fig. 5.16. Similar to the previous study, the new device also shows zero-magnetic-field enhanced superconductivity ($T_c \sim 200$ mK; can be higher, see Chapter 6) in a wide density range. Key differences are that superconductivity onsets at larger D fields ($D/\epsilon_0 \gtrsim 0.9$ V/nm) and the flavor-polarized phase hosting superconductivity appears to have multiple (four) minority Fermi pockets together with two majority pockets (denoted as FP(2,4)₊). The variations of the correlated phases among different devices could originate from ground state selection by Ising SOC of different magnitudes, i.e., the second device here has Ising SOC $\lambda_I \approx 1.6$ meV, stronger than $\lambda_I = 0.7$ meV for the previous device. The variation of SOC for different devices originates from the alignment between BLG and WSe₂; see Chapter 6 for the tunability of Ising SOC by interfacial angle twisting.

The nature of superconductivity in graphene-based systems—both moiré and crystalline [185–191]—presents an ongoing puzzle. The enticing general similarity between BLG-WSe₂ and moiré graphene superlattices [16, 44, 45, 48, 49] can be noticed, as in both systems superconductivity appears intimately connected to the symmetry-broken state in which two out of four spin-valley flavors are predominately populated. Future efforts are needed to address the origin of apparent striking distinctions between different superconducting phases in graphene systems. Finally, induced SOC [173–175] along with other parameters such as virtual tunneling [184] depends on the relative orientation of WSe₂ (or other TMDs) and graphene, and is thus tunable—providing a rich landscape for further explorations.

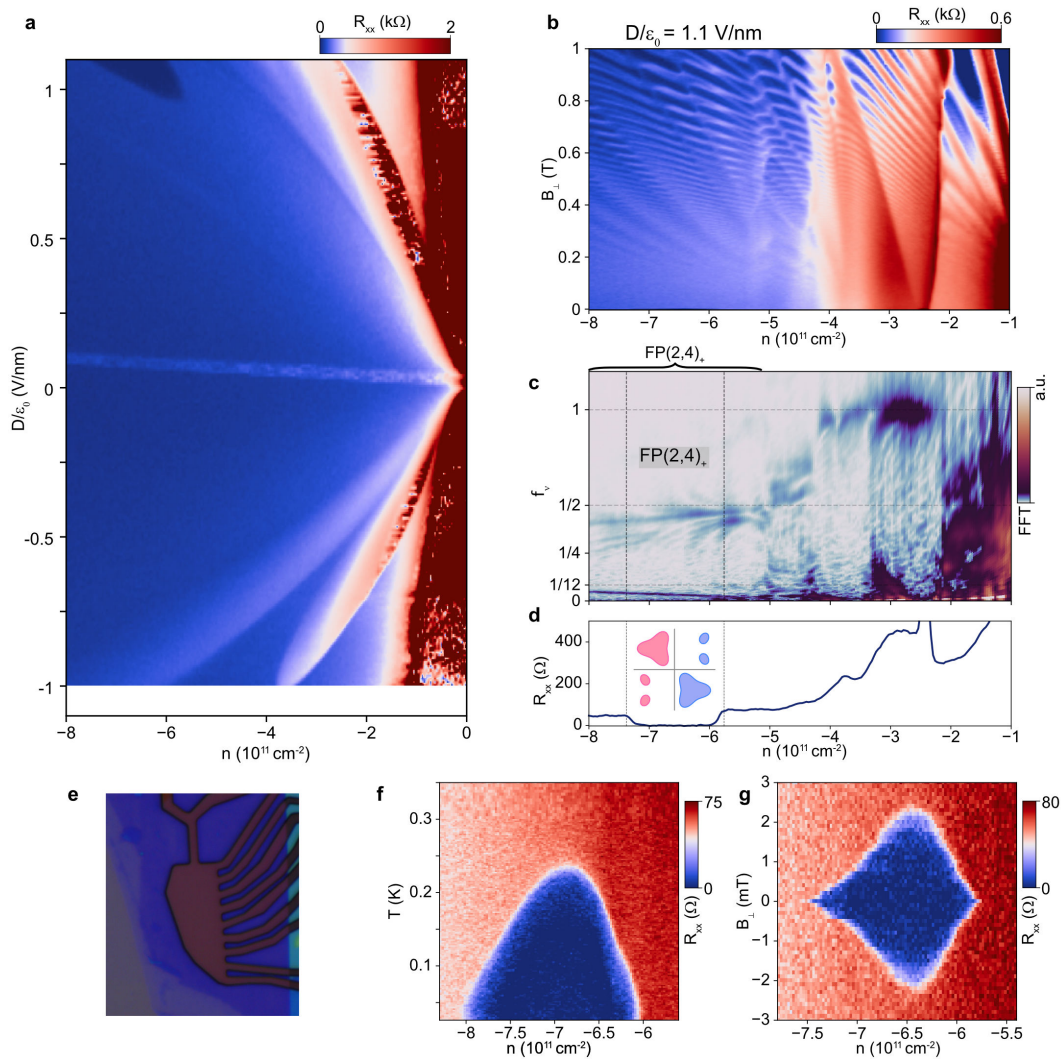


Figure 5.16: Additional device with different Ising SOC. (a) R_{xx} versus doping density n and displacement field D measured at zero magnetic field for an additional device. (b) R_{xx} versus B_{\perp} and doping density n for $D/\epsilon_0 = 1.1$ V/nm. (c) Fourier transform of $R_{xx}(1/B_{\perp})$ versus n and f_v for $D/\epsilon_0 = 1.1$ V/nm. (d) R_{xx} versus n at zero magnetic field for the same D field. The superconducting phase possesses a flavor-polarized normal state with two majority and four minority Fermi pockets (denoted as $FP(2,4)_+$). Schematic depicts the possible Fermi surface structures. (e) Device optical image. (f) R_{xx} versus density n and temperature showing a superconducting dome at $D/\epsilon_0 = 1.15$ V/nm. (g) R_{xx} versus n and B_{\perp} around the superconducting region for $D/\epsilon_0 = 1.1$ V/nm.

TWIST-PROGRAMMABLE SUPERCONDUCTIVITY IN SPIN-ORBIT COUPLED BILAYER GRAPHENE

We established that by placing WSe₂ adjacent to BLG, the system exhibits a *D*-asymmetric phase diagram, suggesting the important role of Ising SOC in defining the correlated phase diagram. More importantly, superconductivity is stabilized at zero magnetic field, and the critical temperature of which is an order of magnitude enhanced to $T_c \approx 300$ mK. We were only focusing on one BLG-WSe₂ device with Ising SOC strength of $|\lambda_I| = 0.7$ meV.

In this chapter, we employ a new fabrication technique: cut a large BLG flake into multiple pieces and sequentially twist them relative to the WSe₂ flake, forming different BLG-WSe₂ interfacial twist angles. The “moiréless” twist tunes the superconductivity together with other correlated orders in BLG-WSe₂. The precise alignment between the two materials systematically controls the strength of the induced Ising SOC, profoundly influencing the phase diagram.

As Ising SOC is increased, superconductivity onsets at a higher displacement field and features a higher critical temperature, reaching up to 0.5 K. Within the main superconducting dome and in the strong Ising SOC limit, we find an unusual phase transition characterized by a nematic redistribution of holes among trigonally warped Fermi pockets and enhanced resilience to in-plane magnetic fields. The behavior of the superconducting phase is well captured by our theoretical model, which emphasizes the prominent role of interband interactions between Fermi pockets arising due to interaction-enhanced symmetry breaking. Moreover, we identify two additional superconducting regions, one of which descends from an inter-valley coherent normal state and exhibits a Pauli-limit violation ratio exceeding 40, among the highest for all known superconductors. Our results provide essential insights into ultra-clean graphene-based superconductors and underscore the potential of utilizing moiréless-twist engineering across a wide range of van der Waals heterostructures.

6.1 Programmable Ising SOC by interfacial twisting between BLG and WSe₂

Theoretically, the induced SOC is predicted to depend on the relative twist angle θ between WSe₂ and graphene [173–175, 184, 192] (Fig. 6.1a).

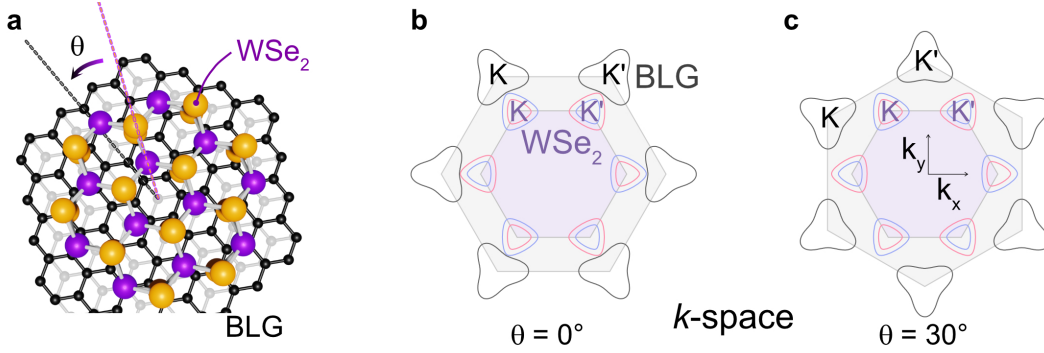


Figure 6.1: Schematics for interfacial twisting between BLG and WSe₂. (a) Schematic showing the twisting of the BLG-WSe₂ interface; tuning the interfacial twist angle θ between the two largely lattice-mismatched materials modifies the Ising SOC strength $|\lambda_I|$ and the correlated phase diagram. (b),(c) The schematics show the relative rotation between the BLG and WSe₂ Brillouin zones. At $\theta \approx 0^\circ$ (b), K/K' valleys of BLG couple more effectively to one of the two WSe₂ valleys, resulting in large induced Ising SOC. In contrast, at $\theta \approx 30^\circ$ (c), inter-valley and intra-valley tunneling between WSe₂ and BLG have the same amplitude by reflection symmetry so that Ising couplings of opposite sign cancel each other and result in vanishing proximity coupling.

Naively, graphene grabs SOC from WSe₂ from so called interlayer tunneling process [173, 184]. One can compute proximitized Ising SOC based on second-order perturbation theory of the microscopic interlayer tunneling and derive that:

$$\lambda_I = \frac{|V_{+\uparrow}^A|^2 - |\bar{V}_{+\uparrow}^A|^2}{W} - \frac{|V_{+\downarrow}^A|^2 - |\bar{V}_{+\downarrow}^A|^2}{W + \delta}. \quad (6.1)$$

Here, W denotes the energy difference between the BLG and WSe₂ valence band edge differences, while δ denotes the Ising SOC splitting strength in WSe₂, in the range of ~ 500 meV. $V_{\tau_s}^\sigma$ is the tunneling strength for the intra-valley process (i.e., graphene K valley to WSe₂ K valley), and $\bar{V}_{\tau_s}^\sigma$ is the tunneling strength for the inter-valley process (i.e., graphene K valley to WSe₂ K' valley). We shall see from Eq. 6.1, to boost the proximitized Ising SOC, less energy difference W between the band edges of graphene and TMD would favor stronger Ising SOC; obviously stronger intrinsic Ising δ would also serve the role. The two parameters are fixed by the material like WSe₂. However, by tuning the twist angle between graphene and WSe₂ (Fig. 6.1a), the proximitized Ising SOC is in principle tunable. Recall that the proximitized Ising (Eq. 6.1) depends on the interplay between intra-valley and inter-valley process $V_{\tau_s}^\sigma$ and $\bar{V}_{\tau_s}^\sigma$. Starting with a special twist angle $\theta = 30^\circ$ (Fig. 6.1c), the graphene K/K' valley is in the middle of K and K' valley of WSe₂,

i.e., the graphene valleys are equal momentum distance to the WSe₂ valleys. Due to the reflection symmetry $R_y: (x, y, z) \rightarrow (x, -y, z)$, the $|\bar{V}_{\tau_s}^\sigma|$ is the same as $|V_{\tau_s}^\sigma|$, which yields $\lambda_I = 0$ from Eq. 6.1; the result simply comes from symmetry. In contrast, for $\theta = 0^\circ$ (Fig. 6.1b), the inter-valley and intra-valley tunneling strengths are clearly asymmetric, which yields finite proximitized Ising SOC.

This angle dependence, however, has not been experimentally studied or utilized with systematic control. Here we employ this novel tuning knob to explore how Ising SOC modifies the correlated phases and emerging superconductivity in BLG. This approach offers several unique opportunities for exploring the properties of ultra-clean and highly tunable superconductors: (i) the strength of the induced Ising SOC in BLG can be precisely quantified, essential for developing theoretical understanding; (ii) the induced SOC is much less sensitive to twist-angle variations compared to moiré systems, allowing for fine control of SOC; and (iii) the proximity to WSe₂ does not induce additional disorder, making experimental insights highly reproducible.

We invented a new twisting scheme, where multiple devices with different twist angles are formed between the graphene/WSe₂ interface. Large flakes of BLG and WSe₂ are exfoliated on SiO₂/Si chips. The crystal orientation of WSe₂ can be identified by second harmonic generation [193] (SHG; Fig. 6.2b), where the directions with maximized SHG signal correspond to the in-plane crystal orientations along the W-Se direction. BLG is somewhat trickier. We identify flakes with long straight edges forming angles that are multiple of 30°, e.g., three edges form two angles of 150° in Fig. 6.2c. The configuration is consistent with the assignment that the straight edges are along the zigzag- or armchair-edge direction of graphene.

After the identification of crystal edges, we attempt to form multiple continuous twisting devices from the same BLG and WSe₂ crystal. We cut the large BLG flake into small pieces [116]; Fig. 6.2d. First, pick up topmost hBN, top graphite gate, top hBN dielectric, and the large WSe₂ flake using PC film on a PDMS. Then, align the straight edge of BLG with the crystal orientation of WSe₂ and control the approach of PC/PDMS stamp so that only one BLG piece is picked up. SiO₂/Si chip was manually rotated by an angle $\theta \sim 6^\circ$, and a second piece of BLG was picked up but not overlapping with the first one. Repeat the same processes for the remaining BLG pieces (Fig. 6.3b,c). Depending on whether the BLG straight edge used for alignment is along the zigzag or armchair direction, the crystal axes of the six BLG pieces are rotated relative to the WSe₂ axis by an angle $\theta \sim 0^\circ, 6^\circ, 12^\circ, 18^\circ, 24^\circ$, and

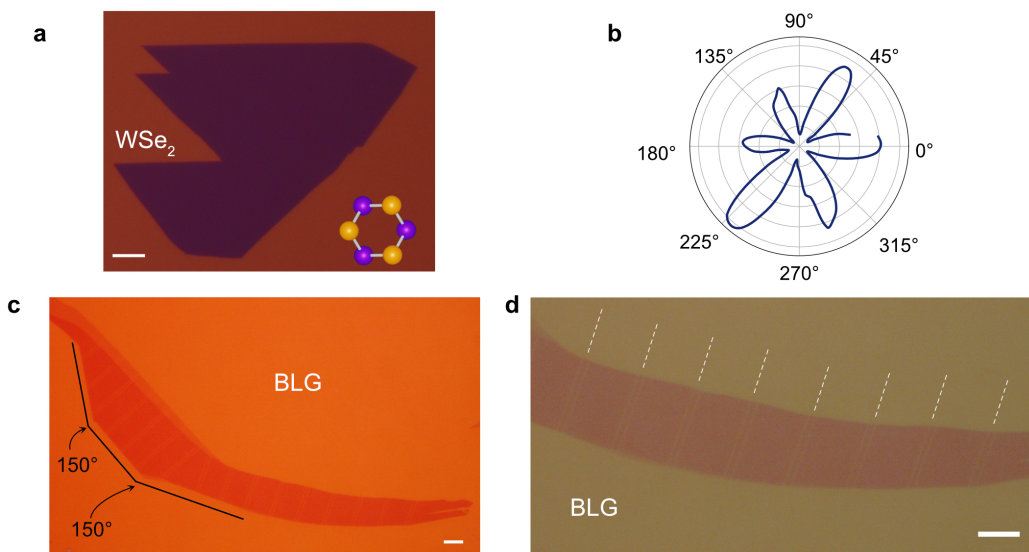


Figure 6.2: Identifying the crystal edges of graphene and WSe₂. (a) Optical image of a WSe₂ crystal. (b) Second harmonic generation for the WSe₂ flake shown in (a). (c) Optical image of a large BLG flake. Straight edges form angles 150° that are consistent with the three straight edges being along zigzag- or armchair-edge direction. (d) Zoom-in image of the BLG in (c), showing small BLG pieces that are separated by atomic-force-microscope-actuated cutting. All the scale bars correspond to 10 μm.

30° (armchair direction), or vice versa (zigzag direction). The two configurations can be distinguished by measuring the Ising SOC strength of the devices at the two ends. The large (small) Ising device corresponds to $\sim 0^\circ$ ($\sim 30^\circ$) alignment due to the reflection symmetry [173–175, 184]. A typical finished stack is shown in Fig. 6.3d; a series of different rotation angles between BLG and WSe₂ can be clearly seen from the optical image. The stack went through standard lithographic and etching processes for final device preparation (Fig. 6.3e).

To characterize the SOC in our devices, we first perform high-resolution measurements of Shubnikov–de Haas oscillations (Fig. 6.4c,d) in regions of the n - D phase diagram (n is the doping density, D is the electrical displacement field) that are well-described by non-interacting theory. When a positive D field $D/\epsilon_0 = 0.2$ V/nm is applied, the hole-carrier wavefunctions are strongly polarized toward the top graphene layer adjacent to WSe₂, which in turn induces Ising SOC in BLG [56, 122, 129, 194]. For this D field, Ising SOC is already maximal, i.e., larger D values do not further increase the Ising SOC strength (see Fig. 6.5 for further discussion). In this regime, we observe a clear beating pattern in longitudinal resistance

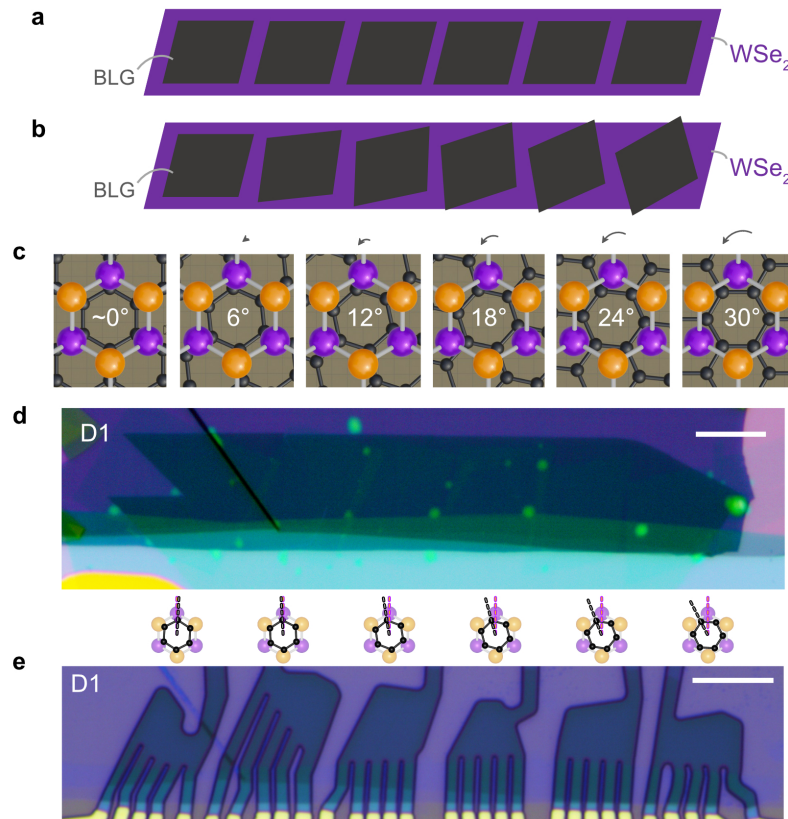


Figure 6.3: Fabricating twisting BLG-WSe₂ on the same chip. (a)-(c) Flake transferring processes for the continuous interfacial twisting. The BLG pieces are sequentially picked up with an angle relative to WSe₂ in increment of 6°, from ~0° to 30°. (d) Optical image of the twisting stack, clearly showing that the BLG pieces form different twist angles relative to the WSe₂ crystal. (e) Optical image of the finished device set D1. All the scale bars correspond to 10 μ m.

R_{xx} as a function of out-of-plane magnetic field (B_{\perp}) at higher doping densities (Fig. 6.4c), indicating two close oscillation frequencies originating from Fermi pockets of slightly different sizes. To quantitatively analyze this Fermi-surface imbalance, we normalize the oscillation frequencies of $R_{xx}(1/B_{\perp})$ to the Luttinger volume corresponding to the total doping density. The resulting normalized frequency f_v reveals the fraction of the total Fermi surface area enclosed by a cyclotron orbit. Figures 6.4e,f show an example comparison of the density-dependent frequencies f_v from two devices with twist angles $\theta \approx 0^\circ$ and 30° , respectively. In both cases, two frequencies ($f_v^{(1)}$ and $f_v^{(2)}$) are found satisfying $f_v^{(1)} + f_v^{(2)} = 1/2$. These frequencies can be understood as a splitting from $f_v = 1/4$, which signals the broken four-fold spin-valley symmetry, and are a direct measure of how the Ising

SOC modifies the single-particle band structure (Fig. 6.4a,b). Due to Ising SOC, nominally four-fold degenerate bands separate into two pairs of spin-valley locked bands with slightly different Fermi-surface areas (illustrated in insets of Fig. 6.4e,f).

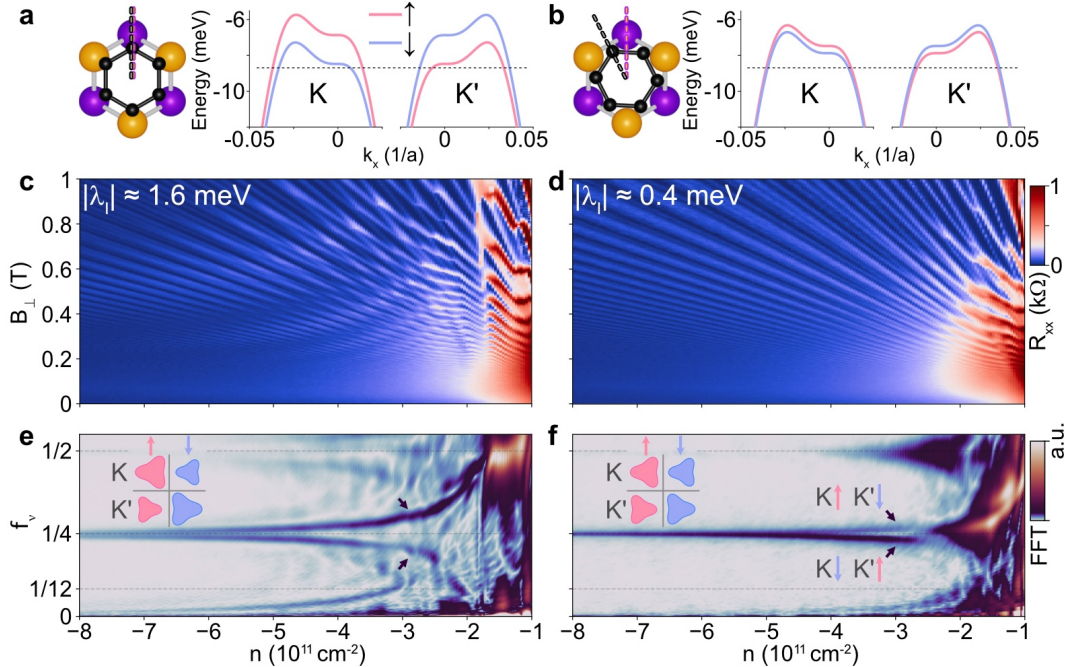


Figure 6.4: Tunable Ising SOC by twisting between BLG and WSe₂. (a),(b) Non-interacting valence bands of BLG near the K and K' points of the Brillouin zone at $D/\epsilon_0 = 0.2$ V/nm, with proximitized Ising SOC $|\lambda_I| \approx 1.6$ meV (a) and 0.4 meV (b), respectively. (c),(d) R_{xx} versus out-of-plane magnetic field B_{\perp} and doping n measured at $D/\epsilon_0 = 0.2$ V/nm for devices with $|\lambda_I| \approx 1.6$ meV (c) and 0.4 meV (d), respectively. (e),(f) Fast Fourier transform (FFT) of $R_{xx}(1/B_{\perp})$ versus n and f_v , where f_v denotes the quantum oscillation frequency normalized to the Luttinger volume. The arrow-marked FFT splittings reflect the Ising-induced Fermi-surface imbalance within each valley, where larger Ising SOC (e) features a larger splitting than small Ising SOC (f).

We can now confirm experimentally that the induced Ising SOC is modulated by the twist angle θ between WSe₂ and BLG. This is evident from the more pronounced splitting shown in Fig. 6.4e compared to the one in Fig. 6.4f. Fig. 6.5b,c shows the doping-dependent FFT splitting B_{split} measured at different D fields within the non-interacting phase (schematics in Fig. 6.4e,f). Ising-type splitting is suppressed with increasing $|n|$, in contrast to Rashba-type splitting which increases with increasing $|n|$ [56]. The detailed mapping of B_{split} as a function of n and D enables comparison to single-particle band structure calculation that quantifies Ising-induced Fermi surface imbalance. The dashed lines in Fig. 6.5b,c are calculated frequency splittings

for $|\lambda_I| \approx 1.4$ meV (Fig. 6.5b) and $|\lambda_I| \approx 0.4$ meV (Fig. 6.5c), respectively. Both cases roughly match the experimental data. The overall trend is that (i) at constant $|\lambda_I|$, higher D features larger B_{split} and (ii) at constant D , higher $|\lambda_I|$ features larger B_{split} . The observed trends put strong constraints on the estimates of the Ising SOC strength. Note that a single Ising SOC strength provides a good fit of the data at different D fields (from $D/\epsilon_0 = 0.2$ V/nm to 1 V/nm; Fig. 6.5b), suggesting that Ising SOC is already maximal at $D/\epsilon_0 = 0.2$ V/nm and larger D values do not further increase the Ising SOC strength. Thus we established that twisting BLG relative to WSe₂ indeed modifies the Ising SOC strength.

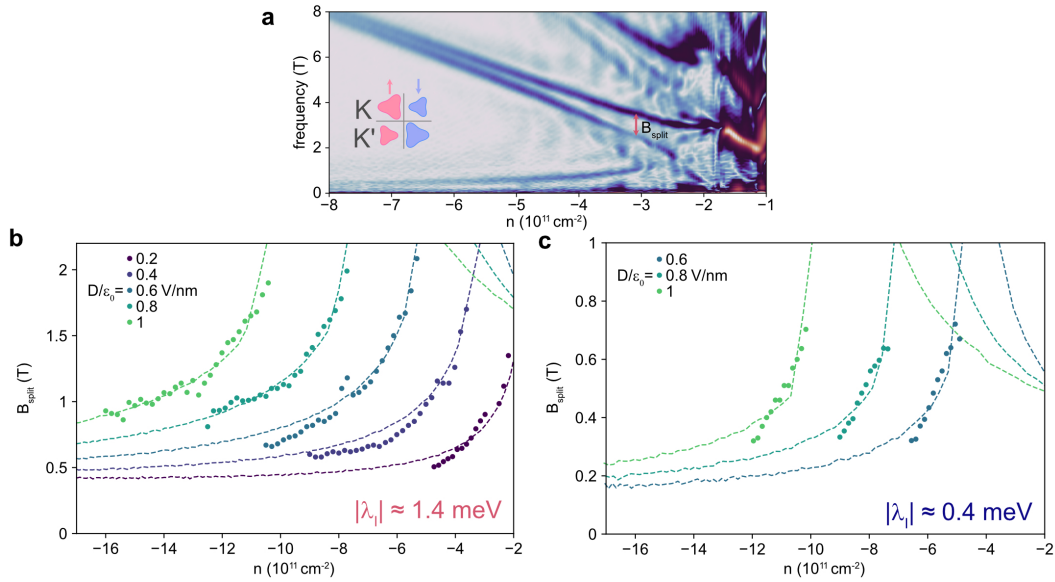


Figure 6.5: Quantifying Ising SOC by quantum oscillations. (a) The same data as the one in Fig. 6.4e, but without frequency normalization to show B_{split} . (b),(c) Experimental (dots) doping-dependent frequency splitting around $f_v = 1/4$ measured at different D fields for a large Ising device (b; $|\lambda_I| \approx 1.4$ meV) and a small Ising device (c; $|\lambda_I| \approx 0.4$ meV). The dashed lines are B_{split} calculated from single-particle band structure using the corresponding Ising SOC values.

Figure 6.6 summarizes systematic measurements across three sets of moiréless twisting BLG-WSe₂ devices (D1-D3), all of which demonstrate robust θ -modulated Ising SOC strengths. Our results are consistent with the picture that virtual interlayer tunneling is responsible for the induced SOC. When the lattices of BLG and WSe₂ are angle-aligned, i.e., $\theta \approx 0^\circ$, the K/K' valleys of BLG couple more effectively to one of the two valleys of WSe₂ (left schematic in Fig. 6.6), resulting in a large induced Ising SOC. In contrast, for $\theta \approx 30^\circ$, the inter-valley and intra-valley tunneling between WSe₂ and BLG have the same amplitude due to reflection symmetry (right

schematic in Fig. 6.6). The induced Ising SOC in BLG vanishes accordingly. The overall twist-angle dependence and the magnitude of Ising SOC are qualitatively consistent with predictions [173–175, 184, 192].

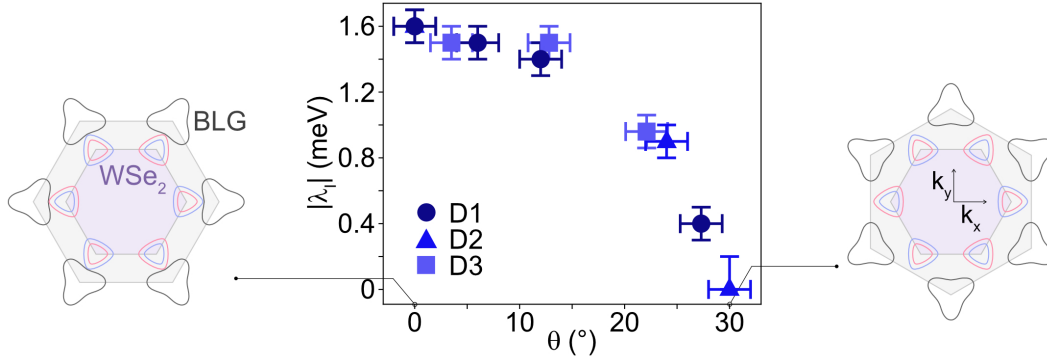


Figure 6.6: Ising SOC strength $|\lambda_I|$ versus BLG-WSe₂ interfacial twist angle θ ; data were extracted from three sets of devices D1-D3. The schematics show the relative rotation between the BLG and WSe₂ Brillouin zones. At $\theta \approx 0^\circ$, K/K' valleys of BLG couple more effectively to one of the two WSe₂ valleys, resulting in large induced Ising SOC. In contrast, at $\theta \approx 30^\circ$, inter-valley and intra-valley tunneling between WSe₂ and BLG have the same amplitude by reflection symmetry so that Ising couplings of opposite sign cancel each other and result in vanishing proximity coupling.

6.2 Twist-programmable superconducting phase diagram

Using the exquisite twist-angle control of the Ising SOC strength, we explore the SOC-dependent correlated phase diagrams occurring at large D fields. Devices with various Ising strengths all show characteristic R_{xx} features that are associated with strong correlations and superconductivity stabilized at zero magnetic field [56, 122, 194] (see Fig. 6.7 for all six n - D phase diagrams). Importantly, the main superconducting pocket, which emerges from a polarized state with a dominant population of two out of the four spin-valley flavors [56, 122], shows a strong dependence on the Ising SOC strength. For low Ising SOC ($|\lambda_I| \approx 0.4$ meV; Fig. 6.7a), the superconducting region occupies a large D field range, starting from $D/\epsilon_0 \approx 0.3$ V/nm and extending up to $D/\epsilon_0 \approx 1.25$ V/nm. For large Ising SOC ($|\lambda_I| \approx 1.5$ meV; Fig. 6.7e,f), however, superconductivity onsets only at $D/\epsilon_0 \approx 0.9$ V/nm. Overall, the value D_{onset} marking the onset of the superconducting pocket grows with increasing $|\lambda_I|$ (Fig. 6.8f).

This trend of D_{onset} can be understood as a consequence of interband interactions

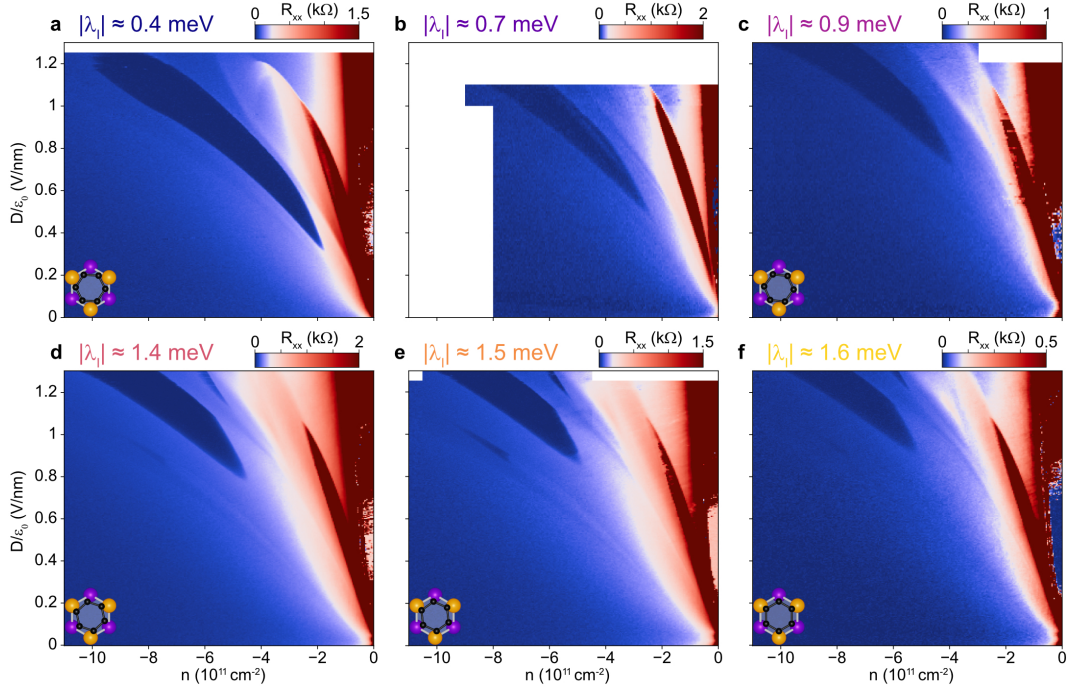


Figure 6.7: n - D phase diagrams for devices with various Ising SOC strengths. (a)-(f) R_{xx} versus doping density n and displacement field D for devices with Ising SOC strength $|\lambda_I| \approx 0.4$ meV (a), 0.7 meV (b), 0.9 meV (c), 1.4 meV (d), 1.5 meV (e), and 1.6 meV (f), respectively.

between the majority ($K \uparrow$, $K' \downarrow$) and the minority ($K \downarrow$, $K' \uparrow$) spin-valley flavors. The difference in hole populations between the majority and minority bands scales with $|\lambda_I|$ and is further enhanced by Coulomb interactions. Consequently, the region in the phase diagram where both bands have a large density of states (DOS) near the Fermi level is pushed toward higher values of D and n as Ising SOC is increased. The experimentally observed trend is well reproduced by a simple model that takes into account the pairing between majority and minority bands. We perform multiband-superconductivity calculations with polarized normal state and find that the residual Cooper-channel repulsion [195] (v_{TAM}^*) grows with increasing $|\lambda_I|$ and decreases at higher D fields (see Fig. 6.9). The majority-minority interactions that scatter electron pairs between the pair of bands, greatly enhance the screening of the bare repulsion compared to the single-band case. A larger density imbalance between the bands effectively suppresses this interaction, shifting D_{onset} to higher values. Note that the significant role of interband interactions in BLG-WSe₂ is in stark contrast to the case of moiré graphene [16, 44, 45, 48, 49], where superconductivity emerges from a polarized phase in the absence of majority and minority carriers.

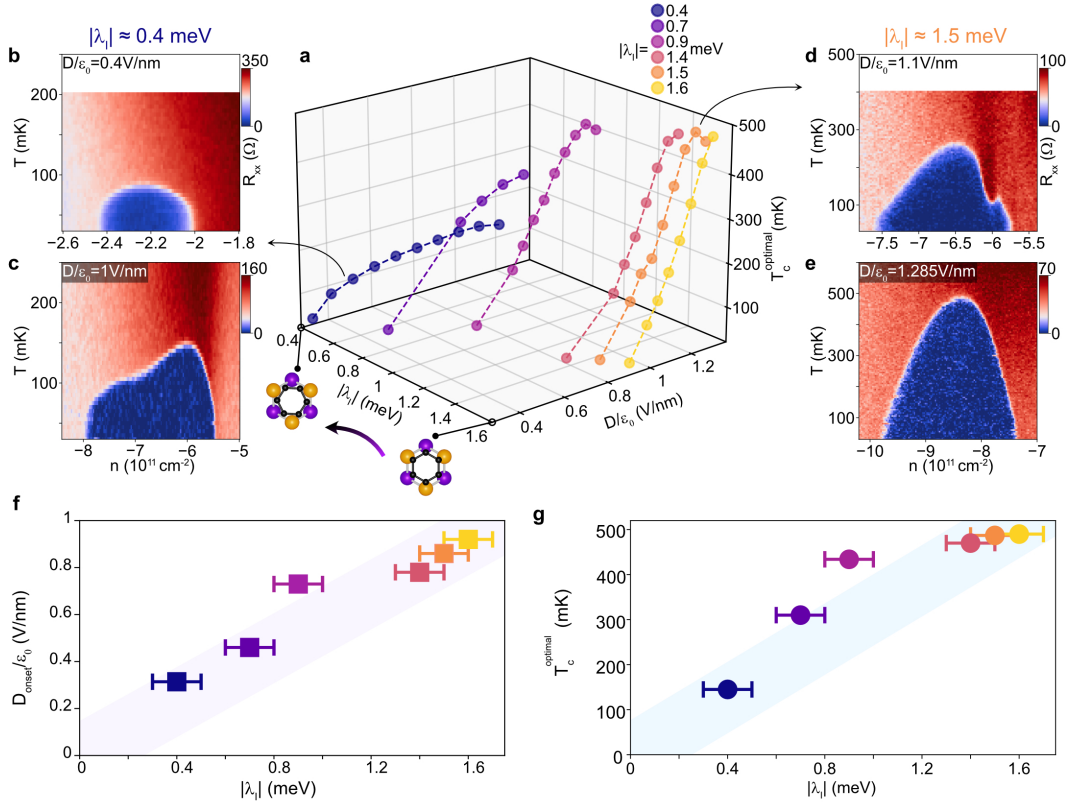


Figure 6.8: Superconducting T_c versus Ising SOC and D field. (a) Optimal superconducting critical temperature T_c^{optimal} versus $|\lambda_I|$ and D . (b),(c) R_{xx} versus doping n and temperature for a device with $|\lambda_I| \approx 0.4 \text{ meV}$, showing superconducting domes at $D/\epsilon_0 = 0.4 \text{ V/nm}$ (b) and 1 V/nm (c), respectively. (d),(e) R_{xx} versus doping n and temperature for a device with $|\lambda_I| \approx 1.5 \text{ meV}$, showing superconducting domes at $D/\epsilon_0 = 1.1 \text{ V/nm}$ (d) and 1.285 V/nm (e), respectively. (f),(g) Displacement field D_{onset} at which superconductivity onsets (f) and optimal critical temperature T_c^{optimal} (g) versus Ising SOC strength $|\lambda_I|$.

Intriguingly, the superconducting critical temperature T_c also shows a striking dependence on $|\lambda_I|$. While D_{onset} is smaller and superconductivity persists over a wide range of D fields for small Ising SOC, the superconducting critical temperature remains low throughout and saturates at $T_c \approx 150 \text{ mK}$ (Fig. 6.8b,c). In contrast, for large Ising SOC, superconductivity onsets only at higher D fields, but T_c quickly increases, reaching $T_c \approx 500 \text{ mK}$ at the optimal D (Fig. 6.8d,e). This is the highest T_c reported for crystalline (untwisted) graphene systems. Thus, the optimal critical temperature also shows an increasing trend with $|\lambda_I|$ (Fig. 6.8g). A detailed three-dimensional map of the optimal critical temperature T_c^{optimal} versus D field and $|\lambda_I|$ extracted from multiple devices is plotted in Fig. 6.8a. These observations

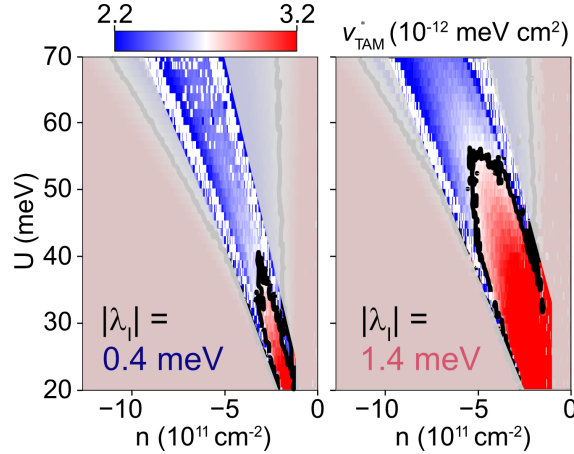


Figure 6.9: The residual Cooper channel repulsion v_{TAM}^* versus doping n and interlayer potential difference U for $|\lambda_I| = 0.4$ meV (left) and 1.4 meV (right), respectively.

motivate further investigations of the phase diagram with even stronger Ising SOC, e.g., through proximity to other transition metal dichalcogenides or the application of pressure [20, 196].

6.3 Superconductivity across nematic redistribution and from inter-valley coherence

The case for investigating devices with large Ising SOC is further emphasized by the observation of two additional superconducting regions in this regime ($1.4 \text{ meV} \lesssim |\lambda_I| \lesssim 1.6 \text{ meV}$; see Fig. 6.10 and Fig. 6.7d-f). We refer to the observed superconducting regions as SC₁, SC₂, and SC₃, enumerated from higher to lower hole doping, respectively (with the main superconducting region discussed above being SC₂; see Fig. 6.11 for additional temperature and B_{\perp} characterizations). Each superconducting pocket descends from a distinct flavor-symmetry-breaking normal state (Fig. 6.12 and Fig. 6.13) and is terminated by a first-order symmetry-breaking phase transition (marked by black dashed lines in Fig. 6.12 and Fig. 6.13) on the low-doping side. Region SC₁ features an optimal critical temperature $T_c \approx 60$ mK (Fig. 6.12a inset), while the critical temperatures for SC₂ and SC₃ are $T_c \approx 500$ mK and 100 mK, respectively (Fig. 6.13c).

The normal state of SC₁ is the only one that can be directly related to the non-interacting band structure. Quantum oscillations in this regime ($-9 \lesssim n \lesssim -7.6 \times 10^{11} \text{ cm}^{-2}$, Fig. 6.12b) show two main frequencies (marked by blue and orange arrows) obeying $2 \cdot f_{\nu}^{(1)} + 6 \cdot f_{\nu}^{(2)} \approx 1$. This indicates two large Fermi pockets

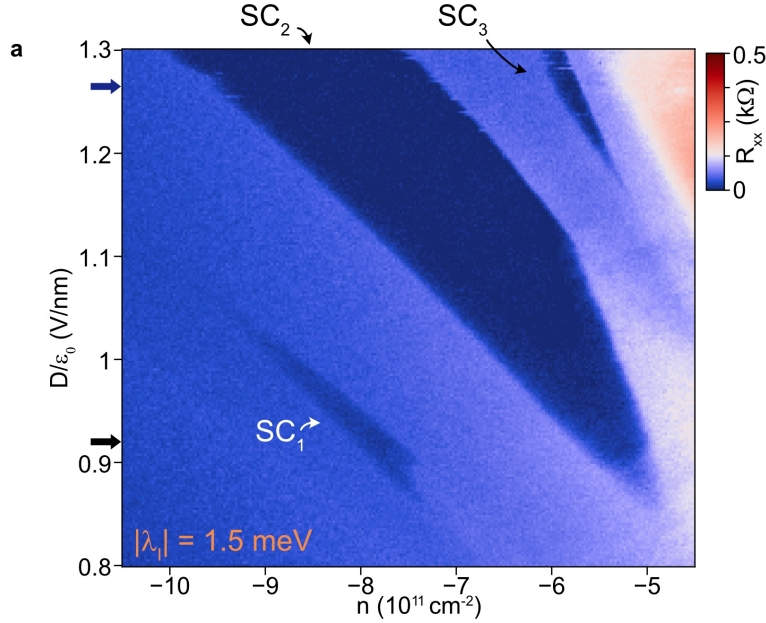


Figure 6.10: Three superconducting regions SC_1 , SC_2 , and SC_3 . (a) R_{xx} versus doping density n and displacement field D for a device with Ising SOC strength $|\lambda_I| \approx 1.5$ meV, focusing around the phase space where the three superconducting regions coexist.

from the two majority Ising flavors and six small pockets originating from trigonal warping [62] of the two minority Ising flavors [122] (Fig. 6.12b left schematic); we denote the flavor-polarized phase as $FP(2, 6)$ ($FP(n, m)$ denotes a flavor-polarized phase with n and m degenerate-sized Fermi pockets, from large to small).

Ultrahigh-resolution quantum oscillations reveal the unusual features of the Fermi surfaces in the correlated normal states forming SC_2 and SC_3 . In the higher-doping region of SC_2 ($n \lesssim -8.25 \times 10^{11} \text{ cm}^{-2}$, Fig. 6.13b), we observe two dominant oscillation frequencies marked by blue ($f_v^{(1)}$) and orange ($f_v^{(2)}$) lines in Fig. 6.13e, satisfying $2 \cdot f_v^{(1)} + 4 \cdot f_v^{(2)} \approx 1$ (black line). Thus, the normal state, denoted as $FP(2, 4)$, is a flavor-polarized phase hosting two majority and four minority Fermi pockets. The occupation of two out of the three trigonal-warping pockets for both the minority spin-valley flavors implies a nematic normal state that breaks the C_3 rotational symmetry [122] (Fig. 6.13e left schematic). Remarkably, we observe a different Fermi-pocket configuration in the doping range $-8.25 \lesssim n \lesssim -7.1 \times 10^{11} \text{ cm}^{-2}$ within the same superconducting pocket. Here, the lowest third frequency $f_v^{(3)}$ (Fig. 6.13e) can be clearly resolved (see Appendix C and Fig. C.1 to C.3 for frequency extraction). Starting from the same value as $f_v^{(2)}$, the value

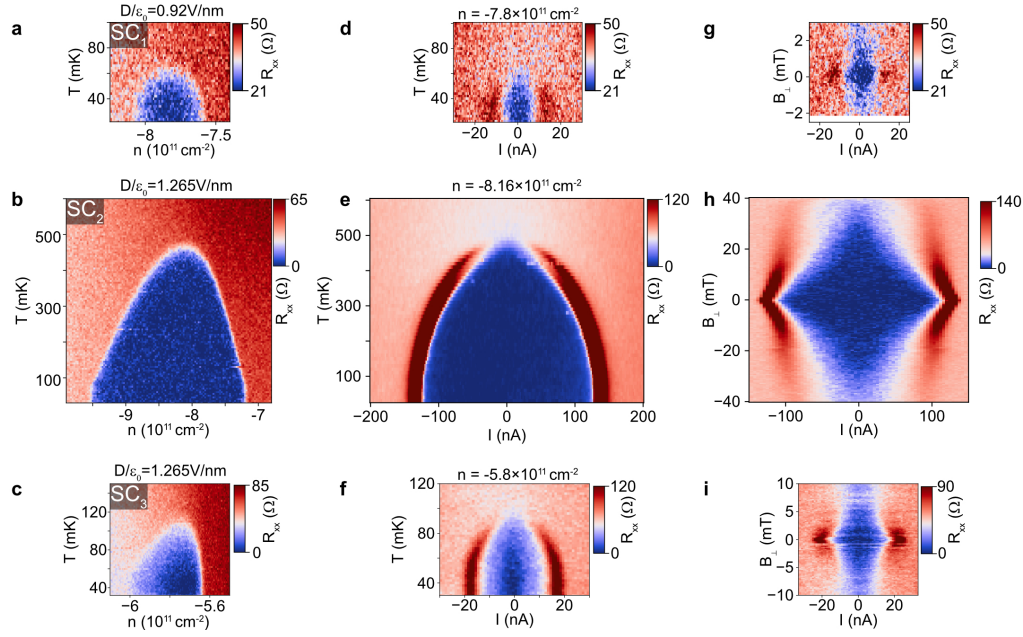


Figure 6.11: Characterization of the three superconducting regions SC_1 , SC_2 , and SC_3 . (a)-(c) Temperature dependence of the three superconducting domes SC_1 (a), SC_2 (b), and SC_3 (c), respectively. (d)-(f) Critical current versus temperature at the corresponding D and n . (g)-(i) Critical current disappearing with B_{\perp} at the same D and n as in (d)-(f).

of $f_v^{(3)}$ rapidly decreases to zero at the low-doping phase boundary, implying that two out of four small Fermi pockets shrink considerably in this density range. We denote this phase as FP(2, 2, 2) in view of the relation $2 \cdot f_v^{(1)} + 2 \cdot f_v^{(2)} + 2 \cdot f_v^{(3)} \approx 1$. Here, the second and third numbers (2 and 2) imply an additional broken symmetry within the trigonal-warping pockets [181, 197] (orange and green pockets of the middle schematic in Fig. 6.13e), signaling a nematic redistribution of holes. This remarkable continuous transition from FP(2, 2, 2) to FP(2, 4) within the superconducting dome has a significant impact on the in-plane magnetic field response of SC_2 (see Section 6.5).

A rather exceptional correlated phase denoted FP(1, 3, 1) emerges upon further decreasing the doping ($-7.1 \lesssim n \lesssim -5.7 \times 10^{11} \text{ cm}^{-2}$; Fig. 6.13b,e). The Fermi-surface configuration is reflected in three oscillation frequencies obeying $f_v^{(4)} + 3 \cdot f_v^{(5)} + f_v^{(6)} \approx 1$, with $f_v^{(4)}$ being larger than 1/2, ensuring that the largest Fermi pocket is non-degenerate (see Appendix C and Fig. C.4 to C.6 for further discussion). Remarkably, this normal state supports the superconducting region SC_3 , although all Fermi pockets have odd multiplicities. The combination of superconductivity and odd Fermi pocket multiplicities strongly points at an inter-valley

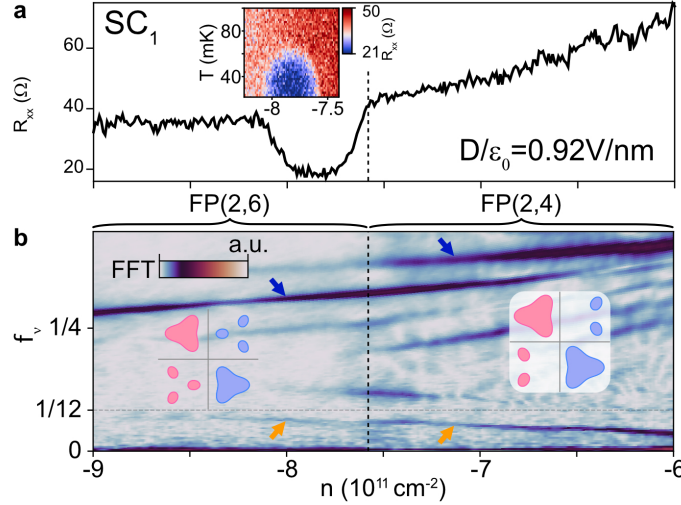


Figure 6.12: Ising symmetry-breaking Fermi surfaces of SC_1 . (a) R_{xx} versus n measured at $D/\epsilon_0 = 0.92$ V/nm. The inset shows R_{xx} versus n and temperature for the superconducting dome SC_1 . (b) Frequency-normalized FFT of $R_{xx}(1/B_{\perp})$ over the same doping range as in (a); schematics show the corresponding flavor symmetry-breaking Fermi surfaces.

coherent state [41, 42, 198–201] (purple schematic of Fig. 6.13e). This is further corroborated by an analysis of the response of the phase boundaries to a B_{\perp} field [199] (see Appendix C and Fig. C.7). The odd multiplicity of all Fermi pockets excludes the possibility of conventional s -wave pairing, suggesting unconventional superconductivity. Moreover, provided that the pockets are intrinsically superconducting, the number of three mid-size Fermi pockets ($f_v^{(5)}$) implies time-reversal symmetry breaking regardless of the inter-valley coherent nature [200, 202–204]. It is interesting that SC_3 only develops in a multi-band situation and not from one of the IVC-ordered normal states at lower hole doping with a single or a smaller number of Fermi pockets (see Fig. C.7).

6.4 Ultra-strong Pauli-limit violation: SC_1 and SC_3

All the three superconducting pockets show extraordinary resilience to in-plane magnetic field B_{\parallel} . SC_1 is characterized by an in-plane critical field $B_{c\parallel} \approx 2.5$ T, significantly higher than observed previously [122] (Fig. 6.14). SC_2 and SC_3 show distinct features in the B_{\parallel} response, reflecting the highly unusual intertwining with the underlying normal states. Fig. 6.15a,b shows the dependence of R_{xx} on in-plane magnetic field B_{\parallel} (Fig. 6.15a) and temperature (Fig. 6.15b) measured at $D/\epsilon_0 \approx 1.265$ V/nm. SC_2 occupies a significantly larger doping range, and its optimal T_c is roughly five times that of SC_3 (Fig. 6.15b). In comparison, the

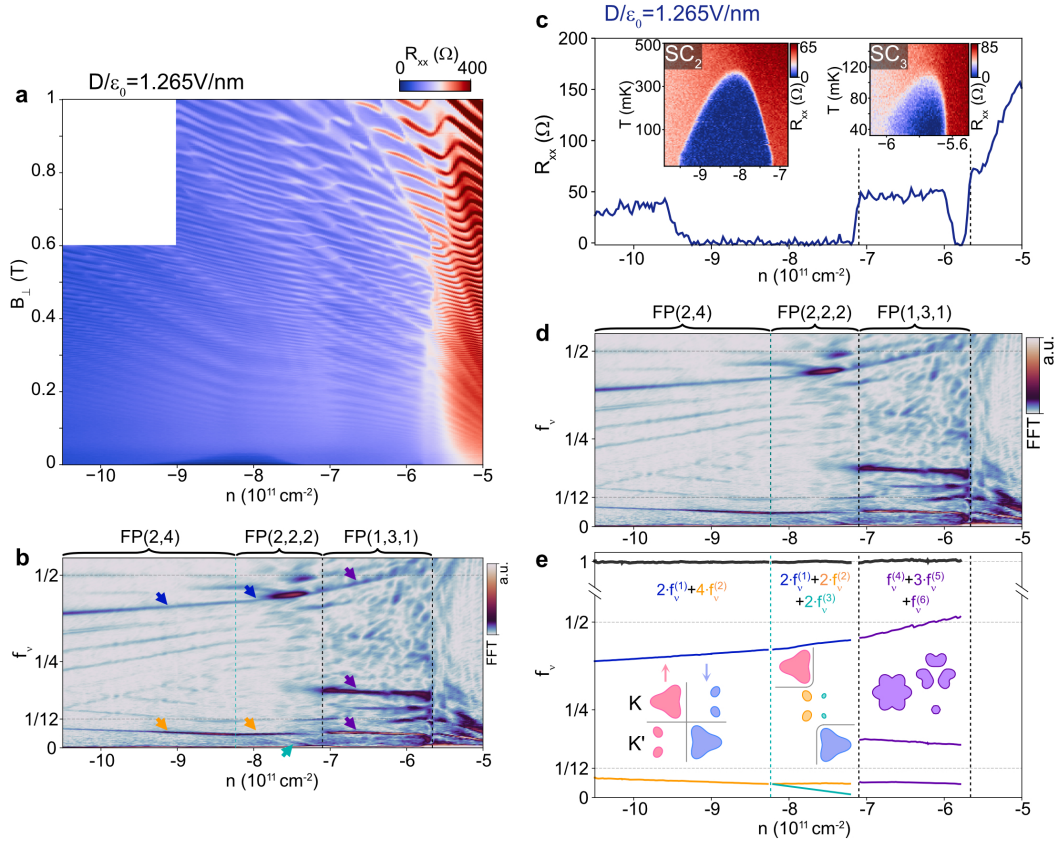


Figure 6.13: SC₂ across nematic redistribution and SC₃ from inter-valley coherence. (a) R_{xx} versus B_{\perp} and doping density n measured at $D/\epsilon_0 = 1.265$ V/nm for a device with $|\lambda_I| = 1.5$ meV. (b) Frequency-normalized Fourier transform of R_{xx} ($1/B_{\perp}$) over the same doping range as in (a). The arrows mark the primary FFT peaks, as shown in (e). (c) R_{xx} versus doping density n measured at $D/\epsilon_0 = 1.265$ V/nm. Insets show R_{xx} versus n and temperature for the superconducting domes SC₂ (left) and SC₃ (right), respectively. (d) the same data as in (b). The green dashed line marks the continuous transition from FP(2,2,2) to FP(2,4); black dashed lines mark first-order flavor symmetry-breaking transitions. (e) Intensity peaks in f_v extracted from (b). The black solid lines around $f_v = 1$ indicate the results from the Luttinger sum rule. Schematics show the possible flavor-polarized phases, from left to right corresponding to spin-valley locked nematic FP(2,4), nematic FP(2,2,2) with two sizes (green and orange) of trigonal-warping pockets, and inter-valley coherent FP(1,3,1).

two superconducting regions show a striking response to B_{\parallel} . While SC₂ is fully suppressed by $B_{\parallel} \approx 3$ T, SC₃ persists up to $B_{\parallel} = 7$ T (Fig. 6.15a) at the phase boundary. Crucially, the optimal critical temperature T_c^{optimal} of SC₃ appears to be insensitive to B_{\parallel} (Fig. 6.16), with the superconducting domes at $B_{\parallel} = 0$ T and $B_{\parallel} = 3$ T being almost the same (Fig. 6.16b,e). For a weak-coupling spin-singlet

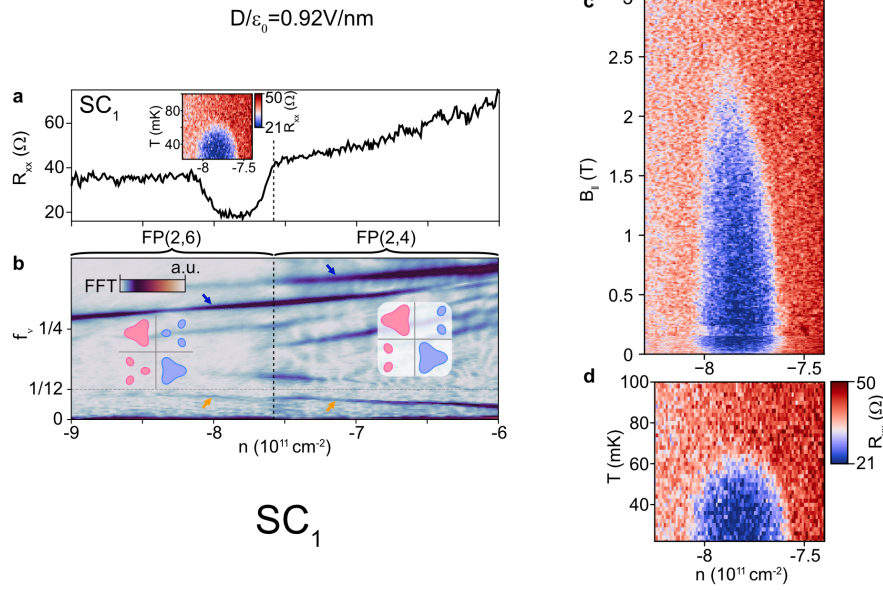


Figure 6.14: B_{\parallel} dependence of SC₁. (a) R_{xx} versus n measured at $D/\epsilon_0 = 0.92 \text{ V/nm}$. Inset shows R_{xx} versus n and temperature for the superconducting dome SC₁. (b) Frequency-normalized FFT of $R_{xx}(1/B_{\perp})$ over the same doping range as in (a). (c),(d) n -dependent R_{xx} versus in-plane magnetic field (c) or versus temperature (d), showing the disappearance of SC₁.

Bardeen–Cooper–Schrieffer (BCS) superconductor, the Pauli limit B_p is related to the zero-magnetic-field critical temperature $T_c(0)$ as $B_p = 1.86 \text{ T/K} \times T_c(0)$. $T_c(0) = 100 \text{ mK}$ for SC₃ would produce $B_p = 0.186 \text{ T}$. Thus, the observed in-plane critical field $B_{c\parallel} = 7 \text{ T}$ yields a Pauli-limit violation ratio (PVR) $B_{c\parallel}/B_p \sim 40$, placing SC₃ among the superconducting phases with the highest Pauli-limit violation ratios [55, 205–207]. Note that the exceedingly large PVR is not present in the other two superconducting regions where Fermi pockets of the same size appear in pairs, further reflecting the remarkable nature of SC₃.

6.5 Nematicity-intertwined B_{\parallel} depairing: SC₂

While overall having significantly lower PVR, the analysis of SC₂ provides further insights into the pairing scenarios. SC₂ features two doping regions with distinct B_{\parallel} responses (Fig. 6.17a,b) that are directly intertwined with the continuous transition from FP(2, 2, 2) to FP(2, 4) (Fig. 6.18). Fig. 6.17a,b shows representative R_{xx} versus temperature and B_{\parallel} measured in the overdoped and underdoped regions ($n = -8.5$ and $6.9 \times 10^{11} \text{ cm}^{-2}$, respectively) for $D/\epsilon_0 = 1.2 \text{ V/nm}$. SC₂ exhibits the same $T_c(0) \approx 200 \text{ mK}$ at both doping densities, but the B_{\parallel} responses are distinct. The overdoped T_c is quickly suppressed by B_{\parallel} following a conventional

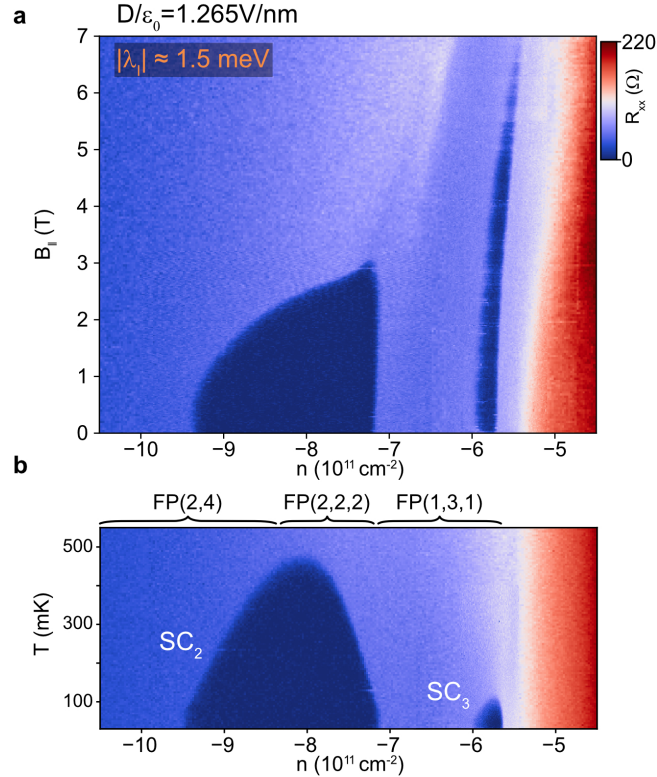


Figure 6.15: In-plane field dependence of SC_2 and SC_3 . (a) R_{xx} versus doping density n and in-plane magnetic field $B_{||}$ at $D/\epsilon_0 = 1.265 \text{ V/nm}$ for a device with $|\lambda_I| = 1.5 \text{ meV}$. (b) R_{xx} versus n and temperature at $D/\epsilon_0 = 1.265 \text{ V/nm}$.

quadratic scaling (Fig. 6.17a). The underdoped T_c , however, is insensitive to $B_{||}$ for $B_{||} \leq 1 \text{ T}$ (Fig. 6.17b), with the depairing at higher fields $B_{||} > 1.5 \text{ T}$ likely due to the Fermi-surface changes induced by $B_{||}$.

To quantify the $B_{||}$ -induced suppression of SC_2 , we fit T_c versus $B_{||}$ by $T_c(B_{||}) = T_c(0) - \alpha \cdot B_{||}^2$, where α quantifies the pair-breaking tendency of $B_{||}$. The resulting α shows a striking dependence on doping (Fig. 6.18a). At higher doping, α plateaus around 0.08 K/T^2 . At lower doping, α approaches zero, indicating vanishing sensitivity to $B_{||}$. Importantly, the qualitative change in α coincides with the redistribution of the trigonal-warping pockets (Fig. 6.18a,b). The region with the plateau ($-8.8 \lesssim n \lesssim -7.3 \times 10^{11} \text{ cm}^{-2}$) and the region with the rapidly changing α ($-7.3 \lesssim n \lesssim -6.6 \times 10^{11} \text{ cm}^{-2}$) correspond to the FP(2, 4) and FP(2, 2, 2) phases, respectively. Within the FP(2, 2, 2), both the value of α and the size of the smallest Fermi pockets (green pockets of the schematics in Fig. 6.18a) approach zero at the phase boundary ($n \approx -6.6 \times 10^{11} \text{ cm}^{-2}$). These observations suggest that the smallest Fermi pockets determine the $B_{||}$ response (see Fig. C.8 to C.10 for additional

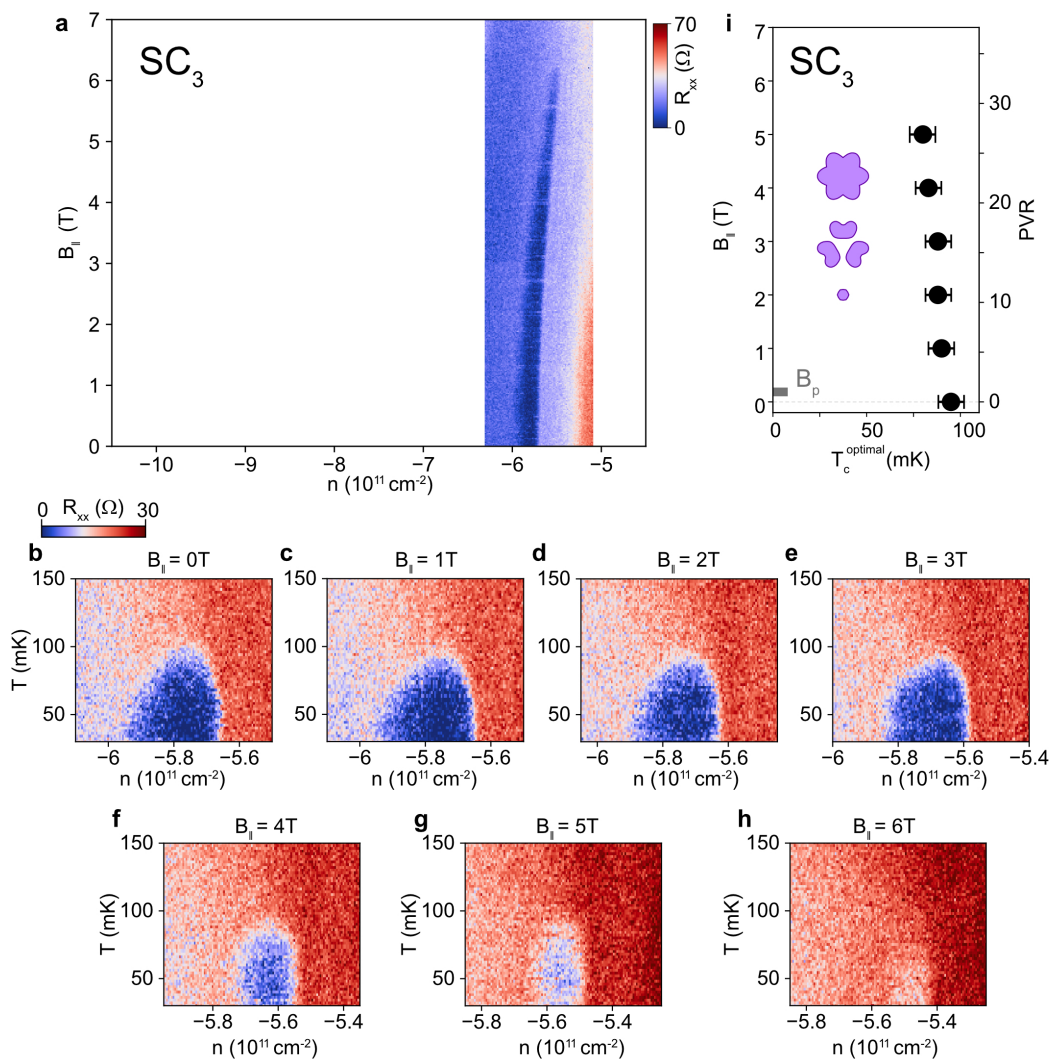


Figure 6.16: Temperature dependence of SC₃ measured at different in-plane magnetic field. (a) R_{xx} versus doping density n and in-plane magnetic field B_{\parallel} showing SC₃ evolution. (b)-(h) R_{xx} versus doping density n and temperature measured from $B_{\parallel} = 0 \text{ T}$ (b) to 6 T (h), 1 T increment step. (i) Optimal critical temperature T_c^{optimal} of SC₃ versus B_{\parallel} . The grey bar marks the Pauli limit B_p .

data).

The disparity in the response of the two SC₂ regions to B_{\parallel} invites an analysis of possible microscopic mechanisms. We propose that this disparity may be attributed to the prominence of majority-minority interband interactions, so that the in-plane magnetic field response and the trend observed in D_{onset} (Fig. 6.8f) share a common origin. Due to strong interactions, a modest B_{\parallel} (compared to $|\lambda_I|$) may lead to significant spin canting, where majority- (minority-) band spins cant toward (away from)

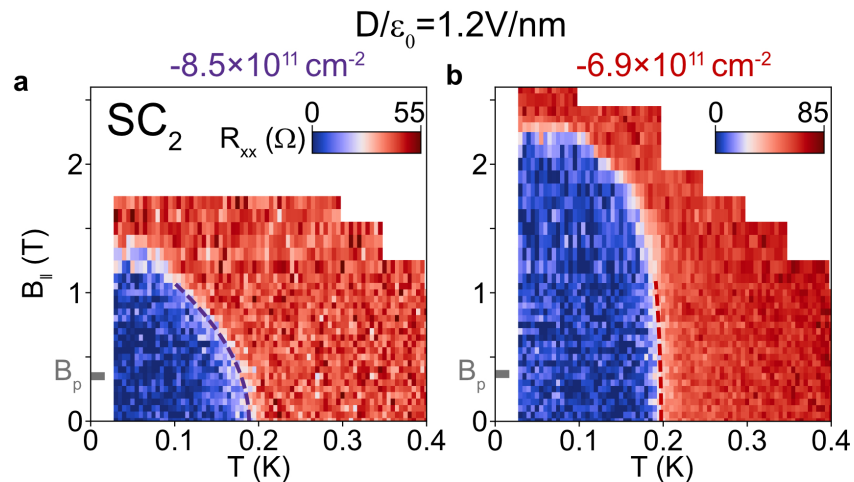


Figure 6.17: In-plane magnetic field dependence of SC_2 . (a),(b) R_{xx} versus temperature and $B_{||}$ at $n = -8.5 \times 10^{11} \text{ cm}^{-2}$ (a) and $-6.9 \times 10^{11} \text{ cm}^{-2}$ (b), respectively for $D/\epsilon_0 = 1.2 \text{ V/nm}$. The colored dashed lines are quadratic fitting by $T_c(B_{||}) = T_c(0) - \alpha \times B_{||}^2$.

the magnetic field direction. In the spin-canted normal state [200, 208], the interband (intra-band) Cooper-channel interactions are naturally suppressed (enhanced) due to the in-plane spin projection of the scattered Cooper pairs. As a consequence, since interband scattering is beneficial to pairing, one expects an appreciable decrease in T_c with applied $B_{||}$ (Fig. 6.19a,c). On the other hand, further symmetry breaking in the minority bands (e.g., spin or valley polarization) may critically suppress pairing between minority carriers and thus decouple them completely from the majority band in the Cooper channel. In such a scenario provided that the minority bands of FP(2, 2, 2) are valley-polarized (right schematic in Fig. 6.19b), one expects the adverse magnetic field effects on the interband interaction to gradually disappear, making the superconductor less field-sensitive (Fig. 6.19b,d). This coincides with the experimental trend in Fig. 6.17 and 6.18. Note that the same interband $B_{||}$ -suppression mechanism is consistent with the hierarchy of PVR between SC_1 , SC_2 , and SC_3 .

Unprecedented control over the strength of Ising SOC in BLG allowed us to explore its rich set of superconducting regions systematically. Superconductivity occurs for a diverse set of Fermi-pocket configurations, including for Fermi pockets with odd multiplicity pointing at unconventional superconductivity. Remarkably, all the superconductors exhibit distinctive resilience to in-plane magnetic field. A newly discovered inter-valley coherent Fermi-pocket configuration exhibits a PVR

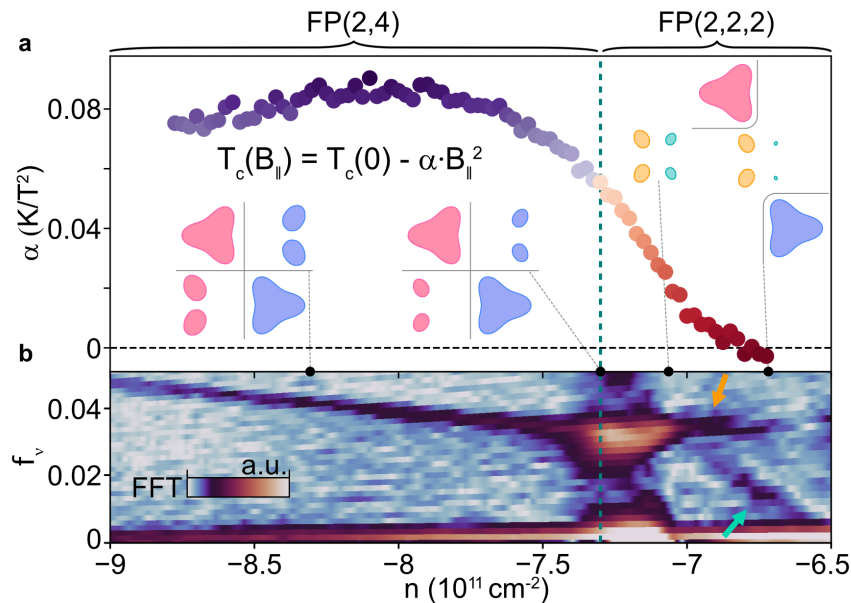


Figure 6.18: Coefficient α versus doping for SC_2 . (a) Coefficient α versus doping n within the SC_2 dome at $D/\epsilon_0 = 1.2 \text{ V/nm}$. (b) Normalized FFT of $R_{xx}(1/B_{\perp})$ over the same n and D range as in (a), focusing at low frequencies. Green dashed line marks the nematic redistribution of holes from FP(2, 4) to FP(2, 2, 2). Schematics in (a) show the Fermi-surface evolution versus n , where the smallest trigonal-warping pockets (green) grow rapidly from low to high doping ($-7.3 \lesssim n \lesssim -6.6 \times 10^{11} \text{ cm}^{-2}$).

value, which reaches one of the highest values for any superconductor to date. All the superconducting regions are multiband superconductors, which we argue to explain differences in their resilience to in-plane fields and their dependence on the displacement field. More generally, the approach of inducing tunable symmetry-breaking fields via moiréless-twist engineering, can be applied to a broad family of van der Waals materials and extended beyond SOC to include magnetism, charge orders, etc. This opens promising avenues toward tailoring desired perturbations and realizing exotic phases of matter on demand.

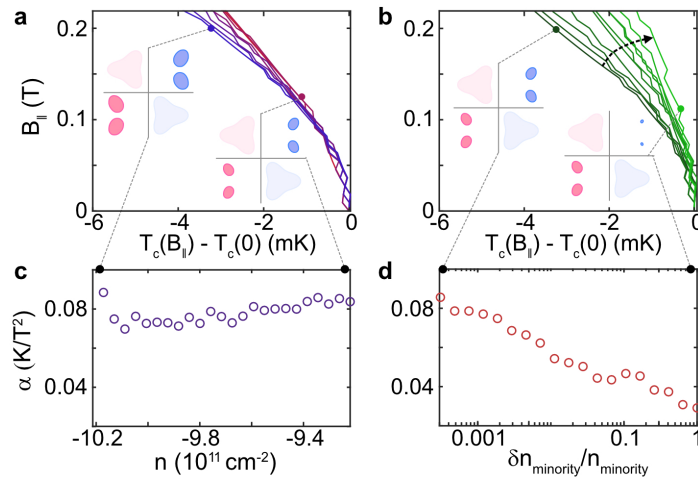


Figure 6.19: B_{\parallel} dependence of pairing by interband interactions. (a),(b) Theoretical B_{\parallel} depairing with the prominent interband pairing (a) and the suppressed case by valley polarization (b). (c),(d) Theoretical α versus n for FP(2, 4) (c) and versus minority imbalance $\delta n_{\text{minority}}/n_{\text{minority}}$ for FP(2, 2, 2) (d).

DISCUSSION AND OUTLOOK

The dissertation focuses on the superconductivity originated from the flat electronic bands of carefully engineered graphene van der Waals heterostructures. The proximity of WSe_2 induces spin-orbit coupling to both moiré graphene and Bernal bilayer graphene. Importantly, superconductivity is stabilized and even an order-of-magnitude enhanced: (i) superconductivity is stabilized in TBG with metallic band structure, i.e., far away from the magic angle; (ii) alternating twisted graphene multilayers is a highly tunable family of strongly coupled superconductors; (iii) proximitized Ising SOC stabilizes and boosts the critical temperature of fragile superconductivity in BLG; and (iv) the moiréless twisting between graphene and WSe_2 demonstrates a new tuning knob and showcases a plethora of exotic superconducting pairing. The interplay between high density of states, strong Coulomb interactions, and explicit spin-orbit coupling offers unique insights and properties, such as intimate connection between superconductivity and flavor symmetry-breaking transitions, the unprecedented superconducting filling ranges in moiré graphene multilayers, Ising-modified nematicity in BLG- WSe_2 , and superconductivity from inter-valley coherence and intertwining with nematic redistribution. There are still countless exciting open questions for further exploration.

7.1 Twisted moiré graphene

Over the past few years of extensive studies, there have been numerous twisted moiré systems demonstrated strong correlations, including alternating twisted graphene multilayers [16, 18, 44, 45, 48, 49], twisted bilayer-bilayer graphene [43, 46], twisted monolayer-bilayer graphene [47, 209], helical twisted trilayer graphene [210], twisted graphitic thin films [211] with various combinations. There are also various twisted TMD homobilayers [212] and heterobilayers [213]. However, the strongest superconductivity, i.e., superconducting transition temperature being ~ 2 K, is still exclusive to alternating twisted graphene multilayers. Recently, by adding WSe_2 to twisted bilayer-bilayer graphene, the previously non-superconducting system becomes superconducting [214]; twisted homobilayer TMDs also shows robust superconductivity with better engineered contacts [57, 58]. The critical temperature of both, however, is considerably lower in comparison to alternating twisted graphene

multilayers. Addressing the discrepancy between these systems would guide us to the nature of pairing mechanism. The pairing strength could be specifically related to the crystal symmetry, e.g., C_{2z} symmetry is only present in TBG while absent in the other structures [215]. While superconductivity in BLG is strongly enhanced with the presence of Ising SOC, the critical temperature for magic angle moiré graphene is not sensitive to the presence of WSe_2 . One possible scenario is that SOC strength is relatively low in compared to the other spontaneous symmetry-breaking terms at the magic-angle condition, while the SOC term might be large enough to change the condition away from the magic angle, where spontaneous correlations are weakened. It is desirable to increase the proximitized SOC by either changing the TMD materials or by apply pressure to increase interlayer coupling [20, 216]. The results will shed light on the limit of critical temperature in moiré graphene. The adding of SOC, for instance, combines with the unique symmetry-broken states in TBG potentially leading to Majorana bound states [202], and further topological superconducting states could be realized by considering moiré patterns with other materials.

There are increasing evidences indicating that superconductivity in moiré graphene is unconventional, including strongly coupled nature [16, 45, 48, 49], nodal tunneling spectrum, coexistence of pseudogap phase, and a larger superconducting gap relative to the critical temperature [39, 40]. It is natural to expect anisotropic pairing symmetries. In high-temperature superconductors, the corner junction geometry is a crucial signature for d wave pairing [87]. Similar ideas maybe adopted to moiré graphene systems, the gate tunability here may help further narrow down the origin. Indeed, planar Josephson junctions [217, 218] and superconducting quantum interference device [219] (SQUID) have been made and show highly tunable Josephson current. However, controllable destructive interference of phases is hard because of the difficulty in identifying pairing symmetry directions of the system. Also the existence of twist-angle inhomogeneity may nucleate various domains [117] that hinder the interpretation of data. Further understanding lies in the improvement of fabrication processes that yield samples with high twist angle homogeneity. The homogeneous sample might be crucial for disentangle the relation between various correlated orders. For example, uniform samples with open surface are suitable for simultaneously measuring electrical transport and scanning probe techniques (specifically scanning tunneling microscopy; STM) together. The result may yield microscopic understanding of certain correlated orders (such as imaging inter-valley coherence) with one-to-one correspondence to global transport. The

in situ control of interfacial twist angle is also an exciting avenue toward twistrionic engineering [220, 221].

7.2 Crystalline graphene multilayers

The adventure of crystalline graphene multilayers is also double aspects: material/quantum phase discoveries and understanding the observed phenomena. The order-of-magnitude T_c enhancement is quite satisfying; we want to ask: to what extent proximitized SOC by WSe₂ favors the formation of superconductivity. Is it simply related to high density of states? Measuring superconducting critical temperature as a function of layer number of crystalline (rhombohedral) graphene may give the answer, since the density of states is monotonically increasing as the layer number is increase. Or the critical temperature is simply related to certain band structure details, such as trigonal warping pockets, and is thus material specific. What is the largest SOC that one can proximitize to graphene system? From the virtual tunneling perspective [184], the value depends on the alignment of graphene and TMD bands, smaller band offsets gives larger values. Changing to another TMD material with smaller band offset may yield a strong SOC value. Applying pressure will increase the interlayer coupling between the two materials [20, 216], and the SOC strength will certainly be boosted. Crystalline graphene multilayers are truly ultra-clean systems where band structure details on the order of sub-Kelvin are clearly resolved and the boundaries between different symmetry-breaking phases are extremely sharp. The sharpness is ideal for microwave low-energy dynamics to probe delicate ground state competitions. Microwave photon can be easily implemented to dilution fridge setup; the photon shining may force the system into different ground states or simply melt the existing orders. The resulting dynamics from the perturbations would be fruitful, regardless. On a side note, the recent discovery of zero-field fractional quantum anomalous Hall effect in rhombohedral graphene aligned with hBN is a closely related system [222]. Combining WSe₂ on one side and align the graphene/hBN moiré on the other side would be potentially interesting.

Other than the exploration of new phase diagram, there are still open questions regarding the existing phenomena urge to be addressed. The advantage of these crystalline graphene multilayers is the ultra-cleanliness, while the drawback is that dual-gate geometry is required to access the correlated phase diagram, detrimental for several scanning probe techniques. The tunneling spectrum would be interesting for several superconductors observed in BLG-WSe₂, especially SC₃ with strong

Pauli-limit violation could be potentially multiple components. Measuring the tunneling spectrum as a function of doping and in-plane magnetic field would be informative for narrowing down the pairing symmetries. One way to get around the dual-gate problem is by fabricating gate-defined quantum point contact that is made by all crystalline components [223]. The crystalline nature of all layers would yield reliable and clean data of subtle phenomena. Scanning probe techniques, such as STM, may work for rhombohedral graphene multilayers: due to the thicker layers, single-gate geometry may cut through a big portion of the correlated phase diagram. Spatial modulation of the parent states, such as inter-valley coherent orders, might be reviewed by the geometry in thick layers. Gate-defined junction geometry [224] may also work here, where the junction region is open surfaced. The junction two sides are dual gated to tune to desired correlated states. Order parameters may leak inside the junction region due to proximity, and scanning probe techniques are thus accessible.

BIBLIOGRAPHY

1. Anderson, P. W. More is different. *Science* **177**, 393–396. doi:[10.1126/science.177.4047.393](https://doi.org/10.1126/science.177.4047.393). <https://www.science.org/doi/10.1126/science.177.4047.393> (1972).
2. Basov, D. N., Averitt, R. D. & Hsieh, D. Towards properties on demand in quantum materials. *Nature Materials* **16**, 1077–1088. ISSN: 1476-1122, 1476-4660. doi:[10.1038/nmat5017](https://doi.org/10.1038/nmat5017). <https://www.nature.com/articles/nmat5017> (2017).
3. Novoselov, K. S. *et al.* Electric field effect in atomically thin carbon films. *Science* **306**, 666–669. doi:[10.1126/science.1102896](https://doi.org/10.1126/science.1102896). <https://www.science.org/doi/full/10.1126/science.1102896> (2004).
4. Geim, A. K. & Novoselov, K. S. The rise of graphene. *Nature Materials* **6**, 183–191. ISSN: 1476-4660. doi:[10.1038/nmat1849](https://doi.org/10.1038/nmat1849). <https://www.nature.com/articles/nmat1849> (2007).
5. Castro Neto, A. H., Guinea, F., Peres, N. M. R., Novoselov, K. S. & Geim, A. K. The electronic properties of graphene. *Reviews of Modern Physics* **81**, 109–162. ISSN: 0034-6861, 1539-0756. doi:[10.1103/RevModPhys.81.109](https://doi.org/10.1103/RevModPhys.81.109). <https://link.aps.org/doi/10.1103/RevModPhys.81.109> (2009).
6. Novoselov, K. S. *et al.* Two-dimensional gas of massless Dirac fermions in graphene. *Nature* **438**, 197–200. ISSN: 0028-0836, 1476-4687. doi:[10.1038/nature04233](https://doi.org/10.1038/nature04233). <https://www.nature.com/articles/nature04233> (2005).
7. Zhang, Y., Tan, Y.-W., Stormer, H. L. & Kim, P. Experimental observation of the quantum Hall effect and Berry's phase in graphene. *Nature* **438**, 201–204. ISSN: 1476-4687. doi:[10.1038/nature04235](https://doi.org/10.1038/nature04235). <https://www.nature.com/articles/nature04235> (2005).
8. Mak, K. F., Lee, C., Hone, J., Shan, J. & Heinz, T. F. Atomically thin MoS₂: A new direct-gap semiconductor. *Physical Review Letters* **105**, 136805. doi:[10.1103/PhysRevLett.105.136805](https://doi.org/10.1103/PhysRevLett.105.136805). <https://link.aps.org/doi/10.1103/PhysRevLett.105.136805> (2010).
9. Xi, X. *et al.* Ising pairing in superconducting NbSe₂ atomic layers. *Nature Physics* **12**, 139–143. ISSN: 1745-2481. doi:[10.1038/nphys3538](https://doi.org/10.1038/nphys3538). <https://www.nature.com/articles/nphys3538> (2016).
10. Huang, B. *et al.* Layer-dependent ferromagnetism in a van der Waals crystal down to the monolayer limit. *Nature* **546**, 270–273. ISSN: 1476-4687. doi:[10.1038/nature22391](https://doi.org/10.1038/nature22391). <https://www.nature.com/articles/nature22391> (2017).

11. Yu, Y. *et al.* Gate-tunable phase transitions in thin flakes of 1T-TaS₂. *Nature Nanotechnology* **10**, 270–276. ISSN: 1748-3387, 1748-3395. doi:[10.1038/nnano.2014.323](https://doi.org/10.1038/nnano.2014.323). <https://www.nature.com/articles/nnano.2014.323> (2015).
12. Yu, Y. *et al.* High-temperature superconductivity in monolayer Bi₂Sr₂CaCu₂O_{8+δ}. *Nature* **575**, 156–163. ISSN: 1476-4687. doi:[10.1038/s41586-019-1718-x](https://doi.org/10.1038/s41586-019-1718-x). <https://www.nature.com/articles/s41586-019-1718-x> (2019).
13. Wang, L. *et al.* One-dimensional electrical contact to a two-dimensional material. *Science* **342**, 614–617. doi:[10.1126/science.1244358](https://doi.org/10.1126/science.1244358). <https://www.science.org/doi/full/10.1126/science.1244358> (2013).
14. Dean, C. R. *et al.* Boron nitride substrates for high-quality graphene electronics. *Nature Nanotechnology* **5**, 722–726. ISSN: 1748-3395. doi:[10.1038/nnano.2010.172](https://doi.org/10.1038/nnano.2010.172). <https://www.nature.com/articles/nnano.2010.172> (2010).
15. Kim, K. *et al.* Van der Waals heterostructures with high accuracy rotational alignment. *Nano Letters* **16**, 1989–1995. ISSN: 1530-6984. doi:[10.1021/acs.nanolett.5b05263](https://doi.org/10.1021/acs.nanolett.5b05263). <https://doi.org/10.1021/acs.nanolett.5b05263> (2016).
16. Cao, Y. *et al.* Unconventional superconductivity in magic-angle graphene superlattices. *Nature* **556**, 43–50. ISSN: 1476-4687. doi:[10.1038/nature26160](https://doi.org/10.1038/nature26160). <https://www.nature.com/articles/nature26160> (2018).
17. Balents, L., Dean, C. R., Efetov, D. K. & Young, A. F. Superconductivity and strong correlations in moiré flat bands. *Nature Physics* **16**, 725–733. ISSN: 1745-2473, 1745-2481. doi:[10.1038/s41567-020-0906-9](https://doi.org/10.1038/s41567-020-0906-9). <https://www.nature.com/articles/s41567-020-0906-9> (2020).
18. Cao, Y. *et al.* Correlated insulator behaviour at half-filling in magic-angle graphene superlattices. *Nature* **556**, 80–84. ISSN: 1476-4687. doi:[10.1038/nature26154](https://doi.org/10.1038/nature26154). <https://www.nature.com/articles/nature26154> (2018).
19. Lu, X. *et al.* Superconductors, orbital magnets and correlated states in magic-angle bilayer graphene. *Nature* **574**, 653–657. ISSN: 1476-4687. doi:[10.1038/s41586-019-1695-0](https://doi.org/10.1038/s41586-019-1695-0). <https://www.nature.com/articles/s41586-019-1695-0> (2019).
20. Yankowitz, M. *et al.* Tuning superconductivity in twisted bilayer graphene. *Science* **363**, 1059–1064. doi:[10.1126/science.aav1910](https://doi.org/10.1126/science.aav1910). <https://www.science.org/doi/10.1126/science.aav1910> (2019).
21. Sharpe, A. L. *et al.* Emergent ferromagnetism near three-quarters filling in twisted bilayer graphene. *Science* **365**, 605–608. doi:[10.1126/science.aaw3780](https://doi.org/10.1126/science.aaw3780). <https://www.science.org/doi/10.1126/science.aaw3780> (2019).

22. Serlin, M. *et al.* Intrinsic quantized anomalous Hall effect in a moiré heterostructure. *Science* **367**, 900–903. doi:[10.1126/science.aay5533](https://doi.org/10.1126/science.aay5533). <https://www.science.org/doi/10.1126/science.aay5533> (2020).
23. Wong, D. *et al.* Cascade of electronic transitions in magic-angle twisted bilayer graphene. *Nature* **582**, 198–202. ISSN: 0028-0836, 1476-4687. doi:[10.1038/s41586-020-2339-0](https://doi.org/10.1038/s41586-020-2339-0). <https://www.nature.com/articles/s41586-020-2339-0> (2020).
24. Zondiner, U. *et al.* Cascade of phase transitions and Dirac revivals in magic-angle graphene. *Nature* **582**, 203–208. ISSN: 0028-0836, 1476-4687. doi:[10.1038/s41586-020-2373-y](https://doi.org/10.1038/s41586-020-2373-y). <https://www.nature.com/articles/s41586-020-2373-y> (2020).
25. Rozen, A. *et al.* Entropic evidence for a Pomeranchuk effect in magic-angle graphene. *Nature* **592**, 214–219. ISSN: 1476-4687. doi:[10.1038/s41586-021-03319-3](https://doi.org/10.1038/s41586-021-03319-3). <https://www.nature.com/articles/s41586-021-03319-3> (2021).
26. Saito, Y. *et al.* Isospin Pomeranchuk effect in twisted bilayer graphene. *Nature* **592**, 220–224. ISSN: 1476-4687. doi:[10.1038/s41586-021-03409-2](https://doi.org/10.1038/s41586-021-03409-2). <https://www.nature.com/articles/s41586-021-03409-2> (2021).
27. Choi, Y. *et al.* Correlation-driven topological phases in magic-angle twisted bilayer graphene. *Nature* **589**, 536–541. ISSN: 1476-4687. doi:[10.1038/s41586-020-03159-7](https://doi.org/10.1038/s41586-020-03159-7). <https://www.nature.com/articles/s41586-020-03159-7> (2021).
28. Das, I. *et al.* Symmetry-broken Chern insulators and Rashba-like Landau-level crossings in magic-angle bilayer graphene. *Nature Physics* **17**, 710–714. ISSN: 1745-2481. doi:[10.1038/s41567-021-01186-3](https://doi.org/10.1038/s41567-021-01186-3). <https://www.nature.com/articles/s41567-021-01186-3> (2021).
29. Nuckolls, K. P. *et al.* Strongly correlated Chern insulators in magic-angle twisted bilayer graphene. *Nature* **588**, 610–615. ISSN: 1476-4687. doi:[10.1038/s41586-020-3028-8](https://doi.org/10.1038/s41586-020-3028-8). <https://www.nature.com/articles/s41586-020-3028-8> (2020).
30. Park, J. M., Cao, Y., Watanabe, K., Taniguchi, T. & Jarillo-Herrero, P. Flavour Hund’s coupling, Chern gaps and charge diffusivity in moiré graphene. *Nature* **592**, 43–48. ISSN: 1476-4687. doi:[10.1038/s41586-021-03366-w](https://doi.org/10.1038/s41586-021-03366-w). <https://www.nature.com/articles/s41586-021-03366-w> (2021).
31. Saito, Y. *et al.* Hofstadter subband ferromagnetism and symmetry-broken Chern insulators in twisted bilayer graphene. *Nature Physics* **17**, 478–481. ISSN: 1745-2481. doi:[10.1038/s41567-020-01129-4](https://doi.org/10.1038/s41567-020-01129-4). <https://www.nature.com/articles/s41567-020-01129-4> (2021).

32. Wu, S., Zhang, Z., Watanabe, K., Taniguchi, T. & Andrei, E. Y. Chern insulators, van Hove singularities and topological flat bands in magic-angle twisted bilayer graphene. *Nature Materials* **20**, 488–494. ISSN: 1476-4660. doi:[10.1038/s41563-020-00911-2](https://doi.org/10.1038/s41563-020-00911-2). <https://www.nature.com/articles/s41563-020-00911-2> (2021).
33. Yu, J. *et al.* Correlated Hofstadter spectrum and flavour phase diagram in magic-angle twisted bilayer graphene. *Nature Physics* **18**, 825–831. ISSN: 1745-2481. doi:[10.1038/s41567-022-01589-w](https://doi.org/10.1038/s41567-022-01589-w). <https://www.nature.com/articles/s41567-022-01589-w> (2022).
34. Xie, Y. *et al.* Fractional Chern insulators in magic-angle twisted bilayer graphene. *Nature* **600**, 439–443. ISSN: 1476-4687. doi:[10.1038/s41586-021-04002-3](https://doi.org/10.1038/s41586-021-04002-3). <https://www.nature.com/articles/s41586-021-04002-3> (2021).
35. Zeng, Y. *et al.* Thermodynamic evidence of fractional Chern insulator in moiré MoTe₂. *Nature* **622**, 69–73. ISSN: 1476-4687. doi:[10.1038/s41586-023-06452-3](https://doi.org/10.1038/s41586-023-06452-3). <https://www.nature.com/articles/s41586-023-06452-3> (2023).
36. Cai, J. *et al.* Signatures of fractional quantum anomalous Hall states in twisted MoTe₂. *Nature* **622**, 63–68. ISSN: 1476-4687. doi:[10.1038/s41586-023-06289-w](https://doi.org/10.1038/s41586-023-06289-w). <https://www.nature.com/articles/s41586-023-06289-w> (2023).
37. Park, H. *et al.* Observation of fractionally quantized anomalous Hall effect. *Nature* **622**, 74–79. ISSN: 1476-4687. doi:[10.1038/s41586-023-06536-0](https://doi.org/10.1038/s41586-023-06536-0). <https://www.nature.com/articles/s41586-023-06536-0> (2023).
38. Cao, Y. *et al.* Strange Metal in Magic-Angle Graphene with near Planckian Dissipation. *Physical Review Letters* **124**, 076801. doi:[10.1103/PhysRevLett.124.076801](https://doi.org/10.1103/PhysRevLett.124.076801). <https://link.aps.org/doi/10.1103/PhysRevLett.124.076801> (2020).
39. Oh, M. *et al.* Evidence for unconventional superconductivity in twisted bilayer graphene. *Nature* **600**, 240–245. ISSN: 1476-4687. doi:[10.1038/s41586-021-04121-x](https://doi.org/10.1038/s41586-021-04121-x). <https://www.nature.com/articles/s41586-021-04121-x> (2021).
40. Kim, H. *et al.* Evidence for unconventional superconductivity in twisted trilayer graphene. *Nature* **606**, 494–500. ISSN: 1476-4687. doi:[10.1038/s41586-022-04715-z](https://doi.org/10.1038/s41586-022-04715-z) (2022).
41. Kim, H. *et al.* Imaging inter-valley coherent order in magic-angle twisted trilayer graphene. *Nature* **623**, 942–948. ISSN: 1476-4687. doi:[10.1038/s41586-023-06663-8](https://doi.org/10.1038/s41586-023-06663-8). <https://www.nature.com/articles/s41586-023-06663-8> (2023).

42. Nuckolls, K. P. *et al.* Quantum textures of the many-body wavefunctions in magic-angle graphene. *Nature* **620**, 525–532. ISSN: 1476-4687. doi:[10.1038/s41586-023-06226-x](https://doi.org/10.1038/s41586-023-06226-x). <https://www.nature.com/articles/s41586-023-06226-x> (2023).
43. Cao, Y. *et al.* Tunable correlated states and spin-polarized phases in twisted bilayer–bilayer graphene. *Nature* **583**, 215–220. ISSN: 1476-4687. doi:[10.1038/s41586-020-2260-6](https://doi.org/10.1038/s41586-020-2260-6). <https://www.nature.com/articles/s41586-020-2260-6> (2020).
44. Hao, Z. *et al.* Electric field–tunable superconductivity in alternating-twist magic-angle trilayer graphene. *Science* **371**, 1133–1138. doi:[10.1126/science.abg0399](https://doi.org/10.1126/science.abg0399). <https://www.science.org/doi/10.1126/science.abg0399> (2021).
45. Park, J. M., Cao, Y., Watanabe, K., Taniguchi, T. & Jarillo-Herrero, P. Tunable strongly coupled superconductivity in magic-angle twisted trilayer graphene. *Nature* **590**, 249–255. ISSN: 0028-0836, 1476-4687. doi:[10.1038/s41586-021-03192-0](https://doi.org/10.1038/s41586-021-03192-0). <https://www.nature.com/articles/s41586-021-03192-0> (2021).
46. Liu, X. *et al.* Tunable spin-polarized correlated states in twisted double bilayer graphene. *Nature* **583**, 221–225. ISSN: 1476-4687. doi:[10.1038/s41586-020-2458-7](https://doi.org/10.1038/s41586-020-2458-7). <https://www.nature.com/articles/s41586-020-2458-7> (2020).
47. Polshyn, H. *et al.* Electrical switching of magnetic order in an orbital Chern insulator. *Nature* **588**, 66–70. ISSN: 1476-4687. doi:[10.1038/s41586-020-2963-8](https://doi.org/10.1038/s41586-020-2963-8). <https://www.nature.com/articles/s41586-020-2963-8> (2020).
48. Zhang, Y. *et al.* Promotion of superconductivity in magic-angle graphene multilayers. *Science* **377**, 1538–1543. doi:[10.1126/science.abn8585](https://doi.org/10.1126/science.abn8585). <https://www.science.org/doi/full/10.1126/science.abn8585> (2022).
49. Park, J. M. *et al.* Robust superconductivity in magic-angle multilayer graphene family. *Nature Materials* **21**, 877–883. ISSN: 1476-4660. doi:[10.1038/s41563-022-01287-1](https://doi.org/10.1038/s41563-022-01287-1). <https://www.nature.com/articles/s41563-022-01287-1> (2022).
50. Arora, H. S. *et al.* Superconductivity in metallic twisted bilayer graphene stabilized by WSe₂. *Nature* **583**, 379–384. ISSN: 0028-0836, 1476-4687. doi:[10.1038/s41586-020-2473-8](https://doi.org/10.1038/s41586-020-2473-8). <https://www.nature.com/articles/s41586-020-2473-8> (2020).
51. Saito, Y., Ge, J., Watanabe, K., Taniguchi, T. & Young, A. F. Independent superconductors and correlated insulators in twisted bilayer graphene. *Nature Physics* **16**, 926–930. ISSN: 1745-2481. doi:[10.1038/s41567-020-0928-3](https://doi.org/10.1038/s41567-020-0928-3). <https://www.nature.com/articles/s41567-020-0928-3> (2020).

52. Stepanov, P. *et al.* Untying the insulating and superconducting orders in magic-angle graphene. *Nature* **583**, 375–378. ISSN: 1476-4687. doi:[10.1038/s41586-020-2459-6](https://doi.org/10.1038/s41586-020-2459-6). <https://www.nature.com/articles/s41586-020-2459-6> (2020).
53. Liu, X. *et al.* Tuning electron correlation in magic-angle twisted bilayer graphene using Coulomb screening. *Science* **371**, 1261–1265. doi:[10.1126/science.abb8754](https://doi.org/10.1126/science.abb8754). <https://www.science.org/doi/full/10.1126/science.abb8754> (2021).
54. Zhou, H., Xie, T., Taniguchi, T., Watanabe, K. & Young, A. F. Superconductivity in rhombohedral trilayer graphene. *Nature* **598**, 434–438. ISSN: 1476-4687. doi:[10.1038/s41586-021-03926-0](https://doi.org/10.1038/s41586-021-03926-0). <https://www.nature.com/articles/s41586-021-03926-0> (2021).
55. Zhou, H. *et al.* Isospin magnetism and spin-polarized superconductivity in Bernal bilayer graphene. *Science* **375**, 774–778. doi:[10.1126/science.abm8386](https://doi.org/10.1126/science.abm8386). <https://www.science.org/doi/10.1126/science.abm8386> (2022).
56. Zhang, Y. *et al.* Enhanced superconductivity in spin-orbit proximitized bilayer graphene. *Nature* **613**, 268–273. ISSN: 0028-0836, 1476-4687. doi:[10.1038/s41586-022-05446-x](https://doi.org/10.1038/s41586-022-05446-x). <https://www.nature.com/articles/s41586-022-05446-x> (2023).
57. Guo, Y. *et al.* Superconductivity in twisted bilayer WSe₂. doi:[10.48550/arXiv.2406.03418](https://doi.org/10.48550/arXiv.2406.03418). arXiv: [2406.03418\[cond-mat\]](https://arxiv.org/abs/2406.03418). <http://arxiv.org/abs/2406.03418> (2024).
58. Xia, Y. *et al.* Unconventional superconductivity in twisted bilayer WSe₂. doi:[10.48550/arXiv.2405.14784](https://doi.org/10.48550/arXiv.2405.14784). arXiv: [2405.14784\[cond-mat\]](https://arxiv.org/abs/2405.14784). <http://arxiv.org/abs/2405.14784> (2024).
59. Bistritzer, R. & MacDonald, A. H. Moiré bands in twisted double-layer graphene. *Proceedings of the National Academy of Sciences* **108**, 12233–12237. doi:[10.1073/pnas.1108174108](https://doi.org/10.1073/pnas.1108174108). <https://www.pnas.org/doi/10.1073/pnas.1108174108> (2011).
60. Lopes dos Santos, J. M. B., Peres, N. M. R. & Castro Neto, A. H. Graphene bilayer with a twist: Electronic structure. *Physical Review Letters* **99**, 256802. ISSN: 0031-9007, 1079-7114. doi:[10.1103/PhysRevLett.99.256802](https://doi.org/10.1103/PhysRevLett.99.256802). <https://link.aps.org/doi/10.1103/PhysRevLett.99.256802> (2007).
61. Nam, N. N. T. & Koshino, M. Lattice relaxation and energy band modulation in twisted bilayer graphene. *Physical Review B* **96**, 075311. ISSN: 2469-9950, 2469-9969. doi:[10.1103/PhysRevB.96.075311](https://doi.org/10.1103/PhysRevB.96.075311). <https://link.aps.org/doi/10.1103/PhysRevB.96.075311> (2017).

62. McCann, E. & Koshino, M. The electronic properties of bilayer graphene. *Reports on Progress in Physics* **76**, 056503. ISSN: 0034-4885, 1361-6633. doi:[10.1088/0034-4885/76/5/056503](https://doi.org/10.1088/0034-4885/76/5/056503). <https://iopscience.iop.org/article/10.1088/0034-4885/76/5/056503> (2013).
63. Jung, J. & MacDonald, A. H. Accurate tight-binding models for the π bands of bilayer graphene. *Physical Review B* **89**, 035405. doi:[10.1103/PhysRevB.89.035405](https://doi.org/10.1103/PhysRevB.89.035405). <https://link.aps.org/doi/10.1103/PhysRevB.89.035405> (2014).
64. Zhou, H. *et al.* Half- and quarter-metals in rhombohedral trilayer graphene. *Nature* **598**, 429–433. ISSN: 0028-0836, 1476-4687. doi:[10.1038/s41586-021-03938-w](https://doi.org/10.1038/s41586-021-03938-w). <https://www.nature.com/articles/s41586-021-03938-w> (2021).
65. Kane, C. L. & Mele, E. J. Quantum spin Hall effect in graphene. *Physical Review Letters* **95**, 226801. ISSN: 0031-9007, 1079-7114. doi:[10.1103/PhysRevLett.95.226801](https://doi.org/10.1103/PhysRevLett.95.226801). <https://link.aps.org/doi/10.1103/PhysRevLett.95.226801> (2005).
66. Sichau, J. *et al.* Resonance microwave measurements of an intrinsic spin-orbit coupling gap in graphene: A possible indication of a topological state. *Physical Review Letters* **122**, 046403. ISSN: 0031-9007, 1079-7114. doi:[10.1103/PhysRevLett.122.046403](https://doi.org/10.1103/PhysRevLett.122.046403). <https://link.aps.org/doi/10.1103/PhysRevLett.122.046403> (2019).
67. Banszerus, L. *et al.* Observation of the spin-orbit gap in bilayer graphene by one-dimensional ballistic transport. *Physical Review Letters* **124**, 177701. ISSN: 0031-9007, 1079-7114. doi:[10.1103/PhysRevLett.124.177701](https://doi.org/10.1103/PhysRevLett.124.177701). <https://link.aps.org/doi/10.1103/PhysRevLett.124.177701> (2020).
68. Kurzmann, A. *et al.* Kondo effect and spin-orbit coupling in graphene quantum dots. *Nature Communications* **12**, 6004. ISSN: 2041-1723. doi:[10.1038/s41467-021-26149-3](https://doi.org/10.1038/s41467-021-26149-3). <https://www.nature.com/articles/s41467-021-26149-3> (2021).
69. Sobota, J. A., He, Y. & Shen, Z.-X. Angle-resolved photoemission studies of quantum materials. *Reviews of Modern Physics* **93**, 025006. ISSN: 0034-6861, 1539-0756. doi:[10.1103/RevModPhys.93.025006](https://doi.org/10.1103/RevModPhys.93.025006). <https://link.aps.org/doi/10.1103/RevModPhys.93.025006> (2021).
70. Xia, Y. *et al.* Observation of a large-gap topological-insulator class with a single Dirac cone on the surface. *Nature Physics* **5**, 398–402. ISSN: 1745-2481. doi:[10.1038/nphys1274](https://doi.org/10.1038/nphys1274). <https://www.nature.com/articles/nphys1274> (2009).
71. Hsieh, D. *et al.* A topological Dirac insulator in a quantum spin Hall phase. *Nature* **452**, 970–974. ISSN: 1476-4687. doi:[10.1038/nature06843](https://doi.org/10.1038/nature06843). <https://www.nature.com/articles/nature06843> (2008).

72. Hsieh, D. *et al.* Observation of unconventional quantum spin textures in topological insulators. *Science* **323**, 919–922. doi:[10.1126/science.1167733](https://doi.org/10.1126/science.1167733). <https://www.science.org/doi/full/10.1126/science.1167733> (2009).
73. Hsieh, D. *et al.* A tunable topological insulator in the spin helical Dirac transport regime. *Nature* **460**, 1101–1105. ISSN: 1476-4687. doi:[10.1038/nature08234](https://doi.org/10.1038/nature08234). <https://www.nature.com/articles/nature08234> (2009).
74. Ihn, T. *Semiconductor Nanostructures: Quantum states and electronic transport* 568 pp. ISBN: 978-0-19-953442-5 (2010).
75. Van Delft, D. & Kes, P. The discovery of superconductivity. *Physics Today* **63**, 38–43. ISSN: 0031-9228. doi:[10.1063/1.3490499](https://doi.org/10.1063/1.3490499). <https://doi.org/10.1063/1.3490499> (2010).
76. Bardeen, J., Cooper, L. N. & Schrieffer, J. R. Theory of superconductivity. *Physical Review* **108**, 1175–1204. doi:[10.1103/PhysRev.108.1175](https://doi.org/10.1103/PhysRev.108.1175). <https://link.aps.org/doi/10.1103/PhysRev.108.1175> (1957).
77. Keimer, B., Kivelson, S. A., Norman, M. R., Uchida, S. & Zaanen, J. From quantum matter to high-temperature superconductivity in copper oxides. *Nature* **518**, 179–186. ISSN: 0028-0836, 1476-4687. doi:[10.1038/nature14165](https://doi.org/10.1038/nature14165). <https://www.nature.com/articles/nature14165> (2015).
78. Lee, P. A., Nagaosa, N. & Wen, X.-G. Doping a Mott insulator: Physics of high-temperature superconductivity. *Reviews of Modern Physics* **78**, 17–85. doi:[10.1103/RevModPhys.78.17](https://doi.org/10.1103/RevModPhys.78.17). <https://link.aps.org/doi/10.1103/RevModPhys.78.17> (2006).
79. Ardavan, A. *et al.* Recent topics of organic superconductors. *Journal of the Physical Society of Japan* **81**, 011004. ISSN: 0031-9015. doi:[10.1143/JPSJ.81.011004](https://doi.org/10.1143/JPSJ.81.011004). <https://journals.jps.jp/doi/10.1143/JPSJ.81.011004> (2012).
80. Stewart, G. R. Heavy-fermion systems. *Reviews of Modern Physics* **56**, 755–787. doi:[10.1103/RevModPhys.56.755](https://doi.org/10.1103/RevModPhys.56.755). <https://link.aps.org/doi/10.1103/RevModPhys.56.755> (1984).
81. Fernandes, R. M. *et al.* Iron pnictides and chalcogenides: a new paradigm for superconductivity. *Nature* **601**, 35–44. ISSN: 0028-0836, 1476-4687. doi:[10.1038/s41586-021-04073-2](https://doi.org/10.1038/s41586-021-04073-2). <https://www.nature.com/articles/s41586-021-04073-2> (2022).
82. Scalapino, D. J. A common thread: The pairing interaction for unconventional superconductors. *Reviews of Modern Physics* **84**, 1383–1417. doi:[10.1103/RevModPhys.84.1383](https://doi.org/10.1103/RevModPhys.84.1383). <https://link.aps.org/doi/10.1103/RevModPhys.84.1383> (2012).

83. Tinkham, M. *Introduction to Superconductivity: Second Edition* 482 pp. ISBN: 978-0-486-43503-9 (2004).
84. Randeria, M. & Taylor, E. Crossover from Bardeen-Cooper-Schrieffer to Bose-Einstein condensation and the unitary Fermi gas. *Annual Review of Condensed Matter Physics* **5**, 209–232. ISSN: 1947-5454, 1947-5462. doi:[10.1146/annurev-conmatphys-031113-133829](https://doi.org/10.1146/annurev-conmatphys-031113-133829). <https://www.annualreviews.org/content/journals/10.1146/annurev-conmatphys-031113-133829> (2014).
85. Uemura, Y. J. *et al.* Basic similarities among cuprate, bismuthate, organic, Chevrel-phase, and heavy-fermion superconductors shown by penetration-depth measurements. *Physical Review Letters* **66**, 2665–2668. ISSN: 0031-9007. doi:[10.1103/PhysRevLett.66.2665](https://doi.org/10.1103/PhysRevLett.66.2665). <https://link.aps.org/doi/10.1103/PhysRevLett.66.2665> (1991).
86. Bednorz, J. G. & Müller, K. A. Possible high T_c superconductivity in the B-La-Cu-O system. *Zeitschrift für Physik B Condensed Matter* **64**, 189–193. ISSN: 1431-584X. doi:[10.1007/BF01303701](https://doi.org/10.1007/BF01303701). <https://doi.org/10.1007/BF01303701> (1986).
87. Wollman, D. A., Van Harlingen, D. J., Lee, W. C., Ginsberg, D. M. & Leggett, A. J. Experimental determination of the superconducting pairing state in YBCO from the phase coherence of YBCO-Pb dc SQUIDs. *Physical Review Letters* **71**, 2134–2137. doi:[10.1103/PhysRevLett.71.2134](https://doi.org/10.1103/PhysRevLett.71.2134). <https://link.aps.org/doi/10.1103/PhysRevLett.71.2134> (1993).
88. Tsuei, C. C. & Kirtley, J. R. Pairing symmetry in cuprate superconductors. *Reviews of Modern Physics* **72**, 969–1016. doi:[10.1103/RevModPhys.72.969](https://doi.org/10.1103/RevModPhys.72.969). <https://link.aps.org/doi/10.1103/RevModPhys.72.969> (2000).
89. Raghu, S., Kivelson, S. A. & Scalapino, D. J. Superconductivity in the repulsive Hubbard model: An asymptotically exact weak-coupling solution. *Physical Review B* **81**, 224505. doi:[10.1103/PhysRevB.81.224505](https://doi.org/10.1103/PhysRevB.81.224505). <https://link.aps.org/doi/10.1103/PhysRevB.81.224505> (2010).
90. Wilczek, F. Majorana returns. *Nature Physics* **5**, 614–618. ISSN: 1745-2481. doi:[10.1038/nphys1380](https://doi.org/10.1038/nphys1380). <https://www.nature.com/articles/nphys1380> (2009).
91. Nayak, C., Simon, S. H., Stern, A., Freedman, M. & Das Sarma, S. Non-Abelian anyons and topological quantum computation. *Reviews of Modern Physics* **80**, 1083–1159. ISSN: 0034-6861, 1539-0756. doi:[10.1103/RevModPhys.80.1083](https://doi.org/10.1103/RevModPhys.80.1083). <https://link.aps.org/doi/10.1103/RevModPhys.80.1083> (2008).
92. Kitaev, A. Y. Unpaired Majorana fermions in quantum wires. *Physics-Uspekhi* **44**, 131–136. ISSN: 1468-4780. doi:[10.1070/1063-7869/44/10S/S29](https://doi.org/10.1070/1063-7869/44/10S/S29).

- <https://iopscience.iop.org/article/10.1070/1063-7869/44/10S/S29> (2001).
93. Leijnse, M. & Flensberg, K. Introduction to topological superconductivity and Majorana fermions. *Semiconductor Science and Technology* **27**, 124003. ISSN: 0268-1242, 1361-6641. doi:[10.1088/0268-1242/27/12/124003](https://doi.org/10.1088/0268-1242/27/12/124003). <https://iopscience.iop.org/article/10.1088/0268-1242/27/12/124003> (2012).
 94. Read, N. & Green, D. Paired states of fermions in two dimensions with breaking of parity and time-reversal symmetries and the fractional quantum Hall effect. *Physical Review B* **61**, 10267–10297. doi:[10.1103/PhysRevB.61.10267](https://doi.org/10.1103/PhysRevB.61.10267). <https://link.aps.org/doi/10.1103/PhysRevB.61.10267> (2000).
 95. Moore, G. & Read, N. Nonabelions in the fractional quantum hall effect. *Nuclear Physics B* **360**, 362–396. ISSN: 0550-3213. doi:[10.1016/0550-3213\(91\)90407-0](https://doi.org/10.1016/0550-3213(91)90407-0). <https://www.sciencedirect.com/science/article/pii/0550321391904070> (1991).
 96. Willett, R. *et al.* Observation of an even-denominator quantum number in the fractional quantum Hall effect. *Physical Review Letters* **59**, 1776–1779. ISSN: 0031-9007. doi:[10.1103/PhysRevLett.59.1776](https://doi.org/10.1103/PhysRevLett.59.1776). <https://link.aps.org/doi/10.1103/PhysRevLett.59.1776> (1987).
 97. Wang, C., Xu, Y. & Duan, W. Ising superconductivity and its hidden variants. *Accounts of Materials Research* **2**, 526–533. doi:[10.1021/accounts.1c00068](https://doi.org/10.1021/accounts.1c00068). <https://doi.org/10.1021/accounts.1c00068> (2021).
 98. Wickramaratne, D. & Mazin, I. I. Ising superconductivity: A first-principles perspective. *Applied Physics Letters* **122**, 240503. ISSN: 0003-6951, 1077-3118. doi:[10.1063/5.0153345](https://doi.org/10.1063/5.0153345). <https://pubs.aip.org/apl/article/122/24/240503/2896133/Ising-superconductivity-A-first-principles> (2023).
 99. Zhang, D. & Falson, J. Ising pairing in atomically thin superconductors. *Nanotechnology* **32**, 502003. ISSN: 0957-4484, 1361-6528. doi:[10.1088/1361-6528/ac238d](https://doi.org/10.1088/1361-6528/ac238d). <https://iopscience.iop.org/article/10.1088/1361-6528/ac238d> (2021).
 100. Lu, J. M. *et al.* Evidence for two-dimensional Ising superconductivity in gated MoS₂. *Science* **350**, 1353–1357. doi:[10.1126/science.aab2277](https://doi.org/10.1126/science.aab2277). <https://www.science.org/doi/10.1126/science.aab2277> (2015).
 101. Saito, Y. *et al.* Superconductivity protected by spin–valley locking in ion-gated MoS₂. *Nature Physics* **12**, 144–149. ISSN: 1745-2481. doi:[10.1038/nphys3580](https://doi.org/10.1038/nphys3580). <https://www.nature.com/articles/nphys3580> (2016).

102. Gor'kov, L. P. & Rashba, E. I. Superconducting 2D system with lifted spin degeneracy: mixed singlet-triplet state. *Physical Review Letters* **87**, 037004. doi:[10.1103/PhysRevLett.87.037004](https://doi.org/10.1103/PhysRevLett.87.037004). <https://link.aps.org/doi/10.1103/PhysRevLett.87.037004> (2001).
103. Frigeri, P. A., Agterberg, D. F., Koga, A. & Sigrist, M. Superconductivity without inversion symmetry: MnSi versus CePt₃Si. *Physical Review Letters* **92**, 097001. doi:[10.1103/PhysRevLett.92.097001](https://doi.org/10.1103/PhysRevLett.92.097001). <https://link.aps.org/doi/10.1103/PhysRevLett.92.097001> (2004).
104. Zhou, B. T., Yuan, N. F. Q., Jiang, H.-L. & Law, K. T. Ising superconductivity and Majorana fermions in transition-metal dichalcogenides. *Physical Review B* **93**, 180501. ISSN: 2469-9950, 2469-9969. doi:[10.1103/PhysRevB.93.180501](https://doi.org/10.1103/PhysRevB.93.180501). <https://link.aps.org/doi/10.1103/PhysRevB.93.180501> (2016).
105. Möckli, D. & Khodas, M. Ising superconductors: Interplay of magnetic field, triplet channels, and disorder. *Physical Review B* **101**, 014510. ISSN: 2469-9950, 2469-9969. doi:[10.1103/PhysRevB.101.014510](https://doi.org/10.1103/PhysRevB.101.014510). <https://link.aps.org/doi/10.1103/PhysRevB.101.014510> (2020).
106. Wickramaratne, D., Khmelevskiy, S., Agterberg, D. F. & Mazin, I. I. Ising superconductivity and magnetism in NbSe₂. *Physical Review X* **10**, 041003. ISSN: 2160-3308. doi:[10.1103/PhysRevX.10.041003](https://doi.org/10.1103/PhysRevX.10.041003). <https://link.aps.org/doi/10.1103/PhysRevX.10.041003> (2020).
107. Hamill, A. *et al.* Two-fold symmetric superconductivity in few-layer NbSe₂. *Nature Physics* **17**, 949–954. ISSN: 1745-2481. doi:[10.1038/s41567-021-01219-x](https://doi.org/10.1038/s41567-021-01219-x). <https://www.nature.com/articles/s41567-021-01219-x> (2021).
108. Lui, C. H., Ye, Z., Keiser, C., Barros, E. B. & He, R. Stacking-dependent shear modes in trilayer graphene. *Applied Physics Letters* **106**, 041904. ISSN: 0003-6951, 1077-3118. doi:[10.1063/1.4906579](https://doi.org/10.1063/1.4906579). <https://pubs.aip.org/apl/article/106/4/041904/28897/Stacking-dependent-shear-modes-in-trilayer> (2015).
109. Nguyen, T. A., Lee, J.-U., Yoon, D. & Cheong, H. Excitation energy dependent Raman signatures of ABA- and ABC-stacked few-layer graphene. *Scientific Reports* **4**, 4630. ISSN: 2045-2322. doi:[10.1038/srep04630](https://doi.org/10.1038/srep04630). <https://www.nature.com/articles/srep04630> (2014).
110. Cong, C. *et al.* Raman characterization of ABA- and ABC-stacked trilayer graphene. *ACS Nano* **5**, 8760–8768. ISSN: 1936-0851. doi:[10.1021/nn203472f](https://doi.org/10.1021/nn203472f). <https://doi.org/10.1021/nn203472f> (2011).
111. Lui, C. H. *et al.* Imaging stacking order in few-layer graphene. *Nano Letters* **11**, 164–169. ISSN: 1530-6984. doi:[10.1021/nl1032827](https://doi.org/10.1021/nl1032827). <https://doi.org/10.1021/nl1032827> (2011).

112. Giesbers, A. J. M. *et al.* Nanolithography and manipulation of graphene using an atomic force microscope. *Solid State Communications* **147**, 366–369. ISSN: 0038-1098. doi:[10.1016/j.ssc.2008.06.027](https://doi.org/10.1016/j.ssc.2008.06.027). <https://www.sciencedirect.com/science/article/pii/S0038109808003608> (2008).
113. Masubuchi, S., Ono, M., Yoshida, K., Hirakawa, K. & Machida, T. Fabrication of graphene nanoribbon by local anodic oxidation lithography using atomic force microscope. *Applied Physics Letters* **94**, 082107. ISSN: 0003-6951. doi:[10.1063/1.3089693](https://doi.org/10.1063/1.3089693). <https://doi.org/10.1063/1.3089693> (2009).
114. Neubeck, S., Freitag, F., Yang, R. & Novoselov, K. S. Scanning probe lithography on graphene. *physica status solidi (b)* **247**, 2904–2908. ISSN: 1521-3951. doi:[10.1002/pssb.201000186](https://doi.org/10.1002/pssb.201000186). <https://onlinelibrary.wiley.com/doi/abs/10.1002/pssb.201000186> (2010).
115. Biró, L. P. & Lambin, P. Nanopatterning of graphene with crystallographic orientation control. *Carbon* **48**, 2677–2689. ISSN: 0008-6223. doi:[10.1016/j.carbon.2010.04.013](https://doi.org/10.1016/j.carbon.2010.04.013). <https://www.sciencedirect.com/science/article/pii/S0008622310002642> (2010).
116. Li, H. *et al.* Electrode-free anodic oxidation nanolithography of low-dimensional materials. *Nano Letters* **18**, 8011–8015. ISSN: 1530-6984. doi:[10.1021/acs.nanolett.8b04166](https://doi.org/10.1021/acs.nanolett.8b04166). <https://doi.org/10.1021/acs.nanolett.8b04166> (2018).
117. Uri, A. *et al.* Mapping the twist-angle disorder and Landau levels in magic-angle graphene. *Nature* **581**, 47–52. ISSN: 1476-4687. doi:[10.1038/s41586-020-2255-3](https://doi.org/10.1038/s41586-020-2255-3). <https://www.nature.com/articles/s41586-020-2255-3> (2020).
118. Choi, Y. *et al.* Electronic correlations in twisted bilayer graphene near the magic angle. *Nature Physics* **15**, 1174–1180. ISSN: 1745-2481. doi:[10.1038/s41567-019-0606-5](https://doi.org/10.1038/s41567-019-0606-5). <https://www.nature.com/articles/s41567-019-0606-5> (2019).
119. Kerelsky, A. *et al.* Maximized electron interactions at the magic angle in twisted bilayer graphene. *Nature* **572**, 95–100. ISSN: 1476-4687. doi:[10.1038/s41586-019-1431-9](https://doi.org/10.1038/s41586-019-1431-9). <https://www.nature.com/articles/s41586-019-1431-9> (2019).
120. Xie, Y. *et al.* Spectroscopic signatures of many-body correlations in magic-angle twisted bilayer graphene. *Nature* **572**, 101–105. ISSN: 1476-4687. doi:[10.1038/s41586-019-1422-x](https://doi.org/10.1038/s41586-019-1422-x). <https://www.nature.com/articles/s41586-019-1422-x> (2019).
121. Jiang, Y. *et al.* Charge order and broken rotational symmetry in magic-angle twisted bilayer graphene. *Nature* **573**, 91–95. ISSN: 1476-4687. doi:[10.1038/](https://doi.org/10.1038/)

- s41586-019-1460-4. <https://www.nature.com/articles/s41586-019-1460-4> (2019).
122. Holleis, L. *et al.* Nematicity and orbital depairing in superconducting Bernal bilayer graphene with strong spin orbit coupling. doi:10.48550/arXiv.2303.00742. arXiv: 2303.00742[cond-mat]. <http://arxiv.org/abs/2303.00742> (2024).
 123. Zibrov, A. A. *et al.* Tunable interacting composite fermion phases in a half-filled bilayer-graphene Landau level. *Nature* **549**, 360–364. ISSN: 0028-0836, 1476-4687. doi:10.1038/nature23893. <https://www.nature.com/articles/nature23893> (2017).
 124. Krinner, S. *et al.* Engineering cryogenic setups for 100-qubit scale superconducting circuit systems. *EPJ Quantum Technology* **6**, 1–29. ISSN: 2196-0763. doi:10.1140/epjqt/s40507-019-0072-0. <https://epjquantumtechnology.springeropen.com/articles/10.1140/epjqt/s40507-019-0072-0> (2019).
 125. Polski, R. M. *Electronic Correlations and Topology in Graphene Moiré Multilayers and InAs/GaSb-Derivative Systems* PhD thesis (Caltech, 2023).
 126. Kretinin, A. V. *et al.* Electronic properties of graphene encapsulated with different two-dimensional atomic crystals. *Nano Letters* **14**, 3270–3276. ISSN: 1530-6984. doi:10.1021/nl5006542. <https://doi.org/10.1021/nl5006542> (2014).
 127. Wilson, N. R. *et al.* Determination of band offsets, hybridization, and exciton binding in 2D semiconductor heterostructures. *Science Advances* **3**, e1601832. doi:10.1126/sciadv.1601832. <https://www.science.org/doi/10.1126/sciadv.1601832> (2017).
 128. Wang, D. *et al.* Quantum Hall effect measurement of spin–orbit coupling strengths in ultraclean bilayer graphene/WSe₂ heterostructures. *Nano Letters* **19**, 7028–7034. ISSN: 1530-6984. doi:10.1021/acs.nanolett.9b02445. <https://doi.org/10.1021/acs.nanolett.9b02445> (2019).
 129. Island, J. O. *et al.* Spin–orbit-driven band inversion in bilayer graphene by the van der Waals proximity effect. *Nature* **571**, 85–89. ISSN: 1476-4687. doi:10.1038/s41586-019-1304-2. <https://www.nature.com/articles/s41586-019-1304-2> (2019).
 130. Zihlmann, S. *et al.* Large spin relaxation anisotropy and valley-Zeeman spin-orbit coupling in WSe₂/graphene/h-BN heterostructures. *Physical Review B* **97**, 075434. doi:10.1103/PhysRevB.97.075434. <https://link.aps.org/doi/10.1103/PhysRevB.97.075434> (2018).
 131. Wakamura, T. *et al.* Spin-orbit interaction induced in graphene by transition metal dichalcogenides. *Physical Review B* **99**, 245402. doi:10.1103/PhysRevB.99.245402. <https://link.aps.org/doi/10.1103/PhysRevB.99.245402> (2019).

132. Koshino, M. *et al.* Maximally localized wannier orbitals and the extended Hubbard model for twisted bilayer graphene. *Physical Review X* **8**, 031087. doi:[10.1103/PhysRevX.8.031087](https://doi.org/10.1103/PhysRevX.8.031087). <https://link.aps.org/doi/10.1103/PhysRevX.8.031087> (2018).
133. Lilly, M. P. *et al.* Resistivity of dilute 2D electrons in an undoped GaAs heterostructure. *Physical Review Letters* **90**, 056806. doi:[10.1103/PhysRevLett.90.056806](https://doi.org/10.1103/PhysRevLett.90.056806). <https://link.aps.org/doi/10.1103/PhysRevLett.90.056806> (2003).
134. Stewart, G. R. Superconductivity in iron compounds. *Reviews of Modern Physics* **83**, 1589–1652. doi:[10.1103/RevModPhys.83.1589](https://doi.org/10.1103/RevModPhys.83.1589). <https://link.aps.org/doi/10.1103/RevModPhys.83.1589> (2011).
135. Wang, Z. *et al.* Strong interface-induced spin–orbit interaction in graphene on WS₂. *Nature Communications* **6**, 8339. ISSN: 2041-1723. doi:[10.1038/ncomms9339](https://doi.org/10.1038/ncomms9339). <https://www.nature.com/articles/ncomms9339> (2015).
136. Lian, B., Wang, Z. & Bernevig, B. A. Twisted bilayer graphene: A phonon-driven superconductor. *Physical Review Letters* **122**, 257002. ISSN: 0031-9007, 1079-7114. doi:[10.1103/PhysRevLett.122.257002](https://doi.org/10.1103/PhysRevLett.122.257002). <https://link.aps.org/doi/10.1103/PhysRevLett.122.257002> (2019).
137. Guinea, F. & Walet, N. R. Electrostatic effects, band distortions, and superconductivity in twisted graphene bilayers. *Proceedings of the National Academy of Sciences* **115**, 13174–13179. doi:[10.1073/pnas.1810947115](https://doi.org/10.1073/pnas.1810947115). <https://www.pnas.org/doi/10.1073/pnas.1810947115> (2018).
138. You, Y.-Z. & Vishwanath, A. Superconductivity from valley fluctuations and approximate SO(4) symmetry in a weak coupling theory of twisted bilayer graphene. *npj Quantum Materials* **4**, 1–12. ISSN: 2397-4648. doi:[10.1038/s41535-019-0153-4](https://doi.org/10.1038/s41535-019-0153-4). <https://www.nature.com/articles/s41535-019-0153-4> (2019).
139. Kozii, V., Isobe, H., Venderbos, J. W. F. & Fu, L. Nematic superconductivity stabilized by density wave fluctuations: Possible application to twisted bilayer graphene. *Physical Review B* **99**, 144507. doi:[10.1103/PhysRevB.99.144507](https://doi.org/10.1103/PhysRevB.99.144507). <https://link.aps.org/doi/10.1103/PhysRevB.99.144507> (2019).
140. Gu, X. *et al.* Antiferromagnetism and chiral *d*-wave superconductivity from an effective *t*-*J*-*D* model for twisted bilayer graphene. *Physical Review B* **101**, 180506. doi:[10.1103/PhysRevB.101.180506](https://doi.org/10.1103/PhysRevB.101.180506). <https://link.aps.org/doi/10.1103/PhysRevB.101.180506> (2020).
141. Polski, R. *et al.* Hierarchy of symmetry breaking correlated phases in twisted bilayer graphene. doi:[10.48550/arXiv.2205.05225](https://doi.org/10.48550/arXiv.2205.05225). arXiv: [2205.05225](https://arxiv.org/abs/2205.05225)[cond-mat]. <http://arxiv.org/abs/2205.05225> (2022).

142. Xie, M. & MacDonald, A. H. Weak-field Hall resistivity and spin-valley flavor symmetry breaking in magic-angle twisted bilayer graphene. *Physical Review Letters* **127**, 196401. doi:[10.1103/PhysRevLett.127.196401](https://doi.org/10.1103/PhysRevLett.127.196401). <https://link.aps.org/doi/10.1103/PhysRevLett.127.196401> (2021).
143. Qin, W., Zou, B. & MacDonald, A. H. Critical magnetic fields and electron pairing in magic-angle twisted bilayer graphene. *Physical Review B* **107**, 024509. doi:[10.1103/PhysRevB.107.024509](https://doi.org/10.1103/PhysRevB.107.024509). <https://link.aps.org/doi/10.1103/PhysRevB.107.024509> (2023).
144. González, J. & Stauber, T. Kohn-Luttinger superconductivity in twisted bilayer graphene. *Physical Review Letters* **122**, 026801. doi:[10.1103/PhysRevLett.122.026801](https://doi.org/10.1103/PhysRevLett.122.026801). <https://link.aps.org/doi/10.1103/PhysRevLett.122.026801> (2019).
145. Khalaf, E., Kruchkov, A. J., Tarnopolsky, G. & Vishwanath, A. Magic angle hierarchy in twisted graphene multilayers. *Physical Review B* **100**, 085109. doi:[10.1103/PhysRevB.100.085109](https://doi.org/10.1103/PhysRevB.100.085109). <https://link.aps.org/doi/10.1103/PhysRevB.100.085109> (2019).
146. Cao, Y., Park, J. M., Watanabe, K., Taniguchi, T. & Jarillo-Herrero, P. Pauli-limit violation and re-entrant superconductivity in moiré graphene. *Nature* **595**, 526–531. ISSN: 1476-4687. doi:[10.1038/s41586-021-03685-y](https://doi.org/10.1038/s41586-021-03685-y). <https://www.nature.com/articles/s41586-021-03685-y> (2021).
147. Cao, Y. *et al.* Superlattice-induced insulating states and valley-protected orbits in twisted bilayer graphene. *Physical Review Letters* **117**, 116804. doi:[10.1103/PhysRevLett.117.116804](https://doi.org/10.1103/PhysRevLett.117.116804). <https://link.aps.org/doi/10.1103/PhysRevLett.117.116804> (2016).
148. Kwan, Y. H. *et al.* Kekulé spiral order at all nonzero integer fillings in twisted bilayer graphene. *Physical Review X* **11**, 041063. doi:[10.1103/PhysRevX.11.041063](https://doi.org/10.1103/PhysRevX.11.041063). <https://link.aps.org/doi/10.1103/PhysRevX.11.041063> (2021).
149. Bultinck, N. *et al.* Ground state and hidden symmetry of magic-angle graphene at even integer filling. *Physical Review X* **10**, 031034. doi:[10.1103/PhysRevX.10.031034](https://doi.org/10.1103/PhysRevX.10.031034). <https://link.aps.org/doi/10.1103/PhysRevX.10.031034> (2020).
150. Lian, B. *et al.* Twisted bilayer graphene. IV. Exact insulator ground states and phase diagram. *Physical Review B* **103**, 205414. doi:[10.1103/PhysRevB.103.205414](https://doi.org/10.1103/PhysRevB.103.205414). <https://link.aps.org/doi/10.1103/PhysRevB.103.205414> (2021).
151. Xie, F., Regnault, N., Călugăru, D., Bernevig, B. A. & Lian, B. Twisted symmetric trilayer graphene. II. Projected Hartree-Fock study. *Physical Review B* **104**, 115167. doi:[10.1103/PhysRevB.104.115167](https://doi.org/10.1103/PhysRevB.104.115167). <https://link.aps.org/doi/10.1103/PhysRevB.104.115167> (2021).

152. Christos, M., Sachdev, S. & Scheurer, M. S. Correlated insulators, semimetals, and superconductivity in twisted trilayer graphene. *Physical Review X* **12**, 021018. doi:[10.1103/PhysRevX.12.021018](https://doi.org/10.1103/PhysRevX.12.021018). <https://link.aps.org/doi/10.1103/PhysRevX.12.021018> (2022).
153. Qin, W. & MacDonald, A. H. In-plane critical magnetic fields in magic-angle twisted trilayer graphene. *Physical Review Letters* **127**, 097001. ISSN: 0031-9007, 1079-7114. doi:[10.1103/PhysRevLett.127.097001](https://doi.org/10.1103/PhysRevLett.127.097001). <https://link.aps.org/doi/10.1103/PhysRevLett.127.097001> (2021).
154. Kopnin, N. B., Heikkilä, T. T. & Volovik, G. E. High-temperature surface superconductivity in topological flat-band systems. *Physical Review B* **83**, 220503. ISSN: 1098-0121, 1550-235X. doi:[10.1103/PhysRevB.83.220503](https://doi.org/10.1103/PhysRevB.83.220503). <https://link.aps.org/doi/10.1103/PhysRevB.83.220503> (2011).
155. Shavit, G., Berg, E., Stern, A. & Oreg, Y. Theory of correlated insulators and superconductivity in twisted bilayer graphene. *Physical Review Letters* **127**, 247703. ISSN: 0031-9007, 1079-7114. doi:[10.1103/PhysRevLett.127.247703](https://doi.org/10.1103/PhysRevLett.127.247703). <https://link.aps.org/doi/10.1103/PhysRevLett.127.247703> (2021).
156. Ledwith, P. J. *et al.* TB or not TB? Contrasting properties of twisted bilayer graphene and the alternating twist n -layer structures ($n = 3, 4, 5, \dots$). doi:[10.48550/arXiv.2111.11060](https://doi.org/10.48550/arXiv.2111.11060). arXiv: [2111.11060](https://arxiv.org/abs/2111.11060)[cond-mat]. <http://arxiv.org/abs/2111.11060> (2021).
157. Suhl, H., Matthias, B. T. & Walker, L. R. Bardeen-Cooper-Schrieffer theory of superconductivity in the case of overlapping bands. *Physical Review Letters* **3**, 552–554. doi:[10.1103/PhysRevLett.3.552](https://doi.org/10.1103/PhysRevLett.3.552). <https://link.aps.org/doi/10.1103/PhysRevLett.3.552> (1959).
158. Dolgov, O. V., Mazin, I. I., Parker, D. & Golubov, A. A. Interband superconductivity: Contrasts between Bardeen-Cooper-Schrieffer and Eliashberg theories. *Physical Review B* **79**, 060502. doi:[10.1103/PhysRevB.79.060502](https://doi.org/10.1103/PhysRevB.79.060502). <https://link.aps.org/doi/10.1103/PhysRevB.79.060502> (2009).
159. Hirschfeld, P. J., Korshunov, M. M. & Mazin, I. I. Gap symmetry and structure of Fe-based superconductors. *Reports on Progress in Physics* **74**, 124508. ISSN: 0034-4885, 1361-6633. doi:[10.1088/0034-4885/74/12/124508](https://doi.org/10.1088/0034-4885/74/12/124508). <https://iopscience.iop.org/article/10.1088/0034-4885/74/12/124508> (2011).
160. Chen, X., Maiti, S., Linscheid, A. & Hirschfeld, P. J. Electron pairing in the presence of incipient bands in iron-based superconductors. *Physical Review B* **92**, 224514. doi:[10.1103/PhysRevB.92.224514](https://doi.org/10.1103/PhysRevB.92.224514). <https://link.aps.org/doi/10.1103/PhysRevB.92.224514> (2015).

161. Rademaker, L., Abanin, D. A. & Mellado, P. Charge smoothening and band flattening due to Hartree corrections in twisted bilayer graphene. *Physical Review B* **100**, 205114. doi:[10.1103/PhysRevB.100.205114](https://doi.org/10.1103/PhysRevB.100.205114). <https://link.aps.org/doi/10.1103/PhysRevB.100.205114> (2019).
162. Goodwin, Z. A. H., Vitale, V., Liang, X., Mostofi, A. A. & Lischner, J. Hartree theory calculations of quasiparticle properties in twisted bilayer graphene. *Electronic Structure* **2**, 034001. ISSN: 2516-1075. doi:[10.1088/2516-1075/ab9f94](https://doi.org/10.1088/2516-1075/ab9f94). <https://iopscience.iop.org/article/10.1088/2516-1075/ab9f94> (2020).
163. Calderón, M. J. & Bascones, E. Interactions in the 8-orbital model for twisted bilayer graphene. *Physical Review B* **102**, 155149. doi:[10.1103/PhysRevB.102.155149](https://doi.org/10.1103/PhysRevB.102.155149). <https://link.aps.org/doi/10.1103/PhysRevB.102.155149> (2020).
164. Choi, Y. *et al.* Interaction-driven band flattening and correlated phases in twisted bilayer graphene. *Nature Physics* **17**, 1375–1381. ISSN: 1745-2481. doi:[10.1038/s41567-021-01359-0](https://doi.org/10.1038/s41567-021-01359-0). <https://www.nature.com/articles/s41567-021-01359-0> (2021).
165. Kolář, K., Zhang, Y., Nadj-Perge, S., von Oppen, F. & Lewandowski, C. Electrostatic fate of N -layer moiré graphene. *Physical Review B* **108**, 195148. doi:[10.1103/PhysRevB.108.195148](https://doi.org/10.1103/PhysRevB.108.195148). <https://link.aps.org/doi/10.1103/PhysRevB.108.195148> (2023).
166. Liu, X., Zhang, N. J., Watanabe, K., Taniguchi, T. & Li, J. I. A. Isospin order in superconducting magic-angle twisted trilayer graphene. *Nature Physics* **18**, 522–527. ISSN: 1745-2481. doi:[10.1038/s41567-022-01515-0](https://doi.org/10.1038/s41567-022-01515-0). <https://www.nature.com/articles/s41567-022-01515-0> (2022).
167. McCann, E. Asymmetry gap in the electronic band structure of bilayer graphene. *Physical Review B* **74**, 161403. doi:[10.1103/PhysRevB.74.161403](https://doi.org/10.1103/PhysRevB.74.161403). <https://link.aps.org/doi/10.1103/PhysRevB.74.161403> (2006).
168. Zhang, Y. *et al.* Direct observation of a widely tunable bandgap in bilayer graphene. *Nature* **459**, 820–823. ISSN: 1476-4687. doi:[10.1038/nature08105](https://doi.org/10.1038/nature08105). <https://www.nature.com/articles/nature08105> (2009).
169. Gmitra, M., Kochan, D., Högl, P. & Fabian, J. Trivial and inverted Dirac bands and the emergence of quantum spin Hall states in graphene on transition-metal dichalcogenides. *Physical Review B* **93**, 155104. doi:[10.1103/PhysRevB.93.155104](https://doi.org/10.1103/PhysRevB.93.155104). <https://link.aps.org/doi/10.1103/PhysRevB.93.155104> (2016).
170. Gmitra, M. & Fabian, J. Proximity effects in bilayer graphene on monolayer WSe_2 : Field-effect spin valley locking, spin-orbit valve, and spin transistor. *Physical Review Letters* **119**, 146401. doi:[10.1103/PhysRevLett.119.146401](https://doi.org/10.1103/PhysRevLett.119.146401).

146401. <https://link.aps.org/doi/10.1103/PhysRevLett.119.146401> (2017).
171. Wang, Z. *et al.* Origin and magnitude of ‘designer’ spin-orbit interaction in graphene on semiconducting transition metal dichalcogenides. *Physical Review X* **6**, 041020. doi:[10.1103/PhysRevX.6.041020](https://doi.org/10.1103/PhysRevX.6.041020). <https://link.aps.org/doi/10.1103/PhysRevX.6.041020> (2016).
172. Yang, B. *et al.* Strong electron-hole symmetric Rashba spin-orbit coupling in graphene/monolayer transition metal dichalcogenide heterostructures. *Physical Review B* **96**, 041409. doi:[10.1103/PhysRevB.96.041409](https://doi.org/10.1103/PhysRevB.96.041409). <https://link.aps.org/doi/10.1103/PhysRevB.96.041409> (2017).
173. Li, Y. & Koshino, M. Twist-angle dependence of the proximity spin-orbit coupling in graphene on transition-metal dichalcogenides. *Physical Review B* **99**, 075438. ISSN: 2469-9950, 2469-9969. doi:[10.1103/PhysRevB.99.075438](https://doi.org/10.1103/PhysRevB.99.075438). <https://link.aps.org/doi/10.1103/PhysRevB.99.075438> (2019).
174. David, A., Rakyta, P., Kormányos, A. & Burkard, G. Induced spin-orbit coupling in twisted graphene–transition metal dichalcogenide heterobilayers: Twistronics meets spintronics. *Physical Review B* **100**, 085412. doi:[10.1103/PhysRevB.100.085412](https://doi.org/10.1103/PhysRevB.100.085412). <https://link.aps.org/doi/10.1103/PhysRevB.100.085412> (2019).
175. Naimer, T., Zollner, K., Gmitra, M. & Fabian, J. Twist-angle dependent proximity induced spin-orbit coupling in graphene/transition metal dichalcogenide heterostructures. *Physical Review B* **104**, 195156. doi:[10.1103/PhysRevB.104.195156](https://doi.org/10.1103/PhysRevB.104.195156). <https://link.aps.org/doi/10.1103/PhysRevB.104.195156> (2021).
176. Amann, J. *et al.* Counterintuitive gate dependence of weak antilocalization in bilayer graphene/WSe₂ heterostructures. *Physical Review B* **105**, 115425. doi:[10.1103/PhysRevB.105.115425](https://doi.org/10.1103/PhysRevB.105.115425). <https://link.aps.org/doi/10.1103/PhysRevB.105.115425> (2022).
177. Zaletel, M. P. & Khoo, J. Y. The gate-tunable strong and fragile topology of multilayer-graphene on a transition metal dichalcogenide. doi:[10.48550/arXiv.1901.01294](https://doi.org/10.48550/arXiv.1901.01294). arXiv: [1901.01294\[cond-mat\]](https://arxiv.org/abs/1901.01294). <http://arxiv.org/abs/1901.01294> (2019).
178. Khoo, J. Y., Morpurgo, A. F. & Levitov, L. On-demand spin–orbit interaction from which-layer tunability in bilayer graphene. *Nano Letters* **17**, 7003–7008. ISSN: 1530-6984. doi:[10.1021/acs.nanolett.7b03604](https://doi.org/10.1021/acs.nanolett.7b03604). <https://doi.org/10.1021/acs.nanolett.7b03604> (2017).
179. Khoo, J. Y. & Levitov, L. Tunable quantum Hall edge conduction in bilayer graphene through spin-orbit interaction. *Physical Review B* **98**, 115307. doi:[10.1103/PhysRevB.98.115307](https://doi.org/10.1103/PhysRevB.98.115307). <https://link.aps.org/doi/10.1103/PhysRevB.98.115307> (2018).

180. Taychatanapat, T., Watanabe, K., Taniguchi, T. & Jarillo-Herrero, P. Electrically tunable transverse magnetic focusing in graphene. *Nature Physics* **9**, 225–229. ISSN: 1745-2481. doi:[10.1038/nphys2549](https://doi.org/10.1038/nphys2549). <https://www.nature.com/articles/nphys2549> (2013).
181. Dong, Z., Davydova, M., Ogunnaike, O. & Levitov, L. Isospin- and momentum-polarized orders in bilayer graphene. *Physical Review B* **107**, 075108. doi:[10.1103/PhysRevB.107.075108](https://doi.org/10.1103/PhysRevB.107.075108). <https://link.aps.org/doi/10.1103/PhysRevB.107.075108> (2023).
182. Huang, C. *et al.* Spin and orbital metallic magnetism in rhombohedral trilayer graphene. *Physical Review B* **107**, L121405. doi:[10.1103/PhysRevB.107.L121405](https://doi.org/10.1103/PhysRevB.107.L121405). <https://link.aps.org/doi/10.1103/PhysRevB.107.L121405> (2023).
183. Fatemi, V. & Ruhman, J. Synthesizing Coulombic superconductivity in van der Waals bilayers. *Physical Review B* **98**, 094517. doi:[10.1103/PhysRevB.98.094517](https://doi.org/10.1103/PhysRevB.98.094517). <https://link.aps.org/doi/10.1103/PhysRevB.98.094517> (2018).
184. Chou, Y.-Z., Wu, F. & Das Sarma, S. Enhanced superconductivity through virtual tunneling in Bernal bilayer graphene coupled to WSe₂. *Physical Review B* **106**, L180502. doi:[10.1103/PhysRevB.106.L180502](https://doi.org/10.1103/PhysRevB.106.L180502). <https://link.aps.org/doi/10.1103/PhysRevB.106.L180502> (2022).
185. Dong, Z. & Levitov, L. Superconductivity in the vicinity of an isospin-polarized state in a cubic Dirac band. doi:[10.48550/arXiv.2109.01133](https://doi.org/10.48550/arXiv.2109.01133). arXiv: [2109.01133\[cond-mat\]](https://arxiv.org/abs/2109.01133). <http://arxiv.org/abs/2109.01133> (2021).
186. Ghazaryan, A., Holder, T., Serbyn, M. & Berg, E. Unconventional superconductivity in systems with annular Fermi surfaces: Application to rhombohedral trilayer graphene. *Physical Review Letters* **127**, 247001. doi:[10.1103/PhysRevLett.127.247001](https://doi.org/10.1103/PhysRevLett.127.247001). <https://link.aps.org/doi/10.1103/PhysRevLett.127.247001> (2021).
187. Qin, W. *et al.* Functional renormalization group study of superconductivity in rhombohedral trilayer graphene. *Physical Review Letters* **130**, 146001. doi:[10.1103/PhysRevLett.130.146001](https://doi.org/10.1103/PhysRevLett.130.146001). <https://link.aps.org/doi/10.1103/PhysRevLett.130.146001> (2023).
188. You, Y.-Z. & Vishwanath, A. Kohn-Luttinger superconductivity and intervalley coherence in rhombohedral trilayer graphene. *Physical Review B* **105**, 134524. doi:[10.1103/PhysRevB.105.134524](https://doi.org/10.1103/PhysRevB.105.134524). <https://link.aps.org/doi/10.1103/PhysRevB.105.134524> (2022).
189. Cea, T., Pantaleón, P. A., Phong, V. T. & Guinea, F. Superconductivity from repulsive interactions in rhombohedral trilayer graphene: A Kohn-Luttinger-like mechanism. *Physical Review B* **105**, 075432. doi:[10.1103/PhysRevB.105.075432](https://doi.org/10.1103/PhysRevB.105.075432).

- [105.075432](https://link.aps.org/doi/10.1103/PhysRevB.105.075432). <https://link.aps.org/doi/10.1103/PhysRevB.105.075432> (2022).
190. Chou, Y.-Z., Wu, F., Sau, J. D. & Das Sarma, S. Acoustic-phonon-mediated superconductivity in rhombohedral trilayer graphene. *Physical Review Letters* **127**, 187001. doi:[10.1103/PhysRevLett.127.187001](https://doi.org/10.1103/PhysRevLett.127.187001). <https://link.aps.org/doi/10.1103/PhysRevLett.127.187001> (2021).
191. Chou, Y.-Z., Wu, F., Sau, J. D. & Das Sarma, S. Acoustic-phonon-mediated superconductivity in Bernal bilayer graphene. *Physical Review B* **105**, L100503. doi:[10.1103/PhysRevB.105.L100503](https://doi.org/10.1103/PhysRevB.105.L100503). <https://link.aps.org/doi/10.1103/PhysRevB.105.L100503> (2022).
192. Zollner, K., João, S. M., Nikolić, B. K. & Fabian, J. Twist- and gate-tunable proximity spin-orbit coupling, spin relaxation anisotropy, and charge-to-spin conversion in heterostructures of graphene and transition metal dichalcogenides. *Physical Review B* **108**, 235166. doi:[10.1103/PhysRevB.108.235166](https://doi.org/10.1103/PhysRevB.108.235166). <https://link.aps.org/doi/10.1103/PhysRevB.108.235166> (2023).
193. Seyler, K. L. *et al.* Electrical control of second-harmonic generation in a WSe₂ monolayer transistor. *Nature Nanotechnology* **10**, 407–411. ISSN: 1748-3395. doi:[10.1038/nnano.2015.73](https://doi.org/10.1038/nnano.2015.73). <https://www.nature.com/articles/nnano.2015.73> (2015).
194. Li, C. *et al.* Tunable superconductivity in electron- and hole-doped Bernal bilayer graphene. *Nature*, 1–7. ISSN: 1476-4687. doi:[10.1038/s41586-024-07584-w](https://doi.org/10.1038/s41586-024-07584-w). <https://www.nature.com/articles/s41586-024-07584-w> (2024).
195. Morel, P. & Anderson, P. W. Calculation of the superconducting state parameters with retarded electron-phonon interaction. *Physical Review* **125**, 1263–1271. doi:[10.1103/PhysRev.125.1263](https://doi.org/10.1103/PhysRev.125.1263). <https://link.aps.org/doi/10.1103/PhysRev.125.1263> (1962).
196. Kedves, M. *et al.* Stabilizing the inverted phase of a WSe₂/BLG/WSe₂ heterostructure via hydrostatic pressure. *Nano Letters* **23**, 9508–9514. ISSN: 1530-6984. doi:[10.1021/acs.nanolett.3c03029](https://doi.org/10.1021/acs.nanolett.3c03029). <https://doi.org/10.1021/acs.nanolett.3c03029> (2023).
197. Lin, J.-X. *et al.* Spontaneous momentum polarization and diodicity in Bernal bilayer graphene. doi:[10.48550/arXiv.2302.04261](https://doi.org/10.48550/arXiv.2302.04261). arXiv: [2302.04261](https://arxiv.org/abs/2302.04261)[cond-mat]. <http://arxiv.org/abs/2302.04261> (2023).
198. Chatterjee, S., Wang, T., Berg, E. & Zaletel, M. P. Inter-valley coherent order and isospin fluctuation mediated superconductivity in rhombohedral trilayer graphene. *Nature Communications* **13**, 6013. ISSN: 2041-1723. doi:[10.1038/s41467-022-33561-w](https://doi.org/10.1038/s41467-022-33561-w). <https://www.nature.com/articles/s41467-022-33561-w> (2022).

199. Arp, T. *et al.* Intervalley coherence and intrinsic spin–orbit coupling in rhombohedral trilayer graphene. *Nature Physics*, 1–8. ISSN: 1745-2481. doi:[10.1038/s41567-024-02560-7](https://doi.org/10.1038/s41567-024-02560-7). <https://www.nature.com/articles/s41567-024-02560-7> (2024).
200. Koh, J. M., Thomson, A., Alicea, J. & Lantagne-Hurtubise, É. Symmetry-broken metallic orders in spin-orbit-coupled Bernal bilayer graphene. doi:[10.48550/arXiv.2407.09612](https://doi.org/10.48550/arXiv.2407.09612). arXiv: [2407.09612\[cond-mat\]](https://arxiv.org/abs/2407.09612). <http://arxiv.org/abs/2407.09612> (2024).
201. Xie, M. & Das Sarma, S. Flavor symmetry breaking in spin-orbit coupled bilayer graphene. *Physical Review B* **107**, L201119. doi:[10.1103/PhysRevB.107.L201119](https://doi.org/10.1103/PhysRevB.107.L201119). <https://link.aps.org/doi/10.1103/PhysRevB.107.L201119> (2023).
202. Thomson, A., Sorensen, I. M., Nadj-Perge, S. & Alicea, J. Gate-defined wires in twisted bilayer graphene: From electrical detection of intervalley coherence to internally engineered Majorana modes. *Physical Review B* **105**, L081405. doi:[10.1103/PhysRevB.105.L081405](https://doi.org/10.1103/PhysRevB.105.L081405). <https://link.aps.org/doi/10.1103/PhysRevB.105.L081405> (2022).
203. Koh, J. M., Alicea, J. & Lantagne-Hurtubise, É. Correlated phases in spin-orbit-coupled rhombohedral trilayer graphene. *Physical Review B* **109**, 035113. doi:[10.1103/PhysRevB.109.035113](https://doi.org/10.1103/PhysRevB.109.035113). <https://link.aps.org/doi/10.1103/PhysRevB.109.035113> (2024).
204. Zhumagulov, Y., Kochan, D. & Fabian, J. Swapping exchange and spin-orbit induced correlated phases in proximitized Bernal bilayer graphene. *Physical Review B* **110**, 045427. doi:[10.1103/PhysRevB.110.045427](https://doi.org/10.1103/PhysRevB.110.045427). <https://link.aps.org/doi/10.1103/PhysRevB.110.045427> (2024).
205. Ran, S. *et al.* Extreme magnetic field-boosted superconductivity. *Nature Physics* **15**, 1250–1254. ISSN: 1745-2481. doi:[10.1038/s41567-019-0670-x](https://doi.org/10.1038/s41567-019-0670-x). <https://www.nature.com/articles/s41567-019-0670-x> (2019).
206. Ran, S. *et al.* Nearly ferromagnetic spin-triplet superconductivity. *Science* **365**, 684–687. doi:[10.1126/science.aav8645](https://doi.org/10.1126/science.aav8645). <https://www.science.org/doi/10.1126/science.aav8645> (2019).
207. Lu, J. *et al.* Full superconducting dome of strong Ising protection in gated monolayer WS₂. *Proceedings of the National Academy of Sciences* **115**, 3551–3556. doi:[10.1073/pnas.1716781115](https://doi.org/10.1073/pnas.1716781115). <https://www.pnas.org/doi/full/10.1073/pnas.1716781115> (2018).
208. Dong, Z., Lantagne-Hurtubise, É. & Alicea, J. Superconductivity from spin-canting fluctuations in rhombohedral graphene. doi:[10.48550/arXiv.2406.17036](https://doi.org/10.48550/arXiv.2406.17036). arXiv: [2406.17036\[cond-mat\]](https://arxiv.org/abs/2406.17036). <http://arxiv.org/abs/2406.17036> (2024).

209. Chen, S. *et al.* Electrically tunable correlated and topological states in twisted monolayer–bilayer graphene. *Nature Physics* **17**, 374–380. ISSN: 1745-2473, 1745-2481. doi:[10.1038/s41567-020-01062-6](https://doi.org/10.1038/s41567-020-01062-6). <https://www.nature.com/articles/s41567-020-01062-6> (2021).
210. Xia, L.-Q. *et al.* Helical trilayer graphene: a moiré platform for strongly-interacting topological bands. doi:[10.48550/arXiv.2310.12204](https://doi.org/10.48550/arXiv.2310.12204). arXiv: [2310.12204\[cond-mat\]](https://arxiv.org/abs/2310.12204). <http://arxiv.org/abs/2310.12204> (2023).
211. Waters, D. *et al.* Mixed-dimensional moiré systems of twisted graphitic thin films. *Nature* **620**, 750–755. ISSN: 1476-4687. doi:[10.1038/s41586-023-06290-3](https://doi.org/10.1038/s41586-023-06290-3). <https://www.nature.com/articles/s41586-023-06290-3> (2023).
212. Wang, L. *et al.* Correlated electronic phases in twisted bilayer transition metal dichalcogenides. *Nature Materials* **19**, 861–866. ISSN: 1476-4660. doi:[10.1038/s41563-020-0708-6](https://doi.org/10.1038/s41563-020-0708-6). <https://www.nature.com/articles/s41563-020-0708-6> (2020).
213. Tang, Y. *et al.* Simulation of Hubbard model physics in WSe₂/WS₂ moiré superlattices. *Nature* **579**, 353–358. ISSN: 1476-4687. doi:[10.1038/s41586-020-2085-3](https://doi.org/10.1038/s41586-020-2085-3). <https://www.nature.com/articles/s41586-020-2085-3> (2020).
214. Su, R., Kuiri, M., Watanabe, K., Taniguchi, T. & Folk, J. Superconductivity in twisted double bilayer graphene stabilized by WSe₂. *Nature Materials* **22**, 1332–1337. ISSN: 1476-4660. doi:[10.1038/s41563-023-01653-7](https://doi.org/10.1038/s41563-023-01653-7). <https://www.nature.com/articles/s41563-023-01653-7> (2023).
215. Khalaf, E., Chatterjee, S., Bultinck, N., Zaletel, M. P. & Vishwanath, A. Charged skyrmions and topological origin of superconductivity in magic-angle graphene. *Science Advances* **7**, eabf5299. doi:[10.1126/sciadv.abf5299](https://doi.org/10.1126/sciadv.abf5299). <https://www.science.org/doi/10.1126/sciadv.abf5299> (2021).
216. Yankowitz, M. *et al.* Dynamic band-structure tuning of graphene moiré superlattices with pressure. *Nature* **557**, 404–408. ISSN: 1476-4687. doi:[10.1038/s41586-018-0107-1](https://doi.org/10.1038/s41586-018-0107-1). <https://www.nature.com/articles/s41586-018-0107-1> (2018).
217. De Vries, F. K. *et al.* Gate-defined Josephson junctions in magic-angle twisted bilayer graphene. *Nature Nanotechnology* **16**, 760–763. ISSN: 1748-3395. doi:[10.1038/s41565-021-00896-2](https://doi.org/10.1038/s41565-021-00896-2). <https://www.nature.com/articles/s41565-021-00896-2> (2021).
218. Rodan-Legrain, D. *et al.* Highly tunable junctions and non-local Josephson effect in magic-angle graphene tunnelling devices. *Nature Nanotechnology* **16**, 769–775. ISSN: 1748-3395. doi:[10.1038/s41565-021-00894-4](https://doi.org/10.1038/s41565-021-00894-4). <https://www.nature.com/articles/s41565-021-00894-4> (2021).

219. Portolés, E. *et al.* A tunable monolithic SQUID in twisted bilayer graphene. *Nature Nanotechnology* **17**, 1159–1164. ISSN: 1748-3395. doi:[10.1038/s41565-022-01222-0](https://doi.org/10.1038/s41565-022-01222-0). <https://www.nature.com/articles/s41565-022-01222-0> (2022).
220. Inbar, A. *et al.* The quantum twisting microscope. *Nature* **614**, 682–687. ISSN: 1476-4687. doi:[10.1038/s41586-022-05685-y](https://doi.org/10.1038/s41586-022-05685-y). <https://www.nature.com/articles/s41586-022-05685-y> (2023).
221. Tang, H. *et al.* On-chip multi-degree-of-freedom control of two-dimensional quantum and nonlinear materials. doi:[10.48550/arXiv.2311.12030](https://doi.org/10.48550/arXiv.2311.12030). arXiv: [2311.12030](https://arxiv.org/abs/2311.12030)[cond-mat, physics:physics]. <http://arxiv.org/abs/2311.12030> (2024).
222. Lu, Z. *et al.* Fractional quantum anomalous Hall effect in multilayer graphene. *Nature* **626**, 759–764. ISSN: 1476-4687. doi:[10.1038/s41586-023-07010-7](https://doi.org/10.1038/s41586-023-07010-7). <https://www.nature.com/articles/s41586-023-07010-7> (2024).
223. Cohen, L. A. *et al.* Nanoscale electrostatic control in ultraclean van der Waals heterostructures by local anodic oxidation of graphite gates. *Nature Physics* **19**, 1502–1508. ISSN: 1745-2481. doi:[10.1038/s41567-023-02114-3](https://doi.org/10.1038/s41567-023-02114-3). <https://www.nature.com/articles/s41567-023-02114-3> (2023).
224. Xie, Y.-M., Lantagne-Hurtubise, É., Young, A. F., Nadj-Perge, S. & Alicea, J. Gate-defined topological Josephson junctions in Bernal bilayer graphene. *Physical Review Letters* **131**, 146601. doi:[10.1103/PhysRevLett.131.146601](https://doi.org/10.1103/PhysRevLett.131.146601). <https://link.aps.org/doi/10.1103/PhysRevLett.131.146601> (2023).

Appendix A

SUPPLEMENTARY MATERIALS FOR CHAPTER 3

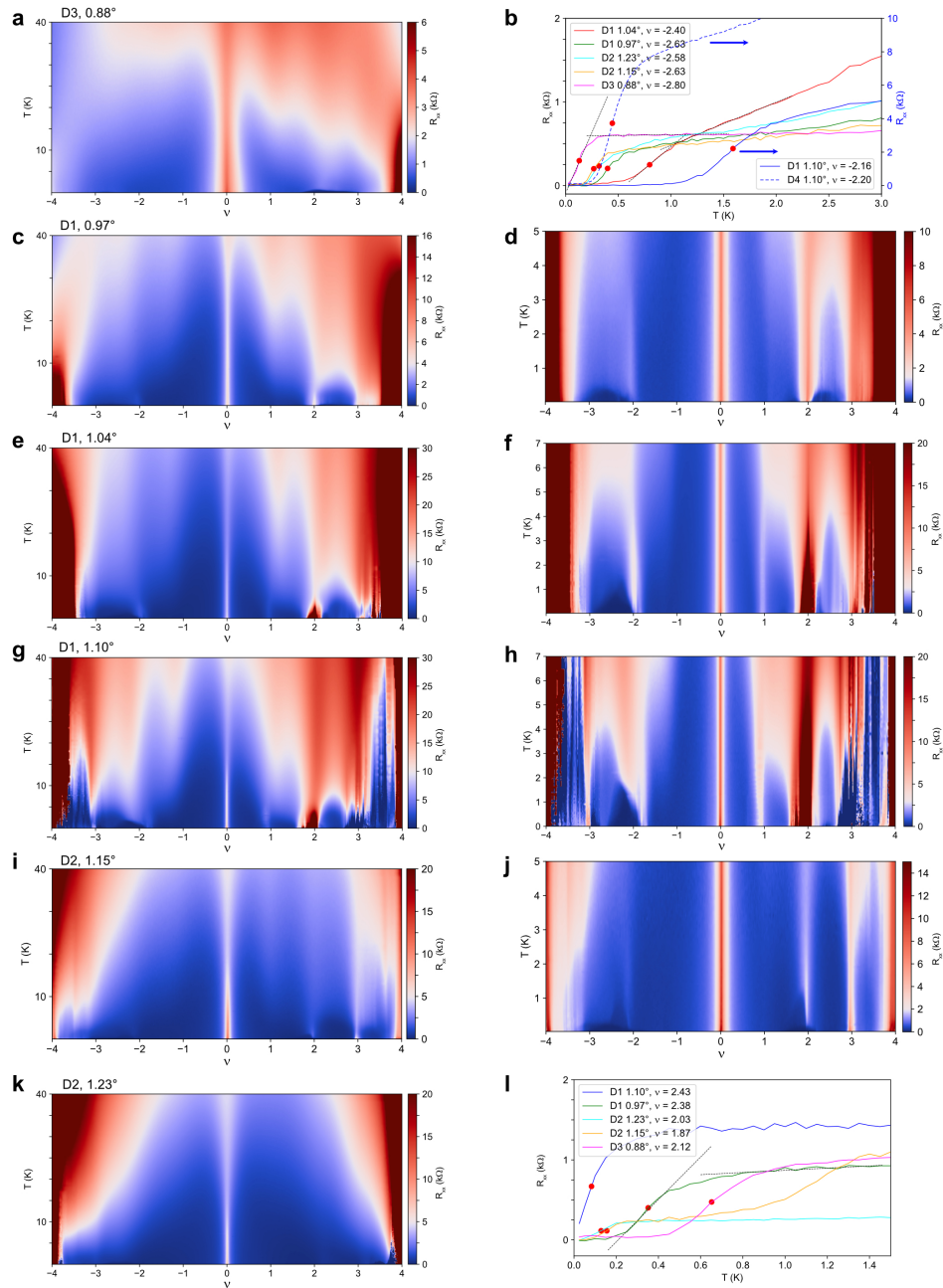


Figure A.1: R_{xx} versus temperature and filling factor ν for a range of TBG-WSe₂ devices at different twist angles.

SUPPLEMENTARY MATERIALS FOR CHAPTER 4

Possible origins of the extended superconducting pocket in TPG

Here we present several scenarios that can result in the superconductivity of TPG extending to $\nu \approx +5$, and discuss these scenarios in the context of experimental observations. We note that in the discussion below, ν denotes the total number of electrons per moiré site, and ν_{flat} denotes the number of electrons per moiré site added to the flat TBG-like bands.

Scenario (i): flat TBG-like bands are filled to $\nu_{\text{flat}} = +3$ at $\nu = +5$

For TBG and TTG, the strongest superconducting pockets normally start from $|\nu| = 2$ and end around $|\nu| = 3$. Therefore, a conventional scenario would suggest that TPG could behave in a similar way, i.e., flat TBG-like bands are filled to $\nu_{\text{flat}} = +3$ when superconductivity is diminished at $\nu = +5$. This scenario implies that the additional two electrons per moiré site are distributed in the dispersive TBG- and MLG-like bands due to the interaction effects, with a large portion of the charge carriers being hosted by the dispersive TBG-like bands. Since vHs of the dispersive TBG-like bands are normally found around half filling, the corresponding Hall density signatures are expected to occur at the same filling, i.e., $\nu = +5$ in this scenario. However, in the experiment we observe vHs signatures originating from the dispersive TBG-like bands near $\nu \approx +6$ instead (see Fig. 4.15). This line of reasoning allows us to completely rule out scenario (i), therefore, we conclude that superconductivity exceeds flat-band filling $\nu_{\text{flat}} = +3$ for electron-doped TPG.

Scenario (ii): flat TBG-like bands are filled close to $\nu_{\text{flat}} = +4$ at $\nu = +5$

As a result of interactions, a fraction of electrons are preferentially distributed in the dispersive TBG- and MLG- like bands [165]. It is therefore possible that for total filling of $\nu \approx +5$, the flat TBG-like bands are filled close to $\nu_{\text{flat}} \approx +4$, with the extra one electron per moiré site being distributed in the other bands. We show the filling correspondence between ν_{flat} and ν for various interaction terms and dielectric constants (see Fig. 4.14). In this scenario, the modeling suggests that the filling of the flat bands is nearly four ($\nu_{\text{flat}} > +3.8$), which is well outside typical TBG behavior.

Scenario (iii): flat TBG-like bands are fully filled to $\nu_{\text{flat}} = +4$ before $\nu = +5$ or hybridization of different bands obscures the distinction between them

The last scenario suggests either that the flat TBG-like bands are fully filled *before* the suppression of superconductivity, in which case superconductivity would exist in the more dispersive bands, *or* that the distinction between the different TBG- and MLG-like bands breaks down due to hybridization (i.e. mixing), even at $D = 0$. As discussed in previous sections, such mixing between flat, dispersive TBG- and MLG-like bands can happen when mirror symmetry is broken. Moreover, layer-to-layer charge inhomogeneity or distant-layer coupling allow for band hybridization even in the presence of mirror symmetry.

In the context of scenario (iii), we speculate on the polarized or un-polarized nature of the active bands in the regime $+4 < \nu < +5$. One simple possibility is that the dispersive TBG-like bands spontaneously break the flavor symmetries on its own, with the flat bands playing relatively little role. Another possibility is that hybridization obviates the distinction between flat and dispersive bands such that flavor polarization is allowed to persist far beyond. Further experiments will be needed to help ascertain the extent of flavor polarization that persists to $\nu = +5$.

Experimental signatures in electron-doped TPG

Experimentally, starting from low D fields, we observe a drop in Hall density at $\nu \approx +4$ which surprisingly does not affect superconductivity in any abrupt way (superconductivity continuously evolves and is present until $\nu \approx +5$). As the D field is increased, this Hall density drop is gradually replaced by a transition where Hall density changes sign (Fig. 4.16a lower panel). The high D -field transition can be interpreted as a “gap” feature emerging in the band structure similar to TTG [45]. Further measurements of R_{xx} show that the corresponding $\nu \approx +4$ feature does not shift with temperature (Fig. 4.16a upper panel) and is significantly broadened at high B fields, resembling the feature associated with the flat-band gap in TTG. These observations indicate that the $\nu = +4$ feature is naturally explained as either marking the end of the flat bands or resulting from band details due to hybridization, which is in line with the scenario (iii). In this context, the alternative possibility that $\nu = +4$ corresponds to a flavor-polarization reset at $\nu_{\text{flat}} = +3$ is highly unlikely. Finally, we note that this line of argument cannot fully rule out scenario (ii) due to the potential presence of small dispersive pockets in the flat bands that may remain unfilled near $\nu = +4$.

Appendix C

SUPPLEMENTARY MATERIALS FOR CHAPTER 6

Identification of FP(2, 2, 2) phase by quantum oscillations

Ultrahigh-resolution quantum oscillations at high D fields allow for resolving subtle symmetry-breaking Fermi pockets. Looking carefully at the FFT frequency $f_v^{(2)}$ in Fig. C.2b and Fig. C.1b,d, $f_v^{(2)}$ decreases monotonically with lowering doping until reaching $n = -8.25 \times 10^{11} \text{ cm}^{-2}$ for $D/\epsilon_0 = 1.265 \text{ V/nm}$ ($n = -7.2 \times 10^{11} \text{ cm}^{-2}$ for $D/\epsilon_0 = 1.2 \text{ V/nm}$), beyond which the dependence of $f_v^{(2)}$ is flattened while $f_v^{(1)}$ keeps increasing throughout. This indicates that the sum rule $2 \cdot f_v^{(1)} + 4 \cdot f_v^{(2)} \approx 1$ of the FP(2, 4) phase at higher doping is no longer satisfied for lower dopings, suggesting an altered Fermi-surface structure. Indeed, measuring quantum oscillations to higher B_\perp field reveals the emergence of a third very low frequency around the phase boundary as marked by the green arrows in Fig. C.3. FFT data shown in Fig. C.2b and Fig. C.1b,d clearly reveal the third frequency $f_v^{(3)}$ growing rapidly from zero at the phase boundary to a value matching $f_v^{(2)}$ at slightly higher doping. The frequencies obey $2 \cdot f_v^{(1)} + 2 \cdot f_v^{(2)} + 2 \cdot f_v^{(3)} \approx 1$, as discussed in the main text corresponding to an additional symmetry breaking with trigonally warped pockets of two sizes $f_v^{(2)}$ and $f_v^{(3)}$.

Identification of FP(1, 3, 1) phase by quantum oscillations

The identification of FP(1, 3, 1) phase is more subtle, involving extensive quantum oscillation measurements. The raw data (Fig. C.3a,b; $n \approx -6.6 \times 10^{11} \text{ cm}^{-2}$ to $-5.3 \times 10^{11} \text{ cm}^{-2}$ taken at $D/\epsilon_0 \approx 1.2 \text{ V/nm}$) reveal three oscillation frequencies. A high frequency marked $f_v^{(4)}$ appears clearly. At really low $B_\perp \sim 0.05 \text{ T}$, a relatively low frequency called $f_v^{(6)}$ onsets. Further increasing B_\perp , each $f_v^{(6)}$ period splits into four, giving rise to $f_v^{(5)}$ which is indeed roughly four times the frequency $f_v^{(6)}$ (Fig. C.3c).

It is natural to ask whether $f_v^{(5)}$ is simply a higher (fourth) harmonic of $f_v^{(6)}$. This can be answered by the measurements at low D fields in the same phase region (Fig. C.4 and C.5). Frequencies are marked by arrows. When lowering the D fields, $f_v^{(4)}$ gradually increases, while $f_v^{(5)}$ and $f_v^{(6)}$ gradually decrease. At $D/\epsilon_0 = 1 \text{ V/nm}$ (Fig. C.4b,d,f), $f_v^{(5)}$ already deviates from being four times the value of $f_v^{(6)}$. Eventually at $D/\epsilon_0 = 0.85 \text{ V/nm}$ (Fig. C.4a,c,e), the frequency $f_v^{(6)}$

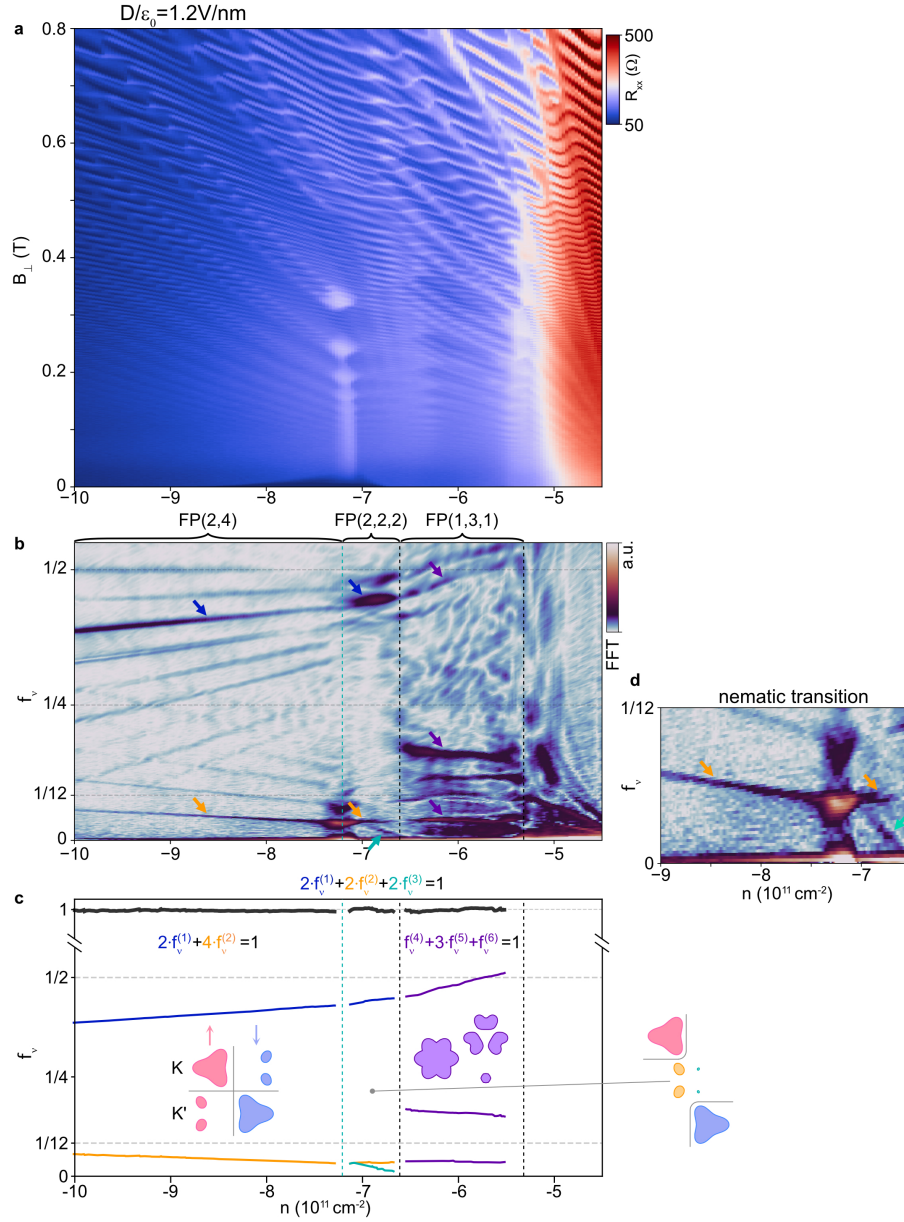


Figure C.1: Quantum oscillations and FFT measured at $D/\epsilon_0 = 1.2 \text{ V/nm}$. (a) R_{xx} versus out-of-plane magnetic field B_{\perp} and doping density n measured at $D/\epsilon_0 = 1.2 \text{ V/nm}$ for a device with $|\lambda_I| \approx 1.5 \text{ meV}$. (b) Frequency-normalized Fourier transform of $R_{xx}(1/B_{\perp})$ over the same density range as in (a). (c) Intensity peaks in f_{ν} from (b). (d) zoom-in image at low frequencies from (b).

completely disappears while $f_{\nu}^{(5)}$ independently survives. This D evolution of the two frequencies ($f_{\nu}^{(5)}$ and $f_{\nu}^{(6)}$) supports their independence. Meanwhile at $D/\epsilon_0 = 0.85 \text{ V/nm}$, the existing two frequencies ($f_{\nu}^{(4)}$ and $f_{\nu}^{(5)}$) obey $f_{\nu}^{(4)} + 3 \cdot f_{\nu}^{(5)} \approx 1$; we denote the flavor-polarized phase at this D field as FP(1, 3). The above D -field

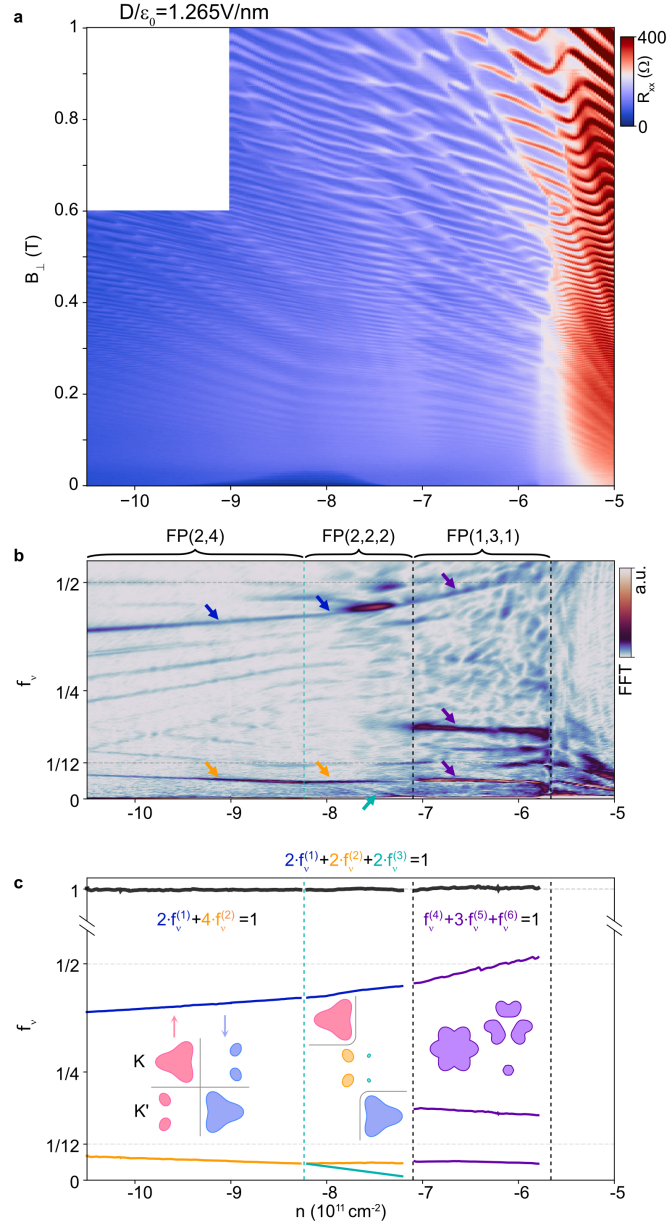


Figure C.2: Quantum oscillations and FFT measured at $D/\epsilon_0 = 1.265 \text{ V/nm}$. (a) R_{xx} versus out-of-plane magnetic field B_{\perp} and doping density n measured at $D/\epsilon_0 = 1.265 \text{ V/nm}$ for a device with $|\lambda_I| \approx 1.5 \text{ meV}$. (b) Frequency-normalized Fourier transform of $R_{xx}(1/B_{\perp})$ over the same doping density range as in (a). (c) Intensity peaks in f_{ν} from (b).

evolution indicates that the FP(1, 3, 1) phase at high D develops from the FP(1, 3) phase at low D as D is increased.

After establishing the existence of three frequencies, we comment on the number of pockets for each type. This relies on the correct identification of intrinsic

Fermi-surface frequencies and their harmonics. At slightly higher B_{\perp} , magnetic breakdown kicks in as B_{\perp} -assisted electron tunneling between different Fermi surfaces. Consequently, the pronounced frequencies might be a sum (or difference) of two base frequencies instead of the intrinsic ones. This is the case for FP(1, 3) and FP(1, 3, 1) phase. Fig. C.4c shows the normalized FFT from quantum oscillations going up to $B_{\perp} = 0.45$ T. The frequency peak at $f_{\nu} \sim 0.75$ is stronger than the one at $f_{\nu} \sim 0.6$ (marked by the arrow). However, the relative intensity changes by reducing the B_{\perp} range to 0.23T (Fig. C.6a). At this condition, the peak at $f_{\nu} \sim 0.6$ is stronger than the one at $f_{\nu} \sim 0.75$, suggesting that the one marked by the arrow ($f_{\nu} \sim 0.6$ in Fig. C.6a) is the intrinsic frequency; the one at $f_{\nu} \sim 0.75$ is instead a sum harmonic $f_{\nu}^{(4)} + f_{\nu}^{(5)}$. By identifying the intrinsic high frequency $f_{\nu}^{(4)}$, one obtains $f_{\nu}^{(4)} + 3 \cdot f_{\nu}^{(5)} \approx 1$, indicating one large and three small Fermi surfaces, i.e., FP(1, 3). A similar situation holds for the other D fields, such as at $D/\epsilon_0 = 1.2$ V/nm (see Fig. C.5c and Fig. C.6c), where we find $f_{\nu}^{(4)} + 3 \cdot f_{\nu}^{(5)} + f_{\nu}^{(6)} \approx 1$.

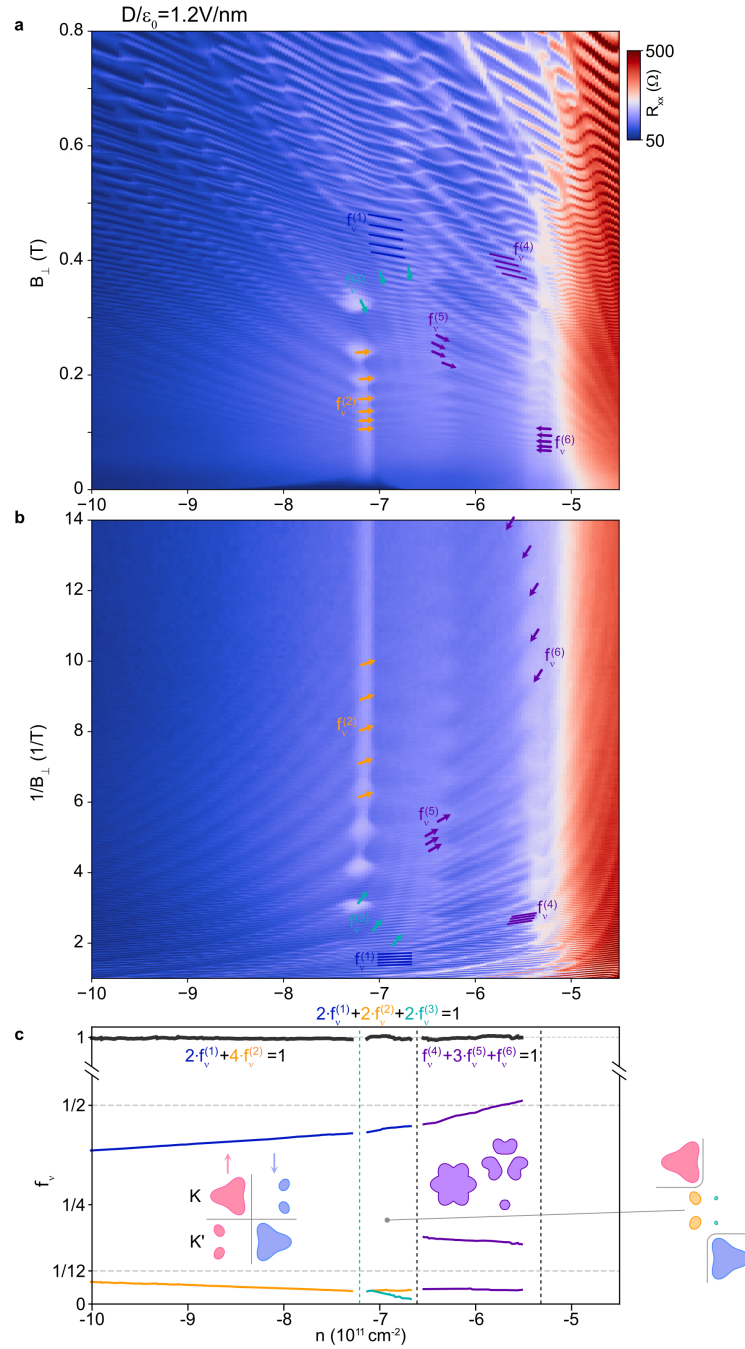


Figure C.3: Identifying FP(2, 2, 2) and FP(1, 3, 1) frequencies from the raw data. (a) R_{xx} versus out-of-plane magnetic field B_{\perp} and doping density n measured at $D/\epsilon_0 = 1.2$ V/nm for a device with $|\lambda_I| = 1.5$ meV. (b) The same data as in (a), but plotted as a function of $1/B_{\perp}$. The corresponding frequencies are marked by colored arrows/lines. (c) Intensity peaks in f_y extracted from the FFT data.

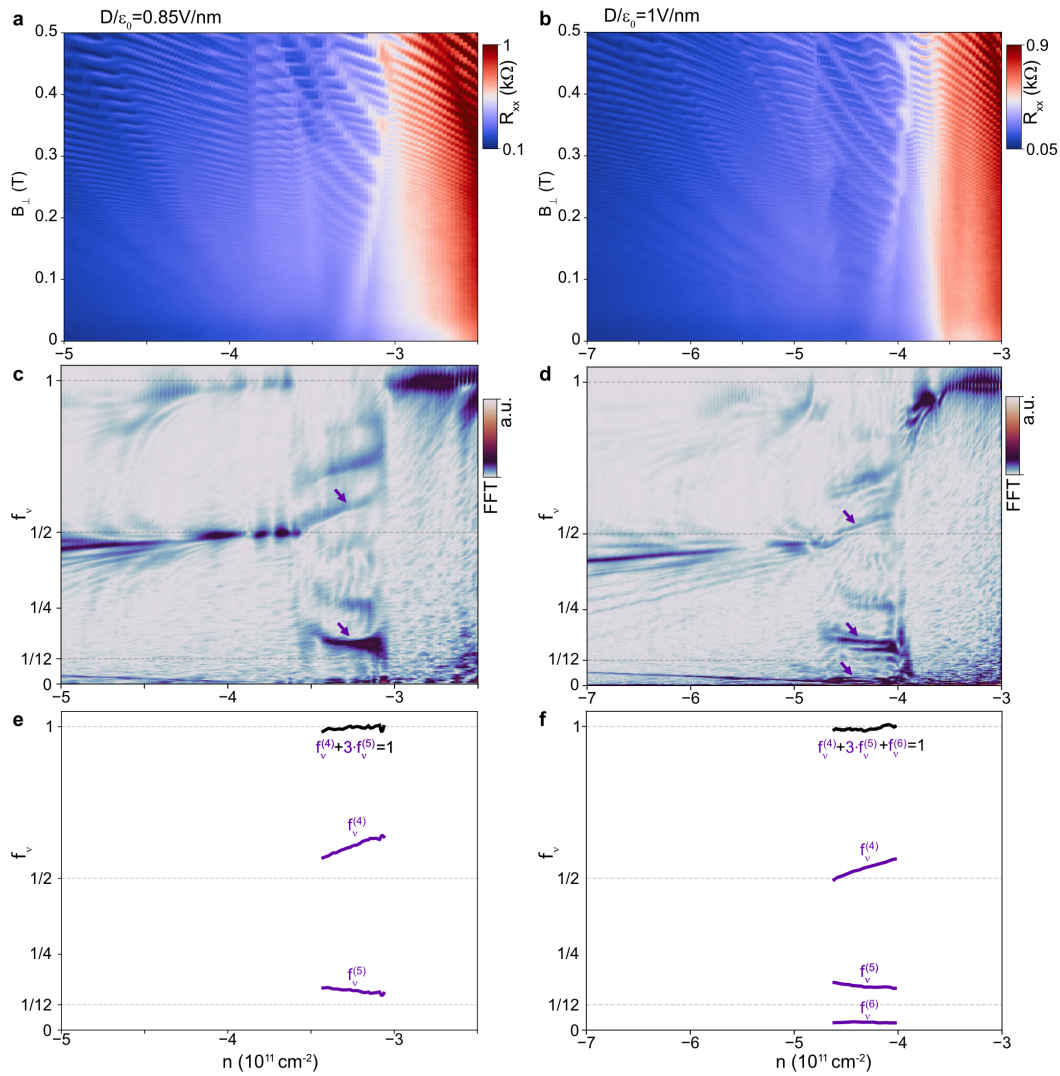


Figure C.4: FP(1, 3) and FP(1, 3, 1) at $D/\epsilon_0 = 0.85 \text{ V/nm}$ and 1 V/nm , respectively. (a),(b) R_{xx} versus out-of-plane magnetic field B_{\perp} and doping density n measured at $D/\epsilon_0 = 0.85 \text{ V/nm}$ (a) and 1 V/nm (b), respectively. (c),(d) Frequency-normalized Fourier transform of R_{xx} ($1/B_{\perp}$) at $D/\epsilon_0 = 0.85 \text{ V/nm}$ (c) and 1 V/nm (d), respectively. (e),(f) Intensity peaks in f_{ν} extracted from the FFT data in (c) and (d).

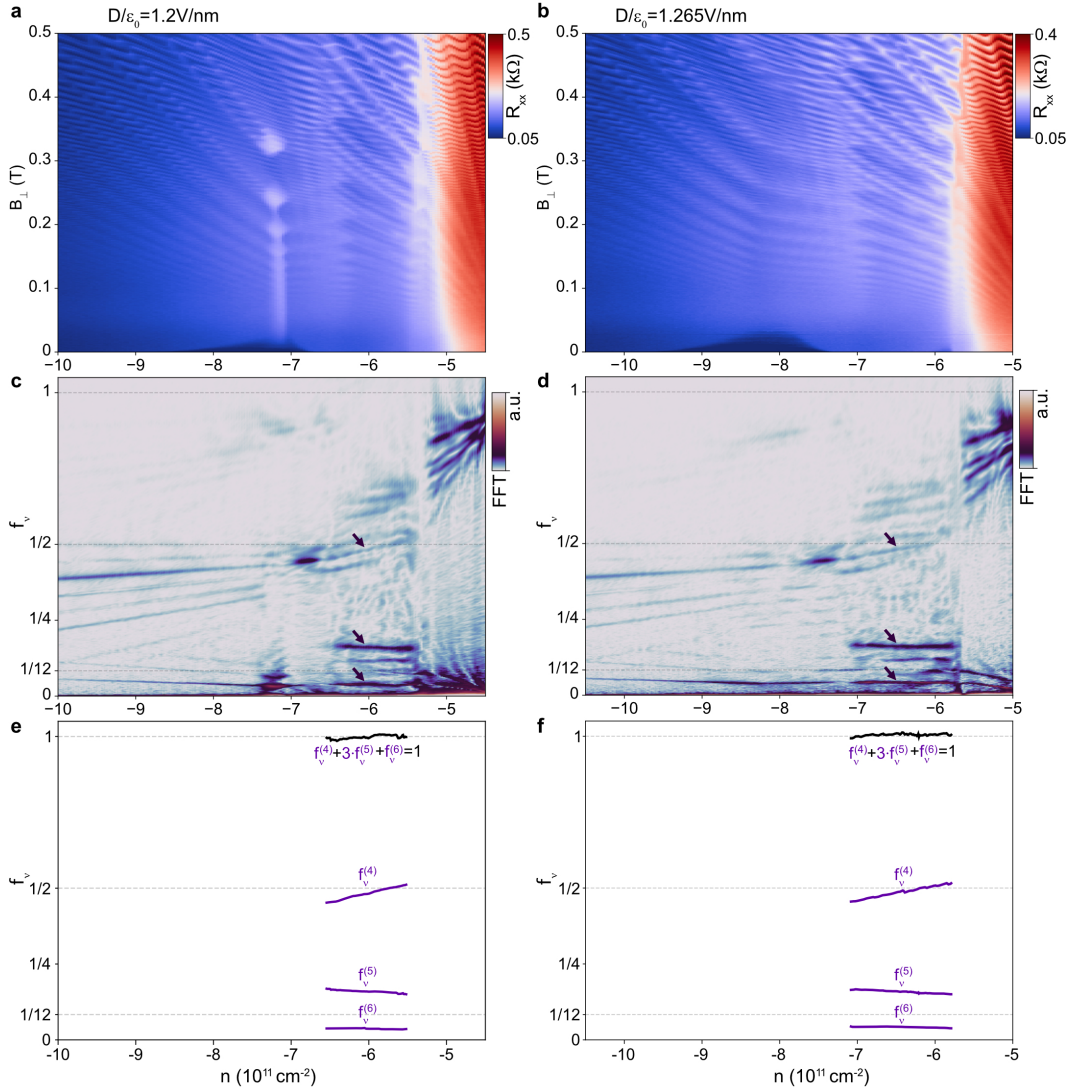


Figure C.5: FP(1, 3, 1) at $D/\epsilon_0 = 1.2$ V/nm and 1.265 V/nm. (a),(b) R_{xx} versus out-of-plane magnetic field B_{\perp} and doping density n measured at $D/\epsilon_0 = 1.2$ V/nm (a) and 1.265 V/nm (b), respectively. (c),(d) Frequency-normalized Fourier transform of $R_{xx}(1/B_{\perp})$ at $D/\epsilon_0 = 1.2$ V/nm (c) and 1.265 V/nm (d), respectively. (e),(f) Intensity peaks in f_{ν} extracted from the FFT data in (c) and (d).

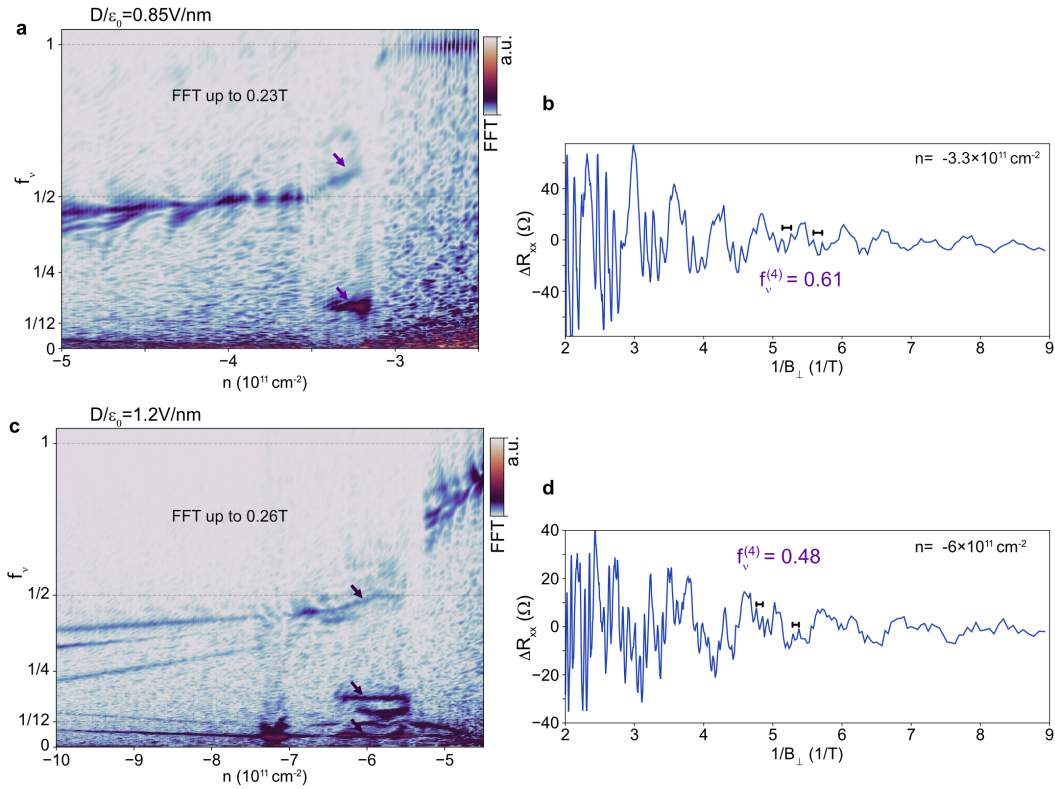


Figure C.6: FFT of FP(1, 3) and FP(1, 3, 1) with data at lower magnetic field. (a),(c) Frequency-normalized Fourier transform of $R_{xx}(1/B_{\perp})$ at $D/\epsilon_0 = 0.85 \text{ V/nm}$ (a) and 1.2 V/nm (c), respectively. The R_{xx} data are used up to 0.23 T and 0.26 T respectively. (b),(d) R_{xx} variation ΔR_{xx} as a function $1/B_{\perp}$ measured at $n = -3.3 \times 10^{11} \text{ cm}^{-2}$, $D/\epsilon_0 = 0.85 \text{ V/nm}$ (b) and $n = -6 \times 10^{11} \text{ cm}^{-2}$, $D/\epsilon_0 = 1.2 \text{ V/nm}$ (d), respectively.

Inter-valley coherence

The occurrence of superconducting state SC_3 in the symmetry-breaking state $FP(1, 3, 1)$ strongly indicates the inter-valley coherent nature of $FP(1, 3, 1)$. Focusing on the single largest Fermi pocket ($f_v^{(4)}$) that is non-degenerate, there are two options: it is either valley-polarized and therefore breaks time-reversal symmetry, or it is inter-valley coherent. Coherence between the K and K' valleys would restore time reversal symmetry for the largest Fermi pocket, naturally more susceptible to pairing. Note that in moiré graphene cases, it is established that superconductivity originates from an inter-valley-coherent order [41, 42].

Independent evidence for inter-valley coherence comes from analyzing the evolution of phase boundaries as a function of B_\perp . An out-of-plane magnetic field B_\perp favors valley-polarized states that are characterized by large orbital moments. As B_\perp field is increased, valley-polarized states with large orbital moments are expected to take over more of the phase space compared to valley-balanced states [199]. The evolution of the phase boundaries with B_\perp can be clearly identified from quantum oscillations (Fig. C.7). Here, the lowest doping density range ($n > -3 \times 10^{11} \text{ cm}^{-2}$) corresponds to a spin-valley locked $FP(6)$ phase [56]. Within this phase, the K and K' valleys are equally populated with opposite spins, resulting in zero net orbital moment. At the doping density $-3 > n > -4.3 \times 10^{11} \text{ cm}^{-2}$, the oscillation frequency peaks at $f_v = 1$ indicating $FP(1)$ phase. The phase space shows a rich evolution: a phase transition develops with increasing B_\perp , consistent with a spin-valley polarized $FP(1)$ (red line) emerges when B_\perp is applied. Importantly, at the lowest B_\perp ($B_\perp \sim 0 \text{ T}$), the phase boundary between $FP(1)$ and $FP(6)$ (black dashed line at $n \approx -3 \times 10^{11} \text{ cm}^{-2}$) does not move with B_\perp , suggesting that the $FP(1)$ at $B_\perp \sim 0 \text{ T}$ is characterized by coherence of the two valleys (over spin-valley polarized phase), so that the orbital moments cancel. The same logic applies to other symmetry-breaking phases at slightly higher doping. A large FFT frequency dominates at $f_v > 1/2$ while the phase boundaries persist in doping without moving when B_\perp is applied, suggesting the existence of one large Fermi pocket with diminished or no orbital moments and hence inter-valley coherence for $FP(1, 3, 1)$.

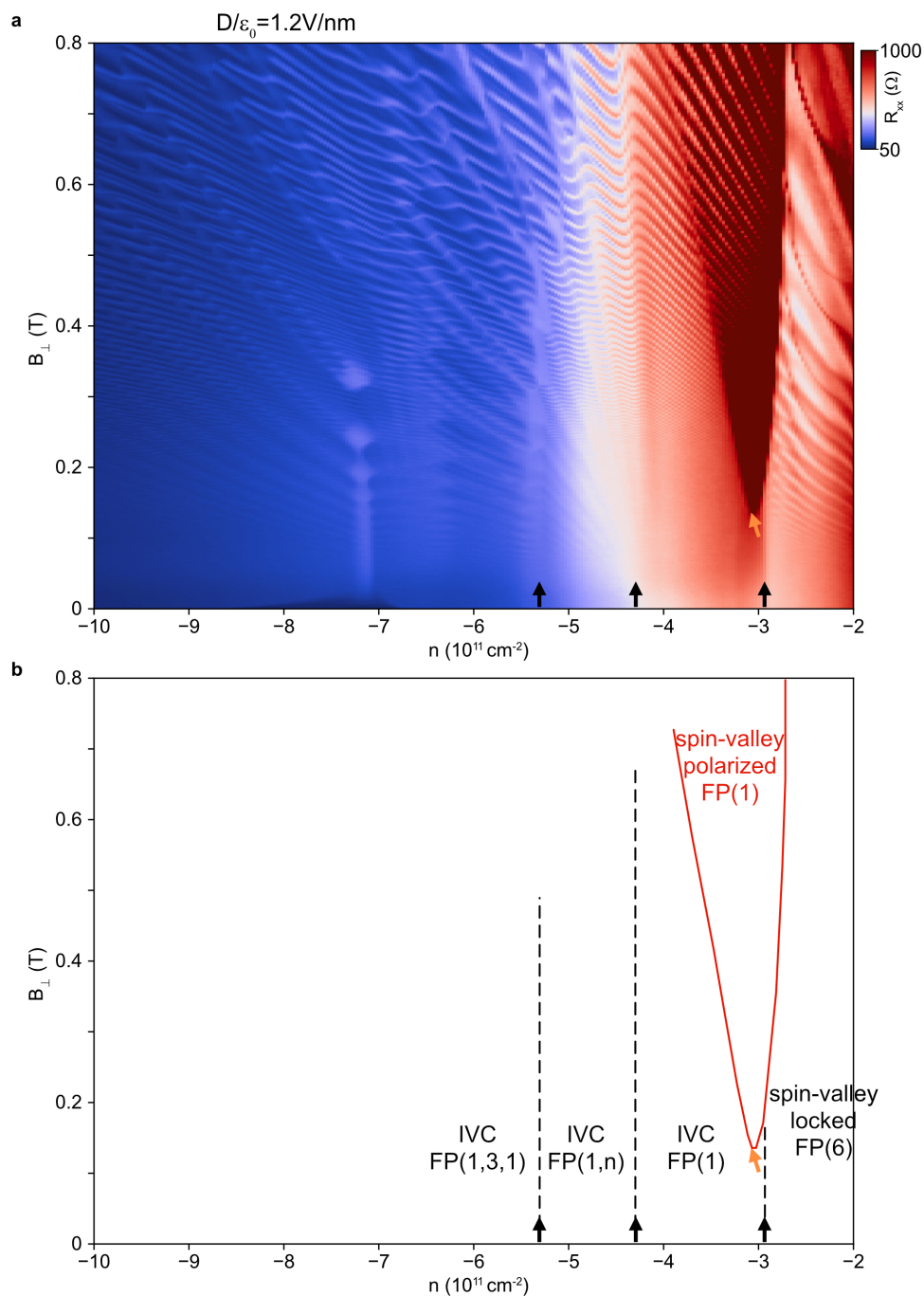


Figure C.7: Evolution of phase boundaries as a function of B_{\perp} . (a) R_{xx} versus out-of-plane magnetic field B_{\perp} and doping density n measured at $D/\epsilon_0 = 1.2 \text{ V/nm}$ for a device with $|\lambda_I| \approx 1.5 \text{ meV}$. Phase boundaries are marked out in (b). The black arrows and dashed lines mark the phase boundaries that are not sensitive to B_{\perp} , suggestive of inter-valley coherence with little or no net orbital moments. The red line draws the phase boundary of the spin-valley polarized FP(1); the boundary grows (orange arrow) with B_{\perp} due to large orbital moments.

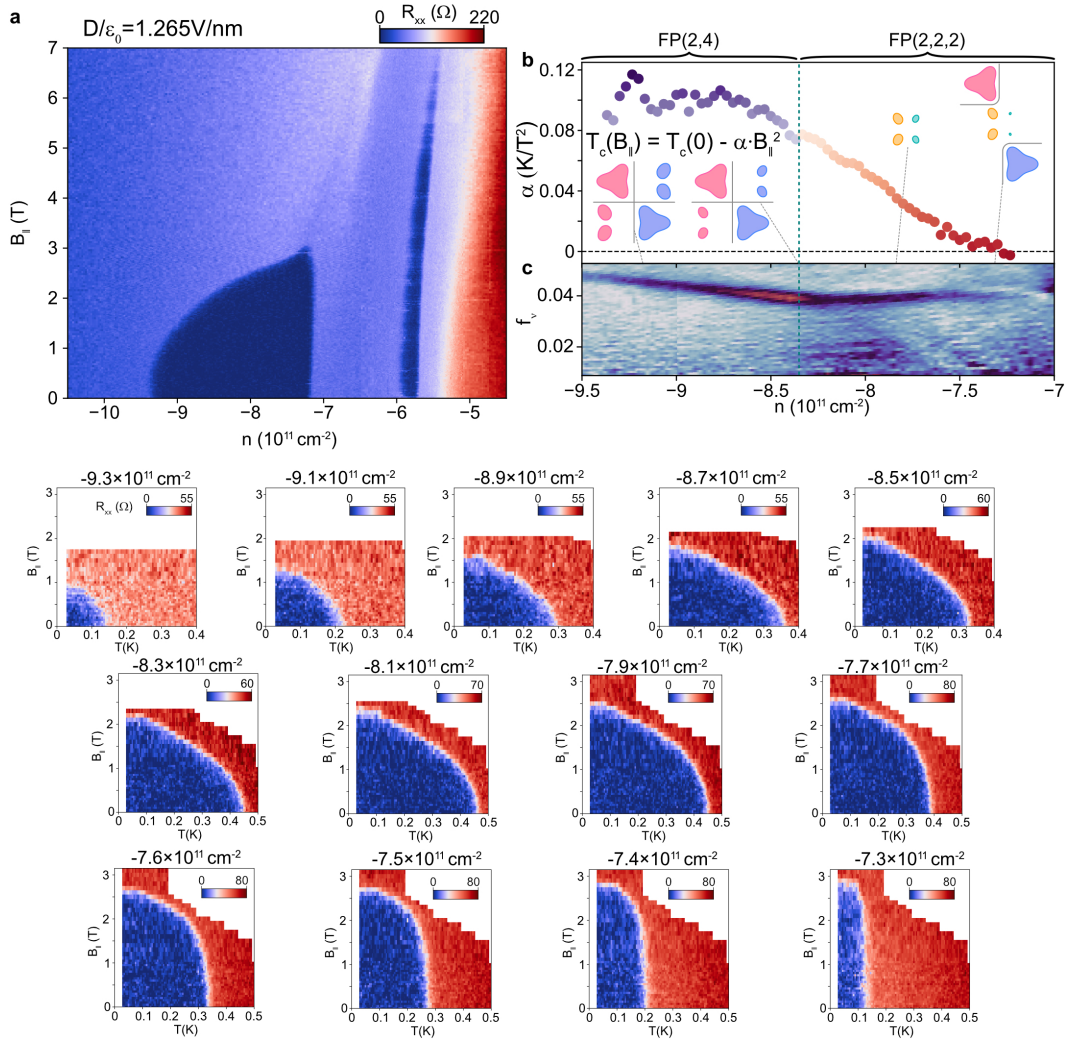


Figure C.8: B_{\parallel} dependence of SC_2 at $D/\epsilon_0 = 1.265 \text{ V/nm}$. (a) R_{xx} versus doping and B_{\parallel} focusing around SC_2 at $D/\epsilon_0 = 1.265 \text{ V/nm}$. (b) Fitting coefficient α versus doping density n for SC_2 at the same D . (c) Frequency-normalized Fourier transform of $R_{xx}(1/B_{\perp})$ over the same doping range as in (b), focusing around low frequencies representing the two types of trigonal-warping pockets. Bottom panels show R_{xx} versus temperature and B_{\parallel} at different doping for $D/\epsilon_0 = 1.265 \text{ V/nm}$.

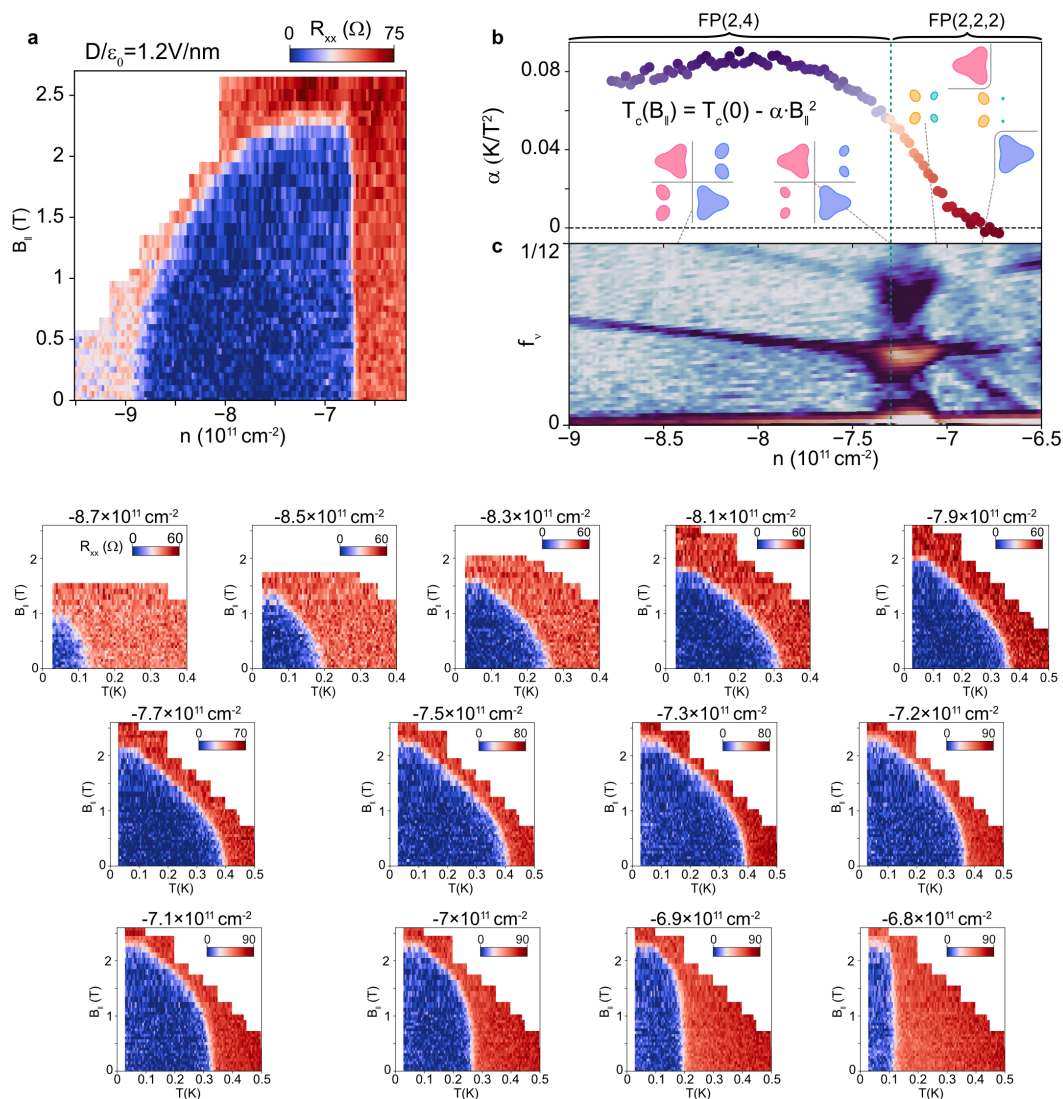


Figure C.9: B_{\parallel} dependence of SC_2 at $D/\epsilon_0 = 1.2 \text{ V/nm}$. (a) R_{xx} versus doping and B_{\parallel} focusing around SC_2 at $D/\epsilon_0 = 1.2 \text{ V/nm}$. (b) Fitting coefficient α versus doping density n for SC_2 at the same D . (c) Frequency-normalized Fourier transform of $R_{xx}(1/B_{\perp})$ over the same doping range as in (b), focusing around low frequencies representing the two types of trigonal-warping pockets. Bottom panels show R_{xx} versus temperature and B_{\parallel} at different doping for $D/\epsilon_0 = 1.2 \text{ V/nm}$.

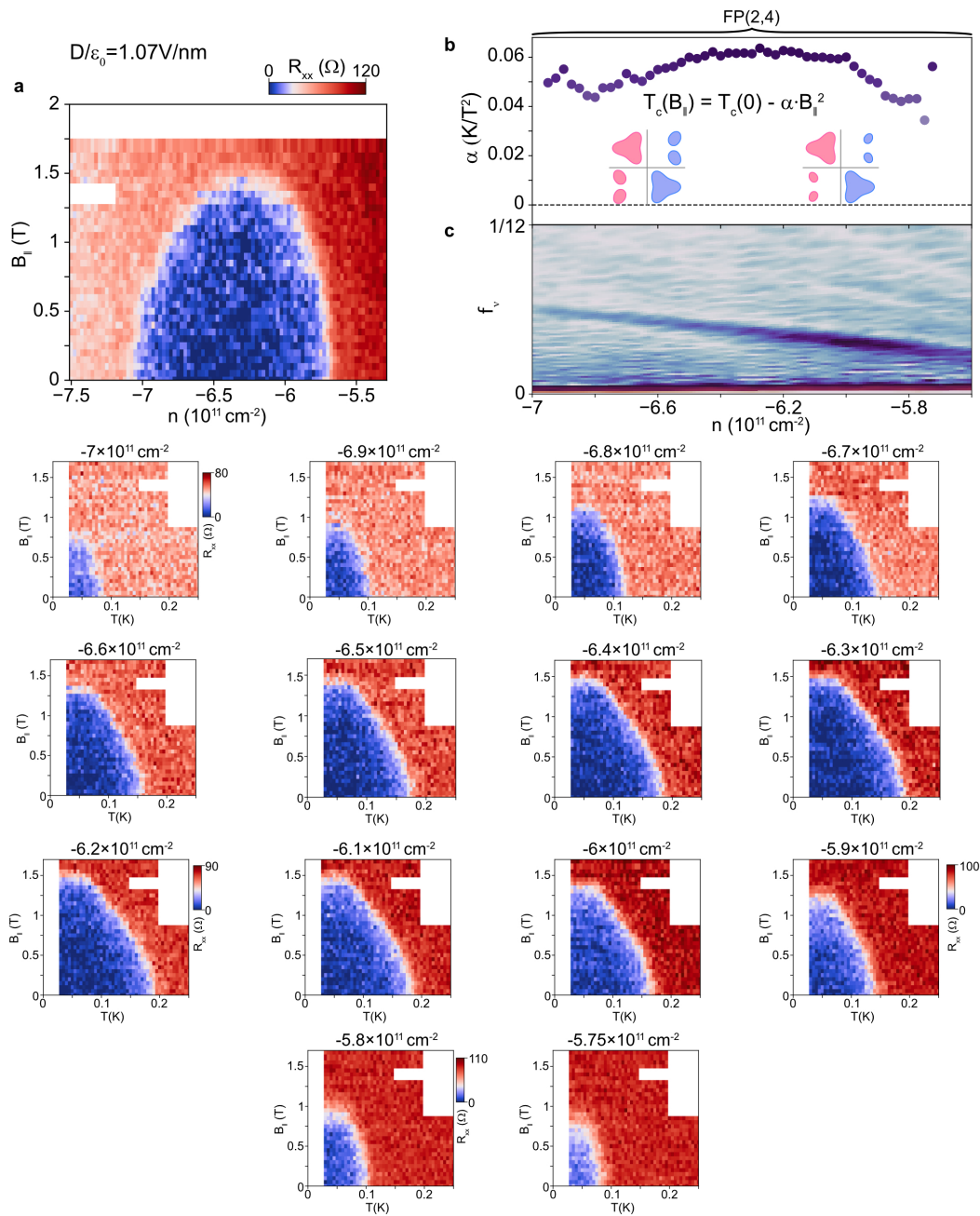


Figure C.10: B_{\parallel} dependence of SC_2 at $D/\epsilon_0 = 1.07 \text{ V/nm}$. (a) R_{xx} versus doping and B_{\perp} focusing around SC_2 at $D/\epsilon_0 = 1.07 \text{ V/nm}$. (b) Fitting coefficient α versus doping density n for SC_2 at the same D . (c) Frequency-normalized Fourier transform of $R_{xx}(1/B_{\perp})$ over the same doping range as in (b), focusing around low frequencies representing the single type of trigonal-warping pockets without nematic redistribution of holes. Bottom panels show R_{xx} versus temperature and B_{\perp} at different doping at $D/\epsilon_0 = 1.07 \text{ V/nm}$. At this D field, SC_2 does not onset from $\text{FP}(2, 2, 2)$. The rapidly changed α with diminished values are accordingly absent.